Computed radiography system modeling, simulation and optimization

Min Yao

Numéro d'ordre 2014ISAL0128 Année 2014

THESE

Computed Radiography System Modeling, Simulation and Optimization

Modélisation, simulation et optimisation d'une chaîne d'imagerie de radiographie numérique avec écrans photo-stimulables

Présentée devant
l'Institut National des Sciences Appliquées de Lyon

pour obtenir
le GRADE DE DOCTEUR

Ecole doctorale :
Electronique, Electrotechnique, Automatique

Spécialité :
Traitement du Signal et de l'Image

par
Min YAO

Thèse soutenue le 12 décembre 2014 devant la Commission d'examen

Jury

Gerd-Rüdiger JAENISCH	Rapporteur	BAM Allemagne
Patrice LAQUERRIERE	Rapporteur	IPHC Strasbourg
Gérard MONTAROU	Examinateur	LPC Clermont-Ferrand
Jérôme ANTONI	Examinateur	INSA de Lyon - LVA
Valérie KAFTANDJIAN	Directrice de thèse	INSA de Lyon - LVA
Philippe DUVAUCHELLE	Co-directeur de thèse	INSA de Lyon - LVA
Angela PETERZOL-PARMENTIER	Invité	AREVA NDE-Solutions
Andreas SCHUMM	Invité	EDF R&D SINETICS
Peter WILLEMS	Invité	GE Measurement& Control

LVA - EA 677
25, avenue Jean Capelle, 69621 Villeurbanne Cedex (FRANCE)

INSA Direction de la Recherche - Ecoles Doctorales – Quinquennal 2011-2015

SIGLE	ECOLE DOCTORALE	NOM ET COORDONNEES DU RESPONSABLE
CHIMIE	**CHIMIE DE LYON** **http://www.edchimie-lyon.fr** Sec : Renée EL MELHEM Bat Blaise Pascal 3e etage 04 72 43 80 46 Insa : R. GOURDON	M. Jean Marc LANCELIN Université de Lyon – Collège Doctoral Bât ESCPE 43 bd du 11 novembre 1918 69622 VILLEURBANNE Cedex Tél : 04.72.43 13 95 directeur@edchimie-lyon.fr
E.E.A.	**ELECTRONIQUE, ELECTROTECHNIQUE, AUTOMATIQUE** **http://edeea.ec-lyon.fr** Sec : M.C. HAVGOUDOUKIAN eea@ec-lyon.fr	M. Gérard SCORLETTI Ecole Centrale de Lyon 36 avenue Guy de Collongue 69134 ECULLY Tél : 04.72.18 60.97 Fax : 04 78 43 37 17 Gerard.scorletti@ec-lyon.fr
E2M2	**EVOLUTION, ECOSYSTEME, MICROBIOLOGIE, MODELISATION** **http://e2m2.universite-lyon.fr** Sec : Safia AIT CHALAL Bat Darwin - UCB Lyon 1 04.72.43.28.91 Insa : H. CHARLES	Mme Gudrun BORNETTE CNRS UMR 5023 LEHNA Université Claude Bernard Lyon 1 Bât Forel 43 bd du 11 novembre 1918 69622 VILLEURBANNE Cédex Tél : 06.07.53.89.13 e2m2@ univ-lyon1.fr
EDISS	**INTERDISCIPLINAIRE SCIENCES-SANTE** **http://www.ediss-lyon.fr** Sec : Safia AIT CHALAL Hôpital Louis Pradel - Bron 04 72 68 49 09 Insa : M. LAGARDE Safia.ait-chalal@univ-lyon1.fr	Mme Emmanuelle CANET-SOULAS INSERM U1060, CarMeN lab, Univ. Lyon 1 Bâtiment IMBL 11 avenue Jean Capelle INSA de Lyon 696621 Villeurbanne Tél : 04.72.68.49.09 Fax :04 72 68 49 16 Emmanuelle.canet@univ-lyon1.fr
INFOMATHS	**INFORMATIQUE ET MATHEMATIQUES** **http://infomaths.univ-lyon1.fr** Sec :Renée EL MELHEM Bat Blaise Pascal 3e etage infomaths@univ-lyon1.fr	Mme Sylvie CALABRETTO LIRIS – INSA de Lyon Bat Blaise Pascal 7 avenue Jean Capelle 69622 VILLEURBANNE Cedex Tél : 04.72. 43. 80. 46 Fax 04 72 43 16 87 Sylvie.calabretto@insa-lyon.fr
Matériaux	**MATERIAUX DE LYON** **http://ed34.universite-lyon.fr** Sec : M. LABOUNE PM : 71.70 –Fax : 87.12 Bat. Saint Exupéry Ed.materiaux@insa-lyon.fr	M. Jean-Yves BUFFIERE INSA de Lyon MATEIS Bâtiment Saint Exupéry 7 avenue Jean Capelle 69621 VILLEURBANNE Cedex Tél : 04.72.43 83 18 Fax 04 72 43 85 28 Jean-yves.buffiere@insa-lyon.fr
MEGA	**MECANIQUE, ENERGETIQUE, GENIE CIVIL, ACOUSTIQUE** **http://mega.universite-lyon.fr** Sec : M. LABOUNE PM : 71.70 –Fax : 87.12 Bat. Saint Exupéry mega@insa-lyon.fr	M. Philippe BOISSE INSA de Lyon Laboratoire LAMCOS Bâtiment Jacquard 25 bis avenue Jean Capelle 69621 VILLEURBANNE Cedex Tél :04.72 .43.71.70 Fax : 04 72 43 72 37 Philippe.boisse@insa-lyon.fr
ScSo	**ScSo*** **http://recherche.univ-lyon2.fr/scso/** Sec : Viviane POLSINELLI Brigitte DUBOIS Insa : J.Y. TOUSSAINT	Mme Isabelle VON BUELTZINGLOEWEN Université Lyon 2 86 rue Pasteur 69365 LYON Cedex 07 Tél : 04.78.77.23.86 Fax : 04.37.28.04.48 viviane.polsinelli@univ-lyon2.fr

*ScSo : Histoire, Géographie, Aménagement, Urbanisme, Archéologie, Science politique, Sociologie, Anthropologie

Remerciements

Tout prend fin un jour, aujourd'hui c'est la fin de ma thèse. Ces trois années de recherche ont été pour moi comme le voyage 'Alice in Wonderland'. Je ne suis pas Alice, mais c'est mon Wonderland. Ce voyage a été rempli de surprises, bonnes et moins bonnes. Il y a eu des moments où tout se passe bien, et aussi des moments où j'étais perdue et je croyais que je ne trouverais jamais la bonne direction. Heureusement, tout au long du voyage, il y a eu beaucoup de personnes qui m'ont conduite vers les droits chemins, qui m'ont accompagnée, qui m'ont encouragée, et sans qui je n'aurais pu finir cette thèse. Je tiens à exprimer ma gratitude à tout le monde.

Tout à bord, je voudrais remercier à mes directeurs de thèse, Valérie KAFTANDJIAN et Philippe DUVAUCHELLE. Je me sens privilégiée de vous avoir eu pour me guider. Vous avez toujours plein d'idées, et j'apprécie sincèrement vos conseils et votre précieuse contribution dans ce travail. En tant qu'étudiante étrangère d'une culture complètement différente, j'ai eu quelques difficultés de communication, et de ce point de vue là, vous y avez sacrifié plus de temps. Je n'oublierai jamais les préparations de mes deux 'grandes' présentations orales, où vous avez vérifié avec moi tous les détails, mot à mot. Valérie, je te remercie pour ta gentillesse. Tu as une vision globale des choses, et tu trouves toujours directement où sont mes problèmes et vois ce que je ne vois pas. Philippe, merci de ta patience et d'avoir passé beaucoup de temps sur les détails (les modèles, les codes etc.) de mon travail. Vous formez une excellente équipe de directeurs de thèse. Je vous remercie du fond du cœur.

Mes sincères remerciements s'adressent aux membres de Jury d'avoir accepté de juger ce travail : Gerd-Rüdiger JAENISCH, Patrice LAQUERRIERE, Gérard MONTAROU, Jérôme ANTONI. Merci de vos remarques, commentaires et suggestions pour cette thèse.

C'est un grand honneur d'avoir travaillé avec Angela PETERZOL-PARMENTIER, Andreas SCHUMM et Peter WILLEMS. Je vous remercie de votre soutien sur les mesures expérimentales et de vos conseils sur ce travail de thèse. Angela et Andreas, merci d'avoir proposé ce projet de thèse entre AREVA, EDF et l'INSA, et merci d'avoir suivi mon travail tout au long de ces trois ans. Angela, je suis vraiment touchée que tu as continué de suivre ma thèse, même pendant ta période de congés. Merci Andreas de m'avoir encouragée à participer à la COFREND et aux Journées des doctorants d'EDF. Merci aussi de tes conseils par rapport à mon projet professionnel. Peter, j'ai apprécié ta participation à ce travail et tes conseils scientifiques. C'est un plaisir de discuter avec toi de science et de la vie en général. Je ressens ta passion de la science, de la famille et de la vie, et cette passion est ce que j'ai envie de poursuivre depuis toujours.

Je tiens à remercier mes collègues du « 2ème étage ». Daniel BABOT, probablement vous ne savez pas que votre attitude envers la science et la vie m'a profondément touchée. Depuis toujours, dans mon esprit, l'image que j'ai du super professeur vous ressemble. Malheureusement, je n'ai pas eu la chance de suivre vos cours. Philippe GUY, ton esprit jeune et ta jovialité me rendent optimiste, et je te remercie pour les discussions sur Matlab et la langue française. Merci à Thomas MONNIER pour ta gentillesse, ton sens de l'humour et aussi ton aide sur la programmation.

A mes collègues de bureau, un grand merci. Merci pour l'ambiance de travail agréable et joyeuse, Meriem DIB, Raissa DE MELO BRANDÃO, et en particulier Corentin CHESNAIS. Merci Corentin d'avoir toujours répondu avec patience à mes questions relatives à la langue et la culture française. Un grand merci de m'avoir invité dans la région de ta famille, et grâce à toi j'ai vu et touché le premier cheval de ma vie. Mes anciens collègues de bureau, je ne vous ai pas oublié : Florian MONTAGNER, Florent MOUGEL, Marjorie PIERRETTE, Xiaodong DENG et Naïma ALAOUI ISMAILI. Je n'oublierai jamais les bons restaurants et les bons moments qu'on a passé ensemble. Naïma, le voyage en Turquie était super.

Merci à mes amis du LVA : Liangfen DU, Liang YU, Ge XIN, Marion BERTON, Laurent BROCOLINI, Youssef GERGES, Michael VANNIER, Thibault LAFONT, Anders LINDBERG, Fulbert MBAILASSEM, Valentin MEYER, Antonio PEREIRA et tout le monde au LVA. J'adore ce laboratoire multiculturel.

Je souhaite aussi remercier Xiaojiao YANG, Wenjing WANG, Liuqing WANG et Xiaolu JIANG. Merci pour vos aides et vos encouragements pendant les périodes difficiles. A Xi YU, tu vois toujours le bon côté des gens et des situations, et merci de ton aide en informatique. Merci à Jing XIE et Hexiang YAN pour le voyage à Barcelone, merci à Mingyuan JIU et Zhenzhong GUO pour le voyage en Norvège et en Suède. Merci à mes amis qui ne sont plus en France, Huagui ZHANG, Rui XU, Xun SUN et Xi JIANG, vous me manquez.

Enfin, je voudrais remercier particulièrement mes parents pour leur soutien inconditionnel, sans qui rien n'aurait pu commencer. Si j'avais eu le choix de mes parents, c'est sans nul doute vous que j'aurais choisi.

Abstract

For over a century, film-based radiography has been used as a nondestructive testing technique for industrial inspections. With the advent of digital techniques in the medical domain, the NDT community is also considering alternative digital techniques. Computed Radiography (CR) is a cost-efficient and easy-to-implement replacement technique because it uses equipment very similar to film radiography. This technology uses flexible and reusable imaging plates (IP) as a detector to generate a latent image during x-ray exposure. With an optical scanning system, the latent image can be readout and digitized resulting in a direct digital image. CR is widely used in the medical field since it provides good performance at low energies. For industrial inspection, CR application is limited by its poor response to high energy radiation and the presence of scattering phenomena. To completely replace film radiography by such a system, its performance still needs to be improved by either finding more appropriate IPs or by optimizing operating conditions. Guidelines have been addressed in international standards to ensure a good image quality supplied by CR system, where metallic screens are recommended for the case of using high energy sources. However, the type and thickness of such a screen are not clearly defined and a large panel of possible configurations does exist.

Simulation is a very useful tool to predict experimental outcomes and determine the optimal operating conditions. The Monte Carlo (MC) methods are widely accepted as the most accurate method to simulate radiation transport problems. It can give insight about physical phenomena, but due to its random nature, a large amount of computational time is required, especially for simulations involving complex geometries. Deterministic methods, on the other hand, can handle easily complex geometry, and are quite efficient. However, the estimation of scattering effects is more difficult with deterministic methods.

In this thesis work, we have started with a Monte Carlo simulation study in order to investigate the physical phenomena involved in IP and in metallic screens at high energies. In particular we have studied separately the behavior of X-ray photons and electrons. Some experimental comparisons have been carried out at the European Synchrotron Radiation Facility. Then, we have proposed a hybrid simulation approach, combining the use of deterministic and Monte Carlo code, for simulating the imaging of complex shapes objects. This approach takes into account degradation introduced by X-ray scattering and fluorescence inside IP, as well as optical photons scattering during readout process. Different simulation configurations have been compared.

Keywords — Computed Radiography, Modeling, Simulation, Optimization, Monte Carlo, Non-Destructive Testing,High energy application

Résumé

Depuis plus d'un siècle, la radiographie sur film est utilisée pour le contrôle non destructif (CND) de pièces industrielles. Avec l'introduction de méthodes numériques dans le domaine médical, la communauté du CND industriel a commencé à considérer également les techniques numériques alternatives au film. La radiographie numérique (en anglais Computed radiography -CR) utilisant les écrans photostimulables (en anglais imaging plate -IP) est une voie intéressante à la fois du point de vue coût et facilité d'implémentation. Le détecteur (IP) utilisé se rapproche du film car il est flexible et réutilisable. L'exposition de l'IP aux rayons X génère une image latente qui est ensuite lue et numérisée grâce à un système de balayage optique par laser. A basse énergie, les performances du système CR sont bonnes ce qui explique son utilisation importante dans le domaine médical. A haute énergie par contre, les performances du système CR se dégradent à la fois à cause de la mauvaise absorption de l'IP mais également de la présence de rayonnement diffusé par la pièce qui, étant d'énergie plus faible, est préférentiellement absorbée par l'IP. Les normes internationales préconisent l'utilisation d'écrans métalliques pour améliorer la réponse des systèmes CR à haute énergie. Néanmoins, la nature et l'épaisseur de ces écrans n'est pas clairement définie et la gamme des configurations possibles est large.

La simulation est un outil utile pour prévoir les performances d'une expérience et déterminer les meilleures conditions opératoires. Les méthodes Monte Carlo sont communément admises comme étant les plus précises pour simuler les phénomènes de transport de rayonnement, et ainsi comprendre les phénomènes physiques en jeu. Cependant, le caractère probabiliste de ces méthodes implique des temps de calcul importants, voire prohibitifs pour des géométries complexes. Les méthodes déterministes au contraire, peuvent prendre en compte des géométries complexes avec des temps de calcul raisonnables, mais l'estimation du rayonnement diffusé est plus difficile.

Dans ce travail de thèse, nous avons tout d'abord mené une étude de simulation Monte Carlo afin de comprendre le fonctionnement des IP avec écrans métalliques à haute énergie pour le contrôle de pièces de forte épaisseur. Nous avons notamment suivi le trajet des photons X mais également des électrons. Quelques comparaisons expérimentales ont pu être menées à l'ESRF (European Synchrotron Radiation Facility). Puis nous avons proposé une approche de simulation hybride, qui combine l'utilisation de codes déterministe et Monte Carlo pour simuler l'imagerie d'objets de forme complexe. Cette approche prend en compte la dégradation introduite par la diffusion des rayons X et la fluorescence dans l'IP ainsi que la diffusion des photons optiques dans l'IP. Les résultats de différentes configurations de simulation ont été comparés.

Mots clés — Radiographie numériques avec écrans photo-stimulable, Modélisation, Simulation, Optimization, Monte Carlo, Contrôle non-destructif, Application à hautes énergies

RESUME ETENDU

1 Introduction

La radiographie à base de film argentique est de plus en plus remplacée par la radiographie numérique (en anglais « Computed radiography » -CR) avec des écrans photo-stimulables (en anglais « imaging plate » -IP). Le système CR ressemble au système de radiographie conventionnelle (Figure 1) à ceci près que le film argentique est remplacé par un IP afin de générer une image latente (91983Sonoda et al.). En gardant l'avantage de la radiographie conventionnelle, notamment le fait que le détecteur est souple, un système CR apporte d'autres avantages : suppression de la chaîne de développement utilisant des produits chimiques ; réduction du temps d'exposition et utilisation possible de sources de faibles énergies (grâce à la grande sensibilité des détecteurs photo-stimulables) ; grande latitude d'exposition (contrôle de pièces avec de fortes variations d'épaisseur et limitation du nombre d'expositions) ; optimisation du temps d'intervention et partage à distance des images. Pour ces raisons, le système CR est un bon remplacement numérique de la radiographie traditionnelle (81999Seggern; 111996bThoms; 121997Thoms; 72011Leblans et al.).

Pour les applications médicales utilisant des sources de basse énergie (entre 10 et 150 keV) (72011Leblans et al.), le système CR est très satisfaisant grâce à la réponse de l'écran photostimulable ($BaFBr : Eu^{2+}$) qui est optimale dans cette gamme d'énergies. Par contre, pour certaines applications industrielles telles que le contrôle des pièces de fortes épaisseurs (exploitant des sources de haute énergie comme l'iridium ou le cobalt), la performance du système CR est médiocre. Comme le montre la Figure 2, l'écran photo-stimulable a une sensibilité très faible aux énergies du Cobalt. La diffusion générée par une forte épaisseur d'objet, étant d'énergie plus faible que le rayonnement direct, correspond à une partie de la réponse spectrale où les écrans sont très sensibles. De ce fait, le contraste obtenu à haute énergie est mauvais.

Selon les normes internationales (22005EN14784-2) et (62013ISO17636-2), le fait d'utiliser un écran métallique (i.e. un écran renforçateur) en contact avec l'écran photostimulable peut potentiellement renforcer le signal de haute énergie et éliminer le signal de basse énergie (la diffusion ou la fluorescence), afin d'améliorer le contraste aux plus hautes énergies.

La simulation est très utile pour prévoir les résultats des expériences sans besoin

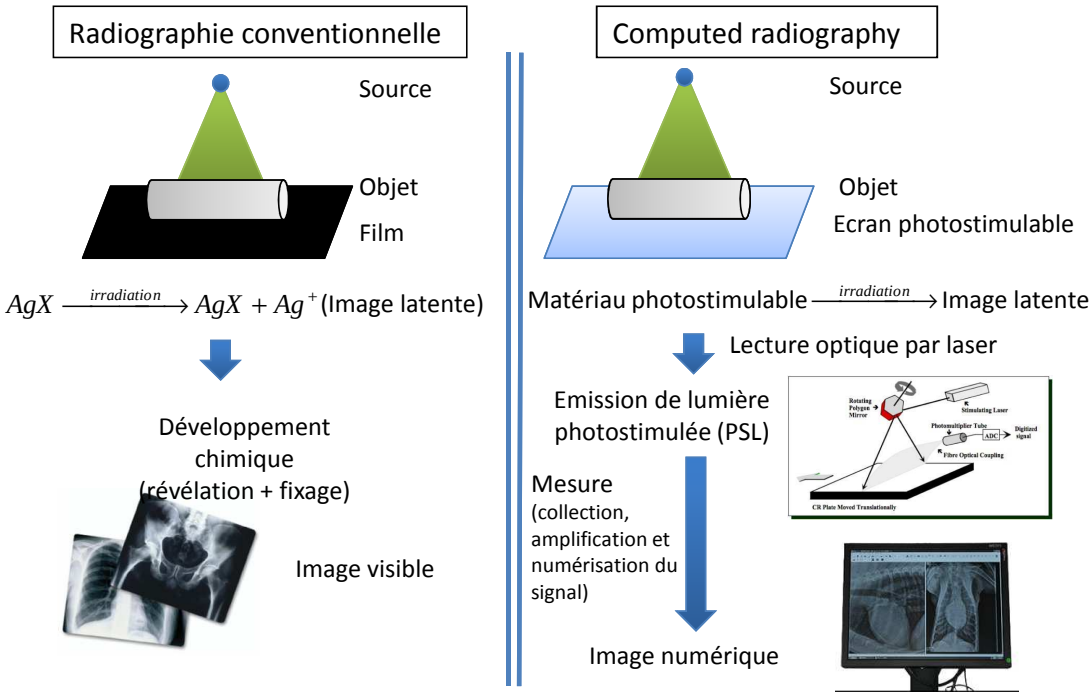

Figure 1: Principes de la radiographie conventionnelle et de la radiographie numérique par les écrans photo-stimulables.

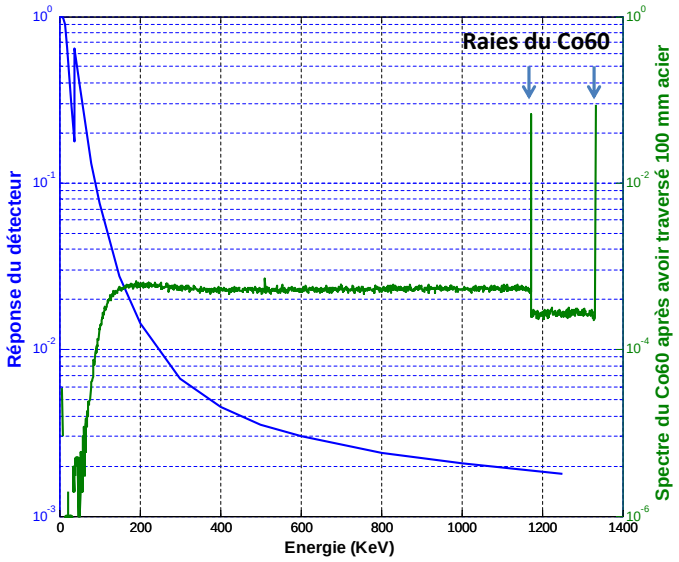

Figure 2: En bleu, la réponse spectrale d'un écran photostimulable: l'écran photostimulable a une sensibilité très faible aux énergies du Cobalt (flèches bleues). En même temps, la diffusion générée par une forte épaisseur d'objet (tracé vert) correspond à une partie de la réponse spectrale où les écrans sont plus sensibles.

d'exposition aux rayonnements. Les études d'un système à l'aide de la simulation permettent d'optimiser sa performance et assurer une bonne qualité d'image. L'objectif de la thèse est de modéliser complètement la formation de l'image dans les systèmes CR: de l'interaction des photons incidents avec l'objet, le dépôt d'énergie et la création d'image latente dans un IP jusqu'à la lecture optique. Cette modélisation sera la base d'un outil de simulation qui est capable de simuler des configurations de paramètres différents afin d'optimiser la qualité de l'image. La thèse s'articule autour de deux thèmes principaux: 1) la compréhension de phénomènes physiques, y compris la réponse d'un IP, les effets d'écrans métalliques[1] et les effets de rayonnement diffusé etc. ; et 2) la modélisation complète de la chaîne d'imagerie du CR. Du point de vue de la simulation de CR industrielle, nous avons besoin d'un modèle raisonnable, sur la base duquel une image réaliste peut être obtenue rapidement, et différents paramètres opératoires tels que la source, la combinaison IP/écrans et la lecture optique peuvent être pris en compte.

[1]Dans la radiographie industrielle, des écrans métalliques minces sont parfois utilisés avec l'IP pour améliorer la qualité d'image.

2 Simulation Monte Carlo de l'exposition aux rayons X

L'objectif de cette première partie de notre étude est d'étudier les phénomènes physiques qui se déroulent pendant l'exposition du système CR aux rayons X, par exemple, le comportement des électrons, le rayonnement diffusé et la fluorescence, etc. A cet égard, nous avons développé un outil de simulation de Monte Carlo, basé sur PENELOPE, qui suit séparément les rayonnements directs et secondaires en différenciant les photons, électrons et positrons. La sortie de simulation fournit les cartes 3D d'énergie déposée dans l'IP due aux rayonnements différents et également l'évaluation de la propagation des spectres de rayonnement après des éléments différents. Cet outil nous permet d'étudier les phénomènes physiques sous-jacents et de caractériser les réponses des écrans. L'utilité de cet outil est montrée par une étude de cas et la caractérisation des réponses de trois écrans.

2.1 Méthode de simulation

Notre outil simule des situations typiques de radiographie c'est-à-dire comprenant une source, un objet et un détecteur (IP seul ou IP avec des écrans métalliques). La Figure 3(a) montre la géométrie adoptée, et les termes employés pour les faisceaux différents issus de l'objet sous test. Après l'objet, la flèche rouge solide représente le rayonnement direct, c'est-à-dire, la partie qui n'a pas subi d'interaction, et tout le rayonnement produit à partir de ce faisceau par la suite que l'on appelle le faisceau utile. Au contraire, la flèche verte pointillé représente le rayonnement secondaire émis par l'objet, et tous les autres rayonnements produits sont désignés comme non-utile. L'information est subdivisée en des signaux dus aux photons dans le faisceau utile ou non-utile (appelé UPS et NUPS), les électrons dans le faisceau utile ou non-utile (noté comme UES et NUES) et, le cas échéant, les positrons dans le faisceau utile ou non-utile (désignés comme UPoS et NUPoS).

La simulation surveille deux types de signaux: le dépôt d'énergie dans l'IP et les spectres après avoir traversé chaque élément entre la source et l'IP (Figure 3(b)). Une grille orthogonale tridimensionnelle uniforme est appliquée sur l'IP pour enregistrer la distribution de dépôt d'énergie. De ce fait, la géométrie de l'IP doit être en forme de parallélépipède.

Le faisceau incident peut être divergente ou non-divergente, émis à partir d'un point ou d'une source étendue, et son spectre peut être spécifique (telle que celui émis par une

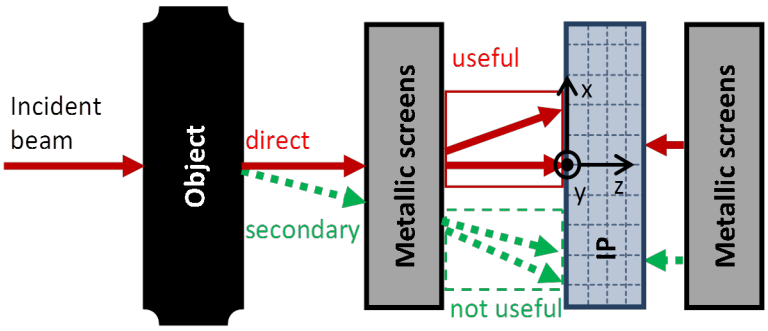

(a)

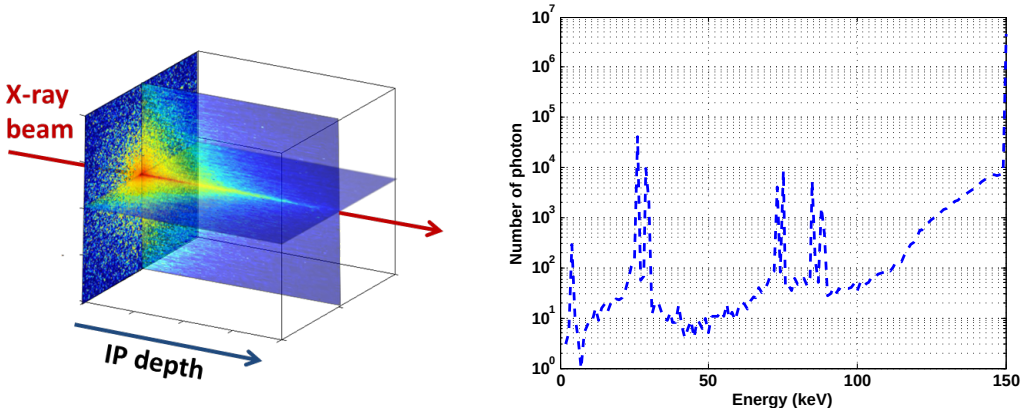

(b)

Figure 3: (a) La géométrie adopté par notre simulation est une chaîne de radiographie classique (le graphique n'est pas à l'échelle). Un système de coordonnées cartésiennes est utilisé pour suivre les trajets des particules. Une grille orthogonale tridimensionnelle uniforme est appliquée sur IP pour enregistrer la distribution de dépôt d'énergie. (b) Exemples des sorties de simulation: carte 3D de dépôt d'énergie dans IP $DEP(x, y, z)$ et un exemple de spectre après l'un des éléments entre la source et l'IP.

source de cobalt ou iridium) ou soit une énergie fixée variant dans une plage précisée $\{\mathrm{E_{min}}, \mathrm{E_{max}}\}$ avec un incrément de $\mathrm{E_{incmt}}$. L'objet et les écrans métalliques peuvent être d'un matériau arbitraire et de forme arbitraire.

La sortie de la simulation nous fournit les données comme suit :

- Carte 3D de dépôt d'énergie due aux faisceaux différents :
  - signal utile de photon $DEP_{UPS}(x, y, z)$;
  - signal non-utile de photon $DEP_{NUPS}(x, y, z)$;
  - signal utile d'électron $DEP_{UES}(x, y, z)$;
  - signal non-utile d'électron $DEP_{NUES}(x, y, z)$;
- Spectre de photon après avoir traversé des éléments différents (c'est-à-dire objet, écrans métalliques et la couche protectrice d'un IP) ;
- Spectre d'électron après avoir traversé des éléments différents (c'est-à-dire objet, écrans métalliques et la couche protectrice d'un IP).

A partir de ces sorties de simulation, les paramètres suivants sont utilisés pour analyser la réponse de l'IP.

- Efficacité d'absorption d'énergie (EAE). EAE est le ratio du dépôt d'énergie total dans l'IP par rapport à l'énergie incidente.
- Fonction de transfert de modulation (MTF) et la fréquence spatiale à 20% de MTF (f_{MTF20}). La MTF est obtenue par :

$$\begin{aligned} MTF(f) &= \mathscr{F}\left(LSF(x)\right) \\ &= \mathscr{F}\left(\sum_{y} PSF(x, y)\right) \\ &= \mathscr{F}\left(\sum_{z,y} DEP(x, y, z)\right) \end{aligned} \tag{1}$$

  où f est la fréquence spatiale, et $\mathscr{F}$ désigne la transformée de Fourier, et $DEP(x, y, z)$ ici est obtenue avec un faisceau incident filiforme.

2.2 Contexte de notre étude : un cas d'inspection typique

Notre cas d'inspection industrielle typique consiste à irradier un objet épais (plaque d'acier de 70 mm) avec une source de haute énergie (Cobalt). Afin d'expliquer le problème de la qualité d'image, nous montrons le résultat obtenu lorsque l'IP seul est utilisé comme un détecteur, sans écran métallique pour intensifier le signal. Un faisceau filiforme est utilisé pour irradier l'objet, afin de montrer la divergence du faisceau (qui est responsable de la dégradation de la résolution spatiale). L'IP est directement placé derrière l'objet, comme dans le cas industriel.

La Figure 4 illustre les images de dépôt d'énergie dans le plan XZ due aux signaux différents. La direction z est la direction du faisceau qui est aussi la direction de la profondeur de l'IP. Comme on peut le voir, les images de signaux utiles (UPS et UES) sont très claires et nettes, tandis que les images de signal non-utiles (NUPS et NUES) sont floues. Dans la Figure 5, nous présentons les courbes de dépôt d'énergie le long de la profondeur de l'IP. Lorsque l'on regarde la profondeur de pénétration, nous voyons que les électrons déposent leur énergie de préférence vers la surface de l'IP (z = 0), tandis que les photons près de la face arrière (z = 150 μm). Dans la Figure 6, nous étudions la contribution des différents signaux à la courbe de MTF globale (noir). Bien que les signaux utiles (UPS et UES) aient une bonne MTF (courbes rouges), la MTF globale (courbe noire) est principalement influencée par les signaux non-utiles (NUPS et NUES). Pour conclure sur notre contexte industriel, nous avons besoin d'un détecteur qui devrait être efficace pour le signal utile de haute énergie, mais insensible au signal utile de basse énergie. Nous voyons qu'une caractérisation des réponses de détecteur est nécessaire.

2.3 Caractérisation des réponses des détecteurs

On étudie maintenant la réponse impulsionnelle du système, ce qui signifie que la réponse à un faisceau filiforme. Tous les éléments (les écrans métalliques et l'IP) ont été mis en parallélépipède, et aucun objet n'est inclus dans le système afin de caractériser les réponses des détecteurs. Une liste des paramètres est montrée dans le tableau 1. Les deux combinaisons IP/écrans ont été comparées avec IP seul. L'écran de configuration « IP+0.2Pb » est celui qui est recommandé par les normes. L'écran d'étain est choisi pour filtrer la fluorescence du Pb.

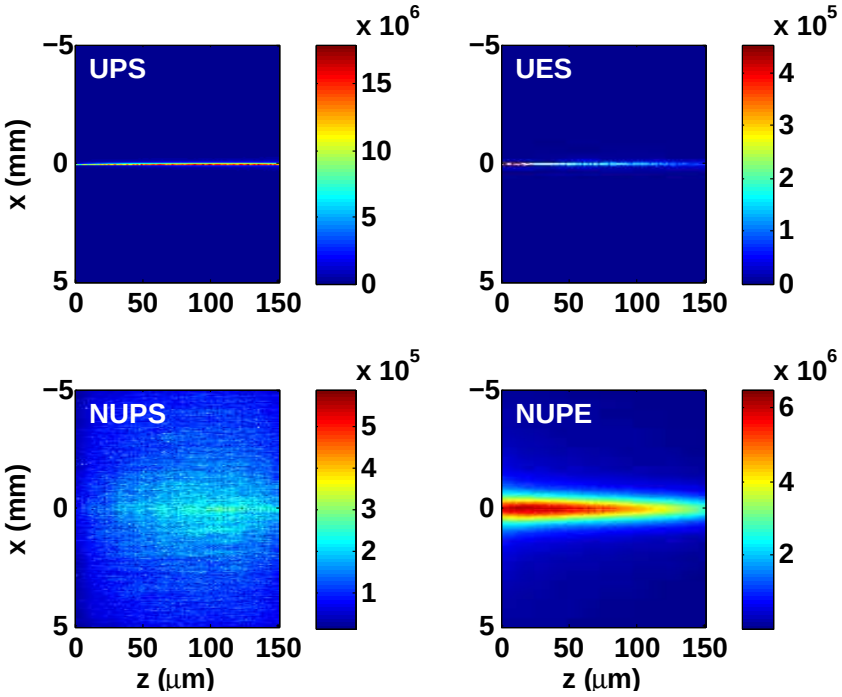

Figure 4: Image de dépôt d'énergie dans le plan XZ, due aux signaux UPS, UES, NUPS et NUES.

Table 1: Liste des paramètres. L'IP était entre les écrans avant et arrière, et les écrans ont été mis en contact avec l'IP.

Eléments			Configurations		
			IP alone	IP+0.2Pb	IP+0.2Pb0.8Sn
Source	Type		photon	photon	photon
	Energies keV $(E_{min}, E_{max}, E_{incmt})$		(2,1300,1)	(2,1300,1)	(2,1300,1)
Object	Objet		non	non	non
Détecteur	Ecrans avants		non	0.2mmPb	0.2mmPb +0.8mmSn
	IP	NbBX×NbBY×NbBZ	100×100×100	100×100×100	100×100×100
		Voxel dimension (μm^3)	10×10×1.5	10×10×1.5	10×10×1.5
	Ecrans arrières		non	0.2mmPb	0.8mmSn +0.2mmPb

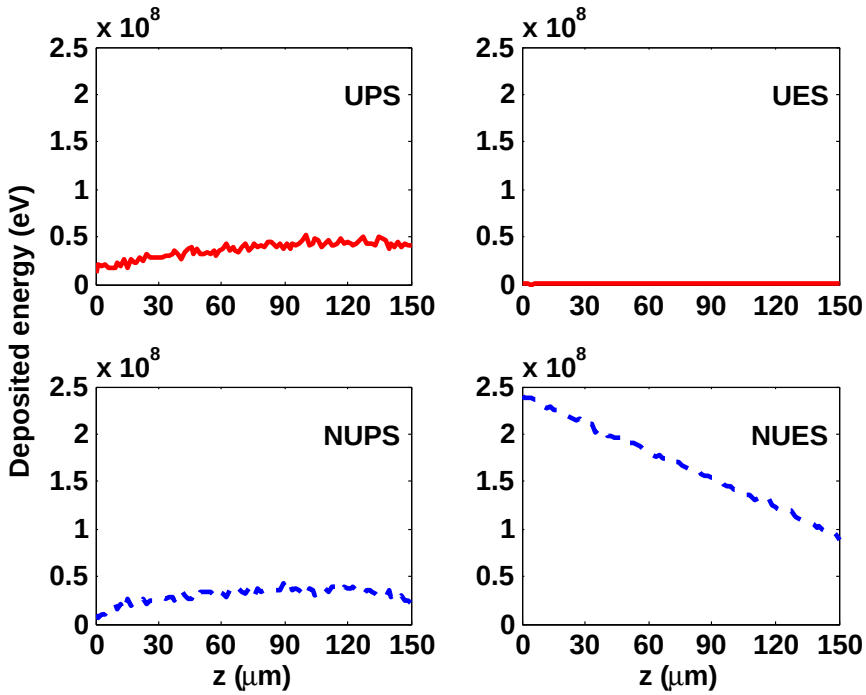

Figure 5: Dépôt d'énergie le long de la profondeur de l'IP (z) due aux signaux utiles (UPS et UES) et non-utile (NUPS et NUES).

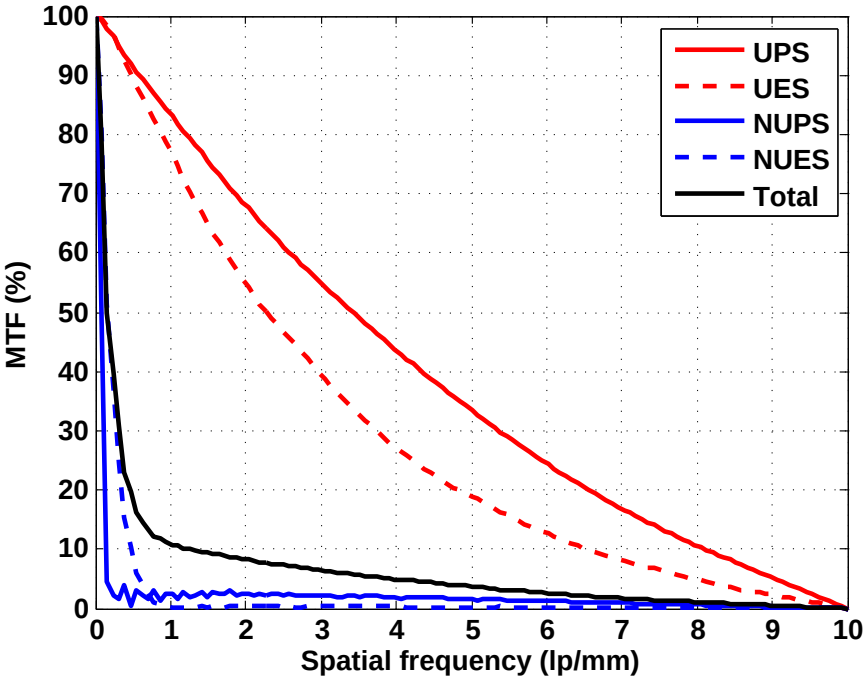

Figure 6: MTFs des images due aux signaux différents et MTF globale.

2.3.1 Réponse spectrale

La Figure 7 montre les courbes d'efficacité d'absorption d'énergie des 3 configurations différentes de détecteur.

- La réponse d'IP alone (courbe rouge) est efficace, à peu près 1, à basse énergie, mais avec l'augmentation de l'énergie d'excitation, la courbe descend rapidement vers zéro. L'augmentation entre 30 et 40 keV correspond à l'absorption du baryum.
- L'écran de plomb (courbe verte) filtre le rayonnement de faible énergie, mais renforce les hautes énergies: la courbe verte est au-dessus de la courbe « IP alone » pour des énergies supérieures à 131 keV. Le bord d'absorption du baryum a disparu en raison de la filtration des faibles énergies. Autour de 89 keV une baisse rapide apparaît, qui est due à l'absorption de plomb.
- Avec « IP+0.2Pb+0.8Sn » (courbe bleue), on observe des effets similaires, sauf que l'intensification du signal commence à partir de 226 keV, et une baisse supplémentaire apparaît à 30 keV, qui correspond à l'absorption de l'étain.

En ce qui concerne seulement l'intensification de l'absorption dans la gamme d'énergie élevée, le détecteur « IP+0.2Pb » est préféré, car il a le niveau d'absorption le plus élevé parmi les trois. Cependant, « IP+0.2Pb0.8Sn » a un meilleur filtrage des basses énergies. Lorsque l'on considère le compromis de rehausser le poids de haute énergie (pour absorber le signal utile) et baisser le poids de faible énergie (signal non-utile), les deux combinaisons d'écrans peuvent être discutées. D'autre part, la résolution spatiale doit être comparée, ce qui est le but de la section suivante.

2.3.2 Réponse spatiale

La Figure 8 montre les courbes MTF d' « IP alone » à différentes énergies d'excitation. De la basse à moyenne énergie (voir courbes bleu foncé, jusqu'à environ 400 keV), la courbe de MTF diminue rapidement avec l'augmentation de l'énergie d'excitation, tandis que, dans la gamme des hautes énergies (voir les courbes bleu clair à rouge foncé, 400 keV à 1300 keV), les courbes de MTF se chevauchent, ce qui signifie que la résolution spatiale pourrait être considérée constante dans cette gamme d'énergie élevée. Les deux trous à 14 keV et 38 keV correspondent à la fluorescence du brome et du baryum. Comme l'émission de fluorescence est isotrope, la MTF diminue rapidement.

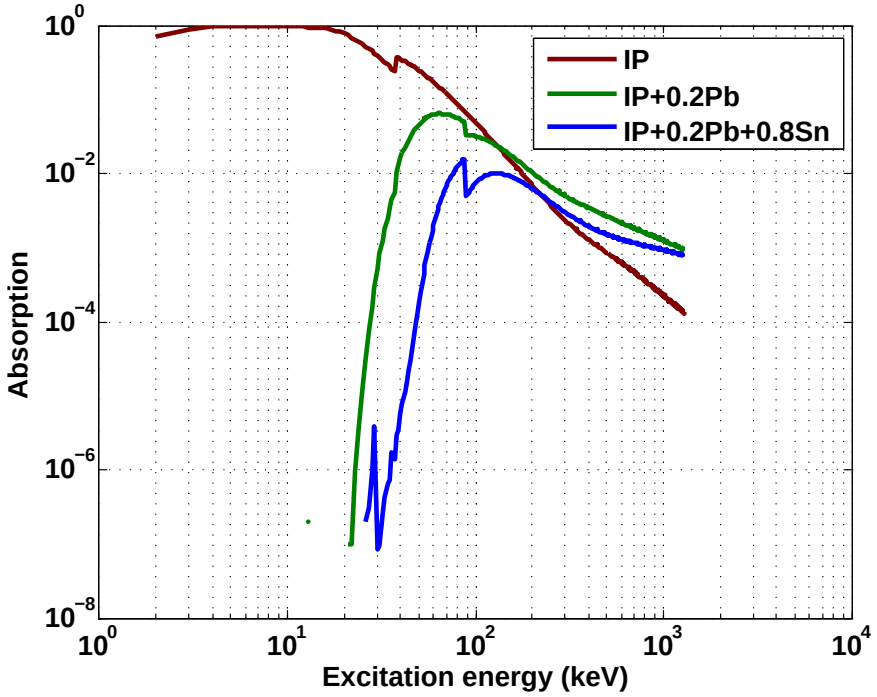

Figure 7: L'efficacité de l'absorption des photons en fonction de l'énergie pour les configurations différentes du détecteur.

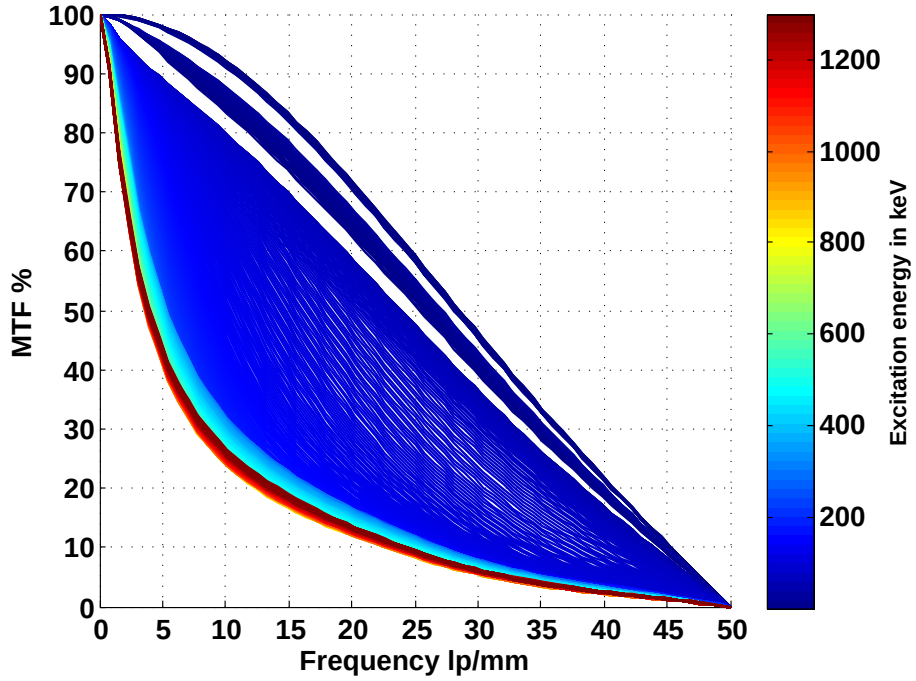

Figure 8: Courbes de MTF à énergies d'excitation différentes pour « IP alone ».

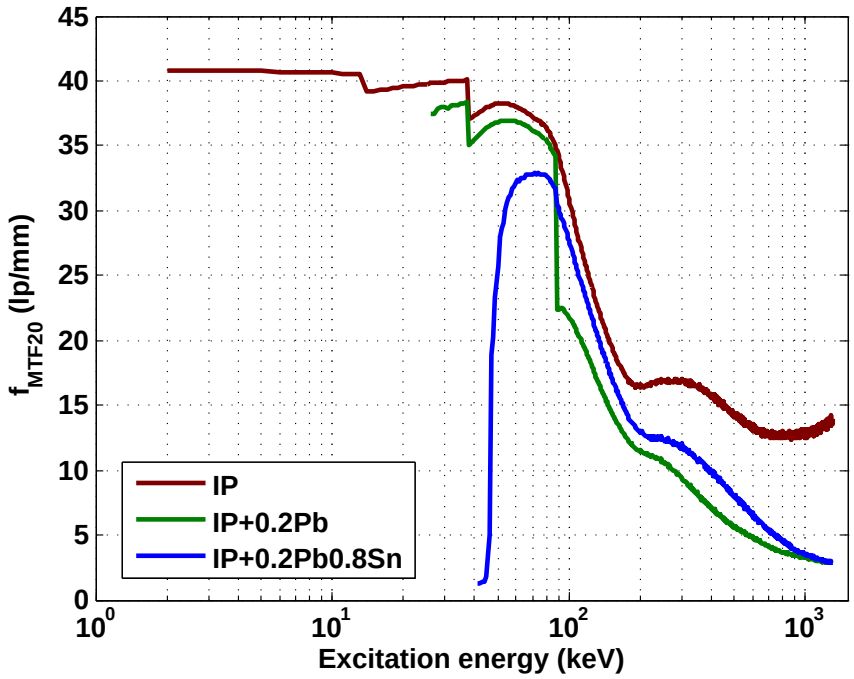

Figure 9: Les courbes f_{MTF20} en fonction de l'énergie d'excitation pour les détecteurs différents.

La Figure 9 compare la résolution des trois configurations de détecteur. Avec les écrans de plomb sur les deux côtés de l'IP, une dégradation de la résolution spatiale est introduite, en particulier à 89 keV, à laquelle la fluorescence du plomb commence à se produire. Comme un photon d'une énergie plus élevée a un libre parcours moyen plus grand, la fluorescence de plomb pourrait s'étendre plus loin que celle de baryum et de brome, et de ce fait la perte de résolution est plus grande à 89 keV, que celle à 14 et à 38 keV. A des énergies inférieures à 89 keV, le fait d'ajouter un écran d'étain entre IP et Pb dégrade la résolution, car il est une autre couche d'étalement du faisceau incident. Cependant, lorsque l'énergie d'excitation est supérieure à 89 keV, la fluorescence de plomb peut être effectivement atténuée par l'écran d'étain, et la résolution s'améliore. Cette amélioration diminue à mesure que l'énergie d'excitation continue à augmenter, et devient négligeable à 1300 keV.

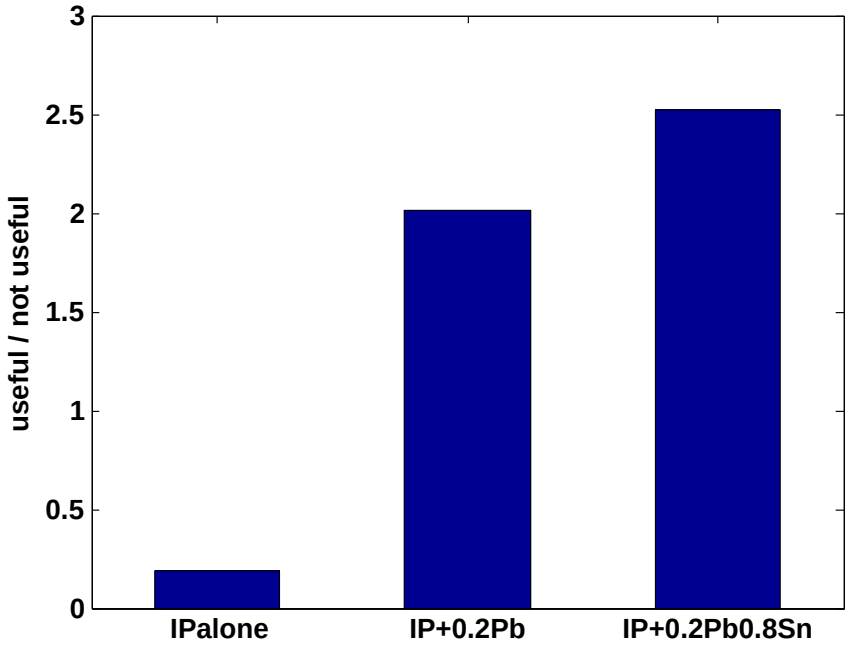

Figure 10: Rapport signal utile sur non-utile obtenu avec les trois détecteurs.

2.4 Résultat : optimisation d'un cas industriel

Selon l'analyse détaillée dans la partie précédente, on constate que les deux configurations d'IP avec des écrans métalliques pourraient augmenter le poids du signal utile dans l'image finale, car ils pourraient effectivement augmenter l'efficacité d'absorption à haute énergie et éliminer l'influence des signaux de faible énergie, en particulier « IP + 0.2Pb0.8Sn » qui a un meilleur effet de filtrage à basse énergie. Tout en limitant le flou introduit par le signal non-utile, les écrans dégradent également la résolution spatiale, par conséquent, un détecteur approprié doit assurer un bon ratio de signal utile par rapport au signal non-utile sans perdre beaucoup de résolution spatiale. Nous montrons ce ratio obtenu avec les trois détecteurs dans la Figure 10, et le ratio est largement augmenté avec «IP + 0.2Pb0.8Sn». Dans la Figure 11, nous voyons que la MTF avec « IP + 0.2Pb » (Figure 11(a)) et avec « IP + 0.2Pb0.8Sn » (Figure 11(b)) sont presque les mêmes. En comparant la fréquence spatiale à 20% MTF, « IP + 0.2Pb0.8Sn » (1,62 lp/mm) est un légèrement meilleure que « IP + 0.2Pb » (1,45 lp/mm). Ainsi « IP + 0.2Pb0.8Sn » est globalement meilleur pour notre cas industriel.

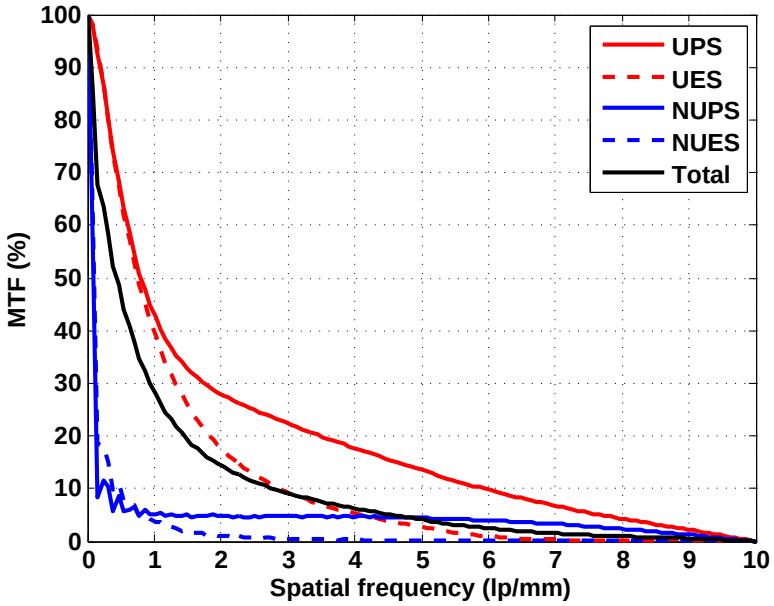

(a)

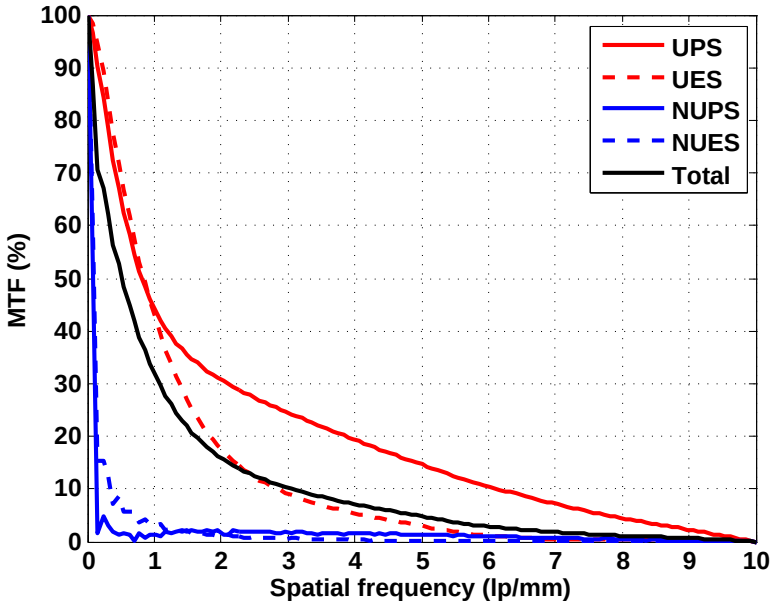

(b)

Figure 11: MTF des images due aux signaux différents et MTF globale pour (a) « IP+0.2Pb » et (b) « IP+0.2Pb0.8Sn ».

2.5 Discussion

Grâce à la caractérisation de la réponse des détecteurs et une analyse détaillée sur les réponses spectrales et spatiales, nous avons optimisé un cas d'inspection. Globalement, « IP+0.2Pb0.8Sn » est la meilleure configuration parmi les trois, car elle augmente le plus le poids du signal utile à haute énergie sans perdre trop en efficacité d'absorption d'énergie et en résolution spatiale. De l'étude réalisée, nous constatons que les écrans métalliques peuvent renforcer le signal de haute énergie et filtrer le signal de basse énergie, mais en même temps ils dégradent la résolution spatiale, surtout à cause de la fluorescence produite par les écrans de plomb. Il faut éviter un contact direct entre l'IP et les écrans de plomb.

Ces études ne concernent que les phénomènes physiques ayant lieu pendant l'exposition CR. Comme le processus de lecture optique CR a également une influence importante sur l'image finale, nous avons besoin d'un modèle complet pour la compréhension de l'ensemble de la chaîne d'imagerie CR. Pour cette raison, la thèse développe une approche complète de simulation CR.

2.6 Comparaison des résultats de simulation et expérimentaux sur l'effet d'intensification des écrans métalliques

En parallèle de la simulation, nous avons aussi effectué des mesures expérimentales à l'ESRF (European synchrotron Radiation Facility). La réponse de l'IP avec des écrans métallique différents a été caractérisée avec une source synchrotron de 35, 40, 50, 75, 100, 150, 200, 400 et 600 keV. Nous avons comparé les résultats de simulation avec les résultats expérimentaux sur l'effet d'intensification des écrans (c'est-à-dire l'énergie déposée totale dans IP avec écrans par rapport à l'énergie déposée totale dans IP seul). Un exemple de comparaison est montré dans la Figure 12. Globalement, les données de simulation sont en accord avec les données expérimentales, sauf à 600 keV. A cette énergie, l'image est fortement affectée par le faisceau secondaire émergeant du bord de tungstène[2] et le rayonnement rétrodiffusé (le côté arrière de l'IP n'a pas été protégé).

[2]Initialement, on voulait mesurer la réponse spatiale, à chaque énergie, et la moitie du faisceau était bloquée par un bord de tungstène (voir chapitre 3 dans la thèse pour plus de détails).

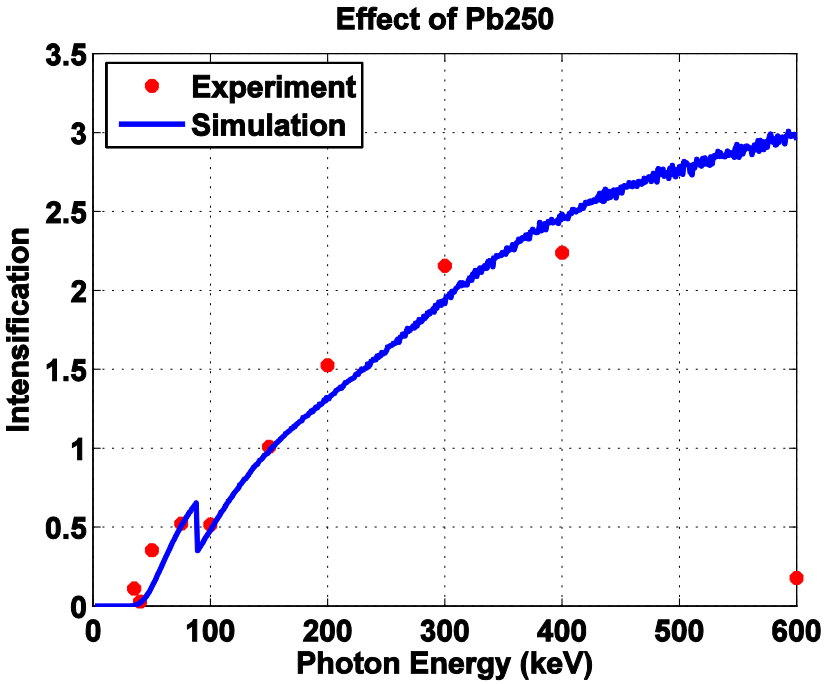

Figure 12: L'effet d'intensification d'un écran de plomb de 0,25 mm. Les points rouges correspondent à la mesure expérimentale; la courbe bleue est obtenue avec la simulation Monte Carlo.

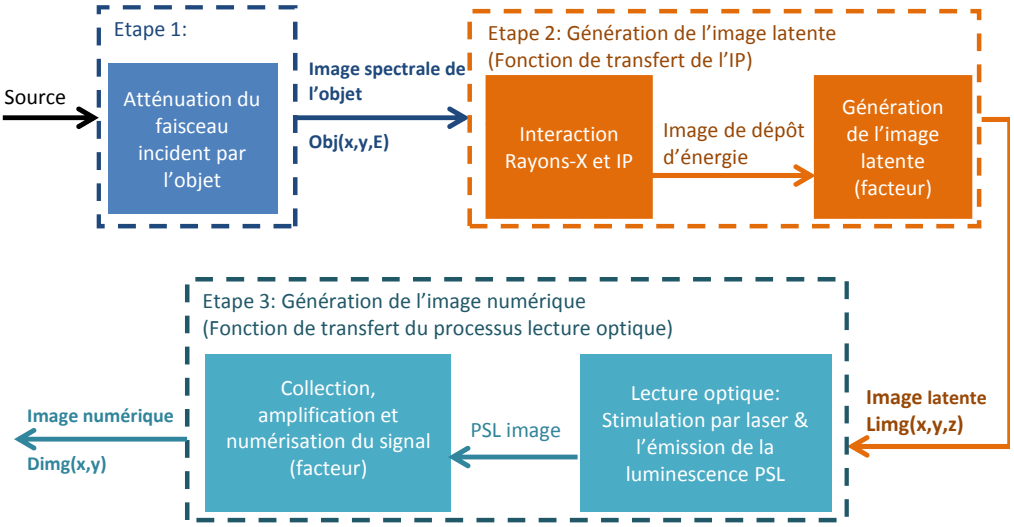

Figure 13: Etapes de simulation de la chaîne d'imagerie CR.

3 Simulation de la chaîne complète de radiographie numérique

L'objectif de cette deuxième partie de la thèse est de développer un modèle complet du système CR, qui permet de prendre en compte les paramètres accessibles du système. Dans cette thèse, la chaîne de l'imagerie CR est modélisée en trois étapes successives (Figure 13) : l'atténuation des rayons X, la génération de l'image latente et la génération de l'image numérique. Des codes Monte Carlo ou déterministes peuvent être appliqués dans les différentes étapes. La méthode de simulation CR se résume comme suit.

i L'atténuation du faisceau des rayons-x ou gamma par un objet complexe. Cette étape peut être réalisée par une simulation Monte Carlo ou déterministe.

ii La génération de l'image latente (réponse de l'IP seul ou l'ensemble constitué de l'IP et les écrans renforçateurs). Cette étape est subdivisée en deux sous-étapes suivantes: a) l'interaction du rayonnement et de l'IP ; et b) génération de l'image latente. Pour la première, le détecteur (IP seul ou IP avec écrans) est modélisé par une fonction de transfert qui est obtenue grâce à une étude paramétrique réalisée hors ligne par simulation Monte Carlo. La deuxième étape est modélisée simplement par un facteur de conversion, car le mécanisme de création de l'image latente n'est pas encore bien connu, et de plus, selon les matériaux, les mécanismes sont différents.

iii La lecture optique. Comme l'étape précédente, cette étape est aussi divisée en deux

sous-étapes : a) lecture par un laser et b) collection, amplification et numérisation du signal (luminescence photostimulée ou PSL). La lecture par le laser est modélisée par une fonction de transfert (générée avec un code Monte Carlo) de la réponse optique de l'IP. La dernière étape est simplifiée en utilisant un facteur multiplicatif.

Différentes méthodes de simulation ont été appliquées aux différentes étapes, elles seront détaillées dans les sections 3.1, 3.2 et 3.3.

3.1 Génération de l'image spectrale de l'objet

Le but de cette étape est de générer l'image spectrale de l'objet $Obj(E, x, y)$ sur le plan du détecteur, où différentes méthodes (Monte Carlo ou déterministe) de simulation peuvent être appliquées. Pour les objets simples, les codes Monte Carlo peuvent prendre en compte tous les phénomènes physiques et permettent d'obtenir des sorties plus précises. Quant aux objets complexes, la simulation MC devient désespérément longue (une simulation peut durer des mois ou plus encore). Dans ce cas, les outils déterministes peuvent simuler rapidement un système complexe sous des approximations raisonnables.

Pour générer $Obj(E, x, y)$ (quelle que soit la méthode de simulation), un détecteur virtuel est placé dans le plan du détecteur. Ce détecteur virtuel est divisé en $M \times N$ pixels pour enregistrer la distribution spatiale du faisceau incident. Chaque pixel est aussi un compteur spectral avec une largeur de canal E_{width} keV. La Figure 14 est un exemple de génération de l'image de l'objet. L'image à gauche est la configuration géométrique générée en utilisant le code VXI (12000Duvauchelle et al.; 42004Freud et al.) : un détecteur virtuel (en vert) est placé au niveau du plan de détection réel. A droite est l'image spectrale détectée par le détecteur virtuel $Obj(E, x, y)$ à une énergie E. Le signal de chaque pixel de $Obj(E, x, y)$ est le nombre de photon reçu par canal d'énergie (unité: $\mathrm{cm}^{-2} \cdot \mathrm{keV}^{-1}$).

3.2 Génération de l'image latente

La Figure 15 nous montre le modèle de génération de l'image latente, où H1 représente l'opérateur de génération de l'image latente. Un outil de simulation Monte Carlo, basé sur PENELOPE (52009Gavaldà et al.), a été développé pour caractériser la réponse de l'IP à différentes énergies monochromatiques. Cet outil nous permet d'obtenir une carte 3D de dépôt d'énergie (voir Figure 15(b)) en différenciant le signal primaire/secondaire et

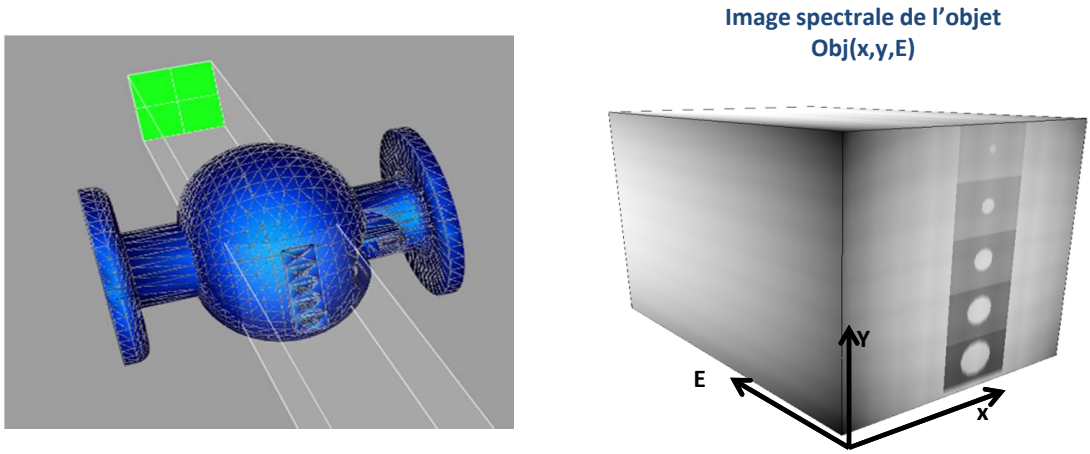

(a) (b)

Figure 14: Etape 1: Génération de l'image spectrale de l'objet avec l'outil déterministe VXI (12000Duvauchelle et al.; 42004Freud et al.).

photon/électron.

Pour pouvoir appliquer l'opérateur H1, on a d'abord fait une étude paramétrique afin d'obtenir le modèle du détecteur $PSF_{det}(E,x,y,z)$ (ratio énergie déposée par énergie incidente par unité de volume, cm^{-3}), qui représente la réponse du détecteur aux Rayons-X ou gamma: on a généré les réponses impulsionnelles (Figure 15(b)) en balayant les configurations du détecteur *det* (la combinaison IP/écrans) et les énergies E entre E_{min} et E_{max} avec un pas d'échantillonnage de E_{pas}. L'ensemble des tableaux $PSF_{det}(E,x,y,z)$ contient la réponse spectrale et spatiale de tous les détecteurs étudiés. La réponse du détecteur (opération H1) est appliquée grâce à une convolution spatiale 2D selon x et y, à chaque énergie E, et pour une profondeur z fixée:

$$\begin{aligned} Limg(x,y,z) &= H1(Obj, PSF_{det}) \\ &= g_{sc} \cdot \int_E E \cdot (obj(E,x,y) * PSF_{det}(E,x,y,z))\, dE \\ &= g_{sc} \cdot \int_E E \cdot \left(\iint_{u,v} obj(E,x,y) \cdot PSF_{det}(E, x-u, y-v, z) du dv \right) dE, \end{aligned} \tag{2}$$

où

- $Limg(x,y,z)$ est l'image latente obtenue dans l'IP à la profondeur z (unité: cm^{-3}) ;
- g_{sc} est le facteur de conversion (unité: keV^{-1}) ;

(a) (b)

Figure 15: (a) Etape 2: Génération de l'image latente à l'aide du modèle du détecteur $PSF_{det}(E, x, y, z)$; et (b) réponse impulsionnelle du détecteur pour une énergie d'excitation E_i. Le tableau $PSF_{det}(E, x, y, z)$ contient toutes les cartes 3D de dépôt d'énergie à toutes les énergies et représente ainsi la réponse spectrale et spatiale du détecteur "det".

- et le terme $\int_E \left[E \cdot \iint_{u,v} Obj(u, v, z) \cdot PSF_{det}(E, x-u, y-v, z)dudv\right] dE$ représente la carte 3D de dépôt d'énergie (unité: keV $\cdot$ cm^{-3}), qui est convertie en image latent par le facteur g_{sc}.

3.3 Modélisation du processus de lecture optique

La Figure 16 nous montre le modèle de génération de l'image numérique ; H2 représente l'opérateur qui modélise la lecture optique. La lecture optique par laser est, en effet, un processus destructif, c'est-à-dire que le laser modifie l'image latente en balayant l'IP. Par conséquent, au contraire de l'étape précédente, le signal de sortie de la lecture optique ne peut plus être modélisé par une convolution de l'image latente avec la réponse impulsionnelle optique de l'IP. Une convolution modifiée (H2) doit être appliquée pour calculer l'image numérique finale (101996aThoms; 32003Fasbender et al.)

$$\begin{aligned} Dimg(x_m, y_n) &= H2(Limg, I) \\ &= \int_z P(z)dz \iint_{x,y} Limg^*(x, y, z)\{1 - exp[-\sigma \cdot I(x - x_m, y - y_n, z) \cdot t_{scan}]\}dxdy, \end{aligned} \tag{3}$$

où

- $Limg(x, y, z)$ est l'image latente obtenue de l'étape précédente ;

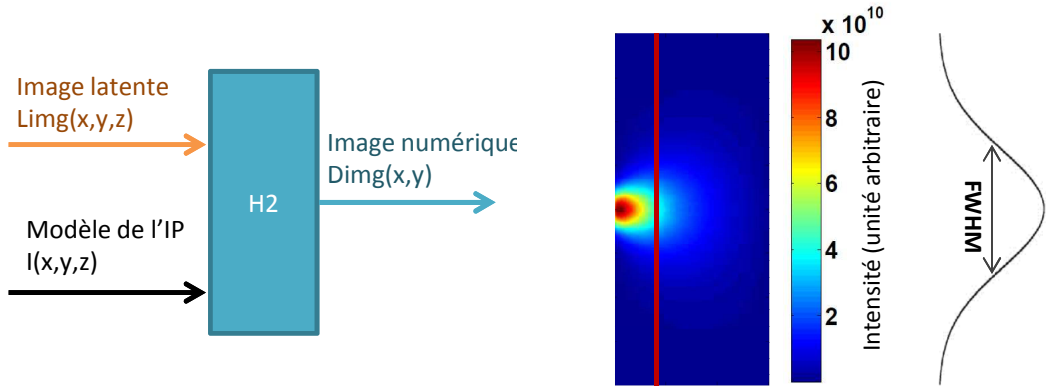

(a) (b)

Figure 16: (a) Etape 3: Génération de l'image numérique à l'aide de la fonction de transfert de lecture optique ; (b) cartographie du modèle optique de l'IP selon (x,z) et profil à z fixé (ligne rouge).

- $Limg^*(x, y, z)$ est l'image latente modifiée par le laser ;
- $I(x, y, z)$ est la réponse optique de l'IP pour le laser (modèle optique de l'IP), c'est-à-dire la distribution de l'intensité du laser dans l'IP, en unité $\mathrm{cm}^{-2} \cdot \mathrm{s}^{-1}$;
- $P(z)$ est la probabilité qu'un photon, émis à la profondeur z, puisse s'échapper de la face avant de l'IP ;
- σ est la section efficace de la photo-stimulation (unité : cm^2) ;
- et t_{scan} est le temps de lecture à (x_m, y_n) en unité s.

Pour obtenir la réponse de l'IP au laser $I(x, y, z)$, nous avons développé un outil de simulation Monte Carlo avec Matlab, où certains traitements d'interaction du laser avec la matière sont basés sur (32003Fasbender et al.) et (131995Wang et al.). La Figure 16(b) nous montre un exemple de réponse, obtenue en envoyant 2×10^6 photons optiques à l'entrée.

Dans le cas où l'on néglige l'effet de la lecture optique, l'image numérique peut être calculée en utilisant la formule :

$$Dimg(x, y) = \int_z Limg(x, y, z)dz. \tag{4}$$

3.4 Résultat

Dans cette partie, on montre quelques résultats de simulation. La configuration géométrique de la Figure 14(a) a été adoptée pour notre simulation. Un objet en acier de forme complexe est irradié par une source monochromatique (100 keV) ponctuelle. Un indicateur de qualité d'image (IQI) en acier a été mis sur l'objet du côté de la source. A noter que seule la partie centrale avec l'IQI a été éclairée.

Le détecteur est une combinaison de l'IP avec écrans renforçateurs, où l'IP est pris en sandwich entre les écrans renforçateurs. L'IP a été modélisé comme une structure multicouche qui consiste en, dans l'ordre, une couche protectrice de 6 μm, une couche de phosphore photostimulable de 150 μm, une couche de support de 254 μm et une couche supplémentaire (en anglais « backing layer ») de 25,4 μm. Les matériaux de ces couches sont respectivement Mylar pour la couche protectrice et le support, BaFBr : Eu^{2+} pour la couche de phosphore et polycarbonate pour la couche supplémentaire. Les réponses (de dose) des deux configurations de détection suivantes ont été simulées: a) IP seul (appelé « HRIP »); b) IP avec deux écrans de plomb de 0.3 mm sur les deux côtés (appelé « 0.3Pb+HRIP+0.3Pb »).

3.4.1 L'image latente

Nous montrons les images latentes générées en utilisant les deux configurations différentes de détecteur (HRIP et 0.3Pb+HRIP+0.3Pb) dans la Figure 17. Afin de comparer la netteté de l'image, nous avons normalisé les images par leur valeur maximale. Nous traçons les profils normalisés le long de la ligne rouge. La netteté de l'image est meilleure avec HRIP que celle avec 0.3Pb+HRIP+0.3Pb. Dans l'image, on a aussi montré (dans légende) l'efficacité d'absorption de chaque détecteur, notée « AE » (l'énergie totale absorbée par la couche phosphore divisée par l'énergie totale à l'entrée du détecteur) : HRIP est plus efficace dans le cas montré.

3.4.2 L'image finale à la sortie de la simulation

Dans cette partie nous avons repris l'image latente générée en utilisant HRIP, puis nous avons simulé la lecture de cette image avec différentes puissances du laser (représentées par un facteur de puissance) : 10^{10}, 10^{13}, 10^{14}, 10^{15} et 10^{16}. Le facteur est d'autant plus grand que la puissance est grande.

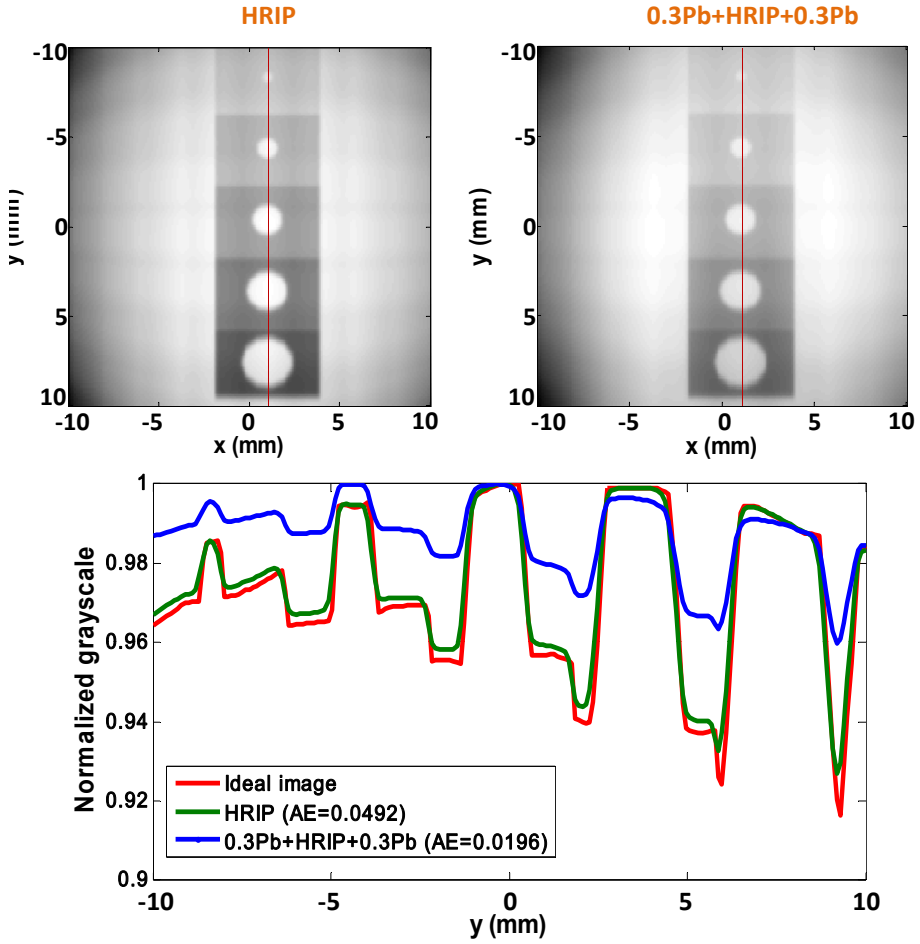

Figure 17: Résultat de simulation sans prendre en compte l'effet de la lecture optique. En haut images latentes obtenues avec les deux configurations de détecteur, et en bas, profils de niveaux de gris le long de la ligne indiquée en rouge dans les images. Le profil idéal représente le profil obtenu dans l'image spectrale de l'objet "$Obj(x, y, z)$".

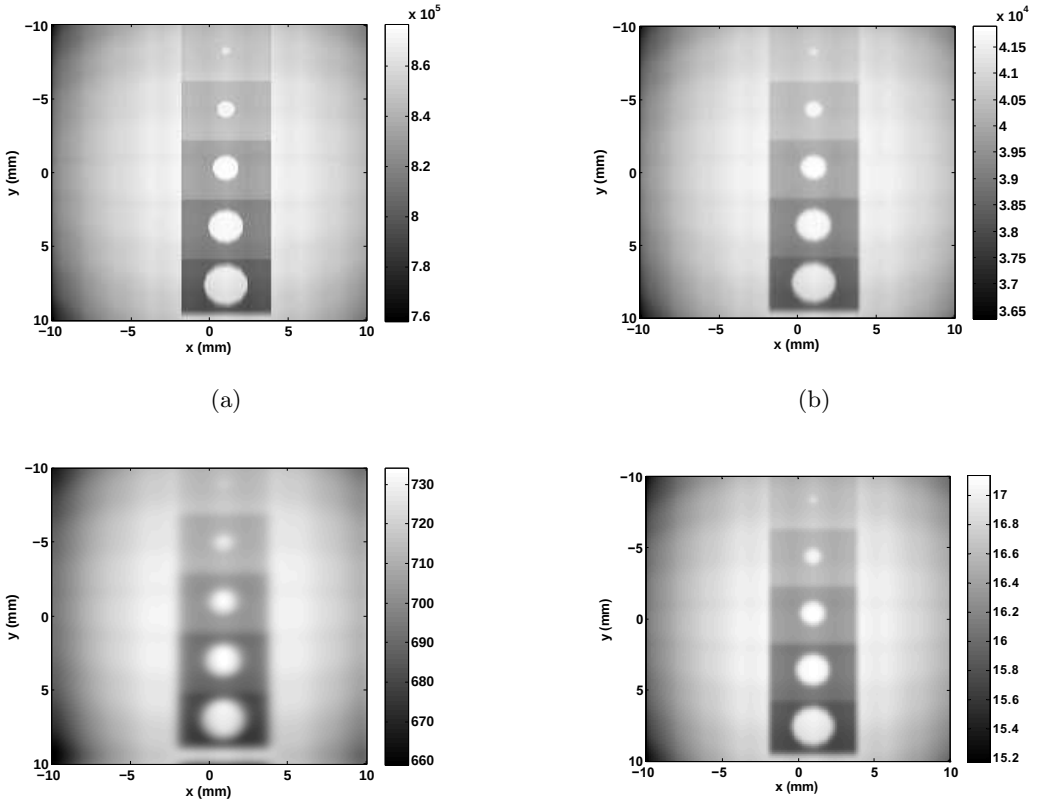

(a) (b)

(c) (d)

Figure 18: Résultats de simulation: (a) l'image idéale de l'objet à la sortie de la première étape, (b) l'image latente à la sortie de la deuxième étape, (c) l'image numérique à la sortie de la troisième étape lue avec une forte puissance de laser (facteur de puissance 10^{16}) et (d) l'image numérique à la sortie de la troisième étape lue avec une faible puissance de laser (facteur de puissance 10^{10}).

La Figure 18 illustre les résultats de simulation en utilisant deux puissances différentes du laser. Avec une grande puissance de lecture, la plupart des électrons piégés dans l'image latente peuvent être libérés, mais une translation de l'image est observée qui provient du balayage de l'image par le laser (comparer les Figures 18(b) et 18(c) sur le bas de l'image notamment).

Nous traçons ensuite l'efficacité de lecture (signal en sortie de lecture par rapport au signal en entrée de lecture) en fonction de la puissance du laser (Figure 19). L'efficacité augmente lentement à basse puissance, puis on remarque une augmentation substantielle entre 10^{13} et 10^{15} ; et à 10^{16} la courbe commence à saturer. On peut remarquer que

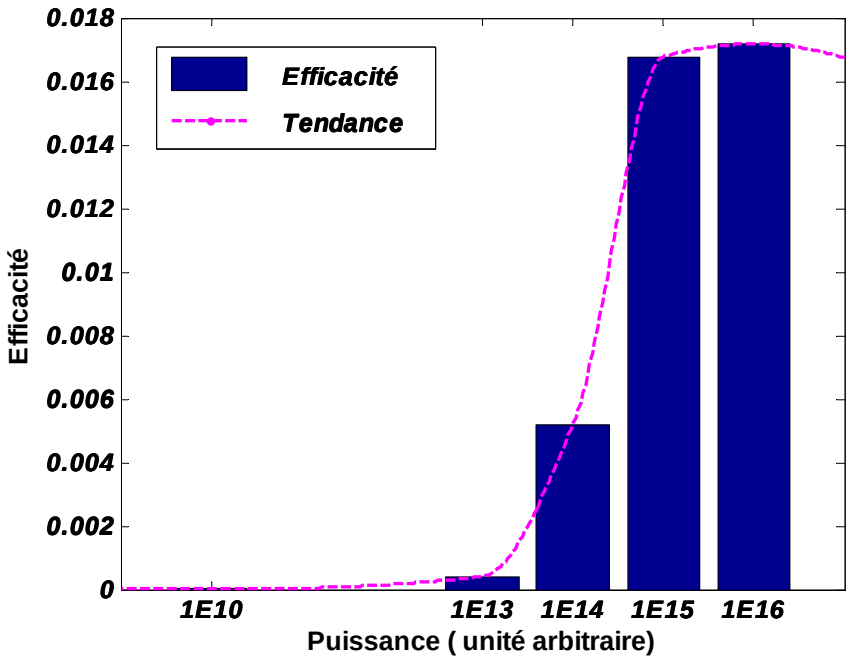

Figure 19: Efficacité de lecture en fonction de la puissance du laser.

l'efficacité maximale n'est pas égale à un. En effet, une forte puissance augmente la photoluminescence, mais les photons sont émis de façon isotrope et seule une petite partie peut sortir de la face avant de l'IP et participer à l'image finale.

Dans la Figure 20, nous présentons les profils le long du centre de l'IQI, normalisés par leurs valeurs maximales. La courbe rouge est le profil de l'image latente. Les courbes des 2 premières puissances sont superposées, puis on perd du contraste en augmentant encore la puissance. En comparant les profils, on voit aussi un décalage latéral évident entre la courbe noire et la courbe rouge dans le sens de la translation de l'IP.

Enfin, nous montrons l'évaluation du profil en sortie des différentes étapes dans la Figure 21. Dans cet exemple, nous avons pris les conditions optimales de chaque étape, c'est-à-dire l'image latente détectée avec HRIP, puis lue avec une puissance de $\ll 10^{15} \gg$. On voit qu'on perd du contraste à chaque étape.

3.5 Discussion

Dans l'exemple de notre étude de cas, nous avons comparé l'image détectée avec différentes configurations de détection, i.e. détecteur et puissance du laser. En comparant les

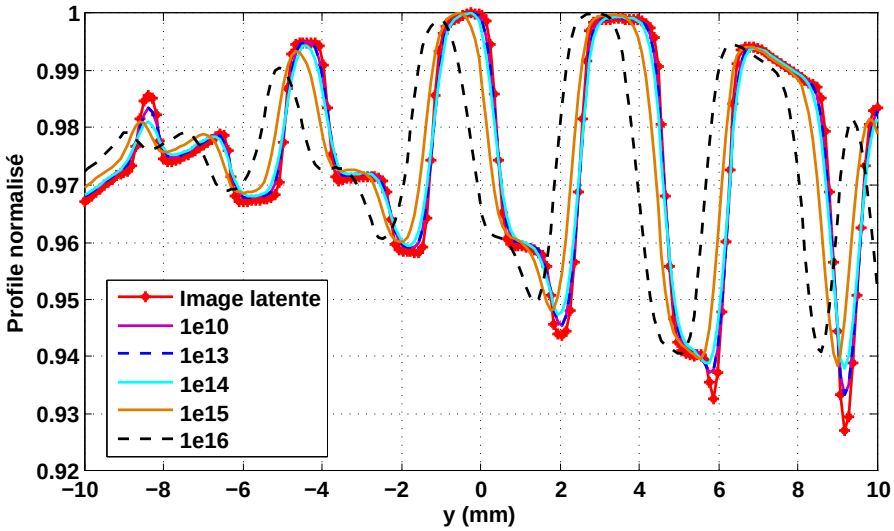

Figure 20: Résultats: profils normalisés, lus avec différentes puissances de laser.

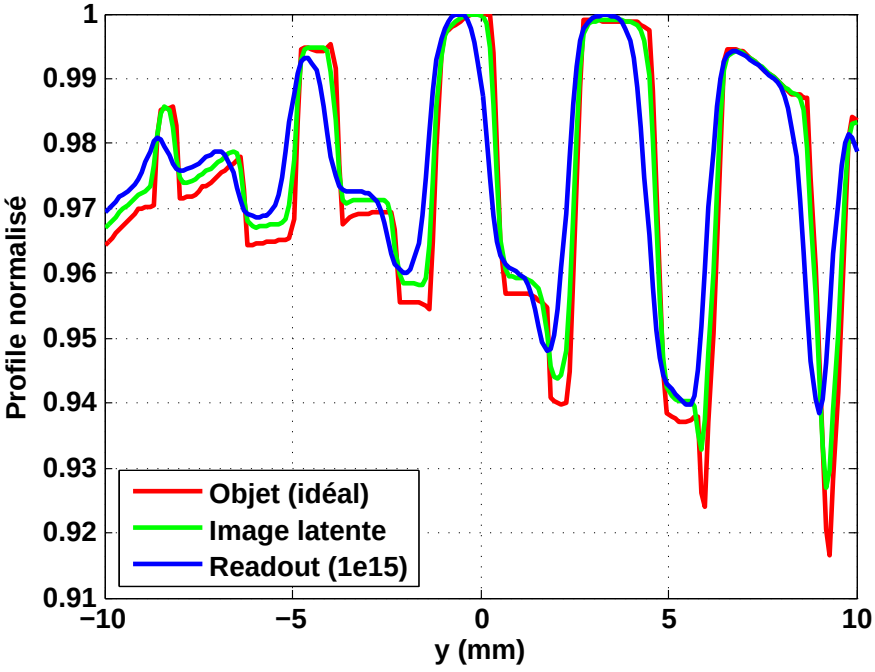

Figure 21: Evolution du profil en sortie des différentes étapes. Dans l'exemple montré, on a pris l'IP seul lu avec une puissance de lecture de « 10^{15} ».

résultats, nous trouvons que la détection avec HRIP seul et la lecture avec une puissance du laser de $\ll 10^{15} \gg$ nous permettent d'obtenir une meilleure qualité d'image. La puissance choisie nous permet d'obtenir une bonne efficacité sans trop perdre de contraste.

Pour la lecture optique, quand l'on augmente la puissance du laser, l'efficacité de lecture augmente, c'est-à-dire la fraction des électrons libérés par le laser ; mais le contraste se dégrade. La raison est que quand on lit un point de coordonnées courantes, une partie des électrons piégés autour ce point est aussi libéré et contribue au signal ce qui donne du flou. Plus on augmente la puissance du laser, plus cette partie est libérée. C'est pour cette raison que l'on voit aussi un décalage en utilisant une très forte puissance. Il faut donc trouver un compromis entre l'efficacité et le contraste.

3.6 Conclusion

Nous avons présenté une approche de simulation de la radiographie numérique dédiée aux objets complexes. Différentes méthodes de simulation sont adoptées: les méthodes Monte Carlo et déterministe. Un outil de simulation a été développé sur cette approche. Par une étude de cas, nous avons montré l'utilisation de notre outil. Il est intéressant pour comparer différentes conditions de mesure et pour optimiser la qualité d'image fournie par le système CR.

La comparaison entre les résultats de simulation et expérimentaux est en cours.

4 Conclusions et perspectives

Le projet de thèse a été lancé dans un contexte industriel de l'adaptation du système de radiographie numérique avec écrans photostimulables pour satisfaire aux exigences de contrôle industriel. La thèse s'articule autour de deux aspects : l'étude des phénomènes physiques et une approche de simulation complète de la chaîne d'imagerie CR. Les résultats principaux sont décrits dans les deux sections suivantes.

4.1 Phénomènes physiques

La première partie de ce travail a porté sur la compréhension des phénomènes physiques. Un outil de simulation Monte Carlo dédié a été développé pour une analyse détaillée. L'utilité de cet outil a été démontrée par l'étude d'optimisation d'un cas industriel réaliste (une pièce de fer de 70 mm exposée à une source Cobalt-60), où le problème de la diffusion

a été illustré et les réponses de trois configurations de détecteurs ont été caractérisées. On a obtenu les compréhensions suivantes.

- Rayonnement secondaire. Le problème de la détection d'une image avec un IP seul était d'abord visualisé avec l'outil. Les images dues au rayonnement direct (de haute énergie) et au rayonnement secondaire (de relativement basse énergie) produite par un objet ont été illustrées séparément. on s'est aperçu que le rayonnement secondaire est responsable du flou dans une image. Comme l'image détectée est principalement due au rayonnement secondaire (seulement 15,7% du signal vient du rayonnement direct), l'image globale a une faible résolution spatiale. Le problème est identifié: afin d'améliorer la qualité de l'image, on devrait augmenter le rapport de rayonnement direct sur secondaire (DSR), à savoir l'intensification de signal de haute énergie et l'élimination de signal de basse énergie. Ici, nous voyons l'importance de la caractérisation de la réponse du détecteur.

- Caractérisation de la réponse du détecteur. Nous avons caractérisé les réponses de trois configurations de détecteur, IP seul, IP avec deux écrans de plomb (0,2 mm) sur les deux côtés, et IP avec des écrans de plomb (0,2 mm) et étain (0,8 mm) sur les deux côtés. Une analyse détaillée des réponses spectrale et spatiale a été fait.

En comparant la réponse des trois détecteurs, on trouve que les écrans métalliques peuvent effectivement intensifier le signal de haute énergie et filtrer le signal de basse énergie. Grâce à ces écrans, l'énergie est déposée plutôt vers la surface d'IP. Cependant, ils dégradent également la résolution spatiale, en particulier la fluorescence émise à partir d'un écran de plomb. On devrait considérer à la fois le DSR et la netteté en choisissant des écrans pour l'optimisation. Il s'avère que la configuration IP avec les écrans de plomb et d'étain est globalement préférable, car il nous donne le meilleur DSR des trois, et de plus, l'écran d'étain peut effectivement atténuer la fluorescence du plomb. Notez que cette combinaison IP/écrans est seulement optimale pour le cas étudié, et ne peut pas être généralisée à tous les cas.

Avec cette étude de cas, nous voyons que pour optimiser la qualité d'image, la réponse de l'objet et du détecteur doivent être prises en considération; il faut trouver un compromis entre le DSR et la netteté; la fluorescence de haute énergie devrait être éliminée avant d'entrer dans IP, c'est-à-dire qu'il faut ajouter d'autres écrans pour absorber la fluorescence.

4.2 Modélisation et simulation du système de radiographie numérique

Dans cette thèse on a développé une approche de simulation qui permet de simuler la chaîne complète d'imagerie CR, de l'exposition aux rayons X jusqu'à la lecture optique. La simulation est réalisée en trois étapes: génération de l'image spectrale d'un objet, génération de l'image latente et génération de l'image numérique finale. Les étapes précises de simulation sont résumées comme suit.

- Génération de l'image spectrale d'un objet. Selon les besoins, il est possible de choisir un code déterministe ou un code Monte Carlo à usage général dans cette étape. La sortie de simulation doit être une image spectrale $Obj(E, x, y)$.

- Génération de l'image latente. Cette étape est réalisée par l'opérateur H1 et un modèle hors ligne de la réponse du détecteur $\mathrm{PSF}_{\mathrm{det}}$: $Limg(x, y, z) = H1(obj, \mathrm{PSF}_{\mathrm{det}})$. Le modèle de la réponse du détecteur est obtenu par la caractérisation Monte Carlo de la réponse du détecteur aux différentes énergies. A hautes énergies, une grande partie du dépôt d'énergie dans la couche sensible de l'IP est due aux effets de diffusion, fluorescence et aux électrons. Avec la simulation MC, la réponse spectrale et spatiale précise peut être obtenue. Une base de données des modèles de détecteur a été créée. Jusqu'à présent, la base de données contient 128 configurations différentes de détecteur, y compris toutes les combinaisons IP/écrans recommandées dans les normes internationales (22005EN14784-2; 62013ISO17636-2).
  Une étude de cas illustre l'utilisation de cette étape. L'image d'un objet complexe a été détectée par trois détecteurs. En comparant les images latentes, nous avons déterminé la configuration optimale du détecteur. Une comparaison avec la simulation utilisant un code Monte Carlo complet montre un bon accord. Une autre comparaison de simulation d'une imagerie complexe est en cours.

- Génération de l'image numérique. L'image est affectée par la réponse optique de l'IP $f(x, y, z)$ et les paramètres de balayage du laser. L'image numérique est générée par $Dimg(x, y, z) = H2(Limg, f,$paramètres de balayage du laser$)$.
  Afin d'étudier la réponse optique d'un IP, un outil de simulation Monte Carlo pour le transport du laser dans IP a été développé, où l'IP est décrit par des paramètres tels que coefficient d'absorption, coefficient de diffusion et les conditions d'interface. Une étude sur l'influence de plusieurs paramètres a été effectuée avec l'outil. Les résultats montrent que la modification de ces paramètres affecte la taille de la région

de diffusion et la quantité de photons à l'intérieur de l'IP. La taille de la région de diffusion et la quantité de photon déterminent respectivement la netteté de l'image et l'efficacité de lecture. Il a été constaté que lorsque nous gagnons la netteté, nous perdons l'efficacité et vice versa. Les deux sont des facteurs contradictoires, et un compromis doit être fait lors de la fabrication. Pour un utilisateur, les propriétés optiques de l'IP ne sont pas accessibles, mais il est possible de régler les paramètres de numérisation pour chercher à optimiser la qualité d'image.

Comme le balayage du laser est un processus de lecture destructive, cet effet est pris en compte dans le modèle H2, avec lequel le balayage laser est suivi pixel par pixel. Comme une illustration, l'image latente obtenue avec IP seul dans la deuxième étape a été lue en utilisant différentes puissances de lecture (produit de la puissance du laser et le temps de lecture). Le résultat montre qu'une puissance laser plus élevée (ou un temps de lecture plus long) entraîne une plus grande efficacité de lecture, mais dégrade le contraste de l'image. Encore une fois, un compromis doit être fait pour déterminer la condition appropriée.

Avec cette méthode, on peut simuler le système CR, et prendre en compte les facteurs de fonctionnement tels que la source (dans la première étape), le détecteur (dans la deuxième étape) et les paramètres de lecture (dans la dernière étape). L'application de H1 et H2 nécessite l'accord d'échantillonnage des tableaux Obj, PSFdet et f. L'efficacité de calcul dépend fortement de la taille des tableaux de $Obj(E, x, y)$, $Limg(x, y, z)$, $PSF_{det}(x, y, z)$ et $f(x, y, z)$. Une grande précision nécessite une petite taille d'échantillon, et par conséquence une grande taille de tableaux, ce qui rend la simulation lente.

Parallèlement au développement de la méthode de simulation et de compréhension physique avec les outils de simulation, deux mesures expérimentales ont également été effectuées. Une première a été réalisée dans un centre de rayonnement synchrotron visait à caractériser la réponse de IP à haute énergie. Bien que certains problèmes inattendus rendent difficile l'exploitation des résultats, nous avons extrait l'intensification des écrans métalliques. Les résultats de simulation et expérimentaux montrent globalement un bon accord. L'autre mesure a été effectuée récemment au BAM, Allemagne (21-29 Août, 2014). L'objectif de cette expérience est de comparer le résultat de la simulation d'une imagerie complexe avec l'image acquise expérimentalement. La comparaison est en cours.

Grâce à l'approche de modélisation développée, un outil de simulation d'imagerie CR est maintenant disponible. Il peut être utilisé pour une étude exhaustive de toutes les

configurations de détecteur pour optimiser une application donnée.

4.3 Perspectives

L'approche de simulation de CR, ainsi que la compréhension physique des phénomènes physiques sous-jacents ont été présentées dans les parties précédentes, alors que dans cette section, plusieurs pistes pour l'amélioration de la simulation et de l'étude des phénomènes physiques sont discutées.

- Comparaison expérimentale. Comme indiqué à la fin de la section précédente, une comparaison avec les résultats expérimentaux est en cours.
- Amélioration de la simulation et de la modélisation.
  - Base de données de modèle de la réponse du détecteur. A ce jour, les modèles sont stockés sous forme de tableaux. Dans le futur, d'autres modèles de détecteurs seront ajoutés pour compléter la base de données, ainsi plus d'espace de stockage est nécessaire. En outre, l'application de la convolution de l'image nécessite que l'image de l'objet et le modèle de détection aient la même fréquence d'échantillonnage, par conséquent on est obligé d'interpoler le modèle de détection pour s'adapter à la matrice de l'image de l'objet. Ce genre de question est surmonté dans la partie de simulation de lecture optique, où la fonction de distribution du laser est fittée par des fonctions analytiques. Comme piste d'amélioration, le fitting peut également être appliqué au modèle de détecteur, de telle sorte que ce dernier peut être représenté par des paramètres d'une fonction analytique. De cette manière, le stockage peut être considérablement réduit, et l'interpolation n'est plus nécessaire.
  - Alors que dans la modélisation Monte Carlo de propagation du laser dans l'IP, la couche de phosphore de l'IP est décrite par les coefficients d'absorption, diffusion et anisotropes, dans les travaux futurs, la théorie de Mie peut être adoptée de manière que l'IP peut être modélisé avec les paramètres intrinsèques telles que les indices de réfraction de phosphore et de liant, la taille des grains et le facteur de remplissage. Une étude de ces paramètres de ces paramètres peut aider à déterminer la taille optimale des grains, le facteur de remplissage ainsi que la nature de liant, ce qui est intéressant du point de vue de la fabrication de l'IP.

- Effet de postluminescence. Dans l'approche de simulation proposée, la postluminescence de PSL n'a pas été prise en compte. Après l'étude bibliographique, nous constatons qu'il est difficile de modéliser l'effet de postluminescence avec un modèle physique de bande complet pour le phosphore, en raison du manque d'informations. Toutefois, une courbe de décroissance de la postluminescence mesurée expérimentalement peut être appliquée au modèle, et bien sûr le coût de calcul va augmenter.
- Effet de la numérisation et de la saturation due à l'IP et des dispositifs optiques. La plage dynamique d'un système CR est limitée à la fois par celui de l'IP et les dispositifs optiques. Bien qu'un IP ait une grande plage dynamique (10^5 ou plus), à cause des dispositifs optiques, le niveau de gris d'une image CR est limitée à 2^{16}. Pour une simulation réaliste, la modélisation des effets de la numérisation et de la saturation devait être aussi intéressante.
- Analyse future. Dans la thèse, une étude systématique sur la réponse du détecteur a été réalisée. Des études similaires peuvent également être effectuées sur les paramètres de lecture optique. Dans le travail montré dans la thèse, nous avons mis en évidence l'influence de la puissance de lecture (produit de la puissance du laser et le temps d'illumination). Une analyse détaillée sur l'influence de la taille des pixels, la puissance du laser et la temporisation pourrait être d'intérêt pour l'optimisation des performances du scanner.

Comme indiqué dans la thèse, l'optimisation implique toujours de trouver un compromis entre la netteté et l'efficacité. Parfois, il est difficile de faire un choix. Un facteur plus global sera intéressant pour une prise de décision objective.

References

Duvauchelle, P., Freud, N., Kaftandjian, V., and Babot, D. (2000). A computer code to simulate x-ray imaging techniques. *Nuclear Instruments and Methods in Physics Research Section B: Beam Interactions with Materials and Atoms*, 170(1):245 – 258.

EN14784-2 (2005). Non-destructive testing - Industrial computed radiography with storage phosphor imaging plates - Part 2: General principles for testing of metallic materials using X-rays and gamma rays.

Contents

List of Figures

List of Tables

Chapter 1

General introduction

"Alice: Would you tell me, please, which way I ought to go from here?
The Cheshire Cat: That depends a good deal on where you want to get to.
Alice: I don't much care where.
The Cheshire Cat: Then it doesn't much matter which way you go.
Alice: ...So long as I get somewhere.
The Cheshire Cat: Oh, you're sure to do that, if only you walk long enough."

Alice in Wonderland

Contents

1.1 Context and objectives

Radiography is an imaging technique which uses high energy radiation sources (such as X-ray tubes and radioisotopes) to inspect the internal structure of an object. With such a technique, one can detect internal defects without altering the examined specimen. It is one of the most commonly used Non-Destructive Testing (NDT) methods including ultrasonic testing and eddy current testing (Willcox and Downes, 2000). A big advantage of radiography over other techniques is that it is suitable for any material, ferrous or not, sound-conducting or not, and this makes it widely applied to the industrial inspection.

With the rise of microprocessors and computers, our life shifts to the computer age. Traditional techniques are fading out, and digital techniques are growing at breathtaking rate. The industrial radiography is also facing this revolution. For over a century, film-based radiography has been applied to the industrial inspection, and nowadays, it is still used a lot. A growing number of testing results are stored in forms of film, which requires more and more physical storage space. More than ever, the digital storage is strongly desired.

Since about 15 years, the NDT community has discussed about effective digital replacement such as Computed Radiography (CR). It uses the same exposure routine as film radiography, except that instead of film, a flexible Imaging Plate (IP) is used to receive the X-ray image. The information is stored as a latent image, which is later read and digitized by an optical scanner. CR is successfully applied in the medical field. However, its performance in industrial application is limited by high attenuation samples which require the use of gamma sources such as Iridium-192 and Cobalt-60. At these energies, the IP efficiency is quite poor and image quality is strongly affected by scattered radiation resulting in image degradation and loss of contrast.

The modeling and computational simulation can help to investigate the underlying problems, improve understanding of basic principles and improve the system performance. In this context, this PhD thesis started in September 2011 at INSA de Lyon, collaborating with EDF and AREVA. The objective of the thesis is to completely model the image formation in CR systems: from the source/object interaction, energy deposition and latent image creation in an imaging plate to the optical readout. This modeling will be the basis of a simulation tool capable of simulating different parameter configurations in order to optimize image quality. The thesis revolves around two main topics: 1) understanding on the physical phenomena including the response of an imaging plate, effects of metallic screens[1] and effects of scattered radiation etc; and 2) modeling the complete CR imaging chain. From an industrial CR simulation perspective, we need a reasonable model, based on which a realistic image can be obtained rapidly, and different operating parameters such as source, IP/screens combination and optical scanning can be taken into account.

1.2 Main contributions of the thesis

The main contribution of this thesis is the construction of the complete CR imaging chain simulation approach. It provides a flexible CR simulation solution by integrating

[1] In industrial radiography, thin metallic screens are sometimes used together with IP to improve image quality.

separately different techniques, Monte Carlo and deterministic codes; a brief introduction of the simulation method will be presented in the next section. Most of the prior CR modeling and simulation works focus on the energy deposition in IP, while this thesis extends the simulation to the optical readout (i.e. laser scattering in IP and laser scanning effect). This thesis also presents a detailed investigation on the physical phenomena taking place during the CR exposure. The precise contributions of this thesis are described as the following two aspects:

- On the physical phenomena understanding (Chapter 3).
  - A Monte Carlo simulation tool (in Fortran) for the physical phenomena investigation. This multipurpose tool is developed for the source-object-detector simulation and detector[2] response characterization. With this tool: 1) the direct/secondary and photon/electron radiations can be tracked separately; 2) the photon and electron spectra propagation is monitored; 3) 3D energy deposition map in IP, due to different radiations, can be stored.
  - Scattered radiation. A case study illustrates the image unsharpness introduced by the scattered radiation, and shows that appropriate metallic screens can lessen the scattered radiation and improve image quality.
  - Detector response characterization. The responses of IP alone and IP with screens are characterized at different energies. The responses are analyzed in terms of energy absorption efficiency, Modulation Transfer Function (MTF) and energy distribution along IP depth direction. This kind of characterization and detailed analysis has not been found in prior works. Meanwhile, an experimental characterization has also been performed at ESRF (European Synchrotron Radiation Facility).
  - Effects of metallic screens and electrons on the energy deposition, as well as the influence of an IP's protective layer.

  The above investigation concerns only the physical phenomena taking place during CR exposure. As the CR optical readout process also has important influence on the final image, we need a model for the complete CR imaging chain comprehension. For this reason, the thesis develops a complete CR simulation approach.

- On the CR modeling and simulation (Chapter 4 and Chapter 5).
  - Complete CR model. The CR simulation is constructed in 3 steps: X-ray attenuation, latent image generation via detector response model and digital image generation via IP's optical response. The last steps are carried out with two analytic models (operators).
  - Simulation and data processing tools. Based on approach proposed, several tools are developed for 1) the latent image generation, 2) digital image generation, 3) detector response model database generation, and 4) Monte Carlo simulation of laser transport in an imaging plate. The tools are programmed in Matlab.

[2]In the following of this thesis, the therm 'detector' refers to an IP alone or a combination of IP with metallic screens.

– Detector response model database. A detector response database has been generated which serves the complete CR chain simulation. The database so far consists of 128 different detector configurations including all the IP/screens combinations recommended in the international standards (EN14784-2, 2005; ISO17636-2, 2013).

1.3 Simulation method

In this thesis, the CR image formation is viewed as a three-step process (Figure 1.1): X-ray attenuation, latent image generation and digital image generation. Different simulation methods (Monte Carlo or deterministic) are applied to different steps. The CR simulation method is summarized as follows.

1. X-ray attenuation (X-ray beam → attenuated X-ray beam) after object. In this step, the source beam interacts with an object resulting in an object image. There exist general purpose Monte Carlo and deterministic codes that can be applied in this step. One can choose his appropriate code according to needs: a Monte Carlo code for a detailed simulation of simple objects or a deterministic code for a fast complex imaging set-up simulation.[3] With whichever method, the output image should contains the energy information namely a spectral image $Obj(E, x, y)$

2. X-ray latent image generation (X-ray photons incoming the detector → storage centers in IP). This step is split into two sub-steps.

   (a) X-ray/detector interaction (X-ray photons incoming the detector → deposited energy in IP), via the detector response model PSF_{det}, resulting in a 3D deposited energy image. The detector response model is obtained by means of an off-line Monte Carlo simulation.

   (b) Latent image formation (deposited energy in IP → storage centers in IP). The latent image is in fact the map of storage center distribution in IP. A part of the deposited energy is stored in IP in forms of storage centers. At present day, the latent image formation mechanism is not clearly understood. Hence this step is modeled a deposited energy to storage center conversion factor g_{sc}.

   The entire Step 2 is modeled by a convolution-based operator H1, $Limg(x, y, z) = \mathrm{H1}(Obj, PSF_{det})$.

3. Digital image generation (storage centers → gray level). This step is also split into two sub-steps.

   (a) Optical readout (storage centers → photo-stimulated luminescence photons). In CR, the latent image is readout by a scanning laser. Due to the IP's granular property, the laser light spreads out in IP; storage centers within the laser

[3] If the MC method is applied, one can deactivate the electron tracking in order to accelerate the simulation. Tracking electron histories takes high computational cost. The weight of electron in the transmitted radiation after an object is small comparing with photon, moreover, the electron radiation can be greatly attenuated by the air between object and detector. Hence it is reasonable to take into account only effects of photons in an object.

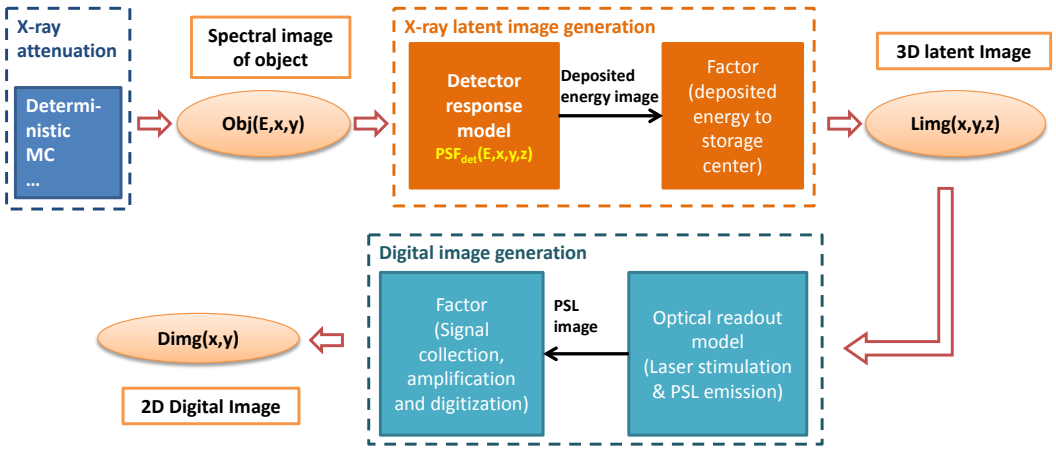

Figure 1.1: Computed radiography imaging chain modeling. The CR image formation is simulated in three steps: 1) X-ray attenuation by an object, 2) latent image generation in an imaging plate and 3) digital image generation. The outputs of the steps provide us the image propagation in a CR system: from the spectral image of an object $Obj(E, x, y)$, to the three-dimensional latent image $Limg(x, y, z)$ and the final two-dimensional digital image $Dimg(x, y)$.

volume can be released resulting in PSL. The laser spreading is simulated with a Monte Carlo tool we developed. This tool outputs a laser distribution function $f(x, y, z)$. The scanning is described by the scanning parameters i.e. laser power P_{laser}, scanning speed v_{scan} and pixel size l_{pxl}.

(b) Signal collection, amplification and digitization (PSL photons $\rightarrow$ gray level). In this sub-step, the emitted PSL is collected by a light guide, then detected and amplified by a photo-multiplier tube (PMT) and finally digitized with an analog-to-digital converter (ADC). A PSL to gray level conversion factor g_{psl} can be applied. In the thesis, the effect of this sub-step is just taken into account by an efficiency factor g_{psl}.

Step 3 is modeled by an operator H2, $Dimg(x, y) = \text{H2}(Limg, f, scanning\ parameters)$.

With the presented method, one can simulate the complete CR imaging chain, and the operating parameters such as source, detector configuration and optical readout parameters can be taken into account by applying H1 and H2.

1.4 Organization of the thesis

This thesis is organized as follows. Chapter 2 presents a bibliographic study on the CR principle, and CR modeling and simulation works. By analyzing the simulation feasibility of each detailed CR image formation step, we propose our simulation approach as presented in the previous section. Chapter 3 dwells on the first aspect of this thesis work, physical phenomena comprehension. A Monte Carlo simulation tool is first presented. The usefulness of the tool is presented by an optimization study of a realistic inspection

case. The optimization is based on the physical phenomena investigation. Chapter 4 and Chapter 5 detail the steps of the complete CR image formation simulation. Chapter 4 presents the simulation of the first two steps. In fact, these two steps can be carried out with a full Monte Carlo simulation. The interest of simulating in two steps is also discussed in this Chapter. A case study is performed, where a complex shape object is simulated. The latent images generated using different detector configurations are compared. The detector model database is presented at the end of the chapter. Chapter 5 describes the last step of the CR simulation. The Monte Carlo modeling of laser photon transport in IP is first presented in this chapter. The influence of changing the IP's optical property such as absorption and scattering factor is studied using the Monte Carlo model. This MC output is then applied to the readout model H2 for generating the final image. Final simulation results are then compared before concluding the chapter. A brief summary of the main results and future perspectives are presented at the end of the thesis.

Chapter 2

Bibliographic study

"Read the directions and directly you will be directed"

Alice in Wonderland

Contents

Computed radiography is a digital radiographic imaging technique. At present, it is widely applied in medical diagnostic, because such a technique provides a number of advantages over the traditional film-based radiography. However, for the industrial application, which uses high energy radiation sources, CR image quality cannot fulfill all requirements. For this reason, the film-based imaging is still used a lot. In the recent years, 'film free' radiography has been put on the agenda. As a promising film alternative, CR performance at high energies still need to be improved. This chapter presents the basic understanding on the computed radiography as well as the state-of-the-art in CR modeling and simulation.

2.1 Understanding on the computed radiography

2.1.1 Introduction: historical background

X-rays were applied to detecting internal defects inside structures soon after being discovered by the German scientist Conrad Roentgen in 1895 (Als-Nielsen and McMorrow, 2011). As a very energetic radiation, it can penetrate opaque and even metallic objects. Another important radiation source is gamma rays (γ-rays), which was also discovered in the same period (radioactivity by Henri Becquerel in 1896 and radium by the Curies in 1903) (Attix, 2008). The γ-ray is also very energetic, and originates from the radioactive decay process of radioisotopes such as Iridium 192. These two kinds of radiation sources are employed in radiographic non-destructive testing (NDT).

Radiography can detect variations of material type or thickness via the intensity variation of the transmitted radiation. Heavy (i.e. high atomic number and/or high density) or thick materials can attenuate greatly the X-ray (or γ-ray) beam. The transmitted beam, which carries the object pattern, is received by a detector. At the beginning, early 1900s, glass radiography plates were used to detect X-ray image. Later, the flexible silver film has been invented (Slide, 2014). Now, with the advent of the digital age, the film is more and more replaced by digital detectors such as storage phosphor plates used in computed radiography (CR) and photoconductor plates used in digital radiography (DR).

The development of digital radiography systems dates back to the 1970s. KODAK first got the patent of a method for producing X-ray imaging using storage phosphor imaging plate (IP) in 1975 (George, 1975). Five years later, Fuji first commercialized the computed radiography system for medical imaging (Kotera et al., 1980). Quickly, the CR became largely used in the clinical application. Until 1990s, a competitive system of CR, named digital radiography (DR), has been invented. In the following years, the invention of DR system grew up. There appear scintillator/flat-panel based DR (1997), amorphous selenium based DR (1995), wireless DR (2009) etc (Lança and Silva, 2009). Meanwhile, needle-structure imaging plates have also been developed as CR detector for achieving dose reduction and sharpness improvement (Leblans et al., 1999; Leblans et al., 2000).

Comparing the digital technologies with the traditional film radiography, both CR and DR are much more dose efficient and have larger dynamic range (Lança and Silva, 2009). The direct digital output allows image processing, long distance sharing, loss-less image copy, elimination of chemical development and physical storage etc. Though digital systems are more expensive than film systems, as films are not reusable, the long-term cost becomes smaller.

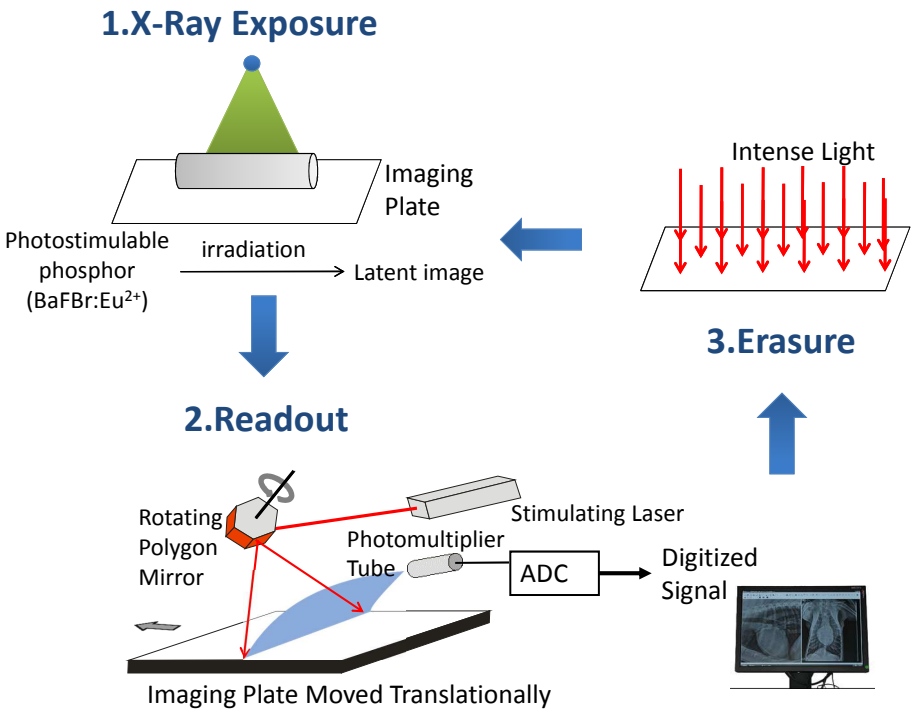

Figure 2.1: Computed radiography procedure: during exposure, an imaging plate is used to receive the transmitted x-ray image creating a latent image (which is stable in hours under room temperature); as a second step, the imaging plate is introduced into an laser scanner, and the latent image is released and digitized resulting in a final digital image which can be viewed through monitors; intense light is used in the last step to erase the residual image in imaging plate.

CR and DR both have their advantages and limitations. In CR, the X-ray image is received by an imaging plate resulting in a latent image, and later the latent image is readout by a laser scanner. The X-ray exposure and readout are two independent processes. Users can keep their existing exposure routine, and simply replace film by phosphor imaging plate. DR has a better performance in image quality (good signal to noise ratio) over CR. However, a DR system is highly expensive. The big advantage of CR over DR is the IP's flexibility which facilitates the measurement in a difficult situation such as a narrow space or cylindrical pieces. Though the independence of the exposure and readout of CR obliges user interaction (handling the imaging plate), it also allows industrial inspections without electrical plugging unlike DR.

In the following, we will discuss in detail the principle of a CR system.

2.1.2 Overview of CR workflow, advantages and limitations

Computed radiography, as shown in Figure 2.1, is based on the use of Photo-stimulated Phosphor (PSP) imaging plate (Sonoda et al., 1983). CR uses same exposure routine as traditional film radiography: by absorption of X- or γ-ray, a latent image is generated in PSP imaging plate. The latent image is stable in hours under room temperature. The

imaging plate, like film, can be handled with a light-tight cassette. In order to enhance the X- or γ-ray absorption efficiency at high energies, metallic screens are usually used together with IP within a cassette. After exposure, the IP is introduced into an optical scanner by users. With the scanning of the finely focused laser light (raster scanning), the latent image stored in IP is released by means of PSL. The emitted signal is guided into photomultiplier by an optical fiber, and then converted into a digital image. An intense light is used in the last step to erase the unreleased information, and then the imaging plate can be reused. An imaging plate can be reused thousands of times (Huang, 2010).

We summarize the strengths and limitations of computed radiography over other techniques as follows.

- Direct digital output. Comparing with film radiography, CR provides directly a digital image which allows image processing, instantaneous long distance sharing and elimination of physical storage.
- High dynamic range ($\sim$5 orders of magnitude). IP's dynamic range is much greater than film, hence fewer retakes are needed for a great thickness variation object and over- or under-exposure can be avoided (Figure 2.2).
- Great sensitivity of imaging plate. CR detector is more dose efficient than film. Therefore, to inspect the same thickness, a lower energy source can be applied with still an acceptable image quality. This advantage is significant in the case of inspecting objects of small thickness with relatively low energy sources.
- No chemical development. The CR latent image is rendered into a visible digital image by an optical scanner, thus there is no environmental pollution of chemical product.
- Flexibility of imaging plate. The imaging plate can be bent and cut according to needs.
- Reusable detector. An imaging plate can be reused thousands of times, thus the long-term cost becomes lower than film.
- Independence of exposure and readout process. The radiation exposure and readout are two independent steps. Users do not have to modify their existing exposure routine, thus it is much easier to implement CR than DR. Moreover in the case of inspecting with gamma sources, CR is more feasible over DR, as it does not need to be plugged.
- Less expensive than DR.

CR also has its limitations as listed in the following.

- Unsharpness introduced by readout scanning. Comparing with film radiography, the additional readout process degrades the image sharpness.
- Independence of exposure and readout process. This independence is less practical for the user when compared with DR, because with DR the user has a direct real time access to the acquired image and thus, can modify the acquisition parameters

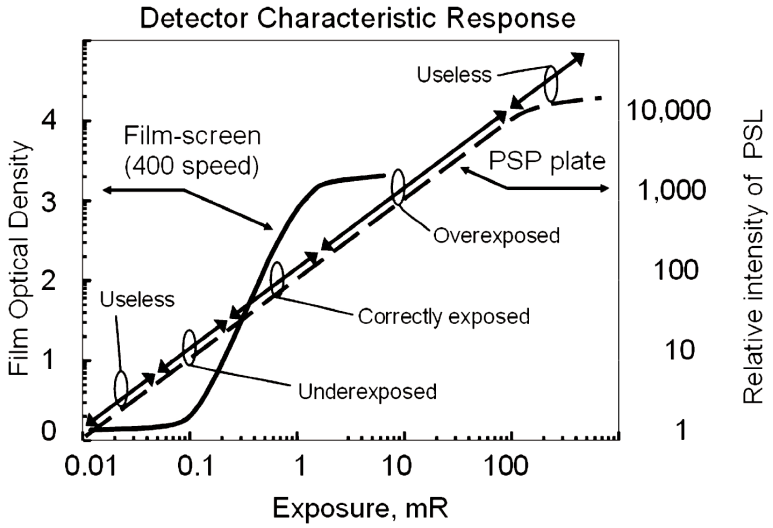

Figure 2.2: A characteristic response example of a 400-speed rare-earth screen-film (solid curve) and a PSP detector (dashed curve) (AAPM Task Group 10, 2006). Great dynamic range eliminates the exposure retakes caused by over- or under-exposure.

to obtain the required image quality; whereas, with CR, one has to wait for the readout process.

- Strong energy dependence (Figure 2.3). The IP phosphor contains high atomic number elements (e.g. barium), which makes IP highly sensitive to low energies and insensitive to high energies. As a result, to inspect a high scattering object with CR, the image quality is not as good as film.

- Less dose sensitivity than DR. CR losses dose sensitivity during latent image formation and readout process. For an identical exam, the necessary dose for CR is much greater than for DR.

All the above mentioned CR strengths and limitations result, in fact, from the IP's characteristics: storage property, X- or γ-ray response and optical response. Imaging plate is the key factor of CR performance; in the following we are going to discuss the imaging plates.

2.1.3 CR detector: Imaging plate

Imaging plate is the recording medium of the latent image, and the CR image depends massively on IP's property. Today's existing imaging plates can be categorized into three families: powder (or granular) plate, needle-structured plate and glass-ceramic plate (see Figure 2.4). Powder plates are the most common commercial imaging plate, in which the phosphor (e.g. $BaFBr : Eu^{2+}$) grains (of about 5 μm diameter) are held in a polymer binder. In needle plates, there is no use of binder, the phosphor crystals (e.g. $CsBr : Eu^{2+}$) are grown into needles (about 5 to 10 μm diameter and 400 to 500 μm length (Leblans et al., 2011) which act as light guides. Hence strong light scattering can be avoided

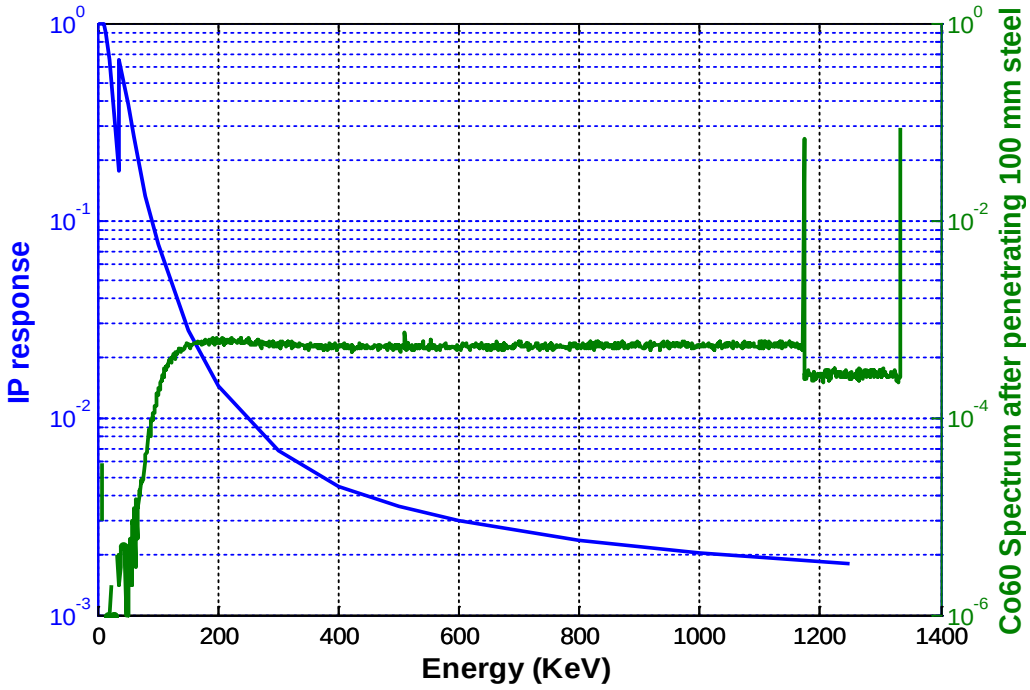

Figure 2.3: Energy dependence of an imaging plate and the Co60 spectrum after penetrating a 100 mm steel object (green).The two peaks of the green curve correspond to the Co60's characteristic energy lines, while the rest is the scattered beam caused by the object. IP is more sensitive to the lower energy scattering (responsible for blurring) than to the primary Co60 peaks (corresponding to object pattern) resulting in poor image quality. Image is obtained by means of Monte Carlo simulation. (The curves were obtained with Monte Carlo simulations as explained in Chapter 3.)

leading to better image quality than a powder plate of the same thickness. The glass-ceramic type IP is not yet commercialized nowadays, in which nano- or micro-crystallites (e.g. $BaCl_2 : Ce^{3+}$) are doped into a glassy material (Selling et al., 2005). Due to the transparency of the glass-ceramic material, the light scattering can be greatly reduced resulting in good spatial resolution. An imaging plate basically consists of three layers (see Figure 2.5): a protective layer (also known as overcoat, topcoat or top layer), a photostimulable phosphor layer and a support layer (or substrate). According to the application, sometimes a reflective (or absorbing) layer is added between phosphor and support layers in order to gain detection efficiency (or spatial resolution) (Rowlands, 2002). The PSP layer is the effective latent image carrying medium.

2.1.4 Existing photostimulable phosphor materials

The first commercially used PSP material is BaFBr by Fuji in their cassette based CR system (Rowlands, 2002). $BaFBr : Eu^{2+}$ is considered as a reference PSP material; the stored signal is stable at room temperature (75% of information remains 8 hours after exposure) (Rowlands, 2002). Since, other PSP materials have also been found (Table 2.1). Among these materials, the rare-earth-doped alkaline-earth halide family $BaFX : Eu^{2+}$, where X is Br, I, Cl or an arbitrary combination of them, are the most successful ones. To improve spatial resolution, Konica proposed a cubic structured crystal[1] phosphor $RbBr : Tl^{+}$. As the latent image stored in such a material is not stable, Konica applied it in their integrated-reader CR system for a quick readout after exposure. In later 1990s, Agfa has found CsBr based phosphors having a good stability of latent image and a good photostimulable property (Leblans et al., 1999; Leblans et al., 2000).

Table 2.1: Types of commercial photostimulable phosphors (Rowlands, 2002; Leblans et al., 2011).

Material	Cubic structure	Form	Stable trap	Manufacturer	Comments
$BaFBr : Eu^{2+}$	No	granular	yes	Fuji	Cassette based CR
$BaFBr_{0.85}I_{0.15} : Eu^{2+}$	No	granular	Yes	Agfa/Kodak	Cassette based CR
$BaFBr : Eu^{2+}$	No	granular	Yes	Konica	Cassette based CR
$RbBr : Tl^{+}$	Yes	needle	No	Konica	Cassetteless integrated CR system
$CsBr : Eu^{2+}$	Yes	needle	Yes	Agfa	Cassette or integrated CR system

Besides the above mentioned commercialized PSP material, other photostimulable materials are also found (see Table 2.2). However, some of these materials are of low K-edge energies (15-17 keV) meaning a low X-ray absorption efficiency. For the others which have higher K-edge energies, either their stimulation bands do not match the semiconductor laser ($\sim$ 670 nm), or their emission bands do not match well the optical amplification or detection device, or they have a long decay time (20 μs) requiring long readout time.

[1]The use of cubic structured crystals in needle IP is to avoid having birefringence as in $BaFX : Eu^{2+}$.

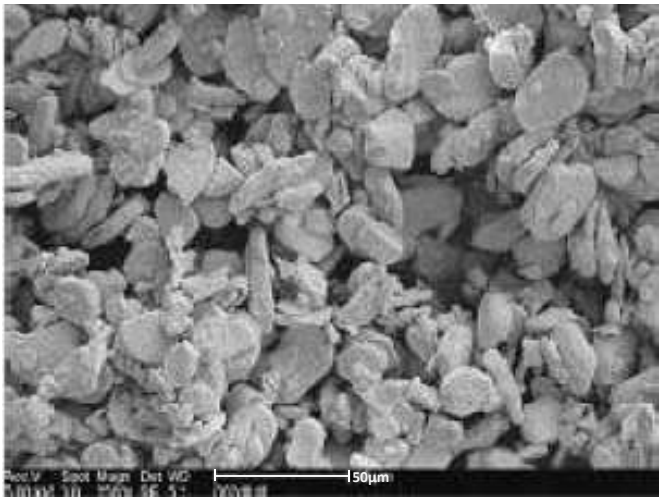

(a)

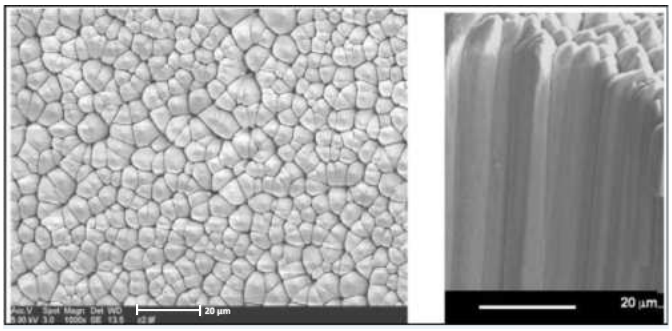

(b)

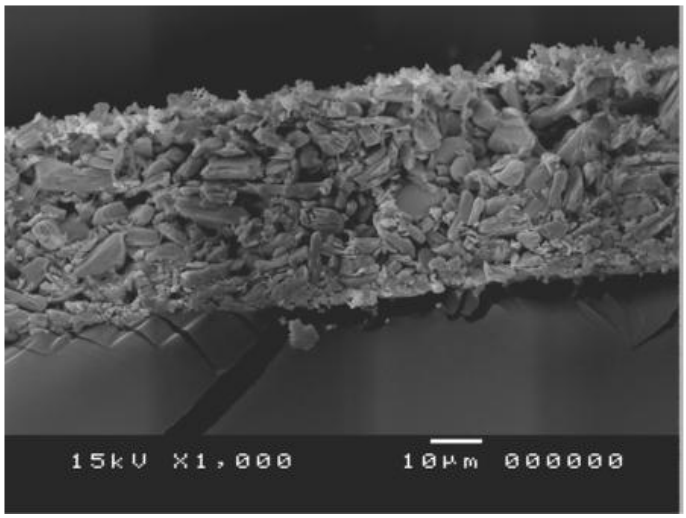

(c)

Figure 2.4: SEM images of three different type imaging plates: (a) powder plate, (b) needle-structured plate and (c) glass-ceramic plate (Winch, 2008; Leblans et al., 2011).

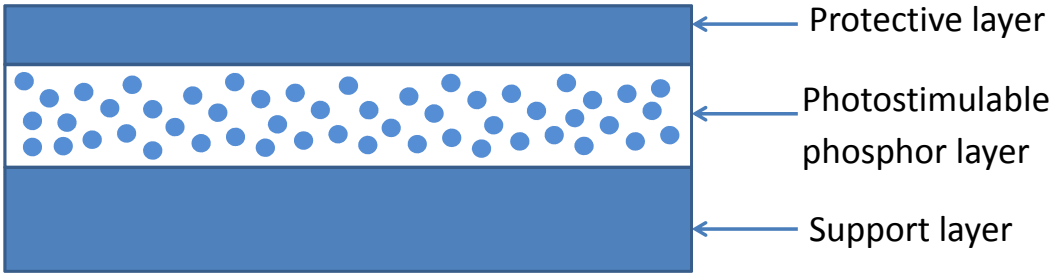

Figure 2.5: Plate structure. An imaging plate basically has a three-layered structure: protective layer, PSP layer and support layer. Some manufacturers add additional layers between PSP and support layers to enhance certain aspects of image quality, e.g. a high absorption layer for a good spatial resolution.

Table 2.2: Alternative photostimulable materials and their properties. Data were found in multiple references (Chernov et al., 1998; Schipper et al., 1993; Bos et al., 2010; Zych et al., 2003; Meijerink et al., 1991; Leblans et al., 2011).

Material	K-edge energy (keV)	Emission band (nm)	Stimulation band (nm)	PSL decay time (μs)
$CsI : Tl^{+}$	36.0	590	950	0.3
$RbBr : In^{+}$	15.2	490	700	NA
$RbBr : Ga^{+}$	15.2	550	705	20
$CsBr : In^{+}$	36.0	504	700	NA
$CsBr : Ga^{+}$	36.0	515	685	0.7
$CsBr : Eu^{2+}$	36.0	440	685	NA
$Ba_3(PO_4)_2 : Eu^{2+}, La^{3+}$	37.4	410	500	NA
$YPO_4 : Ce^{3+}, Sm^{3+}$	17.0	352	460	NA
$Lu_2O_3 : Tb^{3+}$	63.3	545	647	NA
$Y_2SiO_5 : Ce^{3+}, Sm^{3+}$	17.0	340	410	NA

NA: Not Available.

Until present day, a perfect PSP has not been found yet, but some properties have been improved. For example, in order to have a better spectrum match of photostimulation and semiconductor laser, the Br^{-} in BaFBr is partially replaced by I^{-} ($BaFBr_{0.85}I_{0.15} : Eu^{2+}$) to modify the lattice distance. Sometimes blue dye is included in the binder material to limit the scattering region of laser light within IP so that a good spatial resolution can be gained.

To have a good system performance, a good photostimulable phosphor material should have the following characteristics:

- high sensitivity to X- or gamma-ray radiation (good radiation absorption efficiency);
- high X- ray to visible photon conversion efficiency (not all the absorbed X-ray can be stored as latent image and later be released as visible photons);
- good stability at room temperature to assure a long fading (energy loss) time;

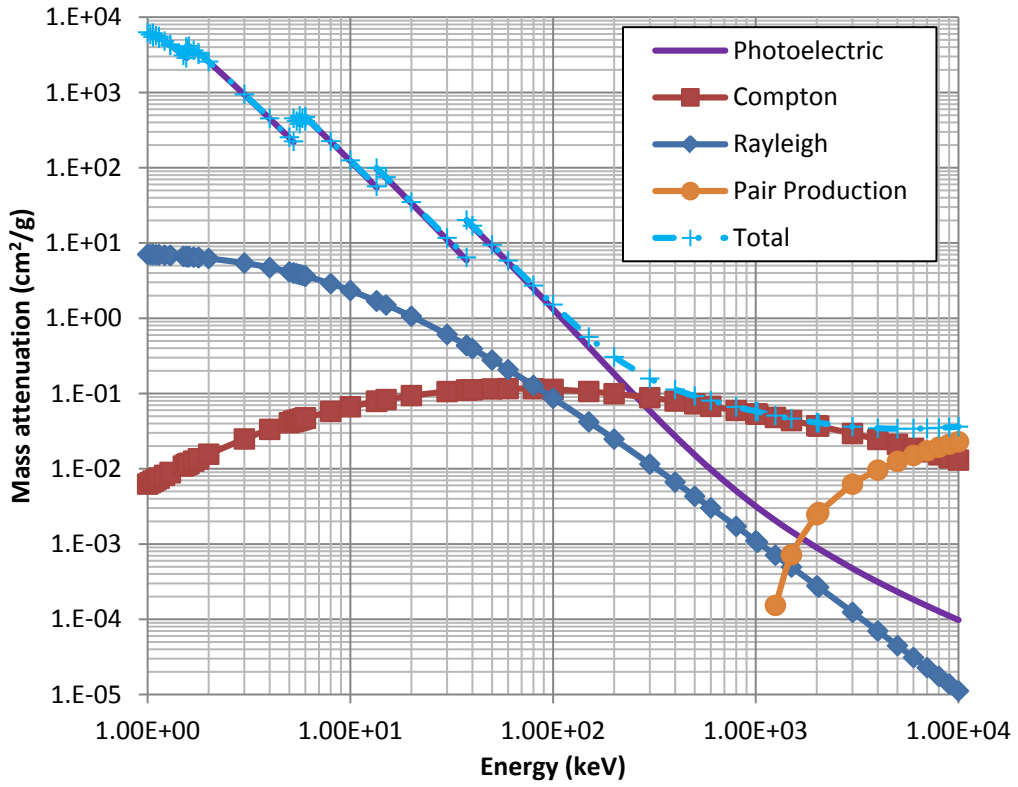

Figure 2.6: Attenuation coefficient of BaFBr: the total X-ray attenuation of BaFBr is mainly resulting from different interactions, photoelectric, Compton, Rayleigh and pair production effects. (Data are from NIST X-ray Attenuation Database: `http://www.nist.gov/pml/data/xcom/index.cfm`).

- short readout decay to gain spatial resolution and have a fast readout;
- sensitivity to the existing semiconductor laser (for a good system integrity and a good optical readout efficiency);
- separate exciting spectrum and emission spectrum.

These factors depend on the PSP's X-ray absorption property, the latent image generation mechanism and the photostimulation mechanism of the phosphor.

2.1.5 X-ray property of BaFBr : Eu^{2+}

The detection of an X-ray image starts from the interaction of the detector (imaging plate) and X-ray photon. There are mainly four types of interactions that might take place within IP (see Figure 2.6): photoelectric effect, Rayleigh scattering, Compton scattering and pair production. Photoelectric effect is predominant until about 200 keV, then Compton scattering become the most important effect.

The interaction of X-ray photons with the phosphor leads to energy deposition in IP. At low energies, where photoelectric (PE) effect is predominant, the deposited energy

$E_{dep,PE}$ can be estimated by:

$$E_{dep,PE} = N_{X-ray} \int_E E\lambda(E) \left\{ 1 - exp \left[-\frac{\mu_{\alpha,PE}(E)}{\rho} \cdot \rho \cdot d \right] \right\} dE, \tag{2.1}$$

where N_{X-ray} is the incident X-ray photon number, $\lambda(E)$ is the normalized incident X-ray spectrum with $\int_E \lambda(E)dE = 1$, ρ is the effective phosphor density, $\frac{\mu_{\alpha,PE}(E)}{\rho}$ is the mass attenuation coefficient (corresponding to the values in purple curve in Figure 2.6), d is phosphor thickness and E is the X-ray photon energy. The deposited energy is directly proportional to the incident X-ray photon number, and this photon number reflects the object pattern. We can also see that at low energies the mass attenuation coefficient is relatively high leading a great absorption efficiency. However at high energies, the absorption efficiency becomes poor.

Equation 2.1 is a very good estimation when the X-ray energy is lower than the K-edge energy of the phosphor. If the photon energy exceeds this energy, the characteristic fluorescence radiation will be emitted by the phosphor, and the fluorescence energy should be subtracted from Equation 2.1. At energies where Compton scattering is pronounced, the deposited energy owing to scattering and multiple scattering should also be taken into account. In this case, Equation 2.1 becomes complicated, and the solution to it is often obtained by means of Monte Carlo simulation or experimental measurement.

For the conventional phosphor (scintillator) used in DR, almost all the deposited energy is converted into visible photons (Rowlands, 2002); while for PSP, only a fraction of the deposited energy forms latent image and contributes to visible photons during read-out (Thoms et al., 1991), and this portion depends on the so-called defect generation mechanism during X-ray exposure.

2.1.6 Latent image formation mechanism

The latent image is in fact constituted by electrons in semi-stable traps (i.e. F centers, also known as storage centers or PSL centers) within the phosphor structure. There are, in general, 3 steps for generating the latent image (Leblans et al., 2011; Seggern, 1999):

- X-ray energy deposition into material through photoelectric, Compton or pair production effects;
- by absorbing energy, electrons in the valence band are excited into the conduction band resulting in electron/hole pairs;
- for a part of electron/hole pairs, the electrons recombine with the holes immediately resulting in spontaneous luminescence; while for others, electrons and holes are spatially separated and form the latent image.

The spatial distribution of the trapped charges (electrons and holes) in a plate containing PSP crystals makes up the latent image in CR. The spontaneous recombination of the trapped electrons and holes results in the fading of signal. For a typical imaging plate, 25% of energy is lost within a fading time of several minutes to 8 hours after exposure (AAPM Task Group 10, 2006). Long fading time (stable traps) at room temperature is a critical parameter.

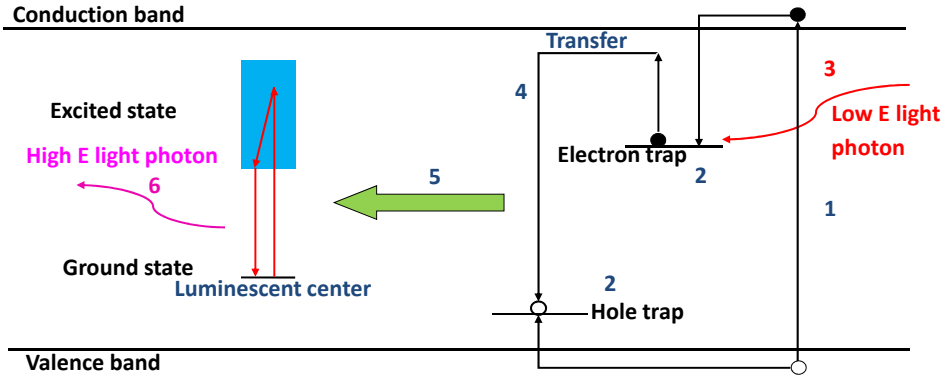

Figure 2.7: Photostimulated luminescence in a storage phosphor (Leblans et al., 2011): 1) X-ray interacts with PSP crystal resulting in electron/hole pair (e/h) creation; 2) e/h are trapped separately forming semi-stable centers (latent image); 3)trapped electron is excited by red laser photon and tunnels to neighboring hole trap; 4) electron recombines with the trapped hole; 5) the energy released by recombination is transferred to the activator Eu^{2+} center (luminescence center) and excite the activator into its excited state; 6) the activator relaxation results in PSL emission.

Once the latent image is generated, the trapped electrons could be excited into their excited energy level or conduction band with relative low energy photon (e.g. red laser) (Seggern, 1999). This makes it possible to combine with a hole in the neighborhood or with a hole in 'long distance' (several lattice lengths) passing energy to the so-called activator or luminescent center (e.g. Eu^{2+}) besides resulting in emission of relatively high energy photons (blue emission). The whole process of generating latent image and PSL emission is presented in Figure 2.7.

The defect generation mechanisms for different PSP materials are different, but it basically involves an electron trap center, a hole trap center and an activator (which provides PSL emission), and the difference is that these centers are played by different elements. For some co-doped materials such as $YPO_4 : Ce^{3+}, Sm^{3+}$, one dopant (Sm^{3+}) traps electrons during X-ray irradiation, and the other plays the roles of a hole trap and an activator (Bos et al., 2010). As another example, Tb^{3+} is a hole trap center and also activator in $Lu_2O_3 : Tb^{3+}$ (Zych et al., 2003). For $BaFBr : Eu^{2+}$, it is well accepted that the dopant Eu^{2+} does not capture holes but only contributes to PSL (Schweizer, 2001; Leblans et al., 2011).

Since the discovery of the photostimulability of $BaFBr : Eu^{2+}$, several works (Takahashi et al., 1984; Thoms et al., 1991; Koschnick et al., 1991; Koschnick et al., 1992; Schweizer, 2001; Meijerink and Blasse, 1991; Meijerink, 1996) have been done attempting to find out the physical mechanism during X-ray radiation. Present day's well accepted electron/hole production mechanism is proposed by Spaeth et *al.* (Koschnick et al., 1991; Leblans et al., 2011). Br^- vacancies are assumed to be already present within BaFBr lattice before exposure. During X-ray exposure, these Br^- vacancies play as electron traps

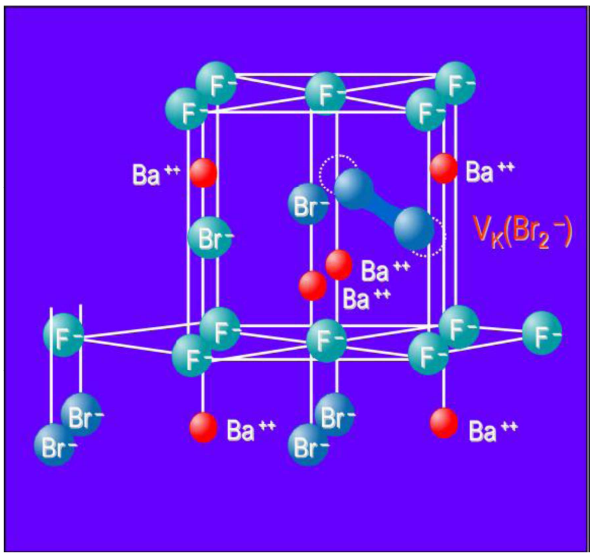

Figure 2.8: Model of the BaFBr lattice cell with $V_k(Br_2^-)$ center (Leblans et al., 2011). $V_k(Br_2^-)$ center is radiation-introduced effect. During exposure, two adjacent Br ions shift towards each other and trap a hole forming a $V_k(Br_2^-)$ center.

forming F centers[2]. The Br^- vacancy is resulting from the oxygen impurity during PSP fabrication. An O^{2-} occupies the site of an F^-; for the charge compensation, a Br^- vacancy is created. Upon X-ray radiation, two adjacent Br^- shift toward each other and trap a hole forming a $V_k(Br_2^-)$ center (see Figure 2.8).

The $F(Br^-)$ center[3] and $V_k(Br_2^-)$ center are directly related to the photostimulation property of $BaFBr : Eu^{2+}$. There are also evidence for the existence of other kinds of centers such as $F(F^-)$ center[4] (Thoms et al., 1991) which do not contribute to latent image.

2.1.7 Photostimulation mechanism

The band model of photostimulation is illustrated in Figure 2.9. The $F(Br^-)$ center has two stimulation bands at 2.1 eV and 2.5 eV, as a result of its Matlockite (non-cubic) structure (see Figure 2.8). The excitation allows the F center electron transition from ground state (1s) to its excited state (2p) from which the electron relaxes into a relaxed excited state ($2p_r$). There are three alternatives (Seggern, 1999) 1) relaxing into its excited ground state ($1s_r$) resulting an infrared radiation; 2) escaping to conduction band by thermal activation and 3) tunneling to the neighboring hole center. Once the electron tunnels to a hole center and recombine with it, the released energy is transferred to the neighboring activator (Eu^{2+}) resulting in PSL (see the right part in Figure 2.9, where F center, hole

[2]F center. An F center or Farbe (German for color) center is a type of crystallographic defect in which an anionic vacancy in a crystal is filled by one or more electrons.

[3] $F(Br^-)$ center. An F center is placed at Br^- site

[4] $F(F^-)$ center. An F center is placed at F^- site

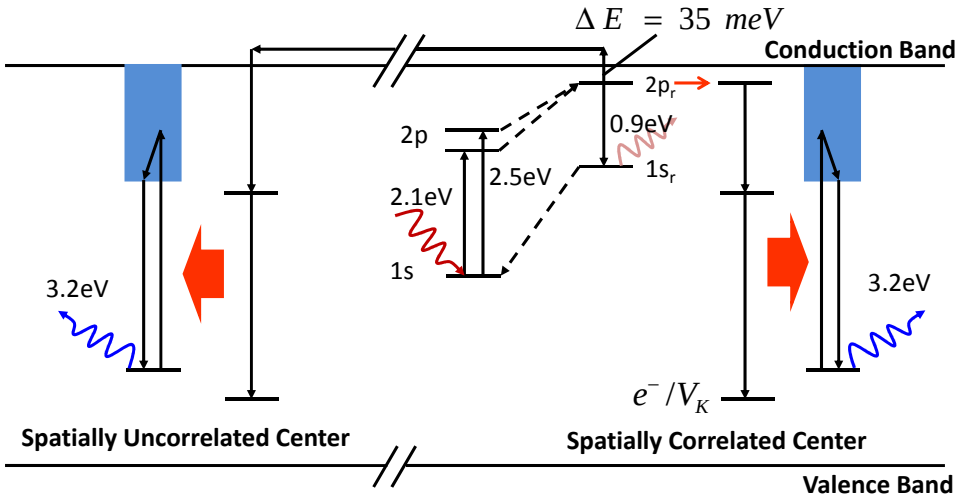

Figure 2.9: Band model of the PSL process in BaFBr : Eu^{2+} (Seggern, 1999): the dotted lines represent the relaxation processes. An electron can recombine with a hole through tunneling or thermal activation. For an effective PSL emission, the recombination site should be close enough to an activator, so that the energy released by the electron/hole recombination can be transferred to an activator resulting in PSL.

center and activator are close to each other). Another way producing PSL is via thermal activation (see the left part in Figure 2.9). The electron in the relaxed excited state ($2p_r$) can be excited into conduction band through thermal activation and move freely in the conduction band. It can arrive at the long distance hole center (which is besides an activator) and recombine with it triggering PSL emission. Note that for an effective PSL emission, the hole center (correlated or uncorrelated) should be close to an activator so that the recombination energy can be passed to the activator resulting in PSL.

2.1.8 Spatial correlation of defects

The tunneling effect and the energy transfer from electron/hole recombination to activator require that the $F(Br^-)$ center, the hole ($V_k(Br_2^-)$) center and the activator (Eu^{2+}) should be spatially correlated with each other. Hence the triple defect aggregates are required for the efficient emission of PSL.

At low temperature, efficient PSL can be detected (Thoms et al., 1991; Schweizer, 2001) which means that triple defect aggregates are already formed, and it is assumed that the excitation decay causing the formation of the $F(Br^-)$ and $V_k(Br_2^-)$ centers preferentially occurs in the vicinity of activator Eu^{2+} site. At high temperature the formation of triple aggregates is assumed to be a dynamic equilibrium. The defects in the crystal lattice are mobile at high temperature. The triple defect aggregate might disappear at one site, but a new one might be formed at another site owing to the mobility of the defect centers. Koschnick et al. (Koschnick et al., 1991) found that after exhaustion (stimulating with a laser until no more PSL can be produced) at low temperature, a phosphor crystal can be stimulated again when it is heated to a temperature greater than 200 K. The reason

is that at this temperature, the defects become mobile, and new defect aggregates can be formed via the replenishment effect.

Thoms et co-workers have also investigated the spatial correlation and photostimulability of defect centers in $BaFBr : Eu^{2+}$. They claimed that different defect centers (see Table 2.3) are created after irradiation, and these centers were identified by their excitation peaks and IR emission peaks (Thoms et al., 1991)). Among these identified centers, only $F(Br^-)$ center was found useful for PSL emission. In the table 2.3 we can see that the total generation rate of all the defects and spontaneous luminescence photons is 40.51 per keV; therefore the average defect generation energy is about 24.7 eV (1keV/40.51). It is generally accepted that energy on the order of 3 times the band-gap energy is needed to form an electron/hole pair (Klein, 1968). The band gap energy of BaFBr is about 8.3 eV, hence 24.9 eV is needed. Their experimental result agrees well with the theoretical estimation. All the correlative $F(Br^-)$ centers and part of the uncorrelated $F(Br^-)$) centers can be stimulated and contribute to PSL (Klein, 1968; Leblans et al., 2011). Therefore the PSL generation rate should be between 1.82 and 7.98 per keV, which also agrees with the data (140 photons/50 keV = 2.8 photons/keV) found in the article of Rowlands (Rowlands, 2002). However Thoms et co-workers have found that the start-up temperature of the uncorrelated defect PSL is 60 K which is different from the value of 200 K found in the work of Koschnick et al. (Koschnick et al., 1991).

Table 2.3: Relative concentration and creation efficiency of radiation induced defects and the spontaneous luminescence photons in a $BaFBr : Eu^{2+}$ crystal (Thoms et al., 1991; Thoms and Seggern, 1994; Seggern, 1999).

Center types	Relative concentration (%)	Generation rate (number/keV)	Photonstimulable (yes/no)
$F_{uncorr}(Br^-)$	12.4	6.16	Yes
$F_{corr}(Br^-)$	3.7	1.82	Yes
$F(F^-)$	13.8	6.86	No
$F_A(Eu^{2+}, F^-)$	15.6	7.75	No
$M(F^-)$	39.0	10.36	No
$M_A(Eu^{2+}, F^-)$	4.8	2.35	No
Spontaneous luminescence photon	10.7	5.21	No
Total	100	40.51	-

2.1.9 Optical effects during the readout process

The CR latent image is stored in the form of trapped electrons. With a scanning laser beam, the latent image is readout (via PSL mechanism) and digitized (i.e. 'pixelized'). During the laser scanning process, optical effects are also involved. In CR scanner, a scanning laser beam enters into IP and interacts with phosphor grains. The exposed phosphor grains which contain trapped electrons (F centers) can be photostimulated releasing PSL. As illustrated in Figure 2.10, due to the granular property of the PSL layer, the laser beam spreads out along its propagation path due to light scattering, which causes a large

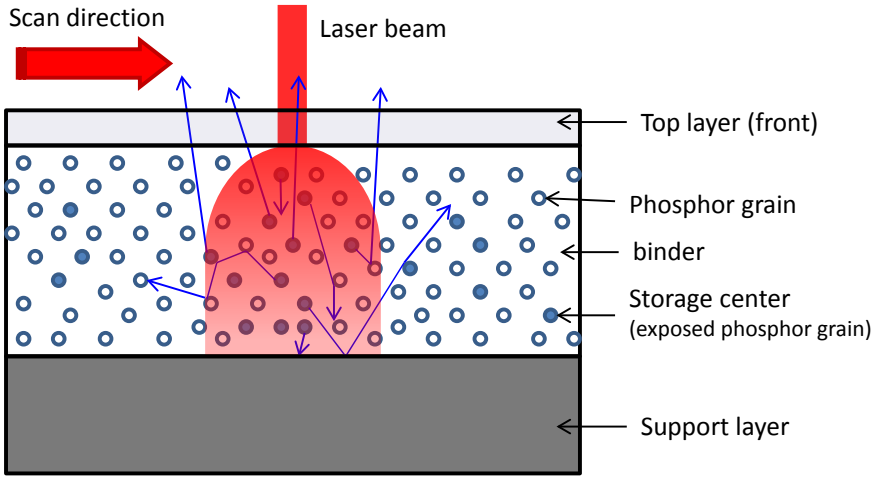

Figure 2.10: Optical effect within imaging plate: the laser beam scans the imaging plate along the scan direction; while entering the phosphor layer, the laser beam diffuses along its propagation path causing a large scattering region and releases also information in the neighboring unwanted region.

reading region (red volume). All the emitted PSL which can be collected will contribute to the signal of the pixel which corresponds to the current laser beam location.

The scattering volume will bleach the storage centers in the unwanted region (neighboring region) and thus degrades the spatial resolution. The best spatial resolution is limited by the laser beam diameter, which is between 50 and 100 μm in medical CR (Leblans et al., 2011). The latest CR scanner of GE provides a laser size of 30 μm.

The PSL emission depends on the laser power and laser dwell time on the 'pixel'. With a greater power and dwell time, more laser photons will arrives in the red volume, thus more PSL photons are emitted. Meanwhile, the neighbor pixels are more affected leading more spatial degradation. However, in the case of short dwell time, the image will be influenced by the after glowing effect. The phosphor continues emitting PSL during a certain time after photostimulation. The afterglow will affect the next pixel to be scanned. For a Eu-doped phosphor, the decay time is about 0.7 μs; the dwell time is usually 5 times longer than the decay (Rowlands, 2002) to avoid afterglow influence.

2.1.10 Discussion

To conclude the above understanding on the CR principle, the IP's (X-ray and optical) properties are the key factor to the CR image quality.

During exposure, the imaging plate stores the transmitted X-ray image in the form of latent image (semi-stable trapped electrons). In the BaFBr (the most common IP material) lattice, the Br^- vacancies play the role of electron trap; although the hole trap mechanism has not been clearly understood, it is well accepted to be the radiation-introduced V_k center.

An effective photosimulated luminescence emission requires spatial correlation of the trapped electron, hole and the activator. When the three defects are close enough to each

other, electrons can effectively recombine with holes and pass the energy to the activator resulting in PSL.

The scanner property and the IP's optical property are two important factors during readout process. The laser beam size and scattering effect in IP determine the sampling limit (spatial resolution). The laser power and scanning time affect PSL emission and also image sharpness.

Beside the experimental studies on the CR property, computational simulation is also an important tool to understand the physics of computed radiography. In the following of this chapter, we focus on the works relevant to the CR modeling and simulation.

2.2 CR modeling and simulation

In this part we resume the important modeling and simulation works concerning computed radiography. CR imaging is a long and complicated process. A few studies work on the entire imaging chain from X-ray exposure to image readout (Vedantham and Karellas, 2010). Most of the works focus on the X-ray dose response (Correa et al., 2009; Hashimoto et al., 2009; Li et al., 2007; Mathy et al., 2011; Sonoda et al., 1983; Souza et al., 2008; Tisseur et al., 2014) , while some other works dwell on the IP screen optics (Lubinsky et al., 1986; Fasbender et al., 2003; Thoms, 1996b). Accordingly, we also split the following discussion into X-ray or gamma-ray exposure, optical readout and complete CR chain simulation.

2.2.1 X- or γ-ray exposure

During the exposure, two processes happen successively: energy deposition and latent image formation. The latent image is in fact the spatial distribution of trapped electrons. The latent image formation refers to the electron trapping mechanism. A lot of simulation works focus on the energy deposition simulation; while for latent image there lacks a solid physical model, and it is commonly modeled as a gain factor.

2.2.1.1 Energy deposition

This step involves the radiation propagation within a system. There are two kinds of numerical techniques for solving the radiation transport problems: Monte Carlo techniques and deterministic techniques. Monte Carlo techniques, also known as statistical simulation techniques, follow all the random walk histories that a particle undergoes in a system; by launching a number of particles, one can approach the statistical behavior of the particle's transport in the system. In deterministic techniques, the system is treated discretely (Lewis and Miller, 1984). The system is divided into finite elements unlike Monte Carlo which treats the geometry continuously using quadric system (Gavaldà et al., 2009; Briesmeister, 2000). An overall transport solution is computed for each element. The most important advantage of deterministic method over Monte Carlo is its fast computational efficiency. While its weaknesses are that errors might be introduced due to the discretization, and it cannot provide particle transport details (e.g. local deposited energy).

2.2.1.1.1 Monte Carlo tools

In Monte Carlo methods, the radiation is considered as a number of independent particles. The Monte Carlo codes follow each independent particle's random walk from radiation source until it is completely absorbed in the system or escapes from the system, as illustrated in Figure 2.11. The MC code follows every movement of the primary particle and its descendants. The random distance to next interaction site and the interaction are generated with the help of a set of probability density functions (PDF) which describes different effects (e.g. photoelectric effect, Compton scattering).

There exist different Monte Carlo codes, such as PENELOPE, GEANT4 and MCNPX, for general purpose simulation. PENELOPE (PENetration and Energy Loss of Positrons and Electrons) is developed in FORTRAN (Gavaldà et al., 2009). The algorithm is based on the cross section models to simulate different interaction mechanisms. It can be applied to simulate arbitrary material systems and complex geometries. The particle energy ranges from a few hundred eV to 1 GeV. The PENGEOM package provides a powerful geometry operation such as anisotropic scaling, rotation and translation. Mixed simulation is adopted for hard and soft scattering of charged particle. Multiple-scattering approach is adopted for soft interaction in order to accelerate MC running.

GEANT4 (GEometry ANd Tracking) is developed by the European Organization for Nuclear Research (Agostinelli et al., 2003). This toolkit is written in C++ for particle physics application. It can simulate the transport of many particle types (e.g. neutrons, protons) with energy ranging from 250 eV up to TeV. Users can use the existing physical process model, and can also create new models.

MCNPX (Monte Carlo N-Particle eXtended) is developed by Los Alamos National Laboratory (Pelowitz, 2008). It is programmed in FORTRAN, which provides the capability of simulating almost all particles. A big difficulty of Monte Carlo methods is the geometry design. Recently, there are researches on the CAD based MCNPX to overcome this difficulty (Mengkuo, 2006; Tautges et al., 2009).

Besides the above general purpose codes, it is worth mentioning the dedicated code MANTIS. It regroups the codes PENELOPE (for X-ray and electron interaction) and DETECT-II (for visible photon transport) dedicated to radiography simulation (Badano and Kanicki, 2001; Badano, 2003; Badano and Sempau, 2006). This tool can successfully simulate the scintillator based radiography as well as the columnar phosphor based CR. However for the granular phosphor based CR, this tool is not suitable, as it does not take into account the laser scattering effect. There is also the dedicated Monte Carlo simulation software MODERATO developed by EDF (France) (Bonin et al., 1998; Bonin et al., 1999; Bonin et al., 2000). This software, which can handle the CAD description of objects, was developed for the simulation of γ-ray radiographic imaging in the EDF's context.

All the above codes allow the simulation of energy deposition in CR detector. Before launching the simulation, one needs to input the physical model of the system such as position, geometry and material of each element (source, object and detector). The IP is usually modeled as multiple-layered structure, which consist of a uniform top layer, a granular phosphor layer and a uniform support (Liaparinos et al., 2006; Mathy et al., 2011; Tisseur et al., 2014). For the phosphor layer, instead of modeling the phosphor grain, an effective layer density (product of phosphor density and grain packing factor) is used.

In the works of Souza et al. (Correa et al., 2010; Souza et al., 2008), the energy deposition was obtained through two steps: they first used MCNPX to obtain the trans-

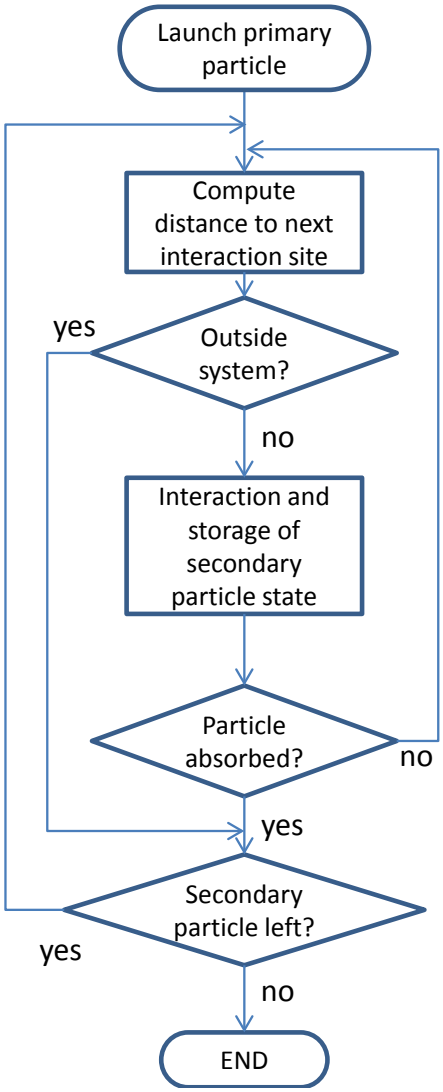

Figure 2.11: Simplified flow chart for general Monte Carlo modeling of a single particle transport in a system.

mitted X-ray image emerging from the object; then they applied the preliminary photon absorption rate of BaFBr to the X-ray image to produce the energy deposition image in IP, where the preliminary photon absorption rate was obtained with MC simulation. However, this model assumes that energy is deposited locally, and no fluorescence- or scattering-introduced blurring was taken into account.

2.2.1.1.2 Deterministic simulations

In deterministic simulations, the to-be-studied system is divided into finite elements. Deterministic codes provide the average particle behavior for each element by means of solving a transport equation. Figure 2.12 illustrates an example of ray tracking principle used in the deterministic code Virtual X-ray Imaging (VXI) (Duvauchelle et al., 2000). A 'pixelized' virtual detector is located after object for registering the transmitted image. The space is divided into elements corresponding to the pixel number. The average photon flux is calculated for each pixel element. For example, for the pixel 'K' in the image, a solid angle $\Delta\Omega$ corresponds to this pixel observed from source point S. Suppose that $N_0(E)$ photons with energy E are emitted by the source per solid angle, then the average photon received by pixel 'K' is given by the Beer Lambert attenuation law:

$$N(E) = N_0(E)\Delta\Omega \cdot \exp\left[\sum_i -\mu_i(E)x_i\right], \tag{2.2}$$

where $\mu_i(E)$ is the linear attenuation coefficient associated with the material i at the energy E, and x_i the total path length through the material i. Note that this solution does not account for the contribution of other effects (e.g. scattering and fluorescence effects). However, it provides very fast simulation (typically 0.1 s). Deterministic codes can be easily coupled with Computer-aided Design (CAD) tool making geometry designing easier and more robust. Appropriate pixel size should be defined in order to avoid missing the detailed variation of the object, but this induces an increase of the pixel number, and the simulation running takes more time.

Some principal deterministic codes are introduced in the following. VXI was developed at Laboratory of Nondestructive Testing using Ionizing Radiation (France) to simulate the radiographic, radioscopic and tomographic imaging. It is a complete deterministic simulation code. The latest version allows the simulation of first order scattering (Duvauchelle et al., 2000; Freud et al., 2004). SINDBAD was developed by CEA (France) and is dedicated to radiographic system simulation in both medical and NDT fields (Tabary et al., 2007). SINDBAD is a mixed simulation tool which combines analytical and Monte Carlo calculation, where MC method is applied for the scattering estimation. CIVA, also developed by CEA, can simulate multiple NDT methods such as ultrasonic testing, eddy current technique, as well as radiographic imaging (Calmon et al., 2006).[5]

To simulate the energy deposition in IP with deterministic codes, as such codes do not provide absorbed energy distribution function, two solutions can be used: 1) estimation with attenuation law (Fasbender et al., 2003; Thoms, 1996a) and coupling with preliminary experimental IP response (Tisseur et al., 2014).

[5]CIVA-RX is the result of the implementation of SINDBAD code into CIVA, with also MODERATO and VXI for the first-order scattering part.

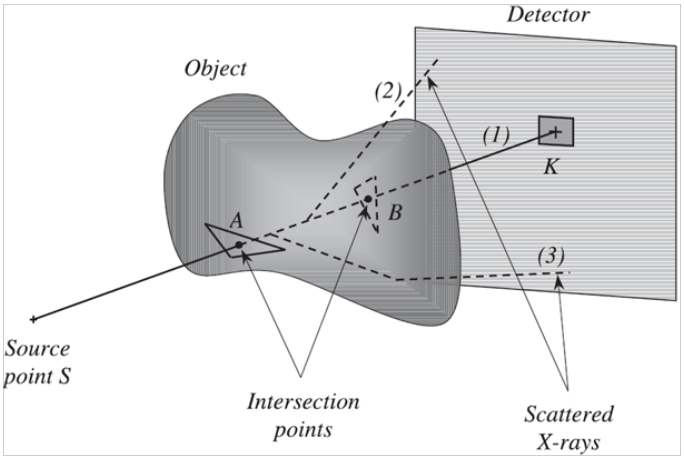

Figure 2.12: Illustration of deterministic simulation principle. The ray SK intersects two meshes at points A and B. Geometrical calculations enable the attenuation path length AB to be determined. Ray (1): transmitted photons. Rays (2) and (3): scattered photons. (source of figure: (Duvauchelle et al., 2000).

2.2.1.1.3 Discussion

The Monte Carlo and deterministic codes are the two main tools for radiographic imaging simulation. Both methods have their advantages and limitations. We summarize the main characteristics of each method below.

- Deterministic methods.
  - They are usually user-friendly, and can be coupled with CAD model; the user can design easily even complex geometries.
  - The first order scattering approximation can be applied for the estimation of the scattering effect.
  - The effect of electrons is not considered.
  - The simulation running is based on finite element theory. The running time depends on the number of elements (sampling).
- MC methods.
  - MC techniques are well accepted as the most accurate simulation methods.
  - MC codes can provide a good estimation of scattering events.
  - Due to the random nature, a MC simulation is often time-consuming.
  - Such methods are ususally not user-friendly. Geometry design is difficult and error-prone; though there exist CAD based models, it makes the running extremely slow.
  - The running time depends on the geometry, energy and material.
  - They have the potential of accounting for all particles (e.g. photon, electron, positron etc.) and all interaction types (e.g. photoelectric, scattering, pair production etc.).

The two methods can be iteratively employed for simulating a fast realistic imaging and still taking into account the detailed interaction effects in order to gain the accuracy.

2.2.1.2 Latent image generation

In most computational studies, the IP's X-ray image to latent image conversion rate is modeled as a gain factor, and sometimes is neglected (which is equivalent to assigning 1 to the gain factor) (Correa et al., 2009; Correa et al., 2010; Fasbender et al., 2003; Mathy et al., 2011; Souza et al., 2008; Thoms, 1996a; Vedantham and Karellas, 2010) .

The complete process is quite complicated and not yet clearly understood. It depends on impurity, oxygen, manufacturing conditions etc. In most of the works, an experimentally measured yielding rate is used to model the latent image formation.

Thoms et *al.* (Thoms et al., 1991) have reported that the F-center (correlated and uncorrelated) generation rate 7.98 per keV of absorbed X-ray energy; in the review work of Rowlands (Rowlands, 2002), it is reported that the absorbed x-ray energy to PSL generation rate is 2.8 ph/keV. These two values are not completely conflicting, as only a part of uncorrelated F-center contributes to the PSL emission. In the work of Vedantham et *al.* (Vedantham and Karellas, 2010), they have assigned the average of the two reported values to the gain factor.

There are also computational studies on the defect-related properties of the crystal lattice. Concerning phosphor crystal defects (e.g. F center, H center and V_k center), Baetzold et *al.* worked on the atomistic simulation of defects in phosphor crystals (Baetzold, 1987; Baetzold, 1989). They have studied parameters such as the lattice constant, the defect energy and the defect mobility. These parameters determine the photostimulation properties such as spectrum and generation rate of PSL. There exist toolkits like HADES III, CASCADE and PARADISE for the computational calculation (Catlow, 1986; Parker et al., 2004). As inputs one needs to provide lots of parameters such as host lattice structure model, interaction model between ions and interatomic potentials. The simulation of defect property is beyond the scope of this thesis. We present it here as an open option for further in depth study.

2.2.2 Optical readout

The optical readout involves a number of processes: laser light diffusion into PSP layer; interaction of laser photon with storage center; escape of PSL from the front surface of IP; detection of PSL; signal amplification and digitization. Each step refers to a number of modeling and simulation work. In CR simulation, the last three steps are often modeled as a gain factor. Thus, we pay more attention on the light transport in IP and the PSL emission.

2.2.2.1 Laser distribution

There are in general two kinds of laser propagation simulation in the imaging plate: analytic and Monte Carlo methods. The former often refers to solve the diffusion function; the latter follows the traveling history of each photon, and with a number of photon histories, one can approach a statistical result of light distribution.

2.2.2.1.1 Analytic methods

Analytic methods refer to solve the radiative equation or the diffusion equation. There are two kinds of approximations: isotropic and forward peaked scattering.

Model of Premoze. In the works of Premoze et *al.* (Premože et al., 2004; Ashikhmin et al., 2004), a practical formula is provided to estimate the multiple scattering. It is assumed that scattering paths comprising the beam have Gaussian distribution, and the beam width varying with travel distance S is given by the following formula:

$$l_{width}(S) = \frac{< \theta^2 > \mu_s S^3}{16(1 + S^2/12 l_{diff}^2)} \tag{2.3}$$

with $< \theta^2 >$ being the mean square scattering angle, μ_α the absorption coefficient, μ_s the scattering coefficient and l_{diff} a diffusive path length $l_{diff}^2 = 1/(\mu_\alpha \mu_s < \theta^2 >)$. The beam width depends on the absorption, beam penetrating distance and the optical property of the medium (i.e. absorption and scattering coefficients, mean scattering angle).

In Figure 2.13, they compare their theory with Monte Carlo simulation. It turns out that the spatial spread width predictions from the model agrees well with the Monte Carlo result, whereas the prediction on the beam attenuation works badly. A better expression for attenuation is needed.

This model, an analytic formula, is simple to use, time-saving and easy to incorporate for a quick estimation of laser spreading. Their beam width spread function includes the optical properties of the medium such as absorption, scattering and anisotropic effect, and it works well in the examples demonstrated. However the study on obtaining better beam attenuation needs to be followed up since the Beer-Lambert law is not a good optical attenuation description in this case. Moreover, they have adopted two assumptions: 1) absorption is much smaller than scattering coefficient; and 2) photons are scattered forwardly by scattering particles.

Model of Thoms. In the work (Thoms, 1996a), Thoms has studied the storage films' property by solving the diffusion equation:

$$\frac{\partial n(\overrightarrow{r}, t)}{\partial t} = S(\overrightarrow{r}, t) + D\left[\Delta n(\overrightarrow{r}, t)\right] - \mu_\alpha c \cdot n(\overrightarrow{r}, t), \tag{2.4}$$

Where $n(\overrightarrow{r}, t)$ is the photon density, $D = l_s c(1 - \mu_\alpha l)/6$ is the diffusion constant, l_s is scattering length (inverse of scattering coefficient μ_s), c is light velocity and μ_α is absorption coefficient for the material and energy considered. The change rate is considered quasi-static then:

$$S(\overrightarrow{r}, t) + D\left[\Delta n(\overrightarrow{r}, t)\right] - \mu_\alpha c \cdot n(\overrightarrow{r}, t) = 0. \tag{2.5}$$

This equation has been solved numerically by iterative calculation. The solution is based on the assumption of isotropic scattering. In order to obtain a relatively accurate solution, a small iteration step size is needed, which will lead a great number of iterations and thus a long computational time.

2.2.2.1.2 Monte Carlo simulation of laser transport in imaging plate

As the IP's effective layer is granular, it can be viewed as turbid medium. There are works dedicated to modeling light transport in turbid media (or tissues) (Wang et al., 1995; Zhu

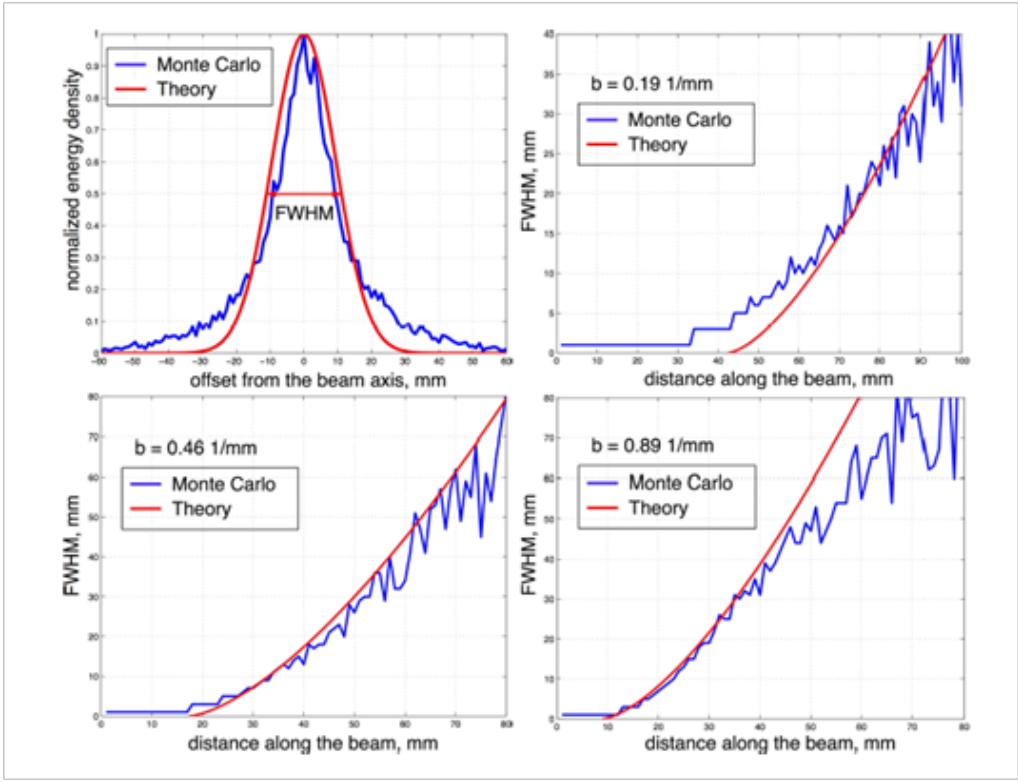

Figure 2.13: Analytic Monte Carlo comparison on spatial spread width: top left plot show the normalized intensity profile compared to a Gaussian with corresponding theoretical width; other plots show spatial spread widths for different scattering coefficients b as a function of distance along the beam z; the scattering medium was simulated using the following parameters: anisotropy factor G=0.9, $< \theta^2 >$=0.24, absorption coefficient $\mu_\alpha = 0.0003$ mm^{-1}.

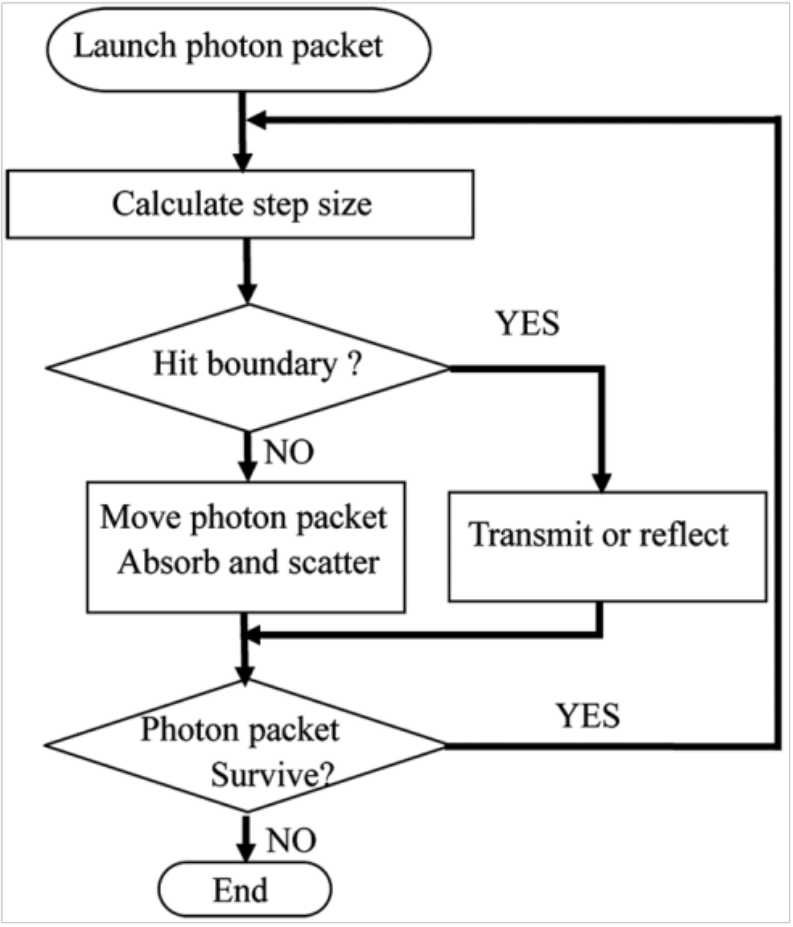

Figure 2.14: Flowchart for Monte Carlo modeling of the propagation of a single optical photon, in which no wavelength change is involved (Zhu and Liu, 2013).

and Liu, 2013; Prahl et al., 1989; Patwardhan et al., 2005; Smithies and Butler, 1995; Maarek et al., 1984; Flock et al., 1989; Margallo-Balbás and French, 2007). Concerning MC modeling of imaging plate, Fasbender (Fasbender et al., 2003) has reported a MC model for laser transport in IP. MC modeling tools commonly follow the flowchart illustrated in Figure 2.14. Similar to the MC modeling of X-ray transport, the optical MC codes also sample the random events with PDFs. The physical model of photon/medium interaction is described via absorption, scattering and anisotropic factors. A more detailed discussion on the optical MC modeling will be presented in Chapter 5.

MCML (Monte Carlo modeling of light transport in Multi-Layered tissues) (Wang et al., 1995) is the most used MC simulation tool for light transport in tissue; there is also a tool developed by Fasbender for investigating the IP readout. The former is an open source programmed in C, which is available for public use since 1992. The latter code is dedicated for light transport simulation in imaging plate; however, it is not available for public use.

In the above codes, the medium is modeled by its absorption coefficient, scattering coefficient and anisotropy factor. Whereas, in the granular plate model of P. L. Liapari-

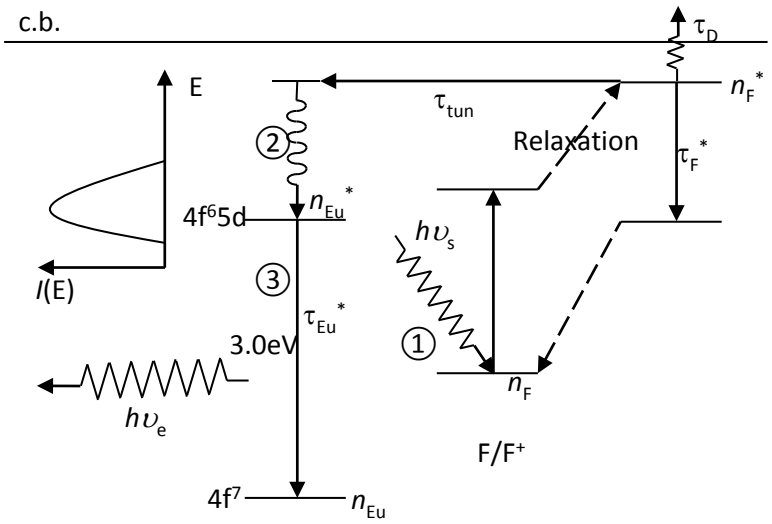

Figure 2.15: Physical model of photostimulated luminescence proposed by Seggern (Seggern et al., 1988)

nos (Liaparinos et al., 2007; Liaparinos et al., 2006; Liaparinos and Kandarakis, 2009), the intrinsic parameters of the material (volume density of phosphor screen, grain size, and the complex refractive index of grain and binder) are used to describe the medium. These parameters can be obtained using Mie theory. Some details on the Mie theory calculation are presented in Appendix A.1.

2.2.2.2 PSL generation model

We introduce three models for PSL generation, the model of Seggern et *al.*, the model of Salis and the practical model of Thoms. The first two models deal in detail with the tunneling and decay effects taking place during photostimulation. The third model gives a practical formula which yields an overall PSL generation rate.

2.2.2.2.1 Model of von Seggern et *al.*

Seggern and co-workers have proposed a physical model of photo-stimulated luminescence (Figure 2.15) in 1988 (Seggern et al., 1988). They assumed that the doped Eu^{2+} was the hole trap center of the phosphor, and lattice virgin Br vacancy was electron trap center (F-center). A trapped electron could be stimulated into its excited energy level using laser, then it relaxes into an energy state near conduction band, then by tunneling, it can recombine with trapped hole resulting in luminescence.

According to their model:

(1) At F-center site, the changing rate of the number of electrons in the excited state

is expressed as:

$$\begin{aligned} \frac{dn_F^*}{dt} &= \sigma \cdot I \cdot n_F - \left(\frac{1}{\tau_F^*} + \frac{1}{\tau_{tun}}\right) n_F^*, \\ and\ \frac{dn_F}{dt} &= -\sigma \cdot I \cdot n_F + \frac{n_F^*}{\tau_F^*}, \end{aligned} \tag{2.6}$$

where n_F^* and n_F are the number of electrons in the F center's excited and ground state, σ is optical cross section of laser photostimulation, I is the laser intensity,τ_F^* is the lifetime of the F center's excited state and τ_{tun} is the tunneling time. The term $\sigma \cdot I \cdot n_F$ represents the optical detrapping rate.

(2) The equation for the changing rate of the number of Eu electrons in the excited state is:

$$\frac{dn_{Eu}^*}{dt} = \frac{n_F^*}{\tau_{tun}} - \frac{n_{Eu}^*}{\tau_{Eu}^*} \tag{2.7}$$

where n_{Eu}^* is the number of electrons in the Eu center excited state and τ_{Eu}^* is the lifetime of the Eu center's excited state.

The initial conditions at the beginning of the optical stimulation after the end of X-ray irradiation are:

$$n_F = n_F^0 = g_{sc} \cdot Dose,\ n_F^* = 0,\ n_{Eu}^0 = 0, \tag{2.8}$$

where n_F^0 is the initial ground state electron number of F center, *Dose* is the X-ray dose, g_{sc} is the dose to F center conversion gain factor.

The stimulating light intensity is given by:

$$I(t) = \begin{cases} 0, & t < 0; \\ I_p, & 0 \le t \le t_p; \\ 0, & t > t_p. \end{cases} \tag{2.9}$$

(3) The recombination (or PSL generation) rate $r = \frac{n_{Eu}^*}{\tau_{Eu}^*}$ is calculated by:

$$r(t) = \begin{cases} 0, & t < 0, \\ \frac{\tau_F^*(s_1+\sigma I_p)(s_2+\sigma I_p)n_F^0}{\tau_{tun}(s_1-s_2)} \left(\frac{exp(s_2 t)-exp(-t/\tau_{Eu}^*)}{1+s_2\tau_{Eu}^*} - \frac{exp(s_1 t)-exp(-t/\tau_{Eu}^*)}{1+s_1\tau_{Eu}^*}\right), & 0 \le t \le t_p, \\ \frac{n_{Eu}^*(t_p)}{\tau_{Eu}^*} exp[-(t-t_p)/\tau_{Eu}^*] - \frac{n_F^*(t_p)}{\tau_{tun}} \frac{exp[-(t-t_p)/\tau_{Eu}^*]-exp[\tilde{\alpha}(t-t_p)]}{1-\tilde{\alpha}\tau_{Eu}^*}, & t > t_p, \end{cases} \tag{2.10}$$

with $s_{1,2} = \left(-\tilde{\alpha} \pm \sqrt{\tilde{\alpha}^2 - 4\beta}\right)/2$, $\tilde{\alpha} = 1/\tau_{tum} + 1/\tau_F^* + \sigma I_p$ and $\beta = \sigma I_p/\tau_{tun}$. Equation 2.10 gives us the PSL generation rate. The advantage of this model is that it accounts for the afterglow effect (the third term in the equation where $t > t_p$) via the excited activator decay time τ_{Eu}^*, the electron tunneling time τ_{tum}, and the excited F center life time τ_F^*. However, the information is missing on the tunneling and excited F center life time, which makes this model not accessible in practice.

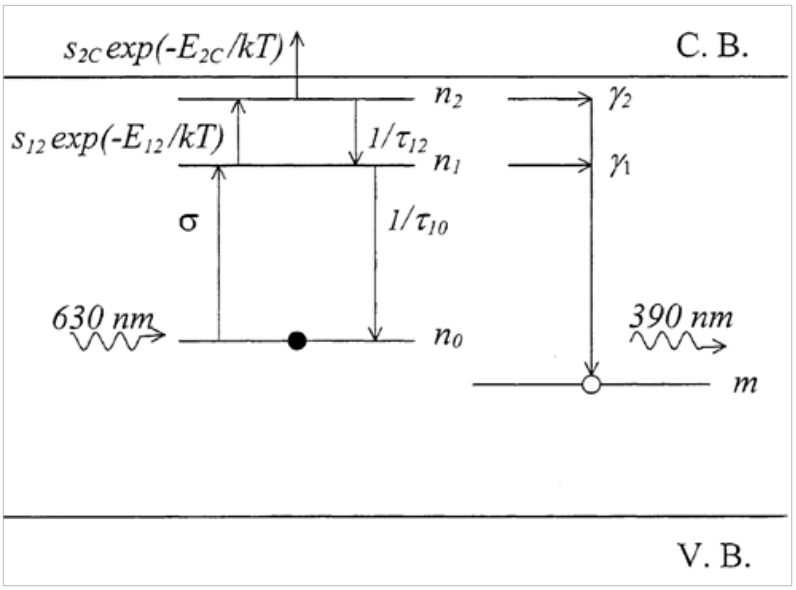

Figure 2.16: Physical model of PSP generation proposed by Salis (Salis, 2003). The F center (left) is assumed to have three energy levels. With laser photons, F center electrons are excited from their ground state into their first excited level (n1); via thermal excitation, electrons can enter into their second excited level or conduction band. The electrons in the first and second excited levels can tunnel to the hole center sites and recombine with them resulting in luminescence.

In addition, experimental studies show that in BaFBr : Eu^{2+}, the dopant Eu^{2+} is not the hole trap, during X-ray irradiation. Therefore Equation 2.7 should be modified in order to accounting for the energy transfer rate from electron/hole recombination site to activator site.

2.2.2.2.2 Model of Salis

In the model of Salis, the F center is assumed to have three energy levels (see the left part in Figure 2.16) (Salis, 2003). With laser photons, F center electrons are excited from their ground state into their first excited level (n_1); via thermal excitation, electrons can enter into their second excited level or conduction band. The electrons in the first and second excited levels can tunnel to the hole center sites and recombine with them resulting in luminescence. The terms γ_1 and γ_2 represent the tunneling rate which corresponds to the inverse of the previous tunneling time τ_{tun}.

Readers are referred to (Salis, 2003) for detailed calculation. We only summarize the advantages and the drawbacks of this model. This model shares the advantages of the previous model, plus its consideration of the thermal excitation. The drawback of this model is also caused by the lack of information on the tunneling rates. Both models are hard to verify experimentally.

2.2.2.2.3 Model of Thoms

In the modeling work of Thoms, a practical PSL generation model is adopted (Thoms,

1996), which is also adopted in a later work (Fasbender et al., 2003). Generally the rate of emitted photons in the plate volume depends on the exciting-photon density in the plate, as given by(Thoms, 1996):

$$\frac{dn_{emission}(\overrightarrow{r})}{dt} = n_{sc}(\overrightarrow{r})\sigma I_{exc}(\overrightarrow{r}) = n_{sc}(\overrightarrow{r})\sigma c\frac{n_{exc}(\overrightarrow{r})}{t_{scan}}, \tag{2.11}$$

where $n_{emission}(\overrightarrow{r})$ is the emitted-photon density, $n_{sc}(\overrightarrow{r})$ is the density of photostimulable storage centers, σ is the optical cross section for photo-stimulation, $I_{exc}(\overrightarrow{r})$ is the intensity of the excitation photons, c is the light velocity, $n_{exc}(\overrightarrow{r})$ is the density of the exciting photons and t_{scan} is laser beam dwelling time.

This model neglects the details on the electron tunneling effect, thermal excitation etc. We can experimentally measure the global optical cross section σ which is a global result of all effects. However, the afterglow is also neglected.

2.2.2.3 Modeling the raster scanning effect

There are few studies on the laser raster scanning effect of CR readout system. In the work of Vedanthan et *al.* (Vedantham and Karellas, 2010), the scanning effect is modeled as a modulation transfer function (MTF) which takes into account the influence of the isotropic scanning speed in the scan and sub-scan directions:

$$MTF(u,\nu) = MTF_{laser}(u,\nu)|\mathrm{sinc}(\pi v_{scan}t_{scan}u)\mathrm{sinc}(\pi v_{sub-scan}t_{scan}\nu)|, \tag{2.12}$$

where u and ν are the spatial frequency in scan and sub-scan directions, $MTF_{laser}(u,\nu)$ accounts for the blurring introduced by Gaussian intensity profile laser, v_{scan} and $v_{sub-scan}$ are the scan and sub-scan velocities, t_{scan} is the dwell time of laser spot at one point, and the term $|\mathrm{sinc}(\pi v_{scan}t_{scan}u)\mathrm{sinc}(\pi v_{sub-scan}t_{scan}\nu)|$ represents the scanning effect in the two directions.

2.2.3 Complete CR system simulation

Cunningham et al. have proposed cascaded models for computing the system performance metrics (e.g. detective quantum efficiency and noise etc) propagation in a linear system (Cunningham et al., 1994; Cunningham et al., 2002; Sattarivand and Cunningham, 2005). Cascaded models are based on linear system theory; the system is split into finite successive elementary processes. The input of the current process is the output of the previous one (Figure 2.17). A simple example on the signal and noise propagation can be given by (Cunningham et al., 1994):

$$\begin{aligned} S_i &= S_{i-1}g_i, \\ \sigma_i^2 &= g_i^2\sigma_{i-1}^2 + \sigma_{gi}^2 S_{i-1}, \end{aligned} \tag{2.13}$$

where S_{i-1} and S_i are input and output signals of process i, σ_{i-1} and σ_i are the input and output noises, g_i and σ_{gi} are respectively the gain and noise introduced by process i.

Based on this theory, Vedantham et al. have developed a complete model dedicated to medical CR imaging system (Vedantham and Karellas, 2010). With their model, metrics such as modulation transfer function (MTF), detective quantum efficiency (DQE) and

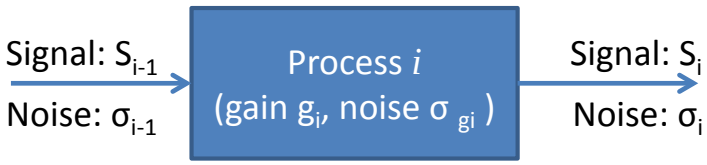

Figure 2.17: Illustration of basic principle of cascaded model.

noise power spectrum (NPS) can be obtained. In this model, several elementary processes such as X-ray fluorescence and optical photon diffusion were coupled with MC simulation. However, this model becomes less accurate when high energy radiation source is involved i.e. where scattering effects are very pronounced, because the scattering effect is not taken into account.

2.2.4 Discussion

In this part, we have discussed the main modeling and simulation techniques concerning different processes in CR imaging. For the energy deposition process, there exist a number of simulation codes employing MC or deterministic techniques, or mixing of the two. The biggest advantage of MC methods is their detailed and accurate solution, which however is time-consuming. On the contrary, deterministic methods can provide realistic simulation image in a short time, but the scattering estimation is difficult. To overcome this issue, first-order scattering theory is proposed to solve the scattering involved problem; there also exist deterministic/MC coupled codes. A mixed use of both methods can be a good solution to obtain fast simulation and still maintain a good accuracy.

It is difficult to simulate detailed processes concerning defects generation and stimulation. Though some detailed models have been proposed (PSL generation), due to the lack of data, it is difficult to simulate such processes in detail. Global factors are used instead to model these processes (i.e. latent image formation and global optical cross section for photostimulation).

Viewing the simulation of optical photon transport within IP, the granular phosphor layer can be treated as a turbid medium where multiple scattering is produced. Here also, two kinds of methods can approach the solution of the multiple-scattering problem: analytic and MC methods. The analytic methods are limited to the situation where absorption is much smaller than scattering, and the scattering is either isotropic or forward-like. While with MC methods, there are no such limits.

2.3 Conclusion

Computed radiography is one of the two main digital radiographic imaging techniques (the other is digital radiography). The image carrying medium (imaging plate) used in CR can be handled with a light-tight cassette, which is very similar to film radiography. Users do not need to modify their existing exposure routine to replace a film-based system by a system. Hence, it is a very attractive alternative digital technique.

The CR imaging is a long and complicated process. It involves an exposure routine and an optical readout system. The digital image formation is summarized below.

1. X-ray exposure
   (a) X-ray/object interaction results in a transmitted X-ray image which carries the object pattern.
   (b) The interaction of this transmitted X-ray image with CR detector (IP alone or with metallic screens) leads to energy deposition within the sensitive layer (PSP layer) of IP. The energy deposition is a result from multiple effects such as photoelectric, Compton scattering, X-ray fluorescence reabsorption and electron etc.
   (c) Owing to the latent image formation mechanism, a portion of the deposited energy is converted into storage centers forming latent image. For different PSP materials, their latent image formation mechanisms are different. In a $BaFBr : Eu^{2+}$ based imaging plate, the storage center (trapped electron site) is experimentally identified to be the $F(Br^{-})$ center. However, the hole trap is not clearly understood.
2. Optical readout
   (a) A laser beam diffuses into the imaging plate. The diffusion region depends on the IP's optical property.
   (b) The laser photons interact with storage centers (latent image) within PSP layer. Here the photostimulation mechanism requires the spatial correlation of the trapped electron, trapped hole and the activator.
   (c) The emitted PSL signal is collected by an optical fiber, and then amplified and digitized resulting in a digital image.

The detected X-ray image is stored in the form of a latent image, which is later read by an optical scanner. The latent image generation rate and image readout rate decrease the efficiency, comparing with scintillator based system. Due to the optical readout, the image sharpness is further degraded. The image sharpness is limited by a number of factors, e.g. the laser spot size, the light diffusion, scanning laser power etc.

On the modeling and simulation works, we have organized our discussion according to the above digital image formation process. There exist a number of models for each step in the X-ray exposure and optical readout. We achieve the following conclusions.

1. X-ray exposure
   (a) There exist a number of Monte Carlo or deterministic tools. Considering the simulation of a radiographic imaging, which involves objects of complex shapes, it is almost impossible with a Monte Carlo code; a single MC running can take months based on our experience. In this case, a deterministic tool is of great interest for obtaining a realistic image in a short time (typically order of second). The scattering estimation is a problem for deterministic simulation. To overcome this problem, some codes adopt the first order scattering approach, and some other codes are coupled with Monte Carlo program for the scattering effect computation.

(b) With a full Monte Carlo code, one can directly compute the energy deposition in an imaging plate. However with a deterministic code, the energy deposition is generally computed with exponential attenuation law or with a preliminary experimental IP response.

(c) The latent image formation is commonly modeled as deposited energy to storage center conversion ratio.

2. Optical readout

(a) There are few works dedicated to the IP optics. The IP can be treated as a turbid medium, and there are modeling works on the light diffusion in tissue (medical image) or in clouds (satellite image), which are applicable in our case. Monte Carlo methods turn to be much more reliable than analytic ones. An optical MC running takes about 1 day on a single processor (from our experience); one does not need to rerun the MC code for the same IP configuration.

(b) There are physical models for photostimulation which take into account the effects such as electron tunneling and activator decay. As there lacks experimental data such as the tunneling efficiency, the incorporation of these models is unfeasible. In the work of Thoms, the photostimulation is modeled by the optical cross section, which is accessible for the PSL emission simulation.

(c) We have not found specific models for PSL collection, amplification and digitization process. It can be treated as a gain factor.

According to the above analysis on the feasibility of the modeling works concerning each CR imaging step, we propose an approach for the CR imaging chain simulation (as presented in the General Introduction).

The next chapter concerns the first aspect of the thesis' objective, physical phenomena investigation. We simulate, with a Monte Carlo code, the CR detector's impulse response in a system which involves a radiation source and a simple shape object. However this kind of code cannot be applied to simulate the image of complex shape object, because it is highly computationally expensive. For this reason, we propose the simulation approach developed in chapter 4. Moreover, for a comprehensive study of a CR system, the optical readout effect should also be considered, and thus we need a complete model for the CR simulation. Chapter 5 extends the simulation to the optical readout process.

Chapter 3

Simulation, method and physical phenomena comprehension

"Curiouser and curiouser..."

Alice in wonderland

Contents

3.1 Introduction of the chapter

The objective of this chapter is to understand the physical phenomena taking place during the CR exposure, e.g. the behavior of electrons, scattered radiation and X-ray fluorescence etc. With this in mind, we have developed a Monte Carlo simulation tool, based on PENELOPE for such investigations. This tool tracks separately direct and secondary radiations, and monitors the behavior of different particles. The simulation output provides 3D distribution of deposited energy in IP and evaluation of radiation spectrum propagation allowing us to visualize the behavior of different particles and the influence of different elements (e.g. object, metallic screens and protective layer of IP etc.). Section 3.2 through 3.8 correspond to our submitted article to the journal 'Spectrochimica Acta, Part B'.[1] In these sections, we present the simulation method, and an image quality optimization case, to achieve which a detailed analysis, on the spectral and spatial response of three detector configurations at different energies has been performed. We have also characterized experimentally several IP/screens combinations responses with a synchrotron source. The experiment is presented at the end of this chapter. Several results are compared with the simulation results.

3.2 Introduction

Computed radiography (CR) system, based on the use of an imaging plate (IP) composed of photostimulable phosphor (PSP) powder embedded in organic binder, is one of the efficient digital replacement techniques of the traditional conventional film radiography (Rowlands, 2002; Sonoda et al., 1983). Aside from keeping the advantage of the traditional radiography such as flexibility of the detector, CR brings other advantages, which are direct digital readout image, reusability of the detector, elimination of the developing process with chemical product, reduction in exposure (through great sensitivity of IP) and dynamic range larger than 5 orders of magnitude in X-ray dose (Seggern, 1999; Miyahara et al., 1986; Thoms, 1996b; Thoms, 1997).
CR proves good performance within low energy range, but regarding the high energy range (up to MeV), which is also normal working energy range for industrial inspection of high attenuation objects, CR image quality is poor. The reason is that IP response is poor to the direct beam which carries the sharp geometry information of the object, but sensitive to secondary beam emerging from the object which is responsible for blurring. This issue has already been addressed for film radiography by the use of metallic screens which increase the dose received in the film thanks to secondary radiations occurring in the screen. Metallic screens should be placed in contact with the film so that emitted electrons can reach the argentic emulsion of the film. As far as IP is concerned, the use of metallic screens is also requested at high energies by current standards, so that the high energy photon beam could be rendered into electrons and lower energy photons, to which IP is more sensitive (EN14784-2, 2005; ISO17636-2, 2013). However, the commercial IPs are usually comprised of a protective layer coated on phosphor layer to provide protection

[1] The text was selected following our presentation at the workshop 'Monte Carlo simulation tools for X-ray imaging and fluorescence'. The authors of the article are Min YAO (INSA de Lyon), Philippe DUVAUCHELLE (INSA de Lyon), Valérie KAFTANDJIAN (INSA de Lyon), Angela PETERZOL-PARMENTIER (AREVA) and Andreas SCHUMM (EDF). DOI:10.1016/j.sab.2014.12.001

against normal handling, and this layer might prevent the rendered photon or electron from entering the phosphor layer.
As regards the spatial resolution, the metallic screens also further spread the incident beam, which means that a compromise should be found between intensifying the signal (by increasing the screen thickness) and improving spatial resolution. Moreover, when compared with film radiography, the spatial resolution is further degraded due to the light scattering at the phosphor grains during readout process (Rowlands, 2002; Seggern, 1999).
In order to follow the interactions involved in the metallic screen and IP detector system, a Monte Carlo simulation is of particular interest. It can give insight on physical phenomena which is difficult or impossible to observe experimentally, such as scattering effect, spatial distribution of deposited energy, K absorption and K fluorescence reabsorption.
Monte Carlo simulation has already been applied for system performance study and optimization as well as experimental result prediction in a number of studies (Rogers, 2006; Boone et al., 1999; Correa et al., 2010; Liaparinos et al., 2007; Kausch et al., 1999; Jaffray et al., 1995; Liaparinos et al., 2006; Liaparinos and Kandarakis, 2009; Souza et al., 2008; Li et al., 2007; Cho et al., 2000; Wu et al., 2005), but lots of these works were conducted for medical application. Though in some works (Souza et al., 2008), (Li et al., 2007) and (Wu et al., 2005), the spectral response of IP material and the spatial response to certain irradiation sources have been reported, there is still a lack of the detailed spatial response characterization up to high energies (MeV). Moreover, in all previous studies, the IP system is studied alone, without taking into account the object under test. At high energies, the object is responsible for a huge amount of secondary radiation, which is not a useful part of signal as regards defect detection, and thus, image quality optimization consists in not only increasing the amount of deposited energy due to the direct beam ($useful\ signal$), but also decreasing the deposited energy due to the secondary beam. Direct and secondary beams must here be understood at the object level.
For the purpose of understanding how the relevant operating parameters affect the X-ray image and optimizing the image quality supplied by CR system, we have developed a Monte Carlo simulation tool based on PENELOPE (Gavaldà et al., 2009). This tool tracks separately the direct and secondary as well as photon and electron radiations. The present paper will show the use of this tool through an optimization study of a realistic inspection case. The optimization was carried out by first characterizing the response of different combinations of IP and screens. The detector response has been analyzed in terms of performance metrics such as Energy Absorption Efficiency (EAE) and MTF for various incident energies up to 1.3 MeV.
The paper is structured as follows: in the next section, we describe our tool, emphasizing on its particularities. In section 3.4 we introduce the context of our study by showing a realistic inspection case where the image quality obtained with $IP\,alone$ is clearly not sufficient. Then, section 3.5 details an extensive investigation of various IP/screen combinations in terms of performance metrics such as deposited energy and spatial resolution. Finally section 3.6 shows the results obtained on the typical inspection case considered, where different IP/screen combinations allow us to improve image quality. The compromise between signal intensification and spatial resolution is discussed, before concluding the paper.

3.3 Simulation tool and performance metrics

3.3.1 Simulation method

Our simulation tool is based on the PENELOPE subroutine package, and involves a classical situation of radiography with a radiation source, an object and a detector. Here, by detector we mean the combination of IP and metallic screens since the purpose of these screens is to optimize the IP response. Figure 3.1(a) shows the geometry adopted, and the terms employed for the different beams issued from the object under test. After the object, the red solid arrow represents the direct radiation, i.e., the part of photons which did not undergo any interaction, and all radiation produced from this beam in the following is called the $useful$ beam. On the contrary, the green dashed arrow represents the secondary radiation issued through the object, and all further radiations produced are denoted as $not\,useful$. The information is subdivided into the signals due to the photons in the $useful$ beam or $not\,useful$ beam (denoted as UPS and NUPS), the electrons in the $useful$ beam or $not\,useful$ beam (denoted as UES and NUES), and, if any, the positrons in the $useful$ beam or $not\,useful$ beam (denoted as UPoS and NUPoS).

The simulation monitors two kinds of signals: the deposited energy distribution inside the IP and the step-by-step transmitted spectra after each element between source and IP (Figure 3.1(b)). A uniform three-dimensional orthogonal grid is used to sample the IP in such a way that the energy deposition distribution is recorded in 3D. For this reason, the IP geometry should be cuboid.

The incident beam could be either diverging or not, emitted from a point or an extended source, and its spectrum can be specified (such as that emitted from a cobalt or iridium source) or be a fixed energy varying within a specified range $\{E_{min}\ ;E_{max}\ \}$ with an increment of E_{incmt}. The object and metallic screens could be of arbitrary material and geometry.

In all the following, the IP was modeled as a multi-layered structure which is comprised of, in sequence, a 6 μm protective layer, a 150 μm phosphor layer, a 254 μm support layer and a 25.4 μm backing layer. The materials of these four layers are respectively Mylar for the protective and support layers, $BaFBr : Eu^{2+}$ with a packing factor of 60% for the phosphor layer, and polycarbonate for the backing layer. As the phosphor layer is the actual effective layer for information storing, the orthogonal grid was applied to the phosphor layer for energy deposition distribution recording.

3.3.2 Performance metrics

The following outputs are available from our simulation tool:

- 3D deposited energy due to each kind of beam and each kind of particle:
  - Useful photon signal $DEP_{UPS}(x, y, z)$;
  - Not useful photon signal $DEP_{NUPS}(x, y, z)$;
  - Useful electron signal $DEP_{UES}(x, y, z)$;
  - Not useful electron signal $DEP_{NUES}(x, y, z)$;
- Transmitted photon spectra after different elements (i.e. object, metallic screens and IP protective layer);

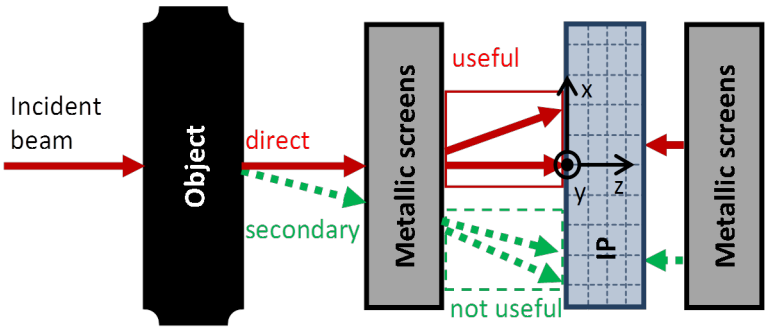

(a)

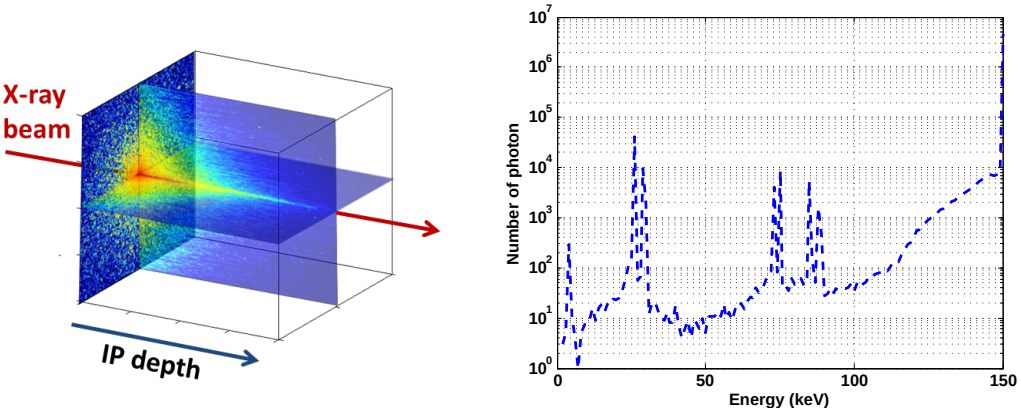

(b)

Figure 3.1: (a) The geometry adopted for our simulation is a classical radiography chain (not drawn to scale). A Cartesian coordinate system is used to track the particle transport. The y-axis points outward. A uniform three-dimensional orthogonal grid is applied to IP to record the deposited energy distribution. (b) Simulation outputs: 3D map of deposited energy in IP $DEP(x, y, z)$ and an example of spectrum after one of the elements between source and IP.

- Transmitted electron spectra after different elements.

From these outputs, the following metrics are used to investigate the IP response under different simulation configurations:

- Energy absorption efficiency (EAE). It is the fraction of X-ray energy absorbed in IP, and is calculated as the total energy deposited in IP divided by the incident beam energy. Here, the total energy is considered, i.e. the sum of all signals due to all particles. If needed, $useful$ versus $not\,useful$ energy can be separated (see the results section).

- Fraction of deposited energy due to electron beam (f_{ElDep}). The f_{ElDep} is calculated as the ratio of the deposited energy due to electrons into IP over the total deposited energy in IP. Note that the electron beam is produced by the metallic screens.

- Modulation Transfer Function (MTF) and spatial frequency at 20% MTF (f_{MTF20}). The MTF is a basic metric to express the system spatial resolution. It is calculated as the modulus of the Fourier transform of the Point Spread Function (PSF) normalized to unity at zero spatial frequency. In practice, the Line Spread Function, describing the system response to a line, is usually measured, and then the corresponding one-dimensional MTF is (Liaparinos et al., 2007):

$$\begin{aligned} MTF(f) &= \mathscr{F}\left(LSF(x)\right) \\ &= \mathscr{F}\left(\sum_{y} PSF(x,y)\right) \\ &= \mathscr{F}\left(\sum_{z,y} DEP(x,y,z)\right) \end{aligned} \tag{3.1}$$

  where f is the spatial frequency, and $\mathscr{F}$ denotes Fourier transform, and $DEP(x,y,z)$ here is obtained with a point non-diverging source (pencil beam). The f_{MTF20} is the spatial frequency at which the MTF equals 20%. Depending on the investigation required, it is possible to consider the energy due to the different combinations of $useful/not\,useful$ and $photon/electron$.

- Energy absorption distribution along IP depth (EAD_z) and its centroid ($EADC$). An originality of our tool is to consider the distribution of deposited energy along the depth of IP (z direction). This is not common in other tools. Our idea is following: the latent image stored in IP (i.e. the deposited energy) is read by a laser light, and while the laser light enters IP, it diffuses along its traveling path due to the absorption, reflection and scattering effects, which contributes to image blurring. The laser power used during readout modifies the penetration of laser light, and thus, has an influence on final spatial resolution. Depending on the deposited energy profile along IP depth, an optimal laser power could be determined. For this reason, we would like to study the energy deposition distribution along the IP depth. The EAD_z is a function of z and is computed as the sum of $DEP(x,y,z)$ over x and y axes normalized by the incident beam energy.

The centroid of EAD_z could be understood as the average position of the deposited energy, which is calculated using the following formula:

$$EADC = \frac{\sum_z z \cdot EAD_z(z)}{\sum_z EAD_z(z)} \tag{3.2}$$

3.4 Context of our study: typical inspection case

Our typical industrial inspection case consists of irradiating a thick object (70 mm steel plate) with a high energy γ source (Cobalt). In order to explain the image quality issue, we show the result obtained when IP is used alone as a detector, without any metallic screen to intensify the signal. A pencil beam is used to irradiate the object, in order to show the spread out responsible for spatial resolution degradation. IP is placed directly behind the object, as in the industrial case.
Figure 3.2 illustrates the deposited energy images in XZ plane due to respectively the $useful$ photon signal (UPS), $useful$ electron signal (UES), $not\,useful$ photon signal (NUPS) and $not\,useful$ electron signal (NUES). Remember that z direction is the incident beam direction, and is limited to 150 μm, which is the thickness of the phosphor layer. As can be seen, the $useful$ signal images from photons and electrons are quite sharp and clear, while the $not\,useful$ signal images are blurry. In order to compare the amount of energy, in Figure 3.3, we plot the deposited energy along z direction for the respective signals. It is worth noting that the $not\,useful$ signals are dominant, as only about 15.7% of deposited energy is due to $useful$ signals. When looking at the depth penetration, we see that the electrons deposit their energy preferably towards the front side of IP ($z = 0$), while the photons near the rear side (z=150 μm).
In Figure 3.4, we investigate the contribution of the different signals to the overall MTF curve (black). Although the $useful$ signals UPS and UES have good MTFs (red curves), the overall MTF is predominantly influenced by the $not\,useful$ signals (NUPS, NUES). This is the quantitative aspect of the visual spread out already shown in Figure 3.2. It must be noted here that in real life, electrons might not have as much influence as what is shown here, because air was not considered in the simulation. However, this does not change the conclusion that $not\,useful$ photons degrade a lot spatial resolution.
Thus, to conclude on our industrial context, we need a detector which should be efficient to the high energy $useful$ signal, but insensitive to the lower energy $not\,useful$ signal. The exact role of electrons must be very carefully tracked, as they might carry quite a lot of energy, but could be absorbed in the protective layer of IP itself. Thus, we see that a fine detector response characterization must be performed. A detailed analysis on the spectral and spatial response will be presented in the next section for physical phenomena comprehension and determination of optimal detector configuration.

3.5 Detector response characterization

We now investigate the impulse response of the system, which means the response to a pencil beam. All the elements (metallic screens and IP) were set cuboid, and no object is included in order to characterize only the detector system. The setting of all parameters is listed in Table 3.1. Two combinations of screens were compared with $IP\,alone$. The

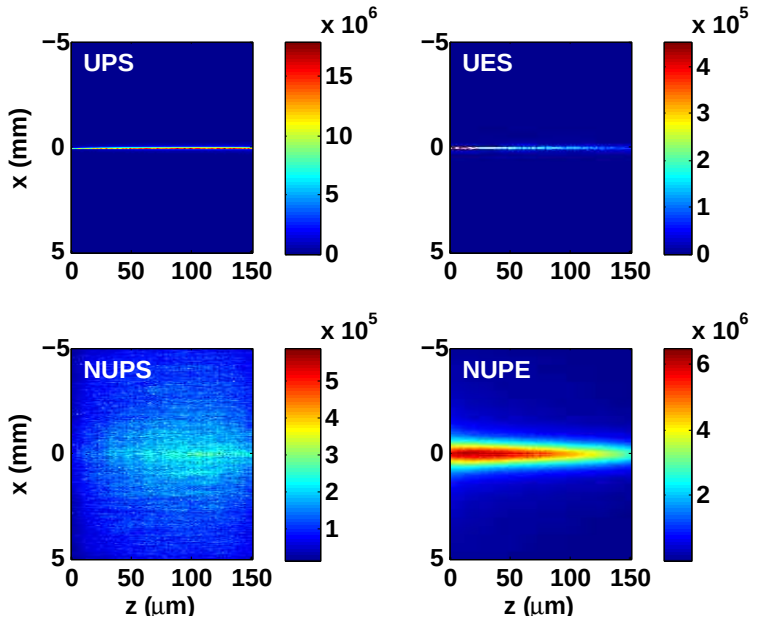

Figure 3.2: Deposited energy image in XZ plane, due to UPS, UES, NUPS and NUES.

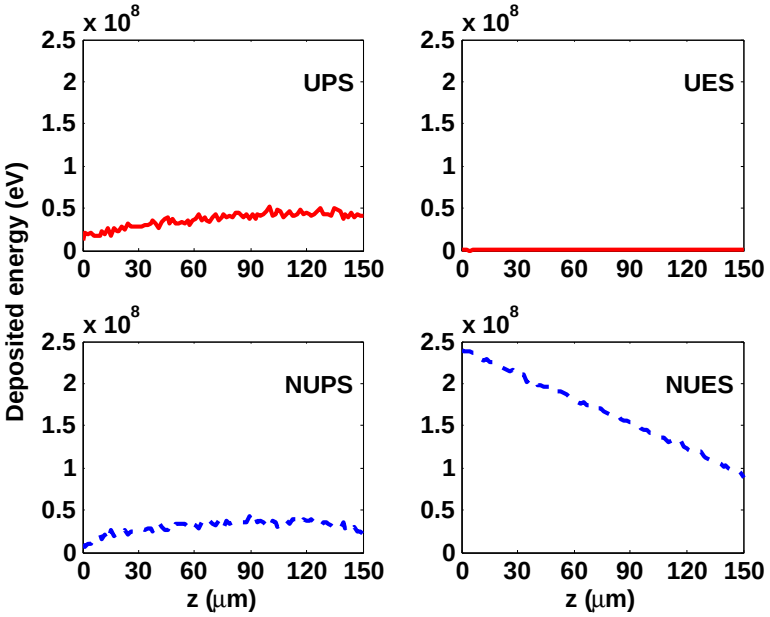

Figure 3.3: The deposited energy distributions along IP depth (z) respectively due to $useful$ photon and electrons (UPS and UES), and $not\,useful$ photons and electrons (NUPS and NUES).

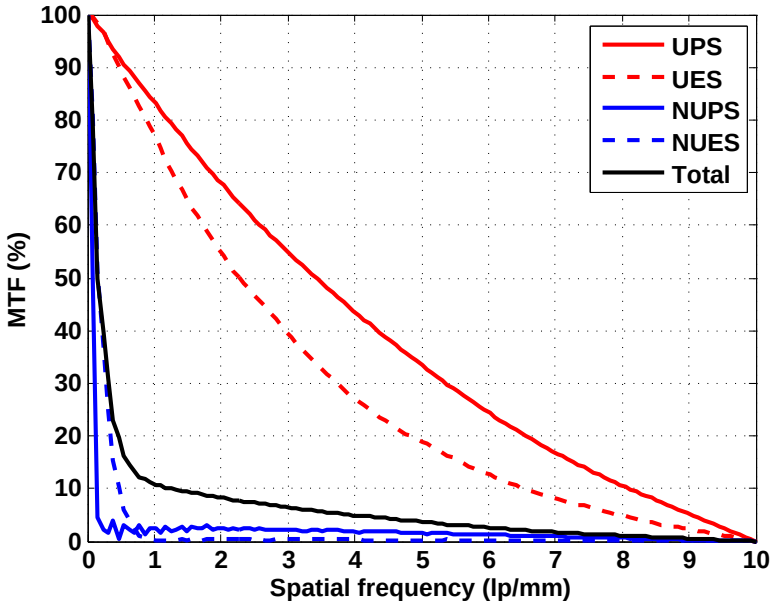

Figure 3.4: MTFs of the deposited energy image due to UPS, UES, NUPS and NUES, and the MTF of total deposited energy image (black curve).

first screen configuration (lead screen) is that requested by current standards. The second configuration (lead and tin) is chosen as an attempt to absorb K fluorescence of lead.

3.5.1 Spectral response analysis

3.5.1.1 Investigation of transmitted step-by-step spectra

In order to investigate the physical phenomena involved in each screen, we follow the photon spectrum after each step of the complete combination of screens (lead and tin). A monochromatic incident beam of 150 keV is chosen in such a way to be in the energy range where fluorescence occurs. Figure 3.5 illustrates the photon spectra:

- The first step in the detector system is the lead layer (asterisk) where it is visible that the initial monochromatic beam results in a continuous spectrum of secondary scattered radiation and fluorescence lines (K lines at 87, 84 and 74, 72 keV and L lines around 15 keV).
- The second step is the tin screen (dashed line): first of all it is observed that tin can effectively absorb the lead fluorescence (about 2 orders of magnitude) and also a big part of the scattered radiation between 30 and 80 keV. However, tin also yields its own fluorescence lines at around 30 keV.
- The last step corresponds to the protective layer of IP (plus sign): the overlapping of the blue and magenta curves indicates that no effect is introduced by the protective layer on the photon spectrum.

Table 3.1: Parameter setting. The IP was between the front and back screens, and the screens were placed in contact with IP

Elements			Configurations		
			IP alone	IP+0.2Pb	IP+0.2Pb0.8Sn
Source	Type:photon source		fixed energy	fixed energy	fixed energy
	Energy range in keV ($E_{min}, E_{max}, E_{incmt}$)		(2,1300,1)	(2,1300,1)	(2,1300,1)
Object	Object		none	none	none
Detector	Front screens		none	0.2mmPb	0.2mmPb +0.8mmSn
	IP	NbBX×NbBY×NbBZ	100×100×100	100×100×100	100×100×100
		Voxel dimension (μm^3)	10×10×1.5	10×10×1.5	10×10×1.5
	Back screens		none	0.2mmPb	0.8mmSn +0.2mmPb

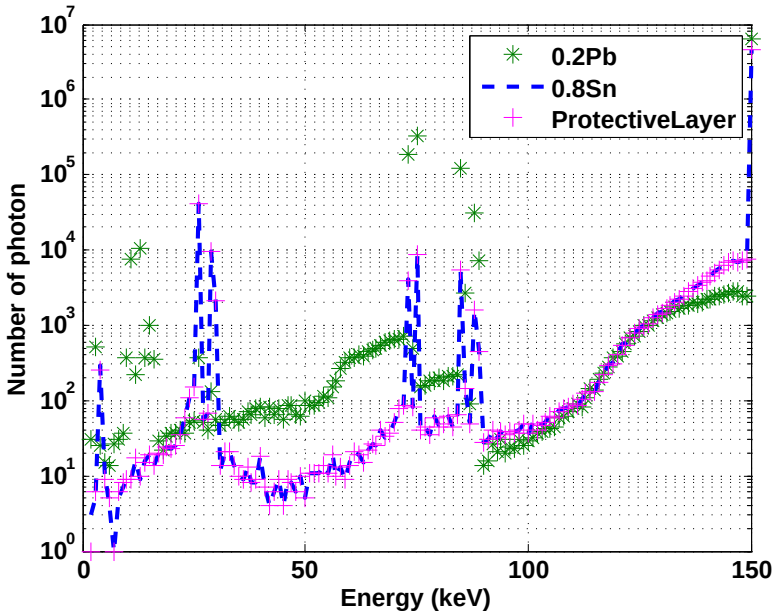

Figure 3.5: Step-by-step photon spectra.

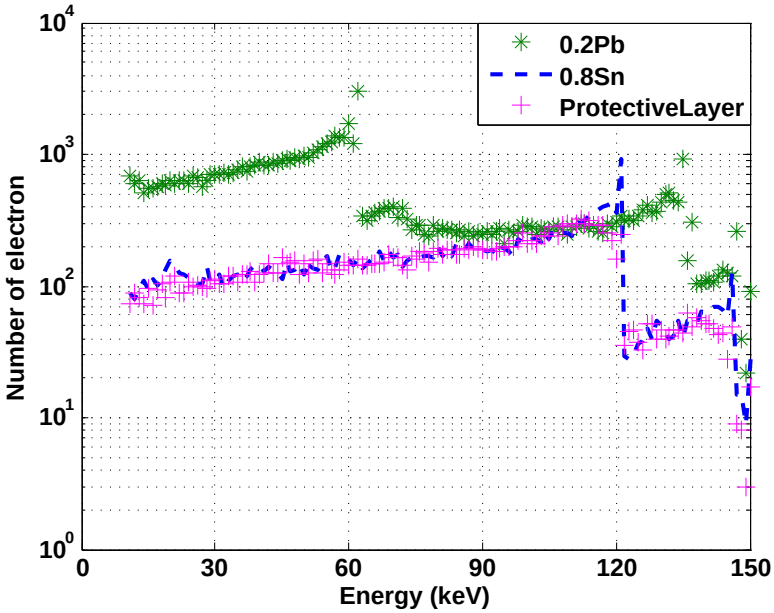

Figure 3.6: Step-by-step electron spectra.

Figure 3.6 shows the electron spectra after the different layers. In the photoelectric effect, an excitation photon of energy E is absorbed by the atom, which leads an excited atom and a photoelectron leaving the atom with a kinetic energy $E_k = E - U_i$, where U_i is the ionization energy of the electron (Beutel et al., 2000).

- The first step (green curve) represents the electron spectrum after the lead screen, where two peaks are visible, respectively at 62 keV and 135 keV, corresponding to the photoelectrons coming from the lead K-shell (whose ionization energy is about 88 keV) and L-shell (whose ionization energy is about 15 keV).
- After the tin layer (whose K- and L-shell ionization energies are about 29 keV and 4 keV respectively), the photoelectron peaks are observed at 121 keV and 146 keV (blue curve).
- When comparing the spectra after tin and after the protective layer (blue and magenta curves), we can observe that the photoelectrons peaks are much reduced, but overall, the energy stopped by the protective layer is negligible with respect to the total incident energy into this layer. Thus, in this energy range, the protective layer do not prevent electrons from entering the phosphor layer.

The study of the spectra is illustrative and helps to understand phenomena, but for high energies, a more global study of absorption efficiency is needed.

3.5.1.2 Energy absorption efficiency

Figure 3.7(a) shows the energy absorption efficiency plots of the 3 different detector configurations.

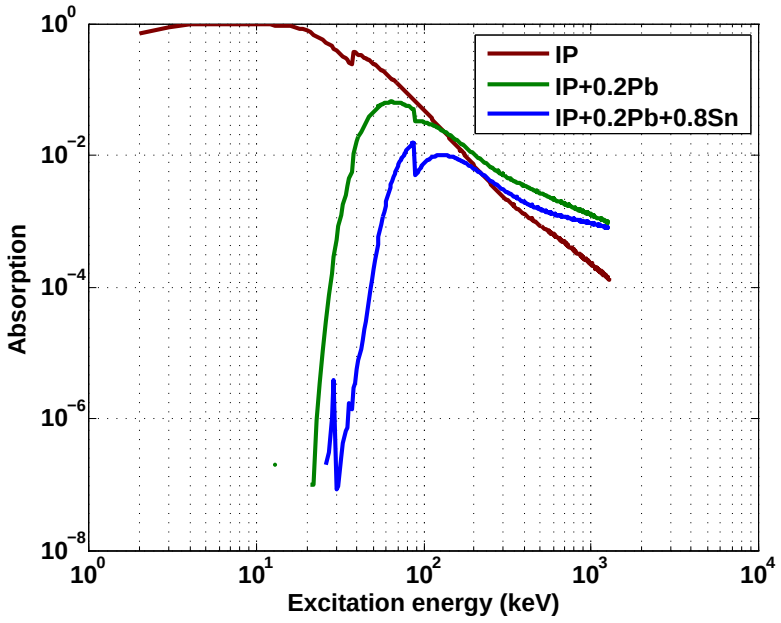

(a)

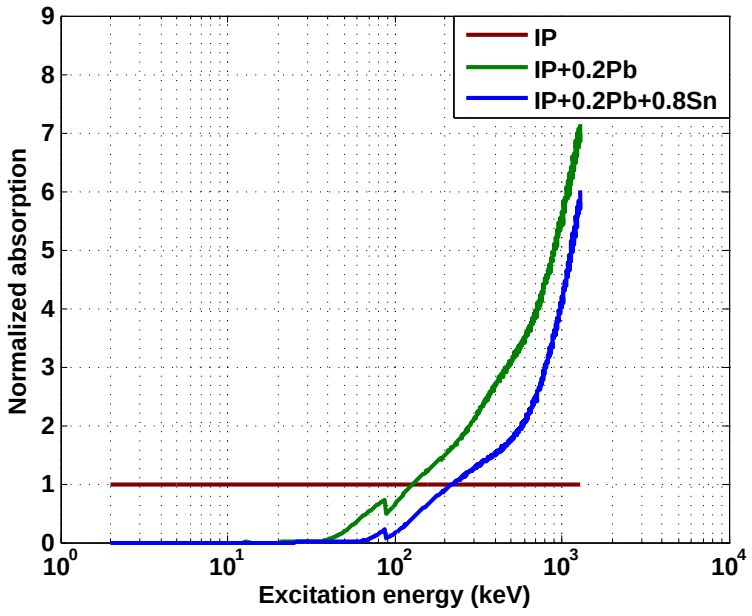

(b)

Figure 3.7: (a) The photon absorption efficiency as a function of energy for different detector configurations and (b) the absorption efficiency curves of different detector configurations normalized by that of *IP alone*.

- The response of $IP\,alone$ (red curve) is quite efficient, nearly 1, at low energies, but with the increase of excitation energy, the curve drops quickly towards zero. The small rise occurring between 30 and 40 keV corresponds to the barium absorption edge.
- The lead screen (green curve) filters the low energy radiation but intensifies the high energies: the green curve is above the curve of $IP\,alone$ for energies greater than 131 keV. The barium absorption edge has disappeared due to the filtering of low energies. At around 89 keV a quick drop arises which is due to the strong K-absorption of lead.
- With the combination of lead and tin screens (blue curve), similar effects are observed, except that the signal intensification starts from 226 keV, and an additional drop appears at 30 keV which corresponds to the K-absorption of tin.

In order to compare the intensification effect of the different combinations of metallic screens, the absorption curves of the two configurations were normalized by that of $IP\,alone$ (Figure 3.7(b)). Starting from 131 and 226 keV respectively, the two kinds of screen combinations intensify the absorbed signal in IP (normalized absorption to 1), and the intensification increases continuously. Regarding only the absorption intensification in the high energy range, the detector configuration with only lead is preferred, as it has the highest absorption level among the three. However, the tin plus lead combination has a better filtering of low energies. Thus, when considering the compromise introduced in section 3.4, namely the need to increase high energy weight (in order to absorb the $useful$ signal) and avoiding the low energy $not\,useful$ signal, the two screen combinations can be discussed (see section 3.6). On the other hand, the spatial resolution must also be compared, which is the aim of the next section.

3.5.2 Spatial response analysis

3.5.2.1 MTF curve and the limit of resolution at 20% MTF (f_{MTF20})

Figure 3.8(a) shows the MTF curves of the $IP\,alone$ for different excitation energies. In the low to medium energy range (see dark blue curves, up to about 400 keV), the MTF curve drops quickly with the increase of excitation energy, whereas, in the high energy range (see light blue to dark red curves, 400 keV to 1300 keV), the MTF curves overlap each other, meaning that the spatial resolution could be considered energy independent in this high energy range. Two gaps appear at 14 keV and 38 keV resulting from the K fluorescence reabsorption of brome and barium, as the fluorescence emission is isotropic, and thus, the PSF spreads out.
Figure 3.8(b) is the plot of f_{MTF20} versus excitation energy for $IP\,alone$. The two slumps correspond again to the K fluorescence reabsorption of brome and barium (like the two gaps just described above). As the excitation energy continues to increase, exceeding the K-edge energy, less fluorescence is produced, so less K fluorescence reabsorption, and hence the limit of resolution improves right after the K-edges, which was difficult to see in Figure 3.8(a) due to the color scale.

Figure 3.9 compares the resolution of the three detector configurations. With the lead screens on both sides of IP, a degradation of spatial resolution is introduced, especially at

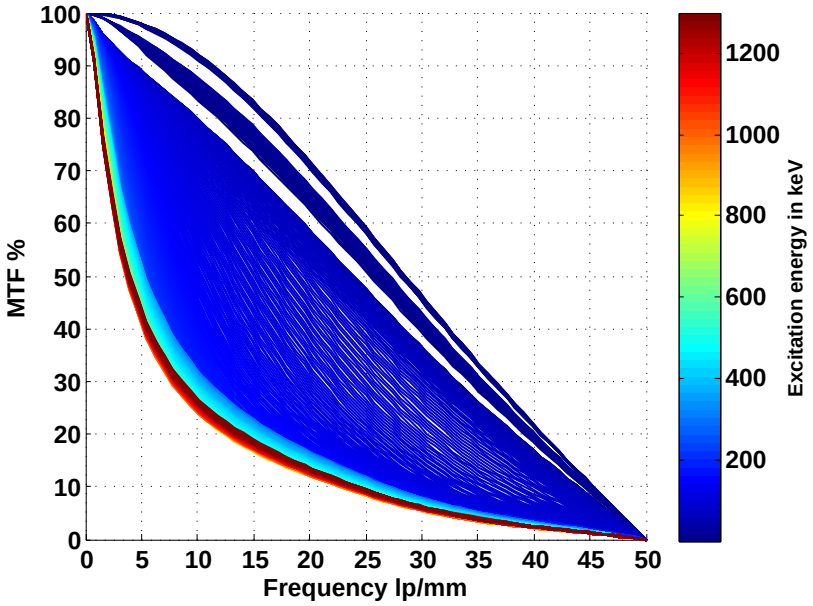

(a)

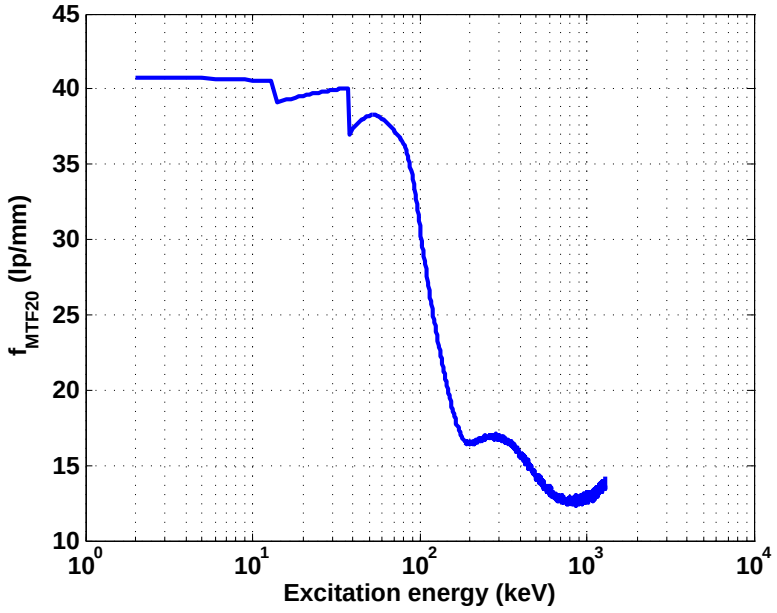

(b)

Figure 3.8: (a) MTF curves at different excitation energies for IP alone and (b) the f_{MTF20} versus excitation energy.

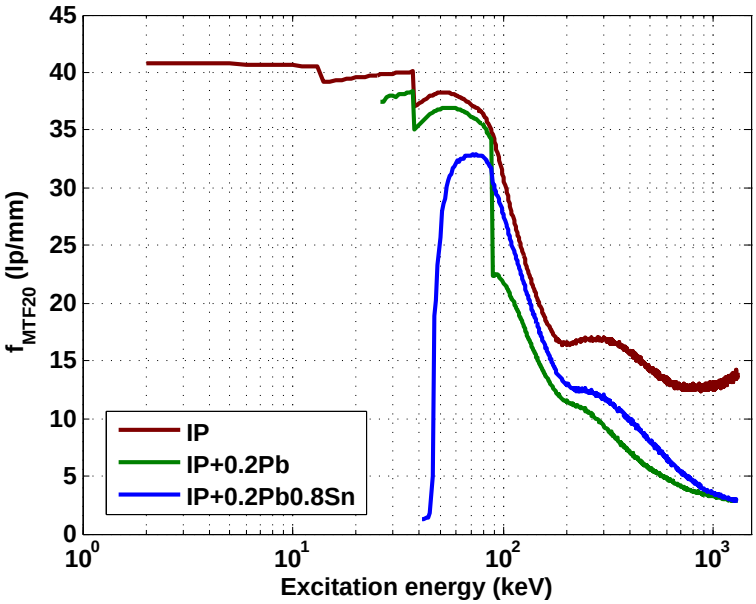

Figure 3.9: The f_{MTF20} versus excitation energy for different detector configurations.

89 keV, at which the fluorescence of the lead starts to yield. As a photon with a higher energy has a larger free traveling path, the lead fluorescence could spread further than that of barium and brome, and hence the resolution drop is much greater at 89 keV than it is at 14 and 38 keV. At energies lower than 89 keV, the addition of a tin screen between lead and IP further degrades the resolution since it is another layer spreading the incident beam. However, when the excitation energy exceeds 89 keV, as the lead fluorescence could be effectively attenuated by the tin screen (Figure 3.5), the resolution improves. This improvement, however, decreases as the excitation energy continues increasing, and becomes negligible at 1300 keV.

As a conclusion of this part, even considering only spatial resolution, it is difficult also to choose the best screen configuration because the behavior respectively at low to medium and high energies is not the same, and both should be considered for our typical industrial case.

3.5.2.2 The energy absorption distribution along z (EAD_z) and its centroid ($EADC$)

Now we would like to investigate the energy deposition with respect to the IP depth (z direction).

Figure 3.10(a) is a 2D visual image of energy absorption (in a color scale) as a function of excitation energy in abscissa, while the IP depth is represented in the vertical direction, with the front side at $z = 0$ and the rear side at $z = 150\,\mu m$. First of all, it is very clear that absorption is better in the low energy range (red color is only near 0 keV), and most of the energy is deposited towards the front side of IP.

In order to have a better visualization of the influence of z direction, Figure 3.10(b) shows

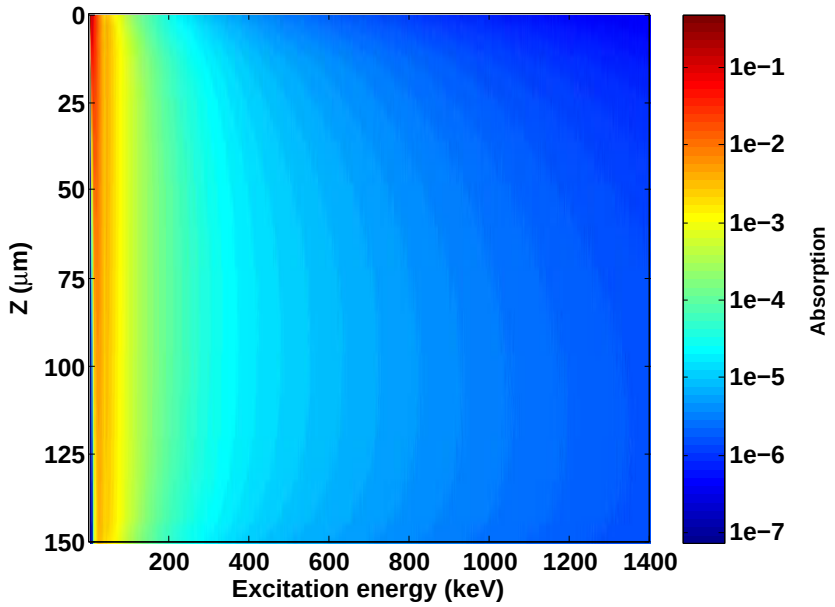

(a)

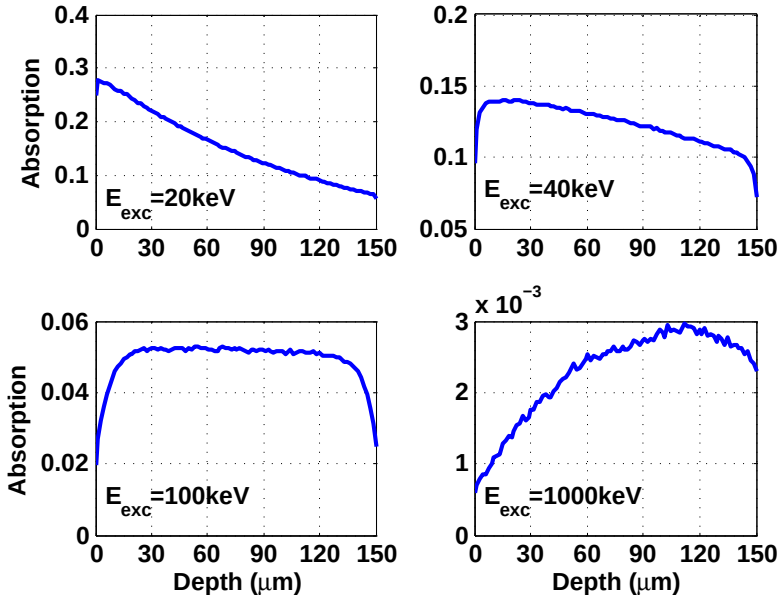

(b)

Figure 3.10: (a) 2D visual of absorption versus IP depth and excitation energy and (b) the EAD_z at 20, 40, 100 and 1000 keV. 0 μm is the front side of IP and 150 μm the rear side.

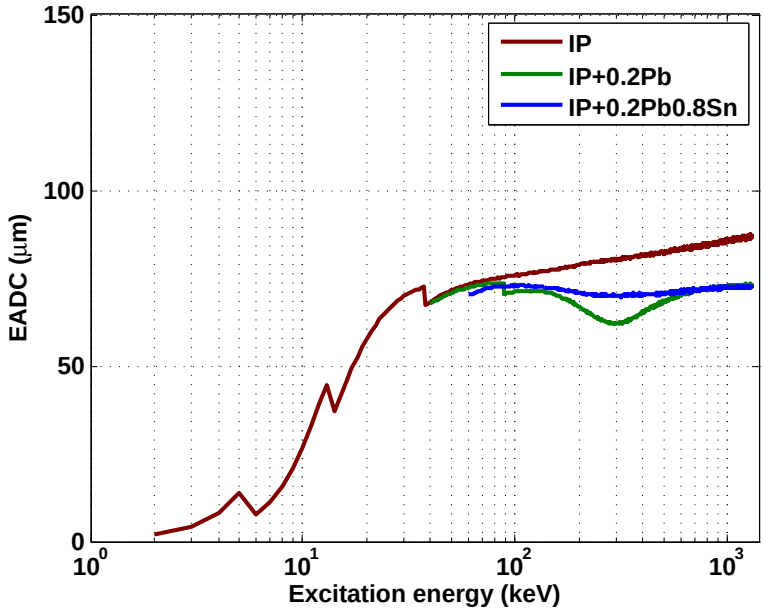

Figure 3.11: The $EADC$ versus excitation energy for different detector configurations.

the profile of energy deposition along z, EAD_z, at 20, 40, 100 and 1000 keV. We see that when excitation energy is small, the deposited energy is mostly near the front surface of IP, while with the increase of the excitation energy, the distribution is more and more towards the rear surface. The dropping at the boundaries is probably due to particle escaping.

In order to facilitate the comparison, we plot the centroid $EADC$ versus excitation energy in Figure 3.11. In our case, the centroid value is between 0 and 150 μm, where 0 μm means that all energy is deposited at the front surface of IP, and 150 μm the rear surface. When viewing the response of $IP\,alone$, at low energies, the energy is preferentially deposited on the front side, and with the increase of excitation energy, the energy tends to be deposited towards the rear side so that the centroid value increases.

When comparing screens (blue and green curves) with $IP\,alone$, we see that the centroid is shifted towards the front side to a different extent. Similarly to the absorption efficiency and sharpness measurements, it is also observed a sudden change due to the K-absorptions of fluorine, brome and barium in the red curve, and lead in the green curve. When comparing both screens, a small decrease of the centroid is observed with only the lead screen, which must be elucidated. It must be noted that the centroid investigation is important because the laser readout process is usually done from the front side of the IP and limited to a small depth. Thus, if we show that the centroid is lower, there is an interest for a best readout process.

As an attempt to elucidate the decrease in the centroid distribution with lead, in Figure 3.12(a), we study separately the centroid obtained for the photon and electron beams: the photon beam $EADC$ curve overlaps the $EADC$ curve of $IP\,alone$, whereas the electron beam $EADC$ is closer to the front surface, and it increases with excitation energy. Here we see that the electron beam is mostly responsible for shifting the deposited energy towards the front side, but the degree of the shift depends on the fraction of the deposited

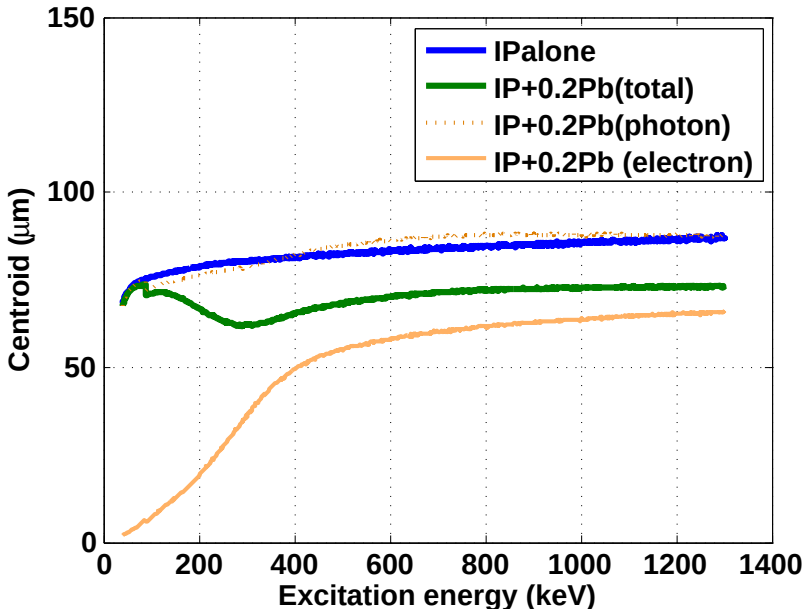

(a)

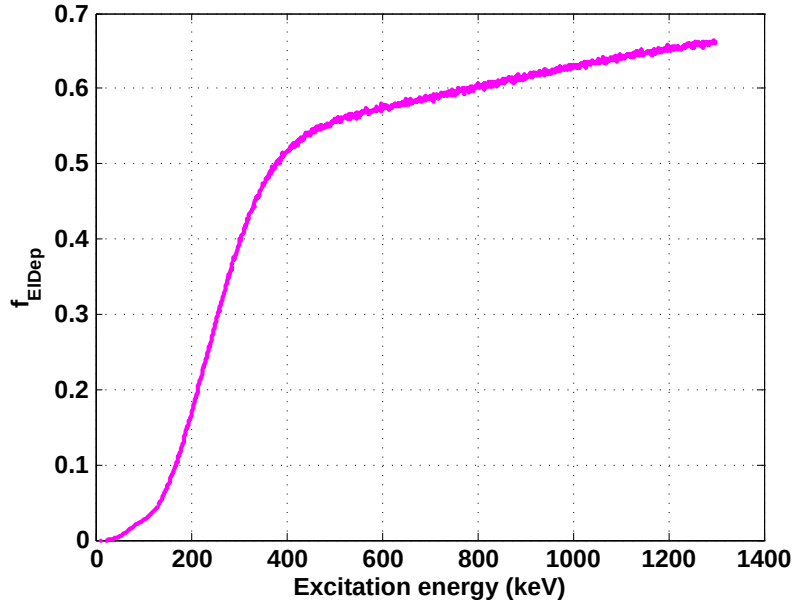

(b)

Figure 3.12: (a) The photon (dotted yellow plot) and electron (solid yellow plot) beam EADCs for $IP + 0.2Pb$, as well as the total EADC for $IP + 0.2Pb$ (solid green plot) and $IPalone$ (solid blue plot), and (b) the f_{ElDep} varying as a function of excitation energy for $IP + 0.2Pb$.

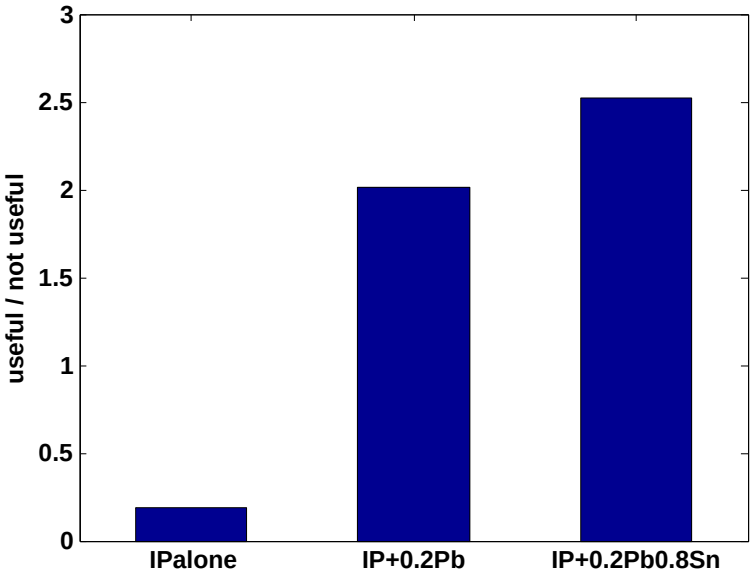

Figure 3.13: The ratio of $useful$ over $not\,useful$ signal.

energy which is due to electron beam. Thus, in Figure 3.12(b) we plot the fraction of the deposited energy due to the electron beam (f_{ElDep}): the f_{ElDep} also increases with excitation energy and at energies over 400 keV, more than half of the deposited energy comes from the electrons emerging from the lead screen. Thus, when comparing lead screen with $IP\,alone$, at low energies, even though the electron beam centroid is very close to zero, as the fraction of deposited energy is small, no obvious shift is observed; with the increase of excitation energy, the centroid shift could be observed, and the optimal centroid is at around 300 keV, an energy for which the electron beam centroid is still small and the fraction of deposited energy is important.

3.6 Results: industrial case optimization

According to the detailed analysis in the previous part, we find that both the two detector configurations with metallic screens could increase the $useful$ signal weight in the final image since they could effectively increase the absorption efficiency at high energies and eliminate the influence of low energy signal, especially $IP + 0.2Pb0.8Sn$ which has better filtering effect at low energies. While limiting the blurring introduced by $not\,useful$ signal, the screens also degrade the spatial resolution, therefore, a suitable detector should provide good $useful$ to $not\,useful$ signal ratio without losing much spatial resolution.
In Figure 3.13 we show the $useful$ over $not\,useful$ signal ratio: the ratio is greatly improved with $IP + 0.2Pb0.8Sn$. In Figure 3.14 we see that the MTF with $IP + 0.2Pb$ (Figure 3.14(a)) and with $IP + 0.2Pb0.8Sn$ (Figure 3.14(b)) are nearly the same. Comparing the spatial frequency at 20% MTF, $IP + 0.2Pb0.8Sn$ ($1.62\,lp/mm$) is a little better than $IP + 0.2Pb$ ($1.45\,lp/mm$). Hence $IP + 0.2Pb0.8Sn$ is overall better for our industrial case.

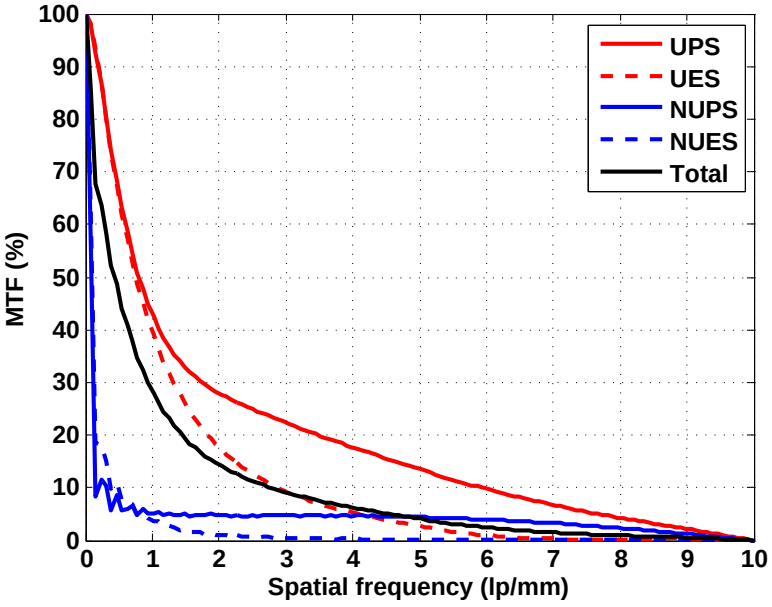

(a)

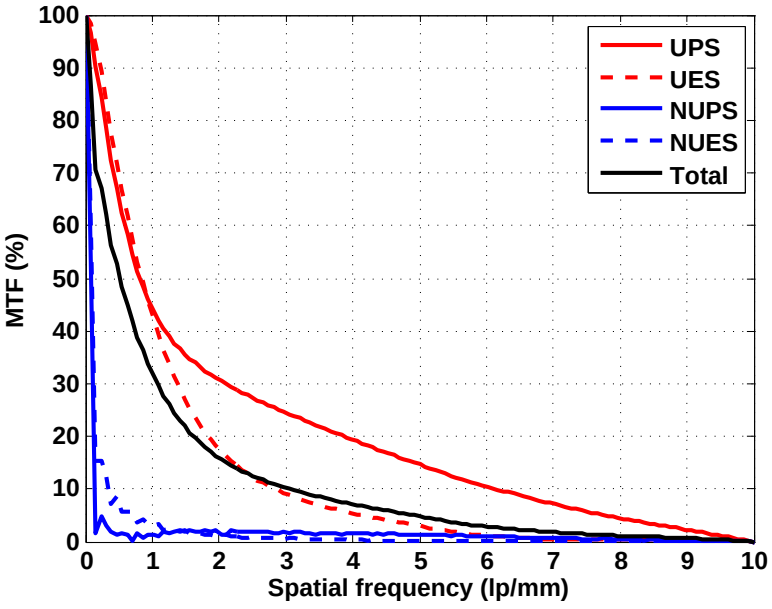

(b)

Figure 3.14: MTFs of the deposited energy image due to different signals for: (a) $IP + 0.2Pb$ and (b) $IP + 0.2Pb0.8Sn$.

3.7 Discussion

Through the IP response characterization and a detailed analysis on the spectral and spatial responses, we optimized an inspection case. $IP + 0.2Pb0.8Sn$ is the overall preferable detector configuration since it increases the most the high energy $useful$ signal weight without losing too much the energy absorption efficiency and spatial resolution.

From the performed study, we find that the metallic screens could: enhance the high energy signal and filter the low energy signal, degrade spatial resolution (the fluorescence of the screens is crucial), and shift the deposited energy toward the front surface of IP. The electron beam is mostly responsible for shifting the energy deposition distribution, and the degree of the shift depends on both the fraction and the centroid of the deposited energy due to electron produced by the metallic screens.

3.8 Conclusion

In this paper, we presented a Monte Carlo simulation tool for investigating the physical phenomena involved in the energy deposition process in IP. This tool allows different case studies on understanding the experimental observations and optimizing the image quality and choose the best IP/screen combination. This tool also provides the evaluation of the spectra transmitted along the different elements so that the fluorescence and scattered radiation production could be monitored as well as the influence of the protective layer of the IP.

As a future work, a comparison between experimental and simulation results of the detector performance (i.e. spectral and spatial response) will be of great interest.

The IP response characterization results obtained by this simulation tool will be applied to our future work on CR imaging chain modeling and optimization.

3.9 Experimental characterization of detector response

In the previous sections, we have characterized the response of several detector configurations with our Monte Carlo tool. This section presents some of our experimental results. The measurements were carried out at ESRF (European Synchrotron Radiation Facility) in Grenoble, France. The synchrotron radiation provides us quasi-monoenergetic X-ray beams. With the synchrotron source (Beamline ID15A), we have measured the response of several detector configuration at energies 35, 40, 50, 75, 100, 150, 200, 400 and 600 keV. We intended to measure the absorption efficiency, MTF and the intensifying effects of metallic screens at these energies. However, due to the unexpected problems we have met, only the screens' intensification is exploitable and is compared with the simulation results in this section.

3.9.1 Experimental set-up

A schema of the experimental set-up is presented in Figure 3.15. The radiation passes through, in order, a monochromator (not drawn in the figure), Diode 1, collimator slit, tungsten (W) edge, cassette and Diode 2. The two diodes monitor the photon flux. The W edge blocks half part of the beam, so that the spatial response can be measured. In

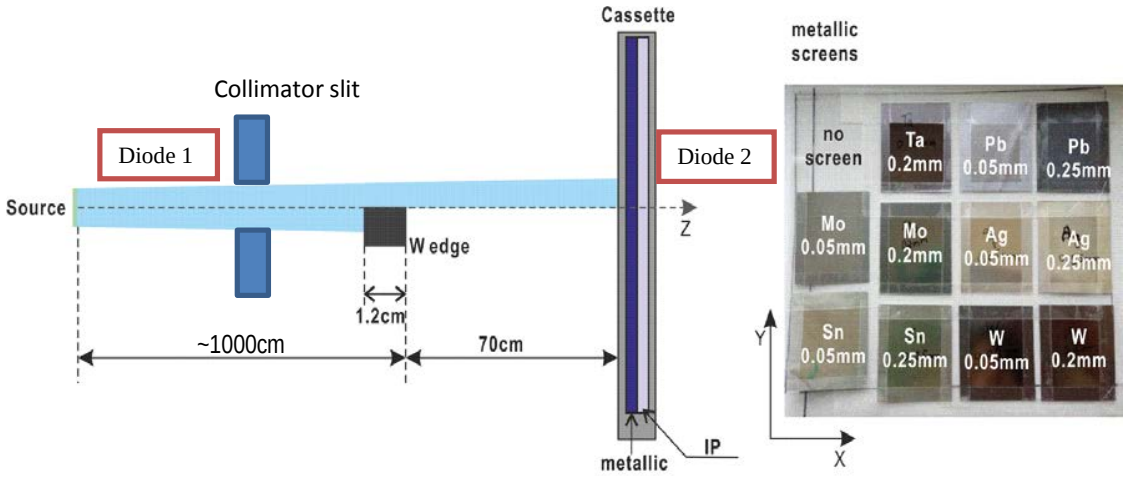

Figure 3.15: Experimental set-up for the detector response characterization.

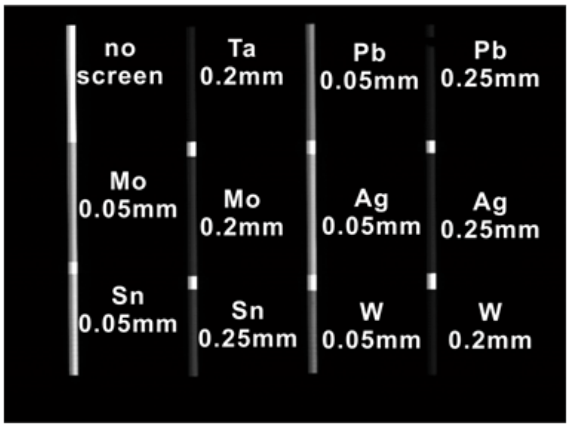

Figure 3.16: An X-ray image example. The 4 vertical white lines correspond to the exposed zones.

the cassette, the IP was put in contact with 11 metallic screens of different materials and thicknesses (right part in Figure 3.15). The IP is divided into 12 zones by the screens; the one without screen is considered as the reference zone.

As the size of the synchrotron X-ray beam is small (from 6×0.0025 mm^2 to 3×4 mm^2 according to the energy employed), the cassette was fixed on a controlling motor so that it could be moved in x and y directions and the beam could scan the whole cassette surface. As the example shown in Figure 3.16, the 4 vertical lines correspond to the exposed zones.

3.9.2 Description of test results

We had a difficult time of processing the acquired results. As it was our fist experience of characterizing the detector response at high energies, we have met several unexpected problems.

- Source beam uniformity (Figure 3.17). In certain measurements, the X-ray beam

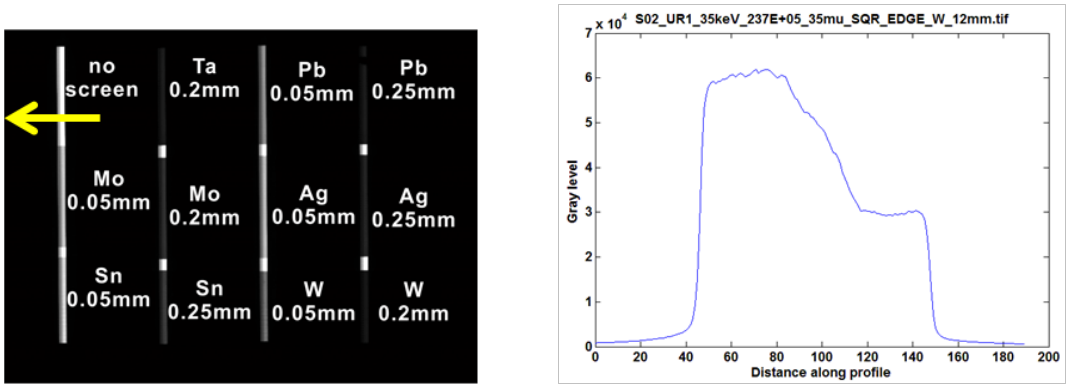

(a) (b)

Figure 3.17: X-ray beam uniformity: (a) an X-ray image; (b) profile along the yellow arrow.

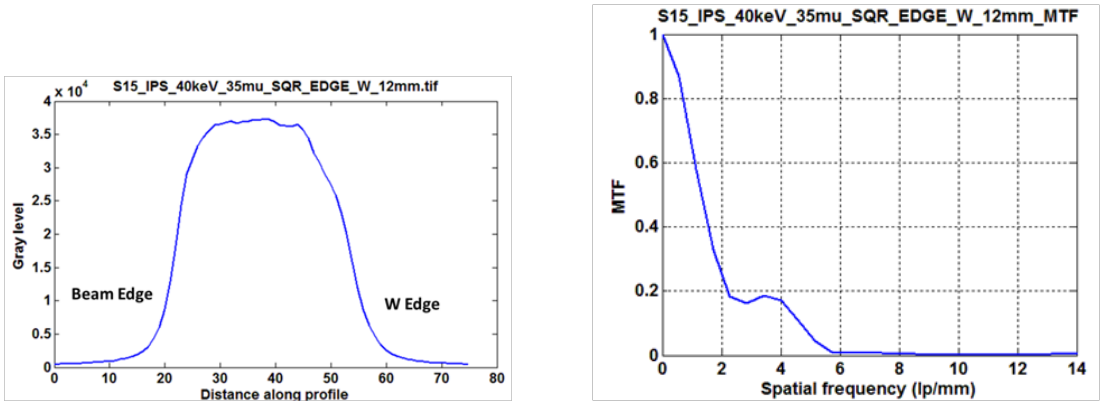

(a) (b)

Figure 3.18: Double-slope problem: (a) an edge profile example; (b) the MTF of the W edge side.

is not uniform, and this might be because of the beamline setting or the upstream equipment in the experiment room.

- Double-slope (Figure 3.18). In some images, two slopes are observed at the W edge side. This problem is probably due to the non-uniformity of the source beam. Another possible reason can be the miss-adjustment of the W edge. The two slopes are resulted from the W edge and the collimator slit. As a consequence, an upturn shows on the MTF curve.

- Vibration (Figure 3.19). The exposed zone is not uniform which is probably due to the mechanic vibration of the motor.

These problems make it difficult to exploit our experimental results, especially the measure of the energy absorption efficiency and MTF. Because of the source uniformity problem,

Figure 3.19: Vibration effect.

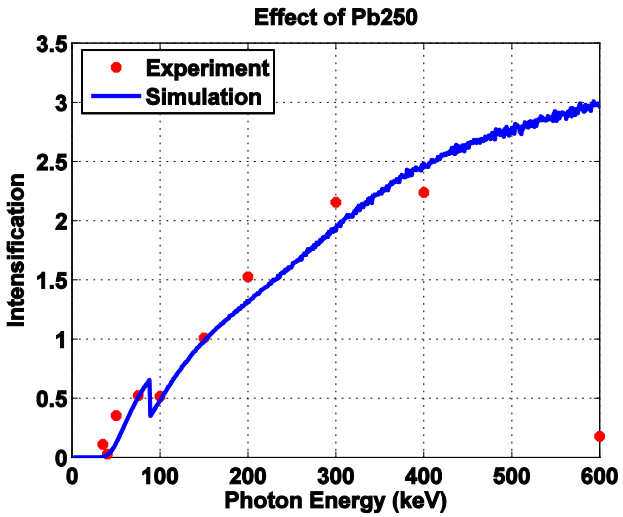

Figure 3.20: Intensifying effect of a 0.25 mm lead screen. The red points correspond to the experimental measurement; the blue curve is obtained with Monte Carlo simulation.

we cannot be sure that the reading of Diode 1 represents the photon flux incident upon the cassette, and thus the measured EAE is not comparable with the simulation result. The MTF we have measured is strongly affected by the double slope and vibration problems, and moreover, it also depends on the material and thickness of the edge used. For these reasons the MTF results are not comparable with the simulation results either. However the above mentioned problems do not affect much the measurement of the effects of metallic screens on the energy absorption efficiency, namely intensification, as in an image, all the 12 zones have the save exposure condition and share the same image problem. The intensification is a relative value between the signal measured in a zone with screen and the reference zone.

3.9.3 Results

In this part we present several experimental results of the screens' effect. Figure 3.20 through Figure 3.22 show the intensifying effect of three different screens (0.25 mm lead, 0.05 mm tungsten and 0.25 mm silver). The experimental and simulation results are compared in these figures: the simulation data are overall in accordance with the experimental data except at 600 keV. At this energy, the image is strongly affected by the secondary beam emerging from the W edge and the back scattered radiation (the back side of the IP was not shielded), and this point should not be taken into consideration. Different screens start to intensify the signal (i.e. value above 1) at different energy. Among these three screens, the lead and silver screens start to intensify at around 150 keV, and the tungsten screen at 100 keV.

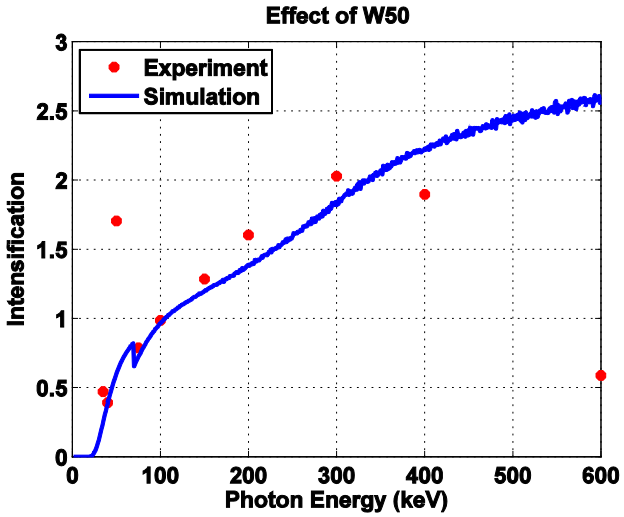

Figure 3.21: Intensifying effect of a 0.05 mm tungsten screen. The red points correspond to the experimental measurement; the blue curve is obtained with Monte Carlo simulation.

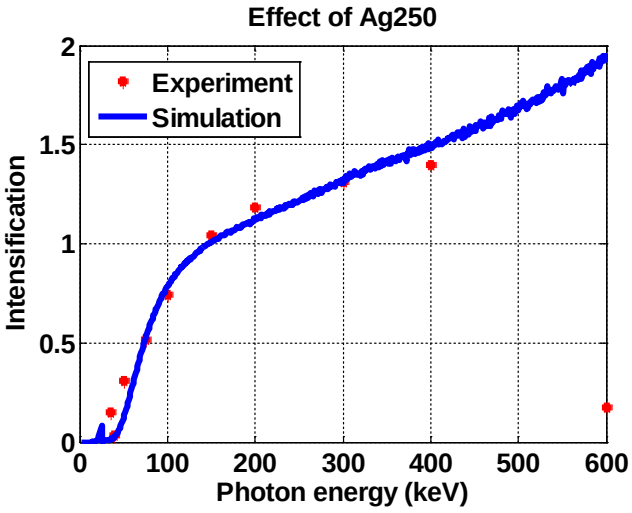

Figure 3.22: Intensifying effect of a 0.25 mm silver screen. The red points correspond to the experimental measurement; the blue curve is obtained with Monte Carlo simulation.

3.10 Concluding remarks

We have presented in this chapter a Monte Carlo simulation tool. With this tool, we have investigated the physical phenomena such as the effects of secondary radiation emerging from a thick object, the effects of metallic screens as well as the influence of fluorescence and electron produced by a metallic screen. An experiment, intended to characterize the response of several detector configurations, has been performed. Only the intensification effect is compared with the simulation results. Due to the unexpected problems we have met in the experiment, it is difficult to exploit the absorption efficiency and MTF. We are still working on the result interpretation. From another point of view, it proves the importance of computational simulation. It can provide solutions which are difficult or impossible to obtain experimentally, provided that the code is validated.

The investigation presented in this chapter concerns only the physical phenomena taking place during CR exposure. As the CR optical readout process also has importance influence on the final image, we need a model for the complete CR imaging chain comprehension. For this reason, the thesis develops a complete CR simulation approach. The next two chapters present step by step the simulation of a CR image formation, where the Monte Carlo tool developed in this chapter will be applied.

Chapter 4

Modeling of CR exposure, latent image generation and detector dose response

"There were doors all round the hall, but they were all locked; and when Alice had been all the way down one side and up the other, trying every door, she walked sadly down the middle, wondering how she was ever to get out again."

Alice in Wonderland

Contents

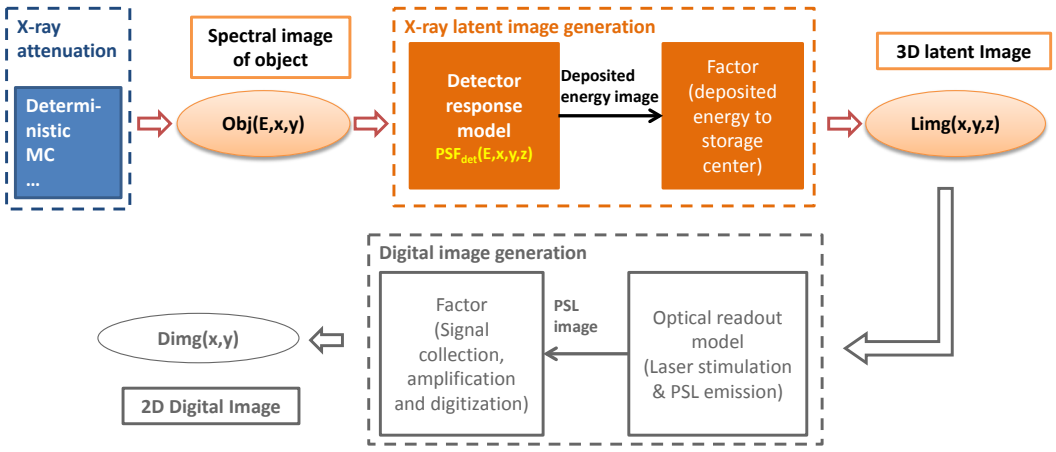

Figure 4.1: Subject of the chapter: from the object spectral image to the 3D latent mage.

4.1 Introduction

The X-ray image propagation in a CR imaging chain is carried out through three main steps: 1) X-ray source attenuation by an object resulting in a transmitted image; 2) X-ray energy deposition resulting in latent image; and 3) optical readout outputting digital image. This chapter deals with the first two steps in the imaging chain (Figure 4.1).

One can simulate these two steps using a full MC code such as the one we presented in the previous chapter. In the industrial radiography context, the specimens (e.g. welding, pipeline etc) are often of a great thickness or a complex structure, and high energy radiation sources are usually required. Hence the simulation using a full MC code is extremely time consuming because of the small number of photons absorbed in the detector. However, if we only simulate the transmitted X-ray fluence (i.e. object image), the MC running time can be greatly reduced, because a relatively small number of photons need to be launched to achieve a good SNR level.[1] Thus, if we adopt a two steps approach, the first step can be either simulated by a MC code or a deterministic approach. The latter one will of course be quicker.

With this in mind, we propose to simulate the X-ray exposure in two steps. According to needs, one can choose a deterministic or Monte Carlo code for object image simulation (first step). It will depend on the simulation method chosen for counting for the scattering or the fluorescence. The second step is modeled as an operator H1 as presented in Figure 4.2(a), which requires an object image $Obj(E, x, y)$ and a detector model as inputs. The detector model is a set of point spread functions for different incident X-ray energies

[1] As the SNR of a MC simulation result is the square-root of photon quanta. Suppose that there are N photons transmitted from the object, with a full MC code, the detector absorption efficiency (EAE) has to be accounted, then the absorbed photon quanta is $N \cdot EAE$. The SNR becomes $\sqrt{N \cdot EAE}$. To achieve $SNR = \sqrt{N}$, $1/EAE$ times more photons need to be simulated, hence $1/EAE$ times running time is needed. Note that EAE is very small ($< 10^{-2}$) at high energies (see Figure 3.7(a) in the previous chapter).

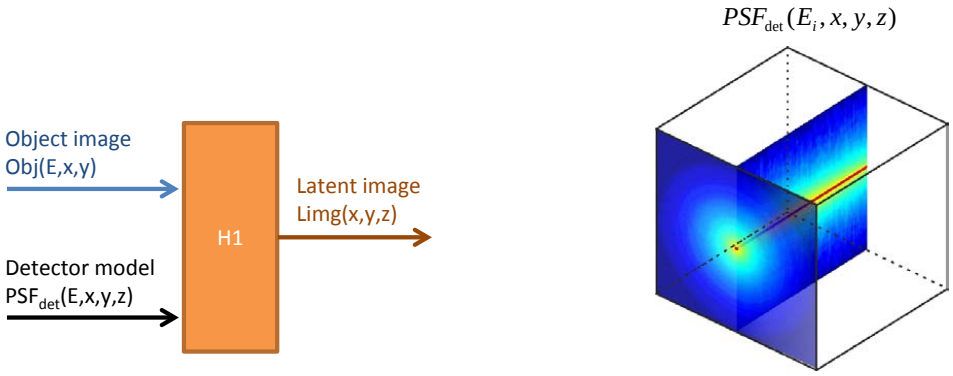

(a) (b)

Figure 4.2: (a) Latent image generation model: the X-ray/detector interaction is modeled as an operation H1, which requires a spectral X-ray image and a detector model as inputs. b) Example of detector model: impulse response of detector *det* to an incident pencil beam of energy E_i (3D energy absorption efficiency map). The complete response of the detector is the set of all point spread functions obtained for all energies.

(Figure 4.2(b)). The latent image $Limg(x, y, z)$ is obtained with the following formula:

$$\begin{aligned} Limg(x,y,z) &= \mathrm{H1}(Obj, PSF_{det}) \\ &= g_{sc} \int_E \left[E \cdot Obj(E,x,y) * PSF_{det}(E,x,y,z)\right] dE \\ &= g_{sc} \int_E \left[E \cdot \iint_{u,v} Obj(E,u,v) \cdot PSF_{det}(E,x-u,y-v,z) dudv\right] dE \end{aligned} \tag{4.1}$$

where

- H1 represents the latent image generation model which is a 2D spatial convolution (along x and y), at a given depth z, integrated over all energies, and finally multiplied by a conversion factor g_{sc} (see below);
- g_{sc} is the absorbed X-ray energy to storage center conversion efficiency (unit: keV^{-1});
- Obj or $Obj(E, x, y)$ is the spectral object image, namely the number of photons per unit surface per energy channel (unit: $\mathrm{cm}^{-2} \cdot \mathrm{keV}^{-1}$);
- PSF_{det} or $PSF_{det}(E, x, y, z)$ is the detector model, which is in fact a set of point spread functions (unit: cm^{-3}) for all energies;
- E is the X-ray photon energy (unit: keV);
- the term $\int_E \left[E \cdot \iint_{u,v} Obj(E,u,v) \cdot PSF_{det}(E,x-u,y-v,z) dudv\right] dE$ represents the deposited energy distribution (unit: $\mathrm{keV} \cdot \mathrm{cm}^{-3}$), which is converted into a storage center distribution (i.e. latent image) by multiplying by g_{sc}.

The output of this step is a 3D latent image (storage center distribution function). The PSF_{det} records the energy-dependence and the unsharpness of a detector. The energy dependence requires the object image containing the energy information (i.e. being a spectral image).

With the previous imaging plate performance investigation, we see that metallic screens can filter low energy signal and intensify high energy signal. At high energies, the electrons produced by the metallic screen play an important role on intensifying the IP energy absorption and modifying the absorbed energy distribution. Therefore, our Monte Carlo tool (detailed in Chapter 3) was applied in our detector model generation to account for different effects (e.g. electrons, metallic screens and scattering etc.) within CR detector (IP alone or with screens). Though the generation takes long time, once the model is obtained, it is stored in our detector database, and no MC rerunning is needed.

This chapter is going to present, step by step, the latent image generation: the object image (Obj) simulation, the detector model (PSF_{det}) preparation and the latent image computation based on Obj and PSF_{det}. To illustrate the use of our model, a case study is presented in the result section, where the latent images obtained with different detector configurations are compared. A comparison with a full Monte Carlo simulation is presented in Section 4.4. After a conclusion on the modeling and case studies, we present our detector database at the end of the chapter.

4.2 Simulation method

The application of this two-step model is based on the following assumptions.

- The application of this model is based on the linear system theory (CR detector is a linear system), so that the operator H1 can be applied to obtain the detector response to any object image Obj.
- The electrons emerging from the object are neglected. The number of electrons emerging from a high attenuation object is small, comparing with the photons. Moreover, before arriving at the detector, a great part of electrons are absorbed by air and the cassette[2]. Be aware that the electrons produced by metallic screens and IP are not neglected, and are taken into account with Monte Carlo simulations (Section 4.2.2) in the detector model.
- Normal incidence of radiation on the detector. In reality, the transmitted X-ray photons arrive at the CR detector with a certain incident angle. To simplify the calculation, we assume all photons enter perpendicularly to the detector.

4.2.1 Object image generation

The detector response model requires that the object image should contain the spectral information. In this way, we can account for a detector's energy-dependence property. In order to store the three-dimensional spectral object image$Obj(E, x, y)$ numerically, one have to sample the transmitted X-ray fluence with discrete pixels in XY plane and energy

[2]IP is often handled with a cassette.

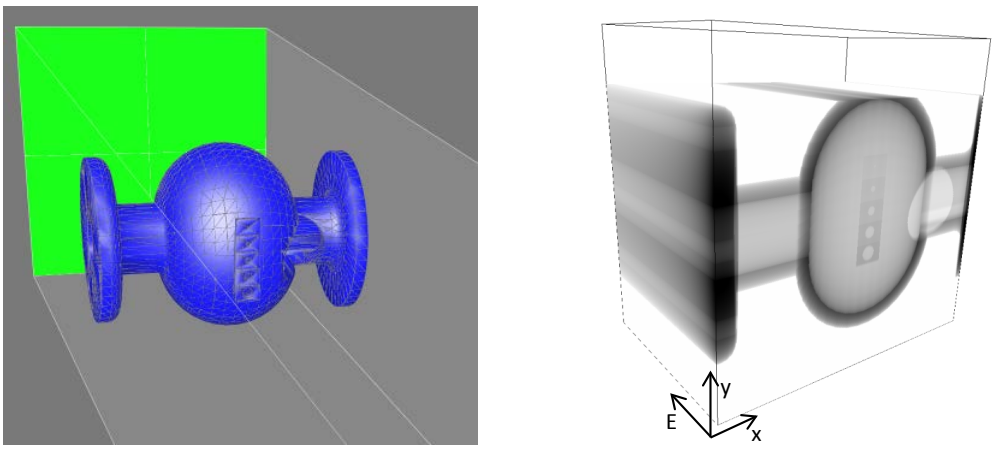

(a) (b)

Figure 4.3: Spectral object image generation: (a) example of geometric set-up using VXI; (b) illustration of a spectral image.

channels. The simulation can be conducted either with Monte Carlo or deterministic codes. If possible, a deterministic code should be prefered at this stage in order to save time while considering complex geometries.

To generate $Obj(E, x, y)$ (with any simulation method), a virtual detector is used and placed at the actual detector plane. This virtual detector is divided into $N_X \times N_Y$ pixels to record the spatial distribution of the incident photons. Each pixel counts the incident photon number, and tallied the photons into different energy channels (with a channel width E_{incmt} keV). The direct output of this virtual detector is the photon number per energy channel per pixel, and the $Obj(E, x, y)$ should be the output value divided by the pixel surface. Figure 4.3(a) is an example of the object image generation: (a) is a geometry set-up generated using VXI (Duvauchelle et al., 2000; Freud et al., 2004), a virtual detector (in green) is placed at the actual detector plane; and Figure 4.3(b) is the spectral image $Obj(E, x, y)$ detected by the virtual detector.

4.2.2 Detector dose response model generation

Our detector dose response model $PSF_{det}(E, x, y, z)$ was generated using the Monte Carlo tool developed in the previous chapter. As the model PSF_{det} is a 4D function, the generation starts by simulating the impulse response (3D PSF) of a fixed detector configuration det to a fixed energy E_i; secondly by scanning all energies, we get the complete response model (at all energies) of the fixed detector det; thirdly, we change the detector configuration, and repeat the first two steps, and then we finally get the detector model database. Though the preparation of the detector model takes very long time[3], once the model is stored, one does not need to rerun the MC simulations.

[3]On a single processor, the MC running of a detector configuration takes about several days to a month, depending on the materials and thickness of the imaging plate and metallic screens.

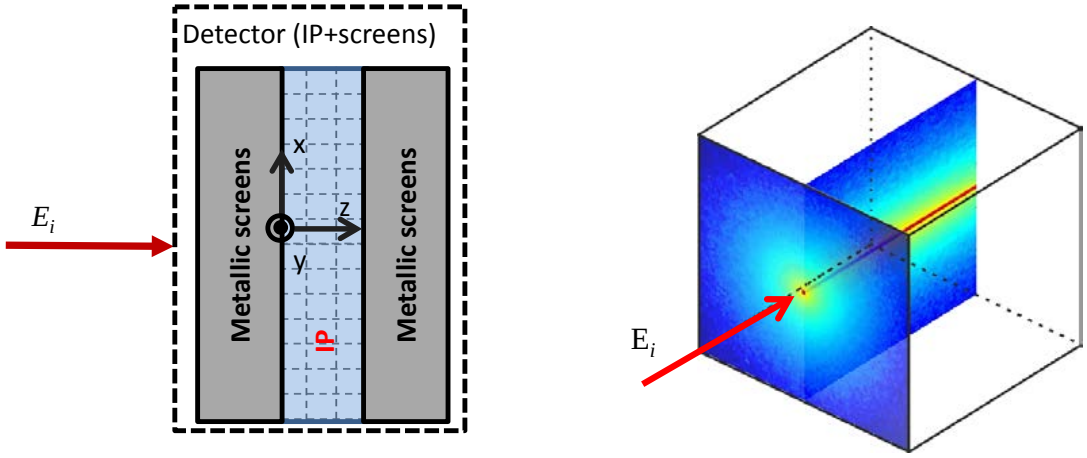

(a) (b)

Figure 4.4: Impulse response of a detector (a) Geometry configuration and (b) 3D energy deposition map $DEP(x, y, z)$: the arrow indicates the beam propagation direction which is also the IP depth direction.

4.2.2.1 Point Spread Function

The detector considered in this study is of a multiple-layered structure, where the imaging plate can be sandwiched between metallic screens. The imaging plate also consists of multiple layers such as overcoat and phosphor layer. The phosphor layer is the effective medium which stores the latent image, and will be later readout by CR scanner. Hence the PSF here is a 3D energy absorption efficiency (EAE) map within the IP's phosphor layer. As shown in Figure 4.4(a), we send a monoenergetic pencil beam (E_i) to strike the detector *det*. The raw output ($DEP(x, y, z)$) of the simulation is illustrated in Figure 4.4(b), which is the deposited energy map (absorbed energy per unit volume keV $\cdot$ cm^{-3}) within the phosphor layer. The PSF is obtained with

$$PSF_{det,E_i}(x, y, z) = \frac{DEP(x, y, z)}{N_i \cdot E_i}, \tag{4.2}$$

where N_i is the number of the incident photons. As a Monte Carlo calculation contains statistical noise, the incident photon number should be as large as possible to limit this noise. The impulse response is of cylinder symmetry around z-axis, hence we also apply a radial averaging to the PSF to reduce the noise (Figure 4.5); and the PSF is reduced a 2D function

$$PSF_{det,E_i}(\rho, z) = \frac{\int_0^{2\pi} PSF_{det,E}(\rho\cos\theta, \rho\sin\theta, z)\rho d\theta}{\int_0^{2\pi} \rho d\theta}, \tag{4.3}$$

where ρ is the radius, and θ is the angle between ρ and x-axis.

In such a way, the storage space can be saved. The storage digits can be further reduced by applying an analytic fitting function to each 1D profile (as illustrated in Figure 4.5(b)) at different z. In order to apply Equation 4.1, we reconstruct the $PSF_{det,E_i}(x, y, z)$ (Fig-

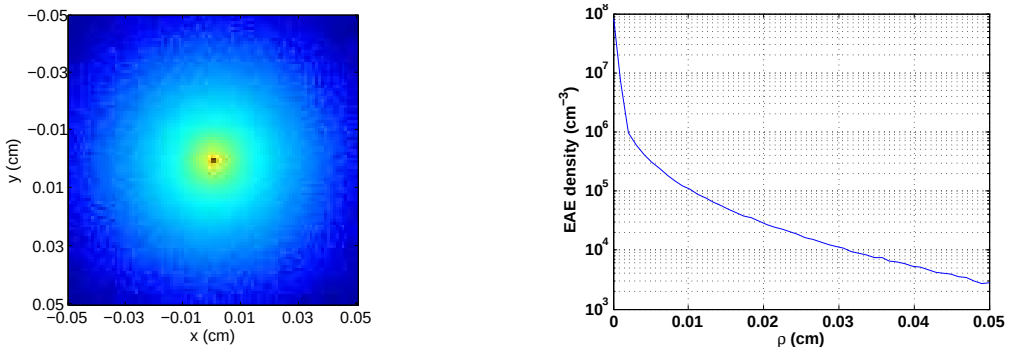

(a) (b)

Figure 4.5: Illustration of (a) $PSF(x, y, z_j)$ and $PSF(\rho, z_j)$. Owing to the cylinder symmetry, the two dimensional image at z_j can be reduced into a 1 dimension profile varying with radius.

ure 4.6(b))by rotating $PSF_{det,E_i}(\rho, z)$ around z-axis.

4.2.2.2 Detector model

The second step of detector response model generation is to repeat the previous operations (i.e. impulse response simulation and radial averaging) by scanning all energies (see Figure 4.7). Energies (ranging from E_{min} to E_{max}) are sampled to excite the detector *det*. After the radial averaging operation, we have a set of PSF_{det,E_i}, and all these PSFs make up the response model of detector *det*. In order to cover the energy range of common NDT radiation sources (such as Ir192 and Co60), E_{min} is assigned 0 keV, and E_{max} 1400 keV.

In order to complete the detector model, we repeat the processes illustrated in Figure 4.7 for different detector configurations. As a first step, we have *det* cover all the metallic screens/film combinations proposed in the standards EN14784-2 and ISO17636-2 (see Section 4.5).

4.2.3 Latent image computation

The latent image generation involves the energy deposition and storage center formation. Only portion of the deposited energy is stored in the form of storage center. As yet, the storage center forming mechanism is not clearly understood; moreover, it is different from one to another material. Therefore, the latent image (storage center) formation process is simply modeled as a conversion factor g_{sc} (unit: keV^{-1}). In the review of Rowlands, the absorbed X-ray energy to storage center ratio is 2.4/keV; while in (Thoms, 1996a), a different ratio 7.98/keV is reported. We have chosen to assign the normalized value 1 keV^{-1} to g_{sc}.

For the sake of clarity, we repeat here the Equation 4.1 already detailed before $Limg(x, y, z) = g_{sc} \int_E [E \cdot Obj(E, x, y) * PSF_{det}(E, x, y, z)]\, dE$. Numerically, this equation is realized energy by energy. For each energy channel, we compute the storage center distribution at different z; by summing the latent images obtained for all energy channels, we get the

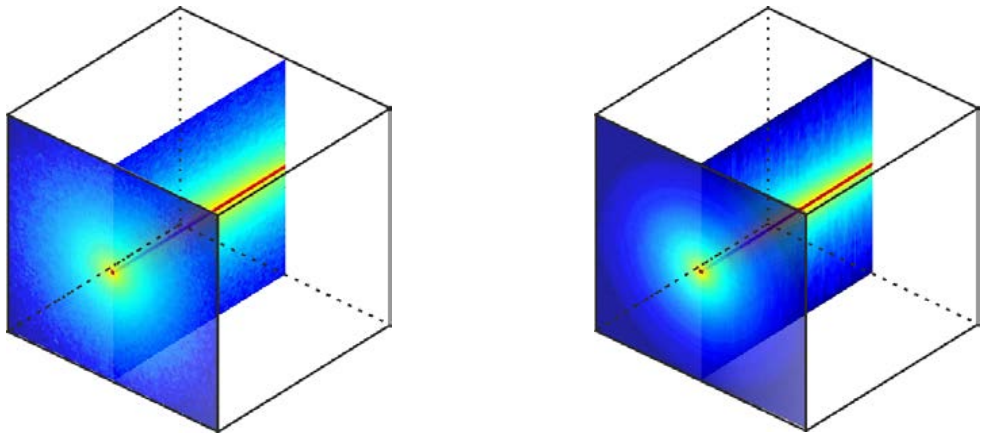

(a) (b)

Figure 4.6: Illustration of a PSF before (a) and after (b) noise reduction by radial averaging.

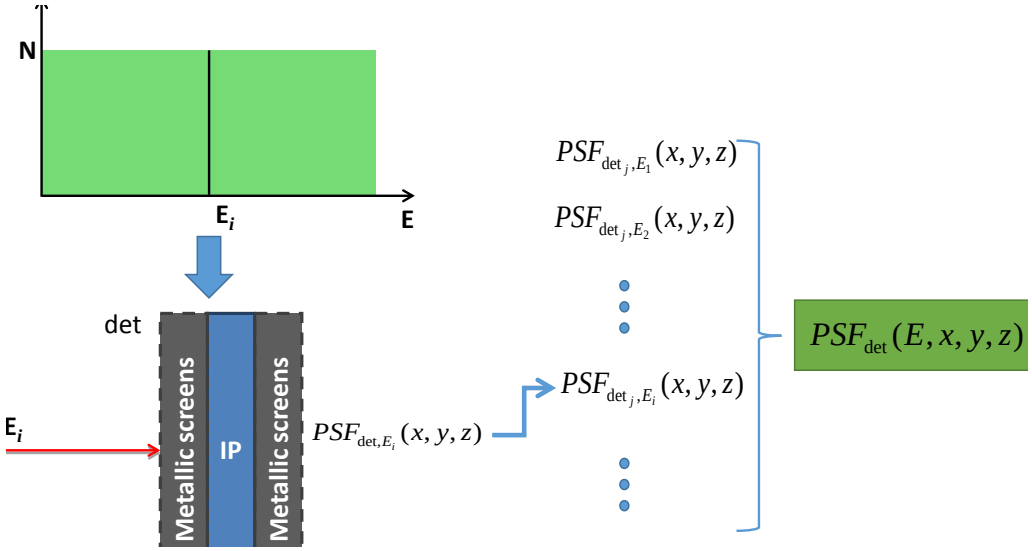

Figure 4.7: Generating the detector dose response function of a fixed detector *det*.

final output latent image. The corresponding computation algorithm is:

Initialize the latent image array $Limg(x, y, z) = 0$.
for *each energy channel:* $E_i \leftarrow 0$ ***to*** E_{max} **do**
  for *each IP depth:* $z_j \leftarrow 0$ ***to*** d **do**
    Compute the latent image at depth z_j given by photons of energy E_i
    $\Delta Limg(x, y) = g_{sc} \cdot \left[obj_{E_i}(x, y) * PSF_{E_i, z_j}(x, y)\right]$;
    Accumulate $\Delta Limg(x, y)$ to the corresponding depth slice z_j in latent image array
    $Limg(x, y, z_j) = Limg(x, y, z_j) + \Delta Limg(x, y)$.
  end
end

Note that the numerical convolution requires the pixel size matching between Obj and PSF_{det}. With an analytic fitting function, one can easily match the PSF with the Obj array. As yet, we have not found suitable fitting functions. In this thesis, the sampling match is achieved by means of interpolation.

The algorithm output is a 3D latent image. We keep the information along detector depth (z) direction, because the latent image is read by a scanning laser, the laser power modifies the penetration of the laser light, thus the storage centers in depth have less contribution to the readout image. With this in mind, we chose to keep the information along z.

4.3 Result: complex imaging set-up simulation

With the modeling method explained above, a complex object imaging case has been studied. The model has been applied to simulate the responses of different detector configurations to the same geometric set-up as illustrated in Figure 4.3(a). We have chosen the deterministic code VXI for the object image simulation, as it is almost impossible to simulate such a complex set-up with a MC code. The MC simulation of a simple object, in the next section (4.4), takes already 64 hours. For a complex shape object, as shown in this case study, the MC running time will take extremely long time, because the geometrical operations take a great fraction of simulation time (Gavaldà et al., 2009).

The complex shape object with a step-hole type image quality indicator (IQI) was exposed to a monochromatic (100 keV) point source. The virtual detector was set 70×70 mm^2 with a spatial resolution of 10×10 μm^2. The photon energy was stored into energy channels ranging from 0 to 100 keV, with a channel width of 1 keV.

The detector was modeled as an imaging plate sandwiched between metallic screens. The imaging plate was set as a multiple-layered structure which comprised of , in sequence, a 6 μm protective layer, a 150 μm phosphor layer , a 254 μm support layer and a 25.4 μm backing layer. The materials of these layers are respectively Mylar for the protective and support layers, $BaFBr : Eu^{2+}$ for the phosphor layer and poly-carbonate for the backing layer.

The responses of the following detector configurations were compared: a) IP alone; b) IP with 0.2 mm lead screens on both sides (denoted as IP+0.2Pb) and c) IP with 0.2 mm lead and 0.8 mm tin screens on both sides, where the tin screens are in contact with IP

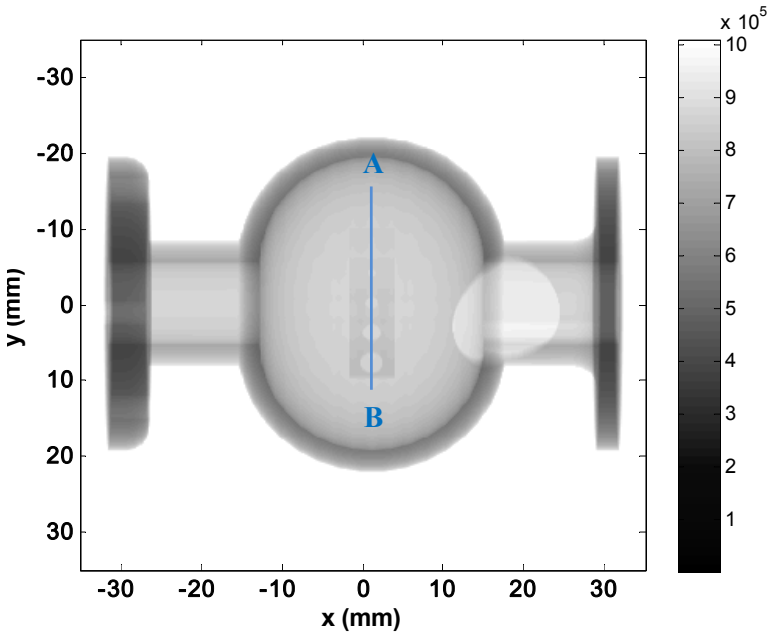

Figure 4.8: Object image obtained with VXI. The gray scale bar indicates the total transmitted energy per pixel.

(denoted as IP+0.2Pb0.8Sn). The sampling size of the detector dose response models is 10×10 μm^2 in XY plane, and 1.5 μm in z-direction, which matches the object image sampling.

We first simulated the object spectral image $Obj(E, x, y)$ in the detector plane with VXI. In order to have a 2D illustration $Obj_{2D}(x, y)$ (Figure 4.8), we have integrated the object spectral image over its energy axis

$$Obj_{2D}(x, y) = \int_E E \cdot Obj(E, x, y) dE. \tag{4.4}$$

We then compute the latent images by applying the three detector models. In order to gain a good visibility of the detectors' effect, we only present the zone where the IQI is placed in Figure 4.9. Owing to the detectors' response, we lose the signal level and the resolution. With the three detectors, the smallest hole can still be identified; however, the sharpness of IP+0.2Pb is not as good as IP alone and IP+0.2Pb0.8Sn. In order to compare the image sharpness, we have normalized the four images to their maximum value, and plot in Figure 4.10 the normalized profiles along AB (see Figure 4.8). The sharpness of IP alone is very close to the object image 'Obj_{2D}', except a small contrast loss at high spatial frequency (difference at sharp edge). With IP+0.2Pb, the image sharpness is the worst.

Figure 4.11 illustrates the energy absorption efficiency (total absorbed energy over total incident energy) of the three detectors in Figure 4.9. Overall (taking into account both efficiency and sharpness), $IPalone$ provides the best image quality for this measurement case. Note that this case study is done for a low energy (100 keV), and thus cannot be generalized.

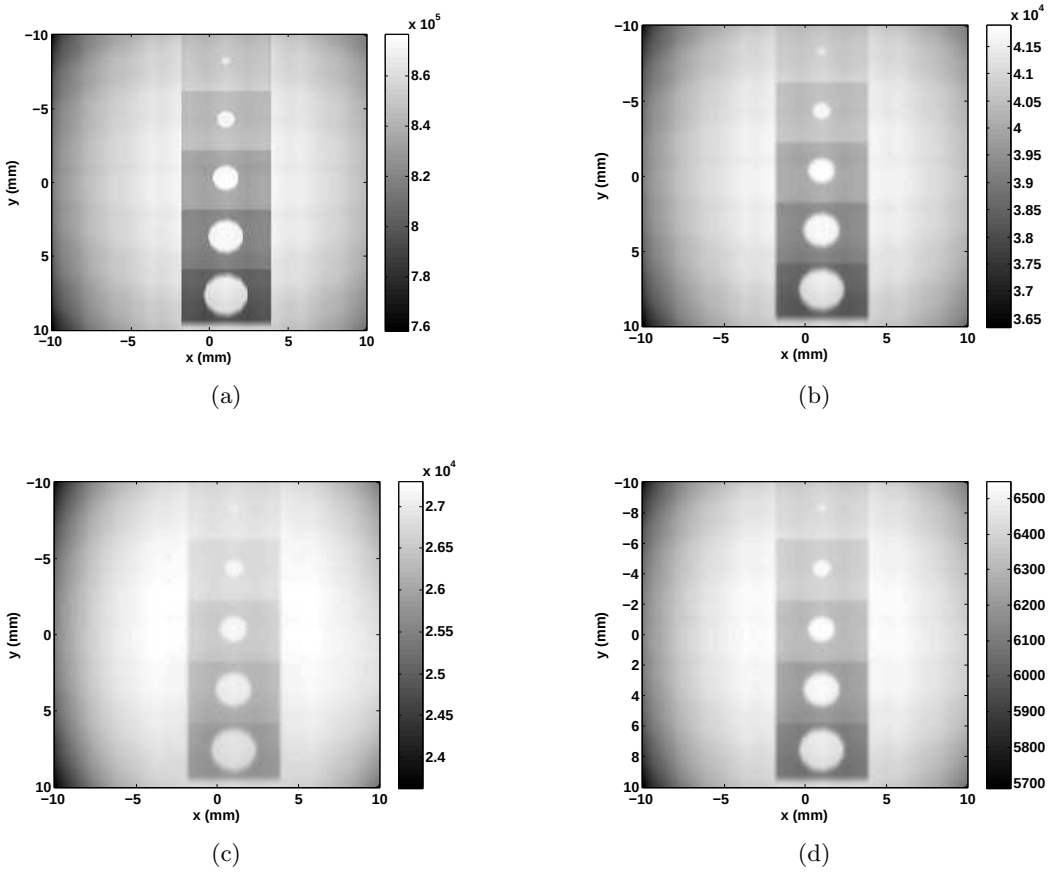

Figure 4.9: Comparison of the latent images using different detectors in the IQI region extracted from Figure 4.8: (a) is the object image Obj_{2D} obtained with an ideal detector; (b) is the latent image detected by IP alone; (c) is the latent image detected by IP with lead screens; and (d) is the latent image detected by IP with lead and tin screens. The gray level in the figures represents the number of storage centers.

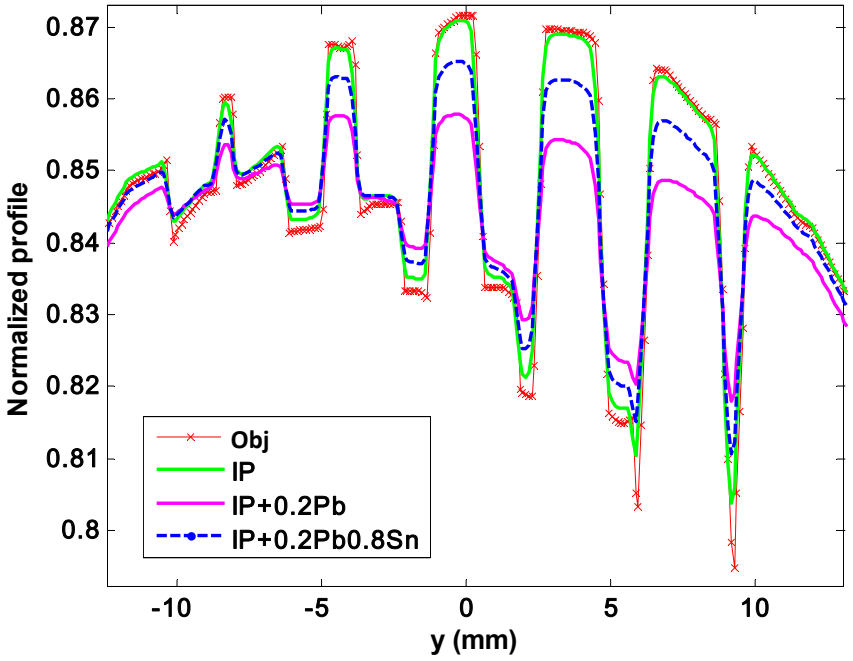

Figure 4.10: Normalized profiles along AB. The latent images and the object image are normalized by their maximum values.

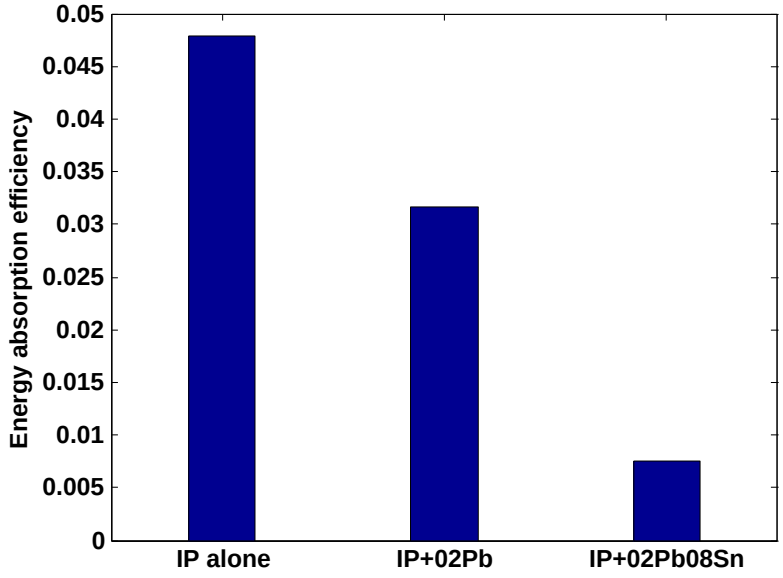

Figure 4.11: Absorption efficiency of different detectors.

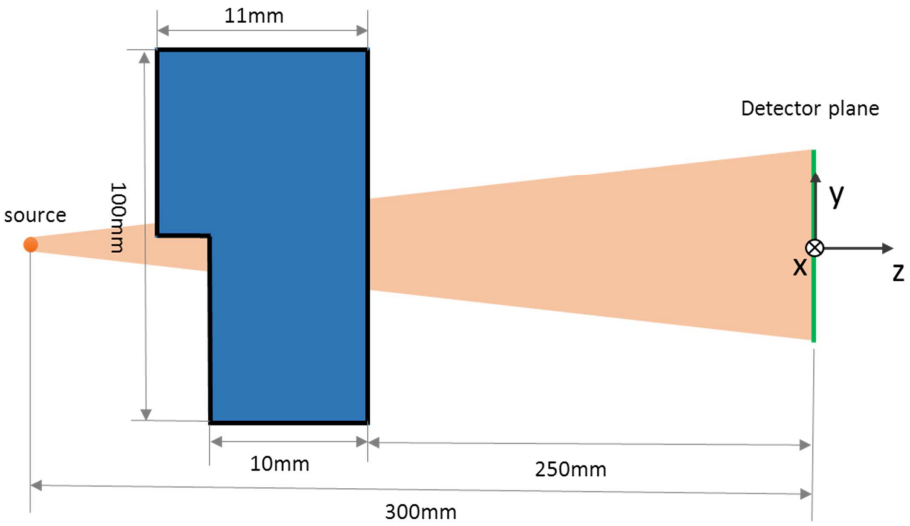

Figure 4.12: Geometric set-up of the comparison simulation. The object is a two-step iron piece. The detector is a 2 $mm \times 2$ mm imaging plate. The beam aperture was set 2/300 rad.

Figure 4.13 presents the object profiles across the iron steps. All profiles have been normalized by their mean signal value. The black one is the object profile. The profile obtained by H1 (blue) agrees perfectly with that obtained with the statistical MC result (magenta).

4.4 Comparison with a full Monte Carlo simulation

Monte Carlo method is commonly considered as a reference for the radiation transport simulation. As a first step to validate our model, we have chosen a very simple imaging set-up to compare the results of our convolution-based model H1 with a full Monte Carlo simulation.

We have simulated the imaging set-up as presented in Figure 4.12 with the two methods. The source used is a fixed energy cone beam, with the energy being 100 keV and the beam aperture being 2/300 rad; the object is a two-step (10 and 11 mm) iron piece; and the detector is set as $IPalone$ of 2 $mm \times 2$ mm. The full Monte Carlo simulation running takes about 64 hours, with the number of incident photons being 10^9; while with the convolution-based model H1, it takes about 1 hour.

4.5 Detector dose response model database

With the computation method presented in Section 4.2.2, we have generated a detector model database. So far, there are in total 128 detector models: 64 for a high resolution IP (IP-HR), and 64 for a high sensitivity IP (IP-HS). The detector structure is illustrated in Figure 4.14. FS2 and FS3 represent the metallic screens placed in front of IP; BS5 and BS6 are the screens behind IP. We list the 64 IP-HR configurations in Figure 4.15. Most of

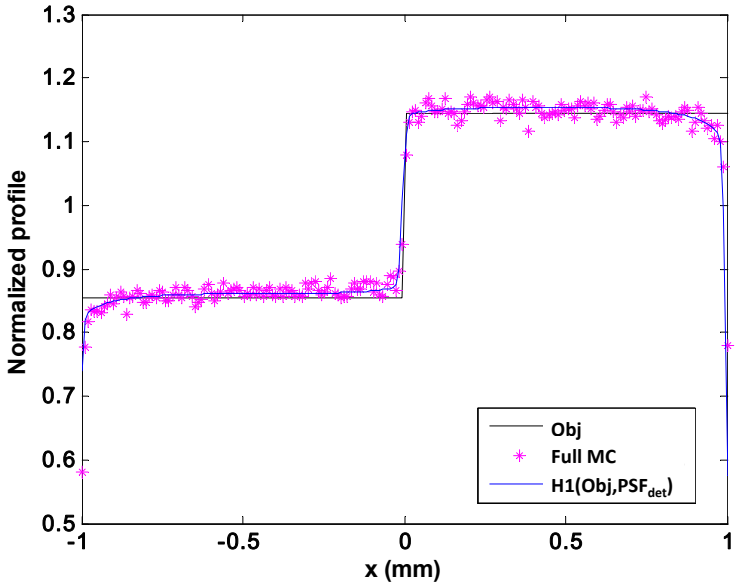

Figure 4.13: Comparison of the simulation result with a full Monte Carlo code and with our convolution model H1. For the latter, the *Obj* is simulated using the deterministic code VXI without accounting for scattering.

the screens combinations are those required by the standards EN14784-2 and ISO17636-2.

In order to gain the storage space, we store the reduced-dimension model $PSF_{det}(E, \rho, z)$ in the database. As an illustration, we present several detector models in Figures 4.16, 4.17, 4.18 and 4.19. The models are presented by means of EAE and f_{MTF20} (explained in Section 3.3.2) versus excitation energy curves.

4.6 Conclusion

In this chapter we have presented our X-ray exposure simulation approach. The latent image is generated in two successive steps: 1) simulation of the transmitted object image and 2) computation of a 3D latent image. For the former, different techniques can be applied, deterministic or Monte Carlo; for the latter, the latent image is obtained by applying the detector response model to the spectral object image (via operation H1).

The interests of this two-step approach are:

- Case where MC techniques are applied in the first step
  - The simulation time can be reduced with respect to a full MC code: indeed, to obtain a same SNR level, the full MC simulation (source-object-detector) takes a lot more (> hundreds of times) running time than a source-object MC simulation at high energies, because of the detector's poor absorption efficiency (<1%).

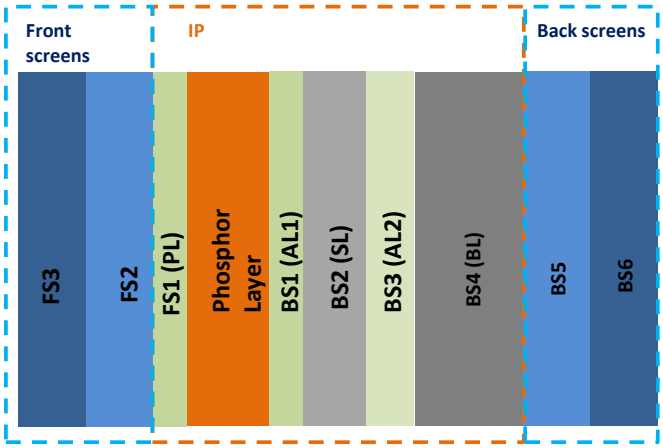

Figure 4.14: Detector structure adopted for the detector model database generation.

  - Quicker decision on the optimal detector configuration. No MC rerunning is needed for obtaining the latent images of different detector configurations. With a full MC simulation, one needs to rerun the MC code for each detector configuration. With the convolution model, one single source-object MC simulation is needed; by applying H1, one can obtain rapidly the latent images of different detector configurations, and determine the optimal detector configuration.

- Case where deterministic techniques are applied in the first step
  - The simulation image can be obtained even more rapidly (with or without simulating scattering effect).
  - A complex object can be handled easily, while for MC simulation codes, complex geometries have a prohibitive computational cost.

The comparison with the full MC simulation, of a simple geometric set-up, has been performed. The result shows a good accordance. A MC comparison of a complex imaging set-up (a step-wedge associated with a wire type IQI) is still in progress. As such a simulation (for obtaining a 3D image) is highly time-consuming, after months of MC running[4], the simulated image is still with a lot of noise. From another point of view, it proves the utility of our approach.

The convolution-based model H1, is based on the use of the off-line detector response models. For future simulations, we have created a detector response model database, which includes all the IP/screens combinations recommended in the current international standards.

As a perspective of this chapter's work, analytic fitting functions can be applied to the detector models, so that the database storage can be greatly reduced. Instead of an array, a PSF can be represented by several analytic function parameters. Moreover, analytic functions eliminate the array interpolation for the sampling matching between object image and detector model PSF_{det}.

[4]The running time corresponds to the simulation using a single processor. The simulation time can be reduced with parallel computing, but a large amount of data will be produced.

No.	Front screens		IP-HR				Back Screens		comment
	FS3	FS2	FS1 (PL)	Sensitive Layer	BS1 (RL/AL)	BS2 (SL)	BS4	BS5	
No	**FS3**	**FS2**	**FS1(PL)**	**Sensitive Layer**	**BS1 (RL/Al**	**BS2 (SL)**	**BS4**	**BS5**	**comment**
1			PMMA 0.005	Ba0.93Sr0.07F1.05Br	PVC 0.01	PET 180			EN & ISO & ESRF
2		Pb 0.1	PMMA 0.005	Ba0.93Sr0.07F1.05Br	PVC 0.01	PET 180	Pb 0.1		EN
3		Pb 0.2	PMMA 0.005	Ba0.93Sr0.07F1.05Br	PVC 0.01	PET 180	Pb 0.2		EN
4		Pb 0.25	PMMA 0.005	Ba0.93Sr0.07F1.05Br	PVC 0.01	PET 180	Pb 0.25		EN & ESRF
5		Pb 0.3	PMMA 0.005	Ba0.93Sr0.07F1.05Br	PVC 0.01	PET 180	Pb 0.3		EN
6		Pb 0.4	PMMA 0.005	Ba0.93Sr0.07F1.05Br	PVC 0.01	PET 180	Pb 0.4		EN
7	Pb 1.5	Fe 0.5	PMMA 0.005	Ba0.93Sr0.07F1.05Br	PVC 0.01	PET 180	Fe 0.5	Pb 1.0	EN
8	Pb 2.0	Fe 0.5	PMMA 0.005	Ba0.93Sr0.07F1.05Br	PVC 0.01	PET 180	Fe 0.5	Pb 1.0	EN
9		Pb 0.1	PMMA 0.005	Ba0.93Sr0.07F1.05Br	PVC 0.01	PET 180			ISO
10		Pb 0.2	PMMA 0.005	Ba0.93Sr0.07F1.05Br	PVC 0.01	PET 180			ISO
11		Pb 0.25	PMMA 0.005	Ba0.93Sr0.07F1.05Br	PVC 0.01	PET 180			ISO
12		Pb 0.3	PMMA 0.005	Ba0.93Sr0.07F1.05Br	PVC 0.01	PET 180			ISO
13		Pb 0.4	PMMA 0.005	Ba0.93Sr0.07F1.05Br	PVC 0.01	PET 180			ISO
14	Pb 1.5	Fe 0.5	PMMA 0.005	Ba0.93Sr0.07F1.05Br	PVC 0.01	PET 180			ISO
15	Pb 2.0	Fe 0.5	PMMA 0.005	Ba0.93Sr0.07F1.05Br	PVC 0.01	PET 180			ISO
16		Fe 0.8	PMMA 0.005	Ba0.93Sr0.07F1.05Br	PVC 0.01	PET 180			ISO
17		Cu 0.8	PMMA 0.005	Ba0.93Sr0.07F1.05Br	PVC 0.01	PET 180			ISO
18		Fe 0.6	PMMA 0.005	Ba0.93Sr0.07F1.05Br	PVC 0.01	PET 180			ISO
19		Cu 0.6	PMMA 0.005	Ba0.93Sr0.07F1.05Br	PVC 0.01	PET 180			ISO
20		Fe 0.3	PMMA 0.005	Ba0.93Sr0.07F1.05Br	PVC 0.01	PET 180			ISO
21		Cu 0.3	PMMA 0.005	Ba0.93Sr0.07F1.05Br	PVC 0.01	PET 180			ISO
22		Fe 0.8	PMMA 0.005	Ba0.93Sr0.07F1.05Br	PVC 0.01	PET 180	Fe 0.8		Hybrid ISO EN
23		Cu 0.8	PMMA 0.005	Ba0.93Sr0.07F1.05Br	PVC 0.01	PET 180	Cu 0.8		Hybrid ISO EN
24		Fe 0.6	PMMA 0.005	Ba0.93Sr0.07F1.05Br	PVC 0.01	PET 180	Fe 0.6		Hybrid ISO EN
25		Cu 0.6	PMMA 0.005	Ba0.93Sr0.07F1.05Br	PVC 0.01	PET 180	Cu 0.6		Hybrid ISO EN
26		Fe 0.3	PMMA 0.005	Ba0.93Sr0.07F1.05Br	PVC 0.01	PET 180	Fe 0.3		Hybrid ISO EN
27		Cu 0.3	PMMA 0.005	Ba0.93Sr0.07F1.05Br	PVC 0.01	PET 180	Cu 0.3		Hybrid ISO EN
28		Pb 0.05	PMMA 0.005	Ba0.93Sr0.07F1.05Br	PVC 0.01	PET 180			ESRF
29		Ag 0.25	PMMA 0.005	Ba0.93Sr0.07F1.05Br	PVC 0.01	PET 180			ESRF
30		Ag 0.05	PMMA 0.005	Ba0.93Sr0.07F1.05Br	PVC 0.01	PET 180			ESRF
31		W 0.2	PMMA 0.005	Ba0.93Sr0.07F1.05Br	PVC 0.01	PET 180			ESRF
32		W 0.05	PMMA 0.005	Ba0.93Sr0.07F1.05Br	PVC 0.01	PET 180			ESRF
33		Ta 0.2	PMMA 0.005	Ba0.93Sr0.07F1.05Br	PVC 0.01	PET 180			ESRF
34		Mo 0.2	PMMA 0.005	Ba0.93Sr0.07F1.05Br	PVC 0.01	PET 180			ESRF
35		Mo 0.05	PMMA 0.005	Ba0.93Sr0.07F1.05Br	PVC 0.01	PET 180			ESRF
36		Sn 0.25	PMMA 0.005	Ba0.93Sr0.07F1.05Br	PVC 0.01	PET 180			ESRF
37		Sn 0.05	PMMA 0.005	Ba0.93Sr0.07F1.05Br	PVC 0.01	PET 180			ESRF
38		Sn 0.8	PMMA 0.005	Ba0.93Sr0.07F1.05Br	PVC 0.01	PET 180	Sn 0.8		other
39	Sn 0.8	Cu 0.1	PMMA 0.005	Ba0.93Sr0.07F1.05Br	PVC 0.01	PET 180	Cu 0.1	Sn 0.8	other
40		Fe 0.7	PMMA 0.005	Ba0.93Sr0.07F1.05Br	PVC 0.01	PET 180			optional ISO
41		Cu 0.7	PMMA 0.005	Ba0.93Sr0.07F1.05Br	PVC 0.01	PET 180			optional ISO
42		Fe 0.5	PMMA 0.005	Ba0.93Sr0.07F1.05Br	PVC 0.01	PET 180			optional ISO
43		Cu 0.5	PMMA 0.005	Ba0.93Sr0.07F1.05Br	PVC 0.01	PET 180			optional ISO
44		Fe 0.4	PMMA 0.005	Ba0.93Sr0.07F1.05Br	PVC 0.01	PET 180			optional ISO
45		Cu 0.4	PMMA 0.005	Ba0.93Sr0.07F1.05Br	PVC 0.01	PET 180			optional ISO
46		Fe 0.7	PMMA 0.005	Ba0.93Sr0.07F1.05Br	PVC 0.01	PET 180	Fe 0.7		optional Hybrid ISO EN
47		Cu 0.7	PMMA 0.005	Ba0.93Sr0.07F1.05Br	PVC 0.01	PET 180	Cu 0.7		optional Hybrid ISO EN
48		Fe 0.5	PMMA 0.005	Ba0.93Sr0.07F1.05Br	PVC 0.01	PET 180	Fe 0.5		optional Hybrid ISO EN
49		Cu 0.5	PMMA 0.005	Ba0.93Sr0.07F1.05Br	PVC 0.01	PET 180	Cu 0.5		optional Hybrid ISO EN
50		Fe 0.4	PMMA 0.005	Ba0.93Sr0.07F1.05Br	PVC 0.01	PET 180	Fe 0.4		optional Hybrid ISO EN
51		Cu 0.4	PMMA 0.005	Ba0.93Sr0.07F1.05Br	PVC 0.01	PET 180	Cu 0.4		optional Hybrid ISO EN
52		Pb 0.45	PMMA 0.005	Ba0.93Sr0.07F1.05Br	PVC 0.01	PET 180	Sn 0.8		APP
53	Pb 0.2	Sn 0.8	PMMA 0.005	Ba0.93Sr0.07F1.05Br	PVC 0.01	PET 180	Sn 0.8		APP
54	Pb 0.2	Ta 0.5	PMMA 0.005	Ba0.93Sr0.07F1.05Br	PVC 0.01	PET 180	Sn 0.8		APP
55	Pb 0.2	W 0.2	PMMA 0.005	Ba0.93Sr0.07F1.05Br	PVC 0.01	PET 180	Sn 0.8		APP
56		Pb 0.6	PMMA 0.005	Ba0.93Sr0.07F1.05Br	PVC 0.01	PET 180	Pb 0.6		other
57		Pb 0.8	PMMA 0.005	Ba0.93Sr0.07F1.05Br	PVC 0.01	PET 180	Pb 0.8		other
58		Pb 1.0	PMMA 0.005	Ba0.93Sr0.07F1.05Br	PVC 0.01	PET 180	Pb 1.0		other
59		Pb 1.2	PMMA 0.005	Ba0.93Sr0.07F1.05Br	PVC 0.01	PET 180	Pb 1.2		other
60		Pb 1.5	PMMA 0.005	Ba0.93Sr0.07F1.05Br	PVC 0.01	PET 180	Pb 1.5		other
61		Fe 1.0	PMMA 0.005	Ba0.93Sr0.07F1.05Br	PVC 0.01	PET 180	Fe 1.0		other
62		Fe 1.5	PMMA 0.005	Ba0.93Sr0.07F1.05Br	PVC 0.01	PET 180	Fe 1.5		other
63		Cu 1.0	PMMA 0.005	Ba0.93Sr0.07F1.05Br	PVC 0.01	PET 180	Cu 1.0		other
64		Cu 1.5	PMMA 0.005	Ba0.93Sr0.07F1.05Br	PVC 0.01	PET 180	Cu 1.5		other

Figure 4.15: List of detector models.

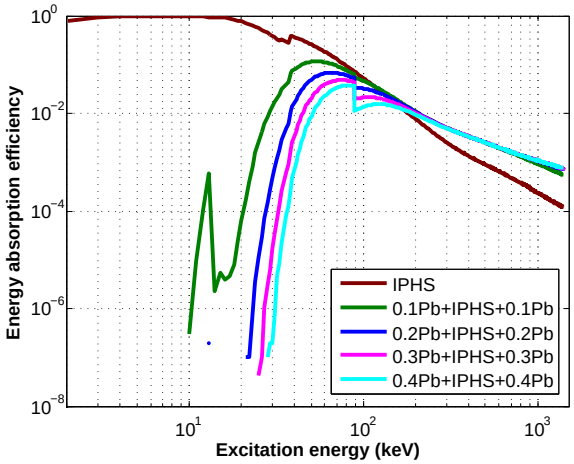

Figure 4.16: Energy absorption efficiency (EAE) versus excitation energy for the detector models of IP-HS with lead screens. With the presented screens, the intensification effects starts at around 150 keV; with the increase of screens' thickness, this starting energy slightly increases. The filtering of low energies greatly depends on the thickness of lead. For the smallest thickness, the L-line fluorescence is visible.

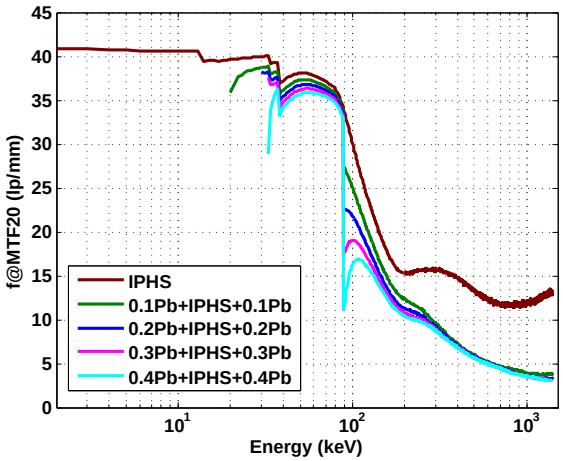

Figure 4.17: f_{MTF20} versus excitation energy for the detector models of IP-HS with lead screens. The presence of the screens causes spatial resolution loss, especially at the energies where lead's fluorescence yields.

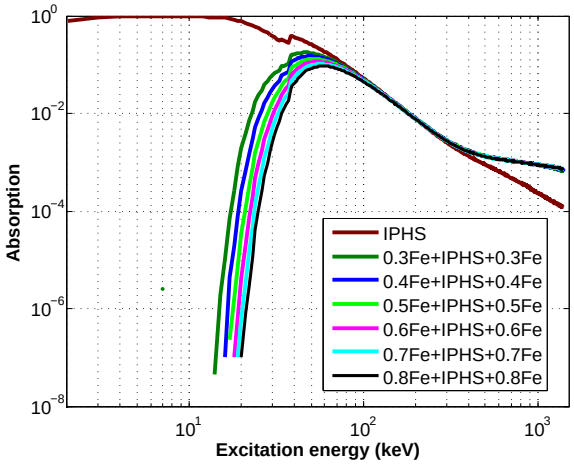

Figure 4.18: Energy absorption efficiency (EAE) versus excitation energy for the detector models of IP-HS with iron screens. The intensification starts at around 180 keV, and the starting energy increase slightly with the increase of screen thickness. The filtering of low energy depends on the thickness.

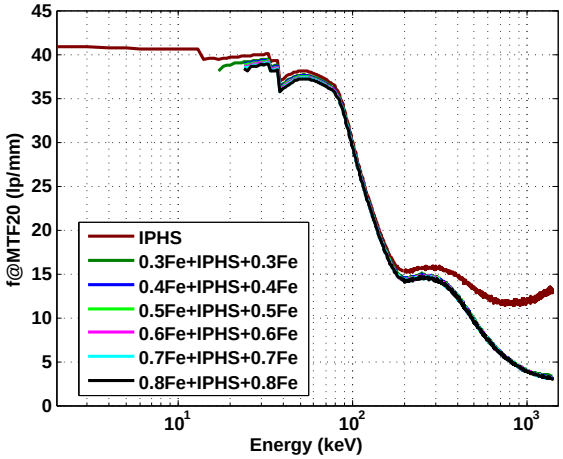

Figure 4.19: f_{MTF20} versus excitation energy for the detector models of IP-HS with iron screens. The spatial resolution is almost independent of the iron screens' thickness. At high energies, the spatial resolution is strongly degraded by the iron screens.

Chapter 5

Optical readout simulation

"Only a few find the way, some don't recognize it when they do - some... don't ever want to."

Alice in Wonderland

Contents

5.1 Introduction

The previous chapter has presented the X-ray latent image generation, while this chapter is going to focus on the digital image generation process (Figure 5.1). This process is split into two sub-steps: optical readout (laser stimulation and photo-stimulated luminescence emission), and the collection and amplification of the emitted photo-stimulated luminescence (PSL). The latter is simply modeled as a multiplicative factor without further blurring the output image.

Readout is a crucial process that affects the final image quality (e.g. efficiency, contrast and spatial resolution). Figure 5.2(a) shows the basic principle of flying spot CR readout: via a rotating mirror, the finely focused stimulating laser beam scans horizontally the imaging plate (IP); together with a continuous translation of IP, the stored information can be released line by line through the whole imaging plate. This scanning process is usually called raster scan (or raster scanning). Figure 5.2(b) shows the diagram of the raster scan of IP. The slight angle between the readout line and the scan direction is due to the simultaneous laser scanning and plate translation (AAPM Task Group 10, 2006)[1]. The value of this angle is related to the velocity in the scan and sub-scan direction, which is not accounted in our simulation work.

The imaging plate has a multiple-layered structure which basically consists of a protective layer, a photostimulable phosphor (PSP) layer (the phosphor grains are embedded in polymer binder) and a support layer. Sometimes, a reflective or a absorbing layer is added between PSP layer and support layer. Concerning the optical readout simulation, we are only interested in the PSP layer and the two layers in contact with it. The reason is that the optical photons are much less energetic comparing with X- or γ-rays, thus the effects of the 'outer layers' can be neglected. Therefore in this chapter, we simulate the light transport problem in a three-layered structure (see Figure 5.3): top layer (the layer on top of PSP layer, e.g. protective layer), PSP layer and bottom layer (the one under the PSP layer, e.g., reflective layer or support layer). The top and bottom layers are considered to be clear media where the laser light travels in a straight line; while the PSP layer is modeled as granular layer where the scattering effect is pronounced.

When we use a laser to perpendicularly strike the imaging plate (see Figure 5.3), the laser beam first passes through the top layer without changing direction or beam size, but due to the the refractive index difference of the air, the top layer and the PSP layer, multiple-reflection will take place, and the laser light partially arrives the PSP layer; then in PSP layer, the transmitted beam diffuses along its traveling path due to the absorption, reflection and scattering effects; at the interfaces top-PSP and PSP-bottom, the absorption, reflection or diffuse reflection might take place depending on the interface condition (will be discussed in section 5.2). Part of the laser photons within the PSP layer can interact with the storage centers[2] and results in the PSL. The emitted PSL also experiences the effects as the laser photon. A fraction of the emitted light can escape from the front surface of the imaging plate and be detected resulting in digital signal. According

[1] AAPM: The American Association of Physicists in Medicine is a scientific, educational, and professional organization of Medical Physicists.

[2] Storage center. The storage center is in fact the trapped electron. After the X-ray exposure, a portion of the excited electrons in the phosphor material are 'trapped' forming 'color centers' (also known as F-centers) in the crystal lattice. The distribution of the storage centers is the latent image.

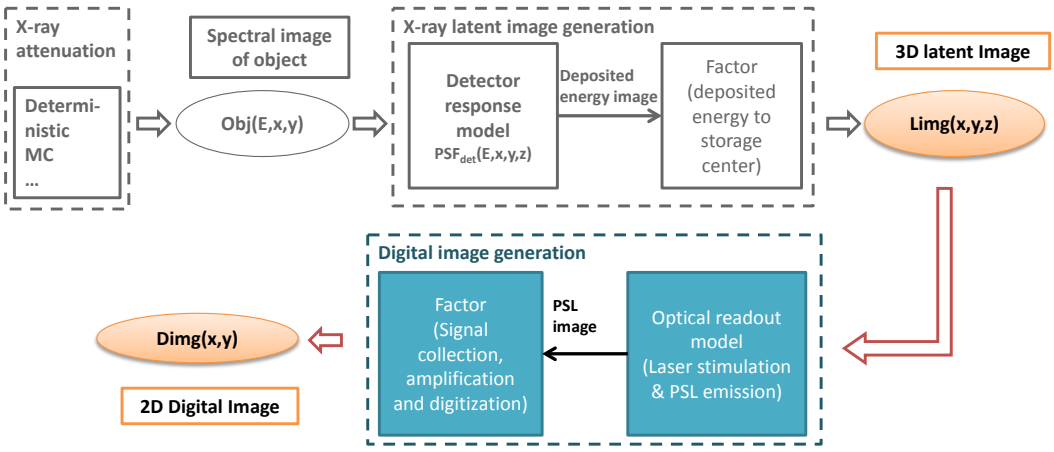

Figure 5.1: Subject of the chapter: from the 3D latent image to the 2D digital image.

to (Thoms, 1996a) and (Fasbender et al., 2003), the detected signal $Dimg(x_m, y_n)$ at (x_m, y_n)[3] can be given as:

$$Dimg(x_m, y_n) = \int_z P(z)dz \iint_{x,y} n_{sc}^{m,n-1}(x, y, z) \left\{1 - \exp\left[-\sigma \cdot I(x - x_m, y - y_n, z) \cdot t_{scan}\right]\right\} dxdy, \tag{5.1}$$

where

- $n_{sc}^{m,n-1}(x, y, z)$ (unit: cm^{-3}) is the storage center distribution map right before the laser beam arrives at (x_m, y_n),[4] and the very initial map $n_{sc}^{0}(x, y, z)$ is the latent image $Limg(x, y, z)$ (see Figure 5.1),
- $I(x, y, z)$ is the laser light intensity[5] function (unit: $\mathrm{photons} \cdot \mathrm{cm}^{-2} \cdot \mathrm{s}^{-1}$),
- $P(z)$ is the probability that a photon (emitted at z) could escape from the front surface of IP,
- σ is the optical cross section of photo-stimulation (unit: cm^2),
- t_{scan} is the dwell time of laser spot at (x_m, y_n) (unit: s).

The light intensity function can be rewritten as the product of the laser power P_{laser} (unit: $\mathrm{photons} \cdot \mathrm{s}^{-1}$) and the laser distribution function $f(x, y, z)$[6] (unit: cm^{-2}), thus Equation 5.1 can be represented as the following form

[3] (x_m, y_n) is the current laser spot location, and m and n are the pixel coordinates.

[4] The laser scanning is a destructive reading process, which is to say that the storage center map $n_{sc}^{m,n-1}(x, y, z)$ is modified by laser: it is changed while laser spot moves from one position to another. For this reason, we emphasize that $n_{sc}^{m,n-1}(x, y, z)$ here is the storage center distribution right before the laser beam arrives at (x_m, y_n).

[5] The light intensity here refers to the radiometric quantity 'irradiance', which has unit watts per meter squared. For the convenience of computation, this quantity is normalized and of unit photons per centimeter squared per second in this chapter.

[6] The $f(x, y, z)$ is the normalized laser light intensity function $I(x, y, z)$ by the laser power P_{laser}.

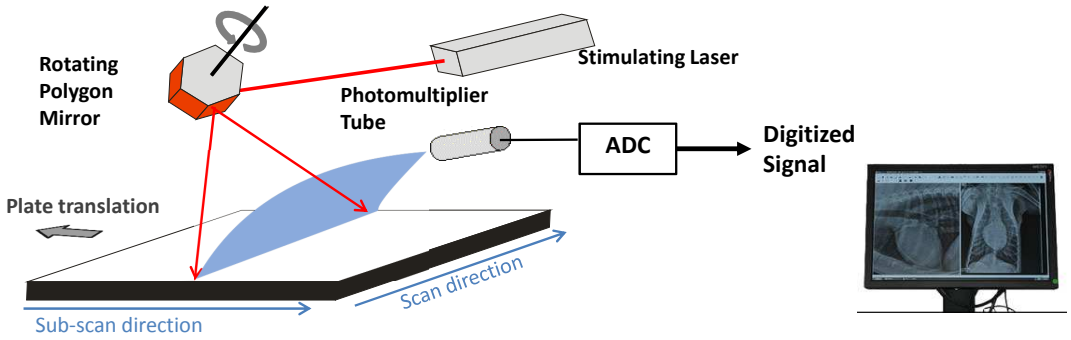

(a)

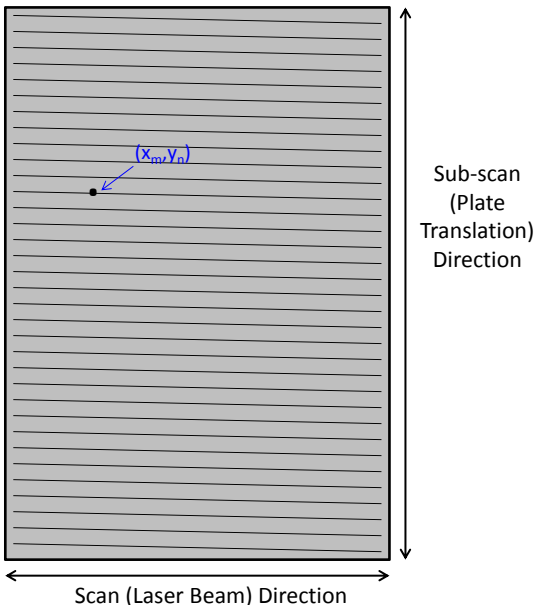

(b)

Figure 5.2: (a)Optical readout principle. (inspired from wikibook: `http://en.wikibooks.org/wiki/Basic_Physics_of_Nuclear_Medicine/Dual-Energy_Absorptiometry`) and (b) Diagram of the raster scan of IP (AAPM Task Group 10, 2006). The output image is constructed by a number of discrete pixels. The location of the pixel (m,n) is (x_m, y_n).

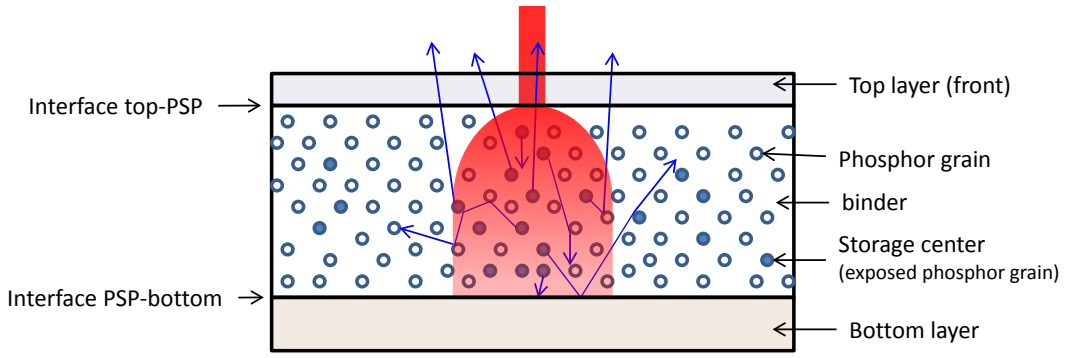

Figure 5.3: Optical effect within imaging plate. A three-layered structure is considered: a top layer, a PSP layer and a bottom layer, where the top and bottom layer are clear media, and the PSP layer is granular. The laser beam (red) strikes perpendicularly the front side of IP; it first passes through the top layer without expanding the beam size; in the PSP layer, the laser light diffuses along its traveling path; at the interfaces, top-PSP and PSP-bottom, the laser photons might be absorbed or reflected. Part of the storage centers within the red volume will be stimulated by laser photon resulting in PSL (blue arrows), which also suffers multiple scattering effect; only a fraction of the emitted PSL could reach the front surface and be detected contributing to the final image.

$$\begin{aligned} Dimg(x_m, y_n) &= \mathrm{H2}(Limg, f, scanning\ parameters) \\ &= \int_z P(z)dz \iint_{x,y} n_{sc}^{m,n-1}(x,y,z)\left\{1-\exp\left[-\sigma \cdot f(x-x_m, y-y_n, z)\cdot P_{laser}t_{scan}\right]\right\} dxdy, \end{aligned} \tag{5.2}$$

where the operator H2 models the readout process, which requires a latent image, a laser distribution function and scanning parameters (i.e. laser power and dwell time) as inputs. The output signal $Dimg(x_m, y_n)$ has a great deal with the laser distribution $f(x, y, z)$, and the scanning parameters P_{laser} and t_{scan}. We summarize the possible parameters that could affect the laser distribution and scanning in the following. These parameters are also listed in Table 5.1, some are the inputs of our simulation.

- Laser distribution $f(x, y, z)$. It depends on the optical properties of the imaging plate and the laser properties.
  - The optical properties of the phosphor layer:
    - IP thickness.
    - Grain size.
    - Packing factor.
    - Refraction index of phosphor material.
    - Refraction index of binder.
    - Dye: high absorption for laser photon, high transparency for the emitted light.
  - Boundary conditions.

    - The roughness of the interface between layers (top layer or the mentioned additional layers).
    - Additional layer for reflection or absorption purpose. Sometime reflective (or absorbing) layer is added between the phosphor layer and support layer in order to increase the detection efficiency (or spatial resolution).
  - The laser properties:
    - Laser spot size. Laser spot size determines the upper limit of the spatial resolution.
    - Spectrum. The phosphor response to the light is energy dependent.

- Scanning.
  - Laser power.
  - Scanning velocity and dwell time. A slow scanning velocity results in long dwell time
  - Pixel size (sampling frequency) determines the scanning speed and dwell time.

Table 5.1: Optical parameters of the imaging plate and the laser scanning.

Parameters			symbol	simulation input?	user-accessible?
PSP layer	thickness		d	yes	no
	grain size (diameter)*		D_{gs}	no	no
	packing factor*		$f_{packing}$	no	no
	refraction index of phosphor*		n_{PSP}	no	no
	refraction index of binder*		n_{binder}	no	no
	absorption coefficient		μ_α	yes	no
	scattering coefficient		μ_s	yes	no
	Anisotropic factor		G	yes	no
Boundary	top layer	refraction index	n_{top}	yes	no
		roughness	rough or smooth	yes	no
	bottom layer	refraction index	n_{BL}	yes	no
		roughness	rough or smooth	yes	no
Scanning	Laser power		P_{laser}	yes	yes
	scanning velocity		v_{scan}	yes	yes
	pixel size		l_{pxl}	yes	yes
	dwell time**		t_{scan}	yes	yes

* These parameters are represented by the absorption, scatter and anisotropic factors.
** The dwell time is obtained using $t_{scan} = l_{pxl}/v_{scan}$

The work of this chapter is based on Equation 5.2. In order to obtain the final output $Dimg(x_m, y_n)$, one needs first the storage center map $n_{sc}^{m,n-1}(x, y, z)$, and the very initial map before the scanning process is the 3D latent image (the $Limg(x, y, z)$ in Figure 5.1). Secondly one needs to know the laser distribution function $f(x, y, z)$ within the PSP layer; the generation of this function will be presented in the next section, where a Monte Carlo (MC) simulation tool (programmed in MATLAB) has been developed to simulate laser propagation in IP. Thirdly, the term $n_{sc}^{m,n-1}(x, y, z)\{1 - \exp[-\sigma \cdot f(x - x_m, y - y_n, z) \cdot P_{laser} t_{scan}]\}$ models the laser scanning process including the photostimulation effect via the sigma term. Finally the term $P(z)$ allows one to take into account the detection probability of an emitted photon at z, i.e. the probability that an emitted photon could escape from the top layer and thus be detected. These last two steps have been modeled with another Matlab tool which is discussed in section 5.3.

Note that as a CR system user, one cannot much change the optical property of the imaging plate, or laser property. However, the scanning parameters can be adjusted so that one can optimize the output image quality. In Section 5.3, the scanning effect associated with a discussion on the determination of the cut-off density is presented. Before concluding this chapter, some simulation examples are presented.

5.2 Laser light propagation in imaging plate

In this part, we intend to obtain the laser distribution function $f(x, y, z)$ in Equation 5.2. The Monte Carlo method has been adopted for simulating the laser light transport within the imaging plate. The reason of choosing this method is that the Monte Carlo simulation is the most accurate way to approach the realistic solution of the multiple scattering problem. In analytic methods, the final solution is based on the assumption that light is scattered isotropically or forwardly, however, for solving light scattering problem within IP, neither is suitable. Therefore, MC method is adopted.

A lot of reported Monte Carlo modeling works (Zhu and Liu, 2013; Prahl et al., 1989; Wang et al., 1995; Fasbender et al., 2003; De Mul, 2003; Atif et al., 2011) use the characteristic factors absorption coefficient, the scattering coefficient (μ_s) and the anisotropy factor (G)[7], which are experimentally measurable. By using Mie theory, the above three factors can be determined based on the grain size, the internal complex refractive index of the IP phosphor and binder. In the works of Liaparinos *et al.* (Liaparinos et al., 2006), this theory has been adopted. In this thesis, we use directly μ_α, μ_s and G, their values being either measured or obtained via Mie theory. In our case, the values have been found in the literature (Thoms, 1996a; Fasbender et al., 2003).

Our program has adopted the photon/medium interaction model commonly used in MC modeling of light transport in tissues (Zhu and Liu, 2013): absorption and scattering are the two events that a photon might undergo during its propagation in a medium, where the scattering event does not change the photon energy, but only the movement direction (see Figure 5.4). In order to improve the simulation efficiency, the statistical weight (W), namely photon packet weight, is introduced. This packet weight W represents a statistical probability. In order to understand this concept, let's consider a simulation tool where

[7]The anisotropy factor reflects the deflection angle θ distribution of the scattered photon; it is the expectation value of $cos\theta$.

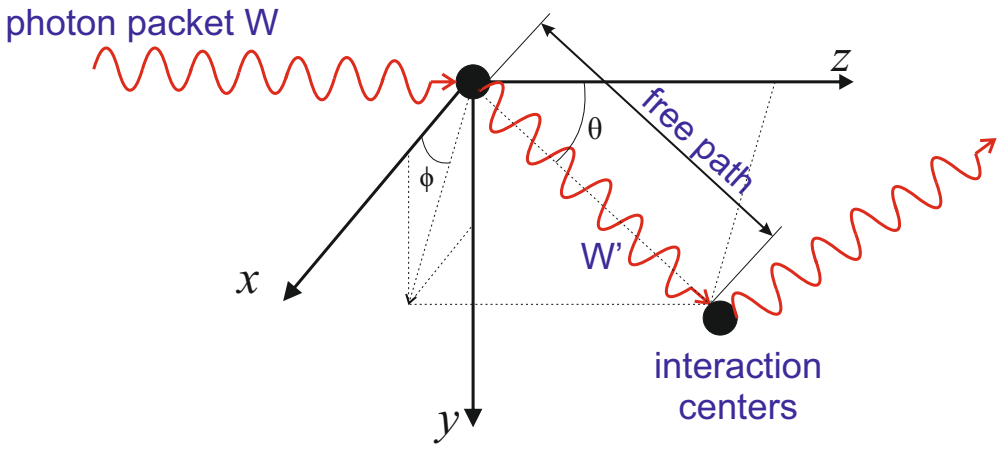

Figure 5.4: Diagram of a random walk of packets in medium. When a photon packet arrives at an interaction center, it will be partially absorbed by the interaction center, and the remaining packet W' will be scattered and continues traveling until next event.

the photons are considered individually: when a photon arrives at the interaction site, it will either be absorbed or scattered, thus a lot of photons need to be launched to obtain a statistical result. With packet weight concept, all the photons are considered as a group (or packet), and a fraction of the weight will be absorbed according to the absorption probability, and the remaining packet will continue propagating in the medium. In such a way, the simulation efficiency can be improved. The packet weight is commonly used in a number of MC codes.

There exists Monte Carlo codes such as 'MCML' (Wang et al., 1995) for simulating the light transport within multiple layered tissues, however, the output does not provide directly the laser distribution function $f(x, y, z)$, which has to be estimated based on the absorbed energy distribution. Hence we have decided to develop our own MC simulation tool for our application of laser transport problem in the imaging plate. Our simulation code has been programmed using MATLAB; it follows the steps of general Monte Carlo simulation of light propagation in turbid medium (Zhu and Liu, 2013); several treatments such as the boundary and the storage of the laser intensity function are specific for the IP simulation. The main program proceeds the following steps:

i Set the initial state of the incident photon packet, that is to assign values to the following variables: the position (x, y, z), the movement direction (u, v, w), and the photon packet weight W (see in Section 5.2.1).

ii Compute the traveling distance S (detailed in Section 5.2.2).

iii Check if the photon packet hits a boundary (detailed in Section 5.2.3).
If the packet hits a boundary: move it to the boundary; if experience an internal reflection event (see Section 5.2.4), update the movement direction (u, v, w) and packet weight W, then go to step *ii*, otherwise, go to step *vii*;

iv Move the photon to the interaction site (see in Section 5.2.5).

v Update the light intensity array $I(x, y, z)$, assign W to all array elements that the packet passes through along S; Compute the absorption at the interaction site (see Section 5.2.6), then update W and the absorption array $A(x, y, z)$.

vi Check the packet weight.
If the packet weight is greater than the threshold W_{abs}[8], compute the scattering event (see Section 5.2.7), and then go to step *ii* to compute the distance to the next event; otherwise, go to step *vii*.

vii Check if the packet is the last one. If yes, end the program; if not, go to step *i*, to launch a new photon packet.

5.2.1 Initialization

This step reads all the inputs and initializes the system accordingly. In Table 5.2, we list all the input variables needed in our Monte Carlo simulation of laser propagation in IP. The simulation is based on a Cartesian coordinate system (Figure 5.5); after reading the inputs, the code will initialize the location of each IP layer, the incident position of the photon packet (x, y, z), the movement direction (u_0, v_0, w_0) and the photon packet weight W. The variables u, v and w are respectively the projected photon movement direction along x, y and z axes. The default value of direction vector (u_0, v_0, w_0) is (0,0,1), which indicates a normal incidence. The following two subsections will detail the initialization of the incident position (x, y, z) and the packet weight W.

5.2.1.1 Initial incident point

The initial photon packet coordinates are sampled according to the input 'laser profile'. The laser profile is commonly assumed to be Gaussian, and its corresponding probability density function is given by (Fasbender et al., 2003)

$$p_{LaserProfile}(r) = \frac{r}{V_{gauss}^2} \exp\left(-\frac{r^2}{2V_{gauss}^2}\right), \tag{5.3}$$

where r is the radius, and V_{gauss}^2 is the Gaussian profile variance. The cumulative distribution function of laser profile is (Fasbender et al., 2003)

$$P_{LaserProfile}(r) = 1 - \exp\left(-\frac{r^2}{2V_{gauss}^2}\right). \tag{5.4}$$

The radius r is sampled by applying the inverse-transform method (Cashwell and Everett, 1959) to the equation 5.4:

$$r = V_{gauss}\sqrt{-2ln(1 - R_r)}, \tag{5.5}$$

[8] W_{abs}. A small value should be assigned to W_{abs} to assure a good accuracy; while in order to have a good simulation efficiency, W_{abs} should have a relative great value. In our simulation, a value smaller than the laser absorption of PSP has been assigned to W_{abs}.

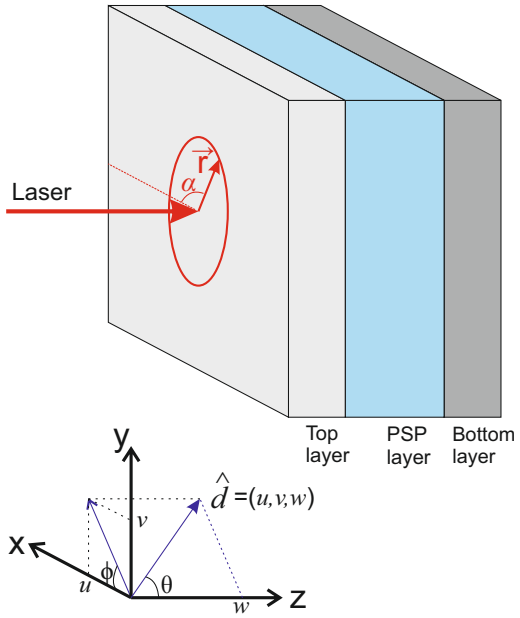

Figure 5.5: Diagram of the coordinate system. In the simulation, a Cartesian coordinate system is used to track the photon packet. Each layer of the IP is limited by its lower (e.g. the plane $x = X^T_{min}$) and upper (e.g. the plane $x = X^T_{max}$) boundaries along x, y and z axes. The laser beam incidents perpendicularly to the IP surface (XY plane). The red circle represents the laser spot: the laser beam exhibits cylindrical symmetry and has a Gaussian profile. The unit vector $\hat{d} = (u, v, w)$ represents the photon movement direction; θ and ϕ are the polar and azimuthal angles of the unit vector.

Table 5.2: Table of inputs: MC simulation of laser transport in imaging plate.

Input variable		Symbols
Laser	1. Desired packet number	N_{desire}
	2. Laser profile	$p_{LaserProfile}$
	3. Initial photon movement direction	(u_0, v_0, w_0)
	4. Initial photon packet weight	W
Top layer	5. Dimension of the top layer	$(X^T_{min}, X^T_{max}, Y^T_{min}, Y^T_{max}, Z^T_{min}, Z^T_{max})$
	6. Refractive index of the top layer	n_{top}
PSP layer	7. Dimension of the PSP layer	$(X^P_{min}, X^P_{max}, Y^P_{min}, Y^P_{max}, Z^P_{min}, Z^P_{max})$
	8. Absorption coefficient	μ_α
	9. Scattering coefficient	μ_s
	10. Anisotropic factor	G
	11. Refractive index of the binder	n_{binder}
Bottom layer	12. Dimension of the bottom layer	$(X^B_{min}, X^B_{max}, Y^B_{min}, Y^B_{max}, Z^B_{min}, Z^B_{max})$
	13. Refractive index of the bottom layer	n_{bottom}
Boundary (interface)	14. Top-PSP interface	rough or smooth
	15. PSP-bottom interface	rough or smooth
Storage	16. Pixel number in x, y and z direction.	$(Npxl_x, Npxl_y, Npxl_z)$

where R_r is a random number[9] between 0 and 1, and we can simplify this formula as

$$r = V_{gauss}\sqrt{-2ln(R_r)}. \tag{5.6}$$

As the laser beam is cylinder symmetric, the incident packet position (x, y) is obtained with

$$x = r \cdot cos(\alpha) \; and \; y = r \cdot sin(\alpha), \tag{5.7}$$

where α is the angle between $\overrightarrow{r}$ and x-axis (Figure 5.5), and is a random number between 0 and 2π. As the multiple-scattering takes place in the PSP layer, by default, the value of Z^P_{min} is assigned to z to force the photon starts the scattering history from the front surface (the one facing the laser beam) of the PSP layer. As a result, the initial value of the packet weight is the transmittance of the top layer which is calculated next.

[9]In this chapter, all the random numbers are sampled uniformly in the corresponding intervals.

5.2.1.2 Multiple reflection and packet weight

When a photon packet enters IP, owing to the refractive index mismatch of the air, the top layer and the PSP layer, the photon packet experiences multiple reflection. A part of the packet (transmitted photon) enters the PSP layer. The initial packet weight is obtained by

$$W = 1 - F_{reflectance}, \tag{5.8}$$

where $F_{reflectance}$ is the specular reflectance (Wang et al., 1995) of the top layer. The $F_{reflectance}$ is given by

$$\begin{aligned} &F_{reflectance} = a_1 + \frac{(1-a_1)^2 a_2}{1 - a_1 a_2}, \\ &with \\ &\qquad a_1 = \frac{(1-n_{top})^2}{(1+n_{top})^2} \\ &\quad and \;\; a_2 = \frac{(n_{binder} - n_{top})^2}{(n_{binder} + n_{top})^2}, \end{aligned} \tag{5.9}$$

where a_1 and a_2 are respectively the Fresnel reflectances at the front and back surfaces of top layer.

5.2.2 Sampling of the travel distance S

Figure 5.4 illustrates the random walk of a photon packet. After traveling a certain distance S, the packet interacts with the PSP; part of the packet weight is absorbed locally at the interaction center; the rest of the packet is scattered with a certain angle.

The probability, that a photon undergoes an interaction after traveling a distance S, is:

$$P(S) = 1 - \exp\left(-(\mu_\alpha + \mu_s)S\right) = 1 - \exp(-\mu_t S) \tag{5.10}$$

where P is between 0 and 1, and μ_t is the interaction coefficient (the sum of μ_α and μ_S). To compute the traveling distance, the inverse-transform method (Cashwell and Everett, 1959) is used:

$$S = -\frac{1}{\mu_t} ln(1 - R_s) \tag{5.11}$$

where R_s is a random number between 0 and 1, and thus the equation 5.11 could be simplified as:

$$S = -\frac{1}{\mu_t} ln(R_s) \tag{5.12}$$

5.2.3 Distance to the boundaries

In this step, the distances between the current photon position and all the boundaries (along its movement direction) are computed (see Figure 5.6). Let's consider a photon packet which is scattered at point C_1 and with a new movement direction (u, v, w). To calculate its travel path lengths to the boundaries, we suppose it propagates freely in its new direction; then it will crosses one or more boundaries. As the example shows in

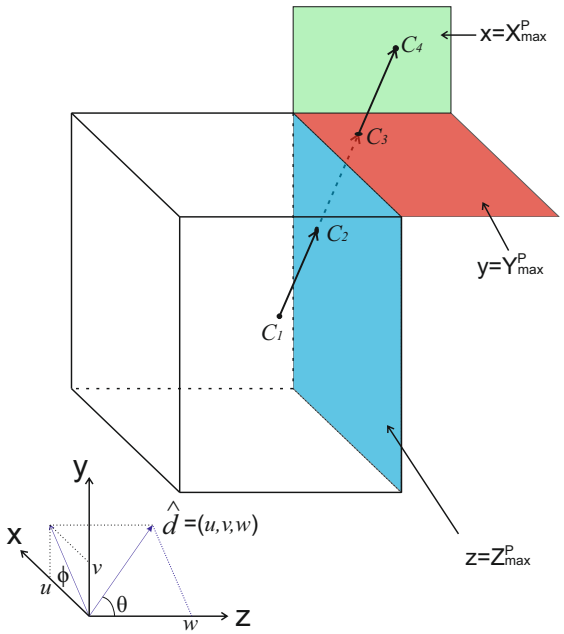

Figure 5.6: Distance to boundary. The transparent box represents the PSP layer. A photon packet is scattered at point C_1 with its new movement direction. Suppose this packet travels freely in this direction, then it will cross one or more boundaries. In the example shown here: it crosses first the plane $z = Z^P_{max}$ at point C_2, and then it crosses $y = Y^P_{max}$ at C_3, and $x = X^P_{max}$ at C_4.

Figure 5.6, the lengths of C_1C_2, C_1C_3 and C_1C_4 are the distances to the boundaries in z, y and x directions that we want to calculate. We name the corresponding lengths d_z, d_y and d_x in the following.

The distance to the boundaries along z direction is given by the following equation:

$$d_z = C_1C_2 = \begin{cases} (Z^P_{max} - z)/w, & \text{if } w \geq 0. \\ (Z^P_{min} - z)/w, & \text{if } w < 0. \end{cases} \tag{5.13}$$

where Z^P_{min} and Z^P_{max} are respectively the lower and upper limits along z direction of the PSP layer.
The distances to the other boundaries are:

$$d_x = C_1C_4 = \begin{cases} \sqrt{(X^P_{max} - x)^2 \cdot [1 + (v/u)^2]}/\sqrt{1 - w^2}, & \text{if } u \geq 0; \\ \sqrt{(X^P_{min} - x)^2 \cdot [1 + (v/u)^2]}/\sqrt{1 - w^2}, & \text{if } u < 0; \end{cases} \tag{5.14}$$

$$d_y = C_1C_3 = \begin{cases} \sqrt{(Y^P_{max} - x)^2 \cdot [1 + (u/v)^2]}/\sqrt{1 - w^2}, & \text{if } v \geq 0; \\ \sqrt{(Y^P_{min} - x)^2 \cdot [1 + (u/v)^2]}/\sqrt{1 - w^2}, & \text{if } v < 0; \end{cases} \tag{5.15}$$

where X^P_{min} and X^P_{max} are respectively the lower and upper limits along x direction of the PSP layer, and Y^P_{min} and Y^P_{max} along y direction.

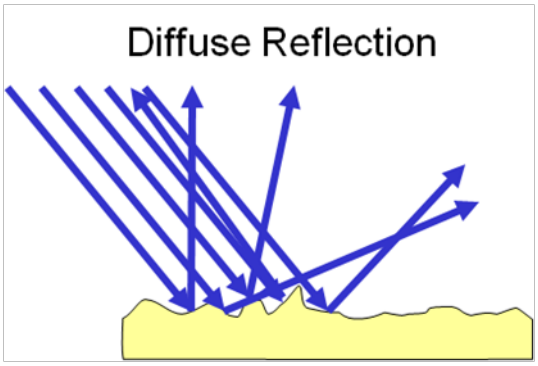

Figure 5.7: Diffuse reflection. When a light beam arrives at a rough surface, it will be deflected in many angles.

If any of the above distances is smaller than the traveling length S, the photon packet will hit a boundary, and we assign the value of the corresponding distance to S. For example, if the photon packet hits the surface $z = Z^P_{max}$, then $S = d_z$.

5.2.4 Internal reflection

The following events might take place when the photon packet hits a boundary.

- Absorption. If the photon packet hits the boundary between the current layer and an absorption layer, there is no internal reflection. If the second layer is not an absorption layer, the internal reflection will take place.
- Internal reflection.
  - Specular reflection. If the photon packet hits a smooth interface, a fraction of the packet might be reflected.
  - Diffuse reflection (see Figure 5.7). Diffuse reflection takes place when a light beam strikes a rough surface. The light is deflected in many angles.

5.2.4.1 Specular reflection: Fresnel Equations

Specular reflection happens when the surface of a boundary interface is smooth.

Suppose a light beam travels from medium 1 (of a reflective index n_1) to medium 2 (of a reflective index n_2) with an incident angle θ_1, due to the reflective index difference, part of the beam is reflected with a reflected angle equals to incident angle; the other part of the beam is refracted with an angle θ_2. We use Fresnel equations to calculate the reflectance (Born and Wolf, 2002). The reflectance for s-polarized light (perpendicular to the plane of incidence) is

$$R_s = \left| \frac{n_1 cos\theta_1 - n_2 cos\theta_2}{n_1 cos\theta_1 + n_2 cos\theta_2} \right|^2 \tag{5.16}$$

The reflectance for p-polarized light (parallel to the plane of incidence) is

$$R_p = \left| \frac{n_1 cos\theta_2 - n_2 cos\theta_1}{n_1 cos\theta_2 + n_2 cos\theta_1} \right|^2 \tag{5.17}$$

In our case, the photon packet experiences multiple scattering before arriving a boundary, therefore, it is considered unpolarized, and we have

$$R = \frac{R_s + R_p}{2} \tag{5.18}$$

Then the photon weight is updated by

$$W' = R \cdot W \tag{5.19}$$

and the new movement direction is

$$(u', v', w') = (u, v, -w) \tag{5.20}$$

A special case of the specular reflection is the total internal reflection. It happens when a light beam strikes a higher-to-lower-refractive-index interface ($n_1 > n_2$) with an incident angle above the critical angle (i.e. $\theta_c = \arcsin\left(\frac{n_2}{n_1}\right)$). In this case, we have $R_s = R_p = 1$, thus the incident beam is 100% reflected.

5.2.4.2 Diffuse reflection

The diffuse reflection happens when light hits a rough surface. The incident beam is reflected in many angles (see Figure 5.7). The deflection angle is generated using the following formula:

$$\phi = 2\pi R_\phi \; and \; \theta = \pi R_\theta / 2, \tag{5.21}$$

where R_ϕ and R_θ are two independent random numbers between 0 and 1. Then the new movement direction can be calculated by (Cashwell and Everett, 1959; Wang et al., 1995)

$$\begin{aligned} u' &= sin\theta \left(uwcos\phi - vsin\phi\right) / \sqrt{1 - w^2} + ucos\theta \\ v' &= sin\theta \left(vwcos\phi + usin\phi\right) / \sqrt{1 - w^2} + vcos\theta \\ w' &= -sin\theta cos\phi \sqrt{1 - w^2} + wcos\theta \end{aligned} \tag{5.22}$$

5.2.5 Move photon to the interaction site

The photon packet is moved by a distance S along its movement direction (u, v, w). New values are assigned to the packet coordinates (x, y, z):

$$\begin{aligned} x &\leftarrow x \; + \; S \cdot u; \\ y &\leftarrow y \; + \; S \cdot v; \\ z &\leftarrow z \; + \; S \cdot w. \end{aligned} \tag{5.23}$$

Meanwhile the current packet weight W is also accumulated in each voxel of $I(x, y, z)$ that it passes through.

5.2.6 Absorption at the interaction site

Once the traveling distance S is determined, the packet will be moved to the interaction site, and a fraction of the photon weight, μ_α/μ_t, will be deposited locally. The photon packet weight becomes:

$$W' = W - \frac{\mu_\alpha}{\mu_t} W. \tag{5.24}$$

The photon weight $\frac{\mu_\alpha}{\mu_t} W$ is accumulated in the voxel of A(x,y,z).

5.2.7 Scattering event

The packet is deflected from the interaction site by the angles θ and ϕ in spherical coordinates. The azimuth angle ϕ, which is uniformly distributed over 0 to 2π, is sampled:

$$\phi = 2\pi R_\phi, \tag{5.25}$$

where R_ϕ is a random number between 0 and 1. The angle θ, on the other hand, does not always follow a uniform distribution. The Henyey-Green function is the most popularly adopted to describe the deflection angle distribution (Zhu and Liu, 2013)

$$HG(\theta) = \frac{1 - G^2}{4\pi(1 + G^2 - 2Gcos\theta)^{3/2}} \tag{5.26}$$

where G is the anisotropy factor which has a value between -1 and 1. $G = -1$ indicates backward scattering; $G = 0$ indicates isotropic scattering and $G = 1$ indicates forward-directed scattering. From equation 5.26, the probability density function of θ can be obtained as

$$P(\theta) = \frac{1 - G^2}{2G} \left[\frac{1}{\sqrt{1 + G^2 - 2Gcos\theta}} - \frac{1}{G + 1} \right] \tag{5.27}$$

By applying the inverse-transform method to equation 5.27, the formula of deflection angle sampling is expressed as

$$\theta = arccos\left(\frac{1 + G^2 - \left[(1 - G^2)/(1 - G + 2R_\theta)\right]}{2G} \right) \tag{5.28}$$

where R_θ is a random number between 0 and 1. The new movement direction is obtained using Equation 5.22 and then assigned to (u, v, w).

5.2.8 Summary of the Monte Carlo simulation procedure

Until here, all the treatments of the photon-IP interactions in our code have been presented. We summarize the simulation process in the flowchart illustrated in Figure 5.8. The step i to step vii will be repeated until the last packet is completely absorbed by the system or escapes from the system; then the program ends and outputs the photon intensity array $I(x, y, z)$ and the absorption array $A(x, y, z)$. For the use later in the scanning

process, the intensity array $I(x, y, z)$ is normalized by the total launched packet number N_{desire}, and we have the photon distribution function $f(x, y, z)$.[10]

5.2.9 Data fitting and examples

With the simulation procedure described above, we have studied the effect of different optical parameters on the laser distribution $f(x, y, z)$. Curve fitting has been applied to the raw output of the simulation, so that the image noise could be reduced and storage space can be saved.

5.2.9.1 Data fitting

The main purpose of employing data fitting is for overcoming the sampling problem. In order to numerically implement Eq. 5.2, the latent image $Limg(x, y, z)$ and the IP response to laser light $f(x, y, z)$ should be of the same sampling rate. Therefore, in order to adapt the sampling rate (sampling step) of the latent image, one needs to either interpolate the obtained laser distribution function $f(x, y, z)$ or fit it with appropriate fitting functions. Moreover the storage of the fitting function is computationally smaller than the storage of the raw array.

After comparing different fitting functions, the **Lorentz-Gaussian Cross Product** (Eq. 5.29) has been selected as good fitting function for the laser distribution profiles. Figure 5.9 shows the simulation result of light distribution in a high sensitivity imaging plate phosphor layer. The raw image was sampled with a spatial resolution of 1 $\times$ 1 $\times$ 1.5 μm^3, and the radial averaging (Equation 4.3) has also been applied to the function $f(x, y, z)$ before data fitting. In Figure 5.10, we plot the fitting curves at several depths (z): 0, 50, 100 and 150 μm (with $z = 0$ μm the front side of the phosphor layer and $z = 150$ μm the rear side).

$$
\begin{aligned}
y = & \frac{a_0}{1 + a_3 \left(\frac{x-a_1}{a_2}\right)^2 \exp\left[(1-a_3)\frac{1}{2}\left(\frac{x-a_1}{a_2}\right)^2\right]} \\
with\ a_0 &= amplitude \\
a_1 &= center \\
a_2 &= width(>0) \\
a_3 &= shape(0 \leq a_3 \leq 1)
\end{aligned}
\tag{5.29}
$$

The correlation between the raw profile and the fitting curve is estimated using the

[10] Monte Carlo is a probabilistic method, and thus its results contains statistical noise, which can be reduced by increasing the packet number N_{desire}. The value of N_{desire} here also reflects the laser power. As we want the laser power to be an independent input parameter of our optical readout model H2, the intensity array is normalized by N_{desire}.

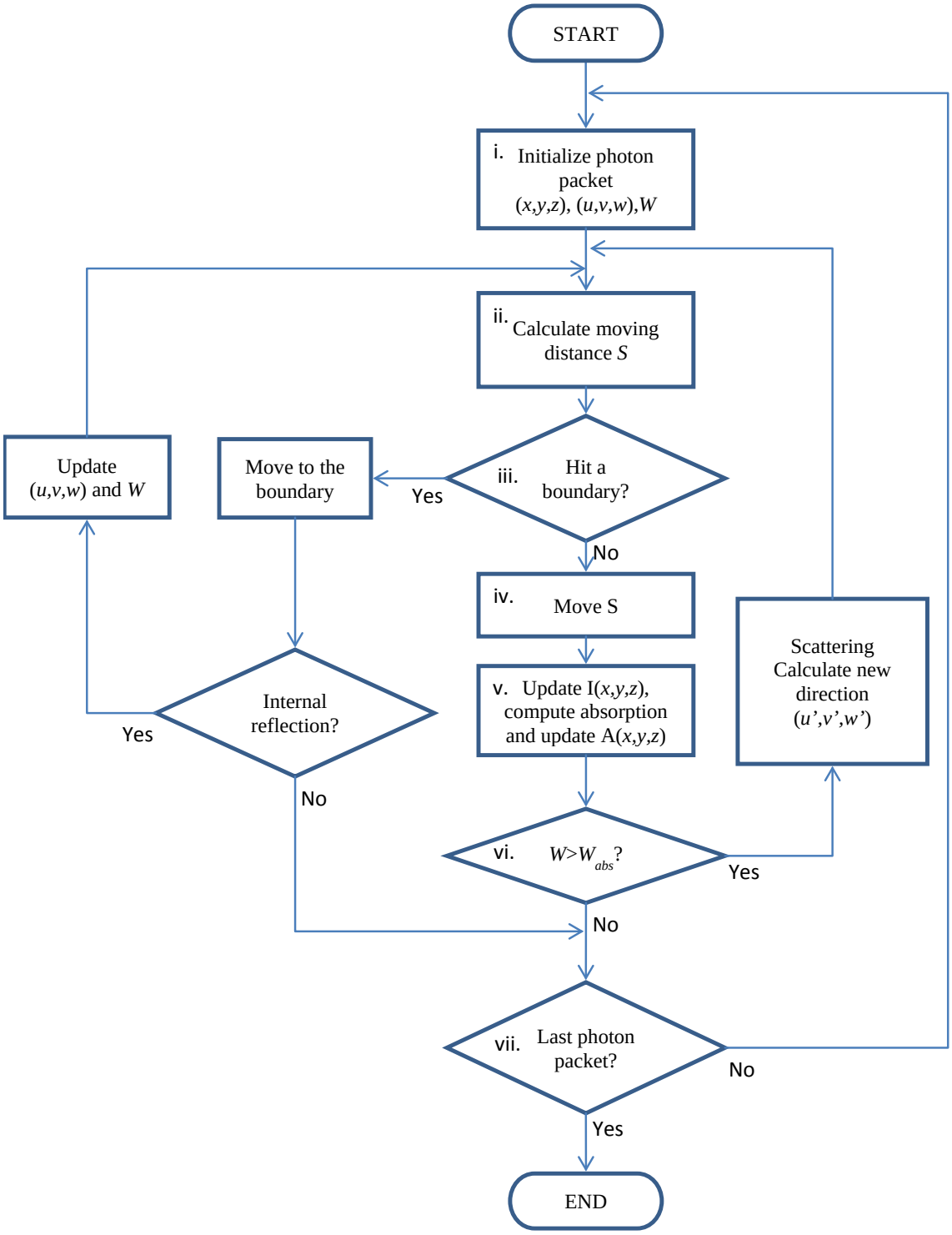

Figure 5.8: Flowchart of the main Monte Carlo program for simulating photon transport within imaging plate.

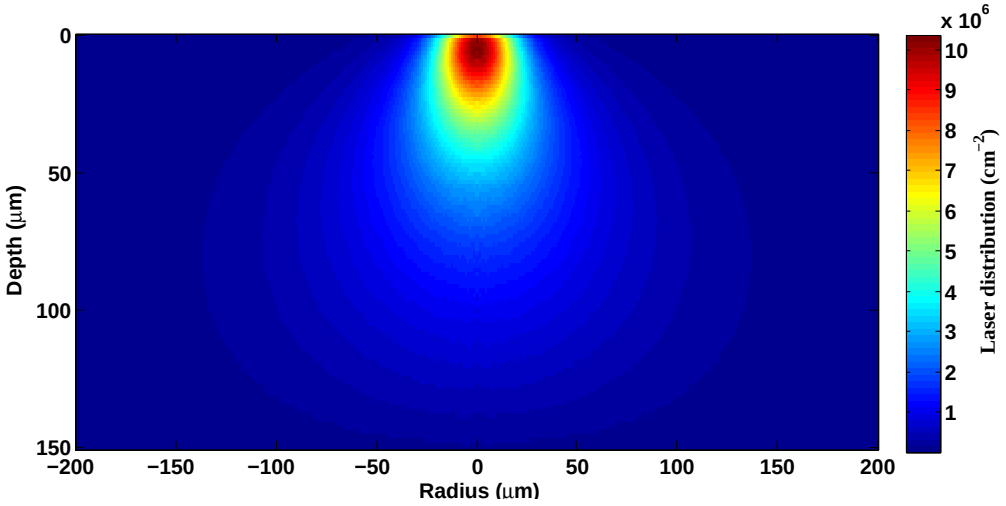

Figure 5.9: Laser distribution function $f(x, y, z)$ in a high sensitivity imaging plate phosphor layer.(Not yet normalized)

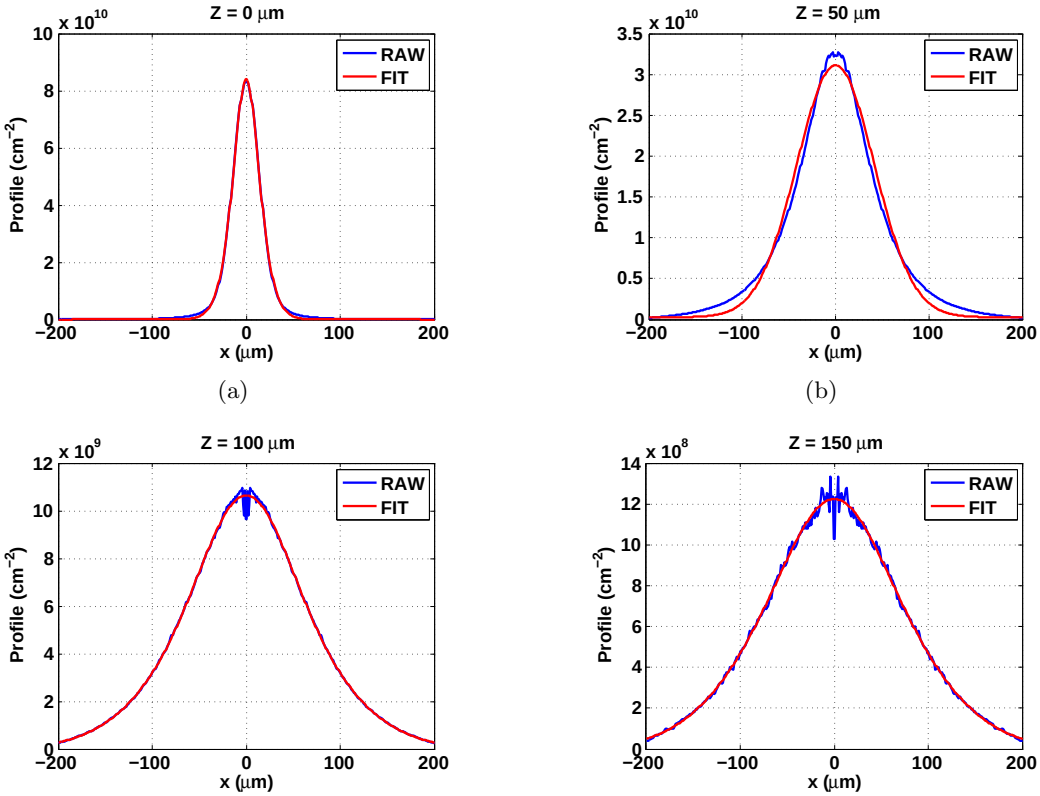

Figure 5.10: Fitting curves at: (a) $Z = 0$ μm, (b) $Z = 50$ μm, (c) $Z = 100$ μm and (d) $Z = 150$ μm.

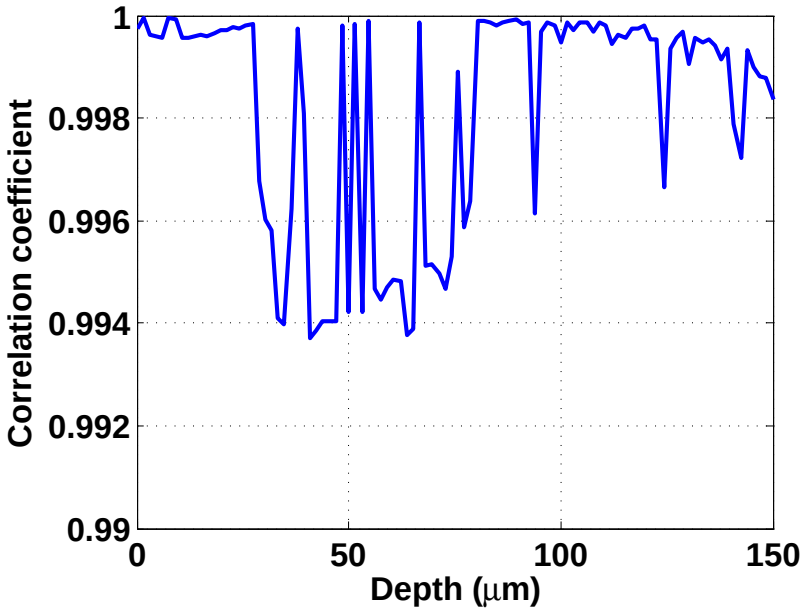

Figure 5.11: Correlation coefficient.

correlation coefficient $R_{Pearson}$ (also known as Pearson's coefficient)

$$\begin{aligned} R_{Pearson} &= \sqrt{1 - \frac{SS_{res}}{SS_{tot}}} \\ with \\ SS_{tot} &= \sum_i (y_i - \overline{y})^2, \\ SS_{res} &= \sum_i (y_i - f_i)^2. \end{aligned} \tag{5.30}$$

The value of $R_{Pearson} = 1$ signifies that the fitting curve overlaps perfectly the original profile, while 0 indicates that there is no correlation. Figure 5.11 plots the correlation coefficient versus IP depth. We see that all the $R_{Pearson}$ values are very close to 1, meaning that the chosen function fits very well.

In Figure 5.12, we plot the FWHM (full width at half maximum) versus IP depth z. Along the light propagation, the laser spot size increases. The light profile has been fitted in XY plane at each z.

5.2.9.2 Study on the effect of different parameters

In order to compare the effects of different parameters (i.e. absorption coefficient, scattering coefficient, anisotropic factor and thickness), we have studied the following cases:

- Case 1: $\mu_\alpha = 4 \times 10^{-5}$ μm^{-1}, $\mu_s = 1/7$ μm^{-1}, $G = 0.37$, $d = 200$ μm;
- Case 2: $\mu_\alpha = 4 \times 10^{-3}$ μm^{-1}, $\mu_s = 1/7$ μm^{-1}, $G = 0.37$, $d = 200$ μm;

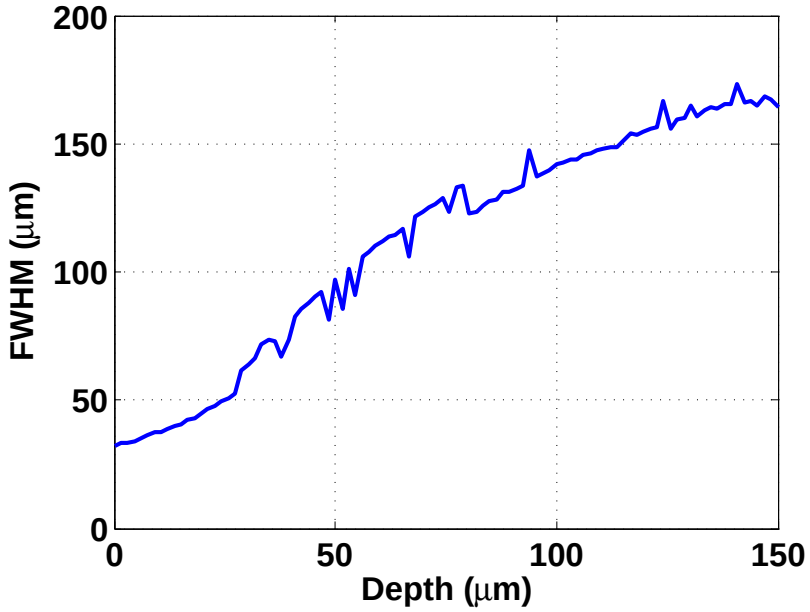

Figure 5.12: FWHM versus z.

- Case 3: $\mu_\alpha = 4 \times 10^{-5}$ μm^{-1}, $\mu_s = 1/0.07$ μm^{-1};$G = 0.37$;$d = 200$ μm;
- Case 4: $\mu_\alpha = 4 \times 10^{-5}$ μm^{-1}, $\mu_s = 1/7$ μm^{-1}, $G = 0.9$, $d = 200$ μm;
- Case 5: $\mu_\alpha = 4 \times 10^{-5}$ μm^{-1}, $\mu_s = 1/7$ μm^{-1}, $G = 0.37$, $d = 50$ μm.

Case 1 is considered as a reference case, for which the parameter values are found in the work (Fasbender et al., 2003). In the cases 2-5, we have changed one single parameter of the reference case, and keep the other parameters identical. The corresponding simulation results are illustrated in Figure 5.13. All the images have been normalized to the same gray level for the convenience of comparing the scattering region. In the following we are going to compare each case with the reference.

- Case 1 VS. Case 2 (Figure 5.13(a) VS. Figure 5.13(b)). In Case 2, we have increased the absorption coefficient by 100 times (from 4×10^{-5} μm^{-1} to 4×10^{-3} μm^{-1}), and the scattering region becomes smaller. The reason is that with higher absorption coefficient, the travel length of the laser photon becomes smaller, and the laser photons are limited within a smaller region. The same conclusion has been drawn in (Fasbender et al., 2003). Figure 5.14 shows their simulation results: the left image corresponds to our case 1 and the right the case 2.[11]
- Case 1 VS. Case 3 (Figure 5.13(a) VS. Figure 5.13(c)). In Case 3, the scattering coefficient has been increased by 100 times (from 0.143 μm^{-1} to 14.3 μm^{-1}). It shows that a high scattering coefficient results in a small scattering region because

[11] Our results are not exactly identical to Fasbender's results, because their simulation parameters has not been all detailed in their paper such as the anitropy factor and the treatment of the boundaries; but still same effect can be observed when changing the absorption coefficient.

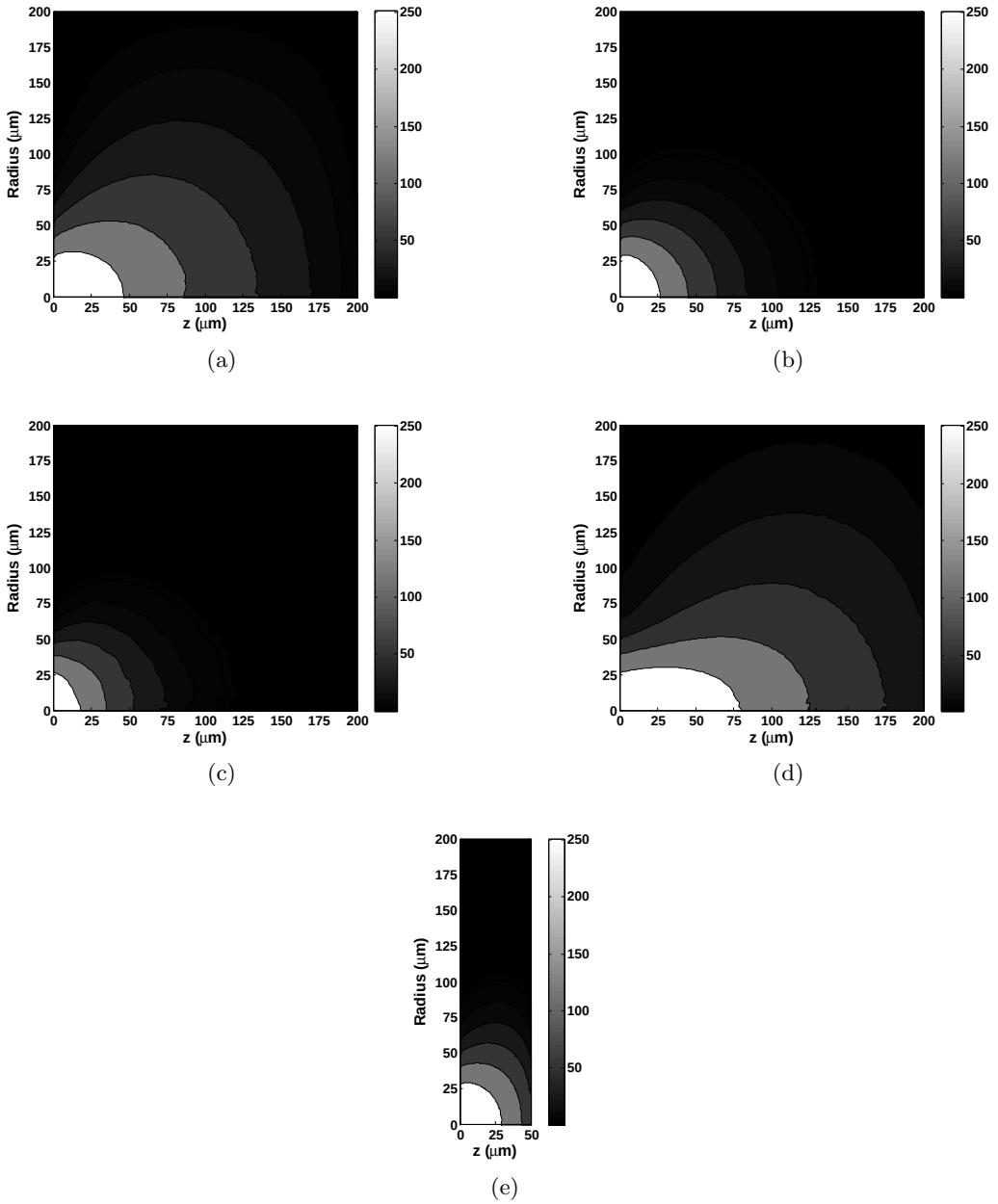

Figure 5.13: Comparison of the effects of different parameters: (a) Case 1: reference; (b) Case 2: high absorption coefficient; (c) Case 3: high scattering coefficient; (d) Case 4: high forward scattering; and (e) Case 5: thin PSP layer.

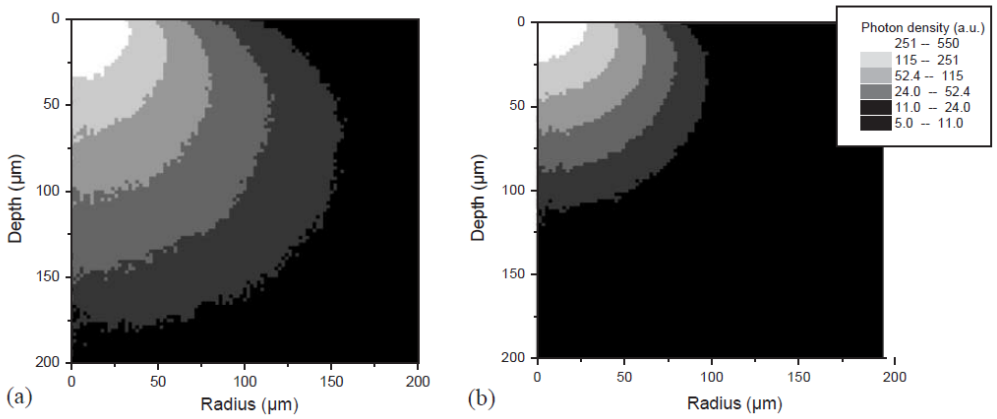

Figure 5.14: Simulated scattering profiles of the laser photons when varying the optical absorption coefficient. (a) 0.4 cm^{-1} and (b) 40 cm^{-1} (Fasbender et al., 2003).

multiple scattering concentrates the photons in a small region. This effect is very similar than changing the absorption coefficient. As the scattering coefficient in these examples is much greater than the absorption coefficient, by increasing it 100 times, the scattering coefficient has a more significant influence; the laser beam is limited to the region closer to the front surface.

- Case 1 VS. Case 4 (Figure 5.13(a) VS. Figure 5.13(d)). In Case 4, the anisotropic factor G has been increased from 0.37 to 0.9. The value 0 indicates that the laser photon is scattered isotropically; 1 indicates that the photons are deflected forwardly; and -1 means the photons are deflected backwardly. While increasing G, the photons can propagate more forwardly, therefore they can penetrate deeper in the material.

- Case 1 VS. Case 5 (Figure 5.13(a) VS. Figure 5.13(e)). Comparing Case 1 and Case 5, we find that a small thickness leads a small scattering region. While we increase the IP thickness, the extra thickness plays a roles of a reflector and results in a larger scattering area.

Similar comparison can also be found in the work of Thoms: the laser beam spreading is increased if the scattering length (inverse of the scattering coefficient, μ_s) and thickness are increased; but it is reduced if the absorption coefficient is increased (Thoms, 1996a).

As another illustration, we then show the laser distribution profile along radius and depth of different cases (see Figure 5.15)

- Profile along radius (Figure 5.15(a)). The global profile along radius is obtained by summing the profiles in Figure 5.13 over z; then each global profile is normalized by its maximum. We see that the profiles width becomes smaller while decreasing the PSP thickness or increasing of μ_α, μ_s and G.

- Profile along depth z (Figure 5.15(b)). The global profile along depth is obtained by summing the profiles in Figure 5.13 over radius; then each global profile is normalized by its maximum. With great absorption or scattering coefficient, the profiles decrease

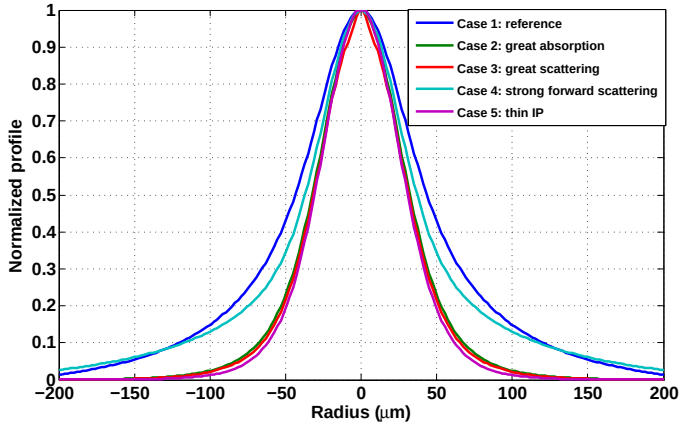

(a)

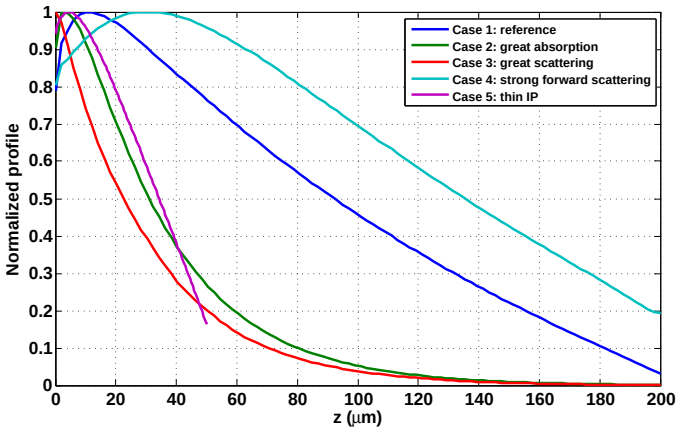

(b)

Figure 5.15: Comparison of laser light distribution along radius and depth z. (a) The normalized global profiles along radius: the global profiles along radius are obtained by summing the profiles in Figure 5.13 over z-axis, and then normalized by their maximums. (b) The normalized profiles along z: the global profiles along z are obtained by summing the profiles in Figure 5.13 over radius, and then normalized by their maximums.

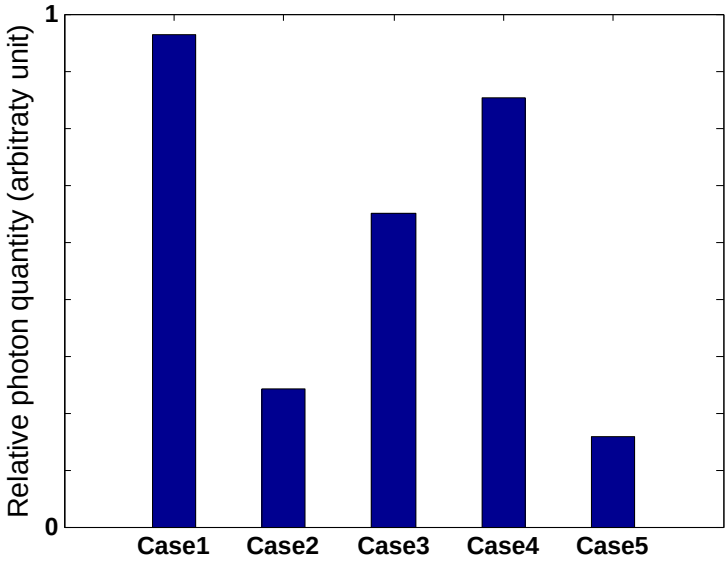

Figure 5.16: Relative photon quantity within different IP configurations. The photon quantity is the total photon number within the PSP volume. A great photon quantity means a great chance to interact with storage center and thus a good reading efficiency.

fast in z-direction. A small fraction of the laser can arrive the rear side. With a greater G (close to 1), more laser photons reach the rear side. The medium with a G close to 1 scatters the photon forwardly, namely the laser is more penetrating in such a medium and more storage centers close to the rear side can be released.

Overall the PSP with G close to 1 can maintain the laser profile width with respect to the reference, so that a good sharpness is assured; meanwhile, as the laser is scattered forwardly, more photons can reach the depth and resulting in a good reading efficiency. From the above comparison we see that a material of great μ_α, μ_s and G can maintain a narrow laser profile in order to assure a good sharpness.

We have also calculated the photon quantity within the PSP volume for the five cases, and the relative photon quantities are shown in Figure 5.16. Increasing the absorption, scattering and anisotropy factor causes a photon quantity reduction; hence less laser photons interact with storage centers and therefore lower reading efficiency. In Case 5, the reduction of the PSP layer thickness also results in a poor efficiency. Here we see that we loose sharpness when we gain reading efficiency and vice versa. These are two conflicting quality factors; a trade-off should be made during the fabrication.

In the above discussion, we have talked about the influence of the characteristic factors used in the simulation. With Mie theory we can see how intrinsic parameters of the IP materials affect the μ_α, μ_s and G. The absorption depends on the chemical compounds; while the scattering depends on the grain/binder refractive index difference, the grain size and shapes (Martelli et al., 2010). There are two special cases, Rayleigh scattering and large particle scattering. Rayleigh scattering happens when the particle size is much smaller than the photon wavelength. In this case, we can assume an isotropic scattering,

i.e. $G \approx 0$; the scattering coefficient depends on the size D_{gs} and the grain volume density[12] Γ of the grain, i.e. $\mu_s \propto \Gamma \cdot D_{gs}^6$ (Hahn, 2006; Martelli et al., 2010).

For large particle scattering, the particle size is much larger than the photon wavelength. In this case, the scattering coefficient depends less on the particle size, $\mu_s \propto \Gamma \cdot D_{gs}$; greater grain size leads a more forward scattering, i.e. greater G (Hahn, 2006; Martelli et al., 2010; Bass et al., 2009).

As for the BaFBr PSP powder, the grain size (~ 5 μm) is neither much smaller nor much greater than the laser wavelength (~ 0.6 μm), thus the scattering is neither isotropic nor forward-direct. This is the reason why we did not choose an analytic method. The change of the grain size or the material compound can lead to an optical performance that we want, but meanwhile, the IP's X- or γ- ray response is also changed, moreover, one cannot assure a good photostimulability of the IP. The IP material engineering is very complicated. There are so many questions that need to be taken into consideration. Is the dose response of the IP to the X- or γ rays good? Is its optical performance good? Is it photostimulable? If yes, is it stable? Does its spectrum of photostimulation match the common solid state laser? Does its emission spectrum match the optical detection device? Is it nontoxic? Is it expensive? At the user-end, these optical parameters are not accessible. It lefts only the scanning parameters to adjust in order to achieve a better efficiency or sharpness.

5.3 Laser scanning effect

The simulation of the optical scanning effect is mainly based on Equation 5.2 $Dimg(x_m, y_n) = \int_z P(z)dz \iint_{x,y} n_{sc}^{m,n-1}(x, y, z) \{1 - \exp[-\sigma \cdot f(x - x_m, y - y_n, z) \cdot P_{laser} t_{scan}]\} dxdy$. Another MATLAB code has been programmed to take into account the scanning parameters and output the final image. In the next we will explain how we get and model the Equation 5.2: starting from the PSL emission, to the emission and detection of PSL. The storage center map is modified by the laser, this effect is also taken into account by our code, and will be discussed in section 5.3.3.

5.3.1 Photostimulation

The PSL generation rate depends on the laser photon intensity $I(x, y, z)$ (unit: photons/cm^2/s), the laser spot dwell time t_{scan} (unit: s) and the optical cross section for photostimulation σ (unit: cm^2). The generation rate is given by (Thoms, 1996a):

$$\begin{aligned} \frac{dPSL^{m,n}(x, y, z)}{dt} &= n_{sc}^{m,n}(x, y, z) \cdot \sigma \cdot I(x - x_m, y - y_n, z) \\ &= n_{sc}^{m,n}(x, y, z) \cdot \sigma \cdot f(x - x_m, y - y_n, z) \cdot P_{laser}, \end{aligned} \tag{5.31}$$

where $n_{sc}(x, y, z)$ is the storage center density function, and (x_m, y_n) is the position coordinate of laser spot. This generation rate is also the decreasing rate of the storage center[13],

[12] The grain volume density is the number of grain per unit volume.

[13] One stimulated center yields one PSL photon

then we have

$$-\frac{dn_{sc}^{m,n}(x,y,z)}{dt} = n_{sc}^{m,n}(x,y,z)\cdot\sigma\cdot f(x-x_m, y-y_n, z)\cdot P_{laser}. \tag{5.32}$$

Thus the residual storage center density after scanning t_{scan} is

$$n_{sc}^{m,n}(x,y,z) = n_{sc}^{m,n-1}(x,y,z)\,\exp\left[-\sigma\cdot f(x-x_m, y-y_n, z)\cdot P_{laser}t_{scan}\right], \tag{5.33}$$

where $n_{sc}^{m,n-1}(x,y,z)$ is the storage center density before laser spot arrives at (x_m, y_n). We see that the storage center distribution is modified while the laser spot passes by. The very initial storage center density (unit: cm^{-3}) before the scanning process is the output of the previous step (explained in Chapter 4) $Limg(x,y,z)$.
It is assumed that one released storage center yields one PSL photon, and thus the PSL emission is given by

$$\begin{aligned} PSL^{m,n}(x,y,z) &= n_{sc}^{m,n-1}(x,y,z) - n_{sc}^{m,n}(x,y,z) \\ &= n_{sc}^{m,n-1}(x,y,z)\left\{1-\exp\left[-\sigma f(x-x_m, y-y_n, z)\cdot P_{laser}t_{scan}\right]\right\}. \end{aligned} \tag{5.34}$$

5.3.2 Detection of PSL

Like the laser light, the PSL also experiences multiple-scattering within IP. For a flying spot type IP scanner, knowing the distribution of the emitted light is not of much interest, because the emitted light is collected at the front surface by the collector (optical fiber or waveguide). Therefore, instead of simulating the emitted light distribution, a detection probability P(z) is used.

Assuming that a photon is emitted at z, the probability density of this photon moves in direction (θ, ϕ) is:

$$p(\theta,\phi,z) = \frac{1}{4\pi} \tag{5.35}$$

The probability of this photon being detected at the front surface is given by

$$\begin{aligned} P(z) &= \frac{1}{4\pi}\int_0^{2\pi} d\phi \int_0^{\frac{\pi}{2}} \exp\left(-\mu_t\cdot\frac{z}{\cos\theta}\right)\sin\theta d\theta \\ &= \frac{1}{2}\int_0^{\frac{\pi}{2}} \exp\left(-\mu_t\cdot\frac{z}{cos\theta}\right)\sin\theta d\theta. \end{aligned} \tag{5.36}$$

The integral $\int_0^{\frac{\pi}{2}} \exp\left(-\mu_t\cdot\frac{z}{cos\theta}\right)\sin\theta d\theta$ is modeled as a function $g_{esp}(z)$

$$g_{esp}(z) = A_1\,\exp\left(-\mu_t\cdot z/A_2\right) + A_3, \tag{5.37}$$

where the coefficients A_1, A_2 and A_3 are obtained using a numerical method (see Figure 5.17). We finally have

$$P(z) = \frac{1}{2}g_{esp}(z). \tag{5.38}$$

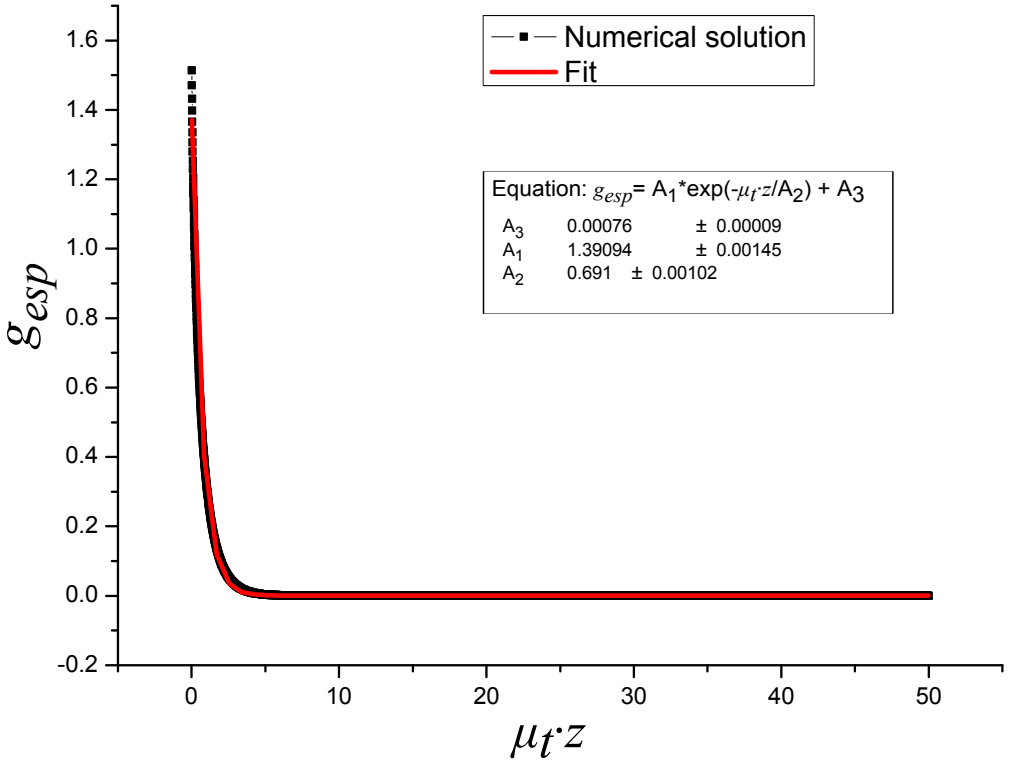

Figure 5.17: Integral of $\int_0^{\frac{\pi}{2}} \exp\left(-\mu_t \cdot \frac{z}{cos\theta}\right) \sin\theta d\theta$ is obtained using a numerical method.

5.3.3 Scanning process

In table 5.3, we list the scanning parameters: the output imaging definition is M pixels in x-direction and N in y-direction; the pixel size is $l_{pxl} \times l_{pxl}$ cm^2; the initial storage center distribution is $n_{sc}^0(x,y,z) = Limg(x,y,z)$; the laser spot dwell time on each pixel is t_{scan}[14], which leads a scanning velocity $v_{scan} = l_{pxl}/t_{scan}$; the laser distribution function within phosphor layer $f(x,y,z)$; and the laser power P_{laser}. One should notice that the output image definition $M \times N$ is different from the definition $Npxl_x \times Npxl_y$ (see Table 5.2) used in the laser light propagation simulation previously. The scanning process can be understood as a 'sampling' of the latent image $Limg(x,y,z)$, the output imaging definition is independent of the latent image or the laser distribution function $f(x,y,z)$.

With Equation 5.33 and the initial storage center distribution $n_{sc}^0(x,y,z) = Limg(x,y,z)$, the residual storage center after reading pixel (m,n) is given by

$$\begin{aligned} n_{sc}^{m,n}(x,y,z) =& Limg(x,y,z)\ \exp\left\{-\left[\sum_{j=0}^{m-2}\sum_{i=0}^{N-1} f(x-i\cdot l_{pxl}, y-j\cdot l_{pxl}, z)\right.\right. \\ &\left.\left. + \sum_{k=0}^{n-1} f(x-k\cdot l_{pxl}, y-(m-1)l_{pxl}, z)\right]\cdot P_{laser}t_{scan}\cdot\sigma\right\}. \end{aligned} \tag{5.39}$$

The calculation is detailed in Appendix A.2. Then we have the PSL distribution

$$PSL^{m,n}(x,y,z) = \begin{cases} n_{sc}^{m-1,N}(x,y,z) - n_{sc}^{m,n}(x,y,z), & \text{if } n=1. \\ n_{sc}^{m,n-1}(x,y,z) - n_{sc}^{m,n}(x,y,z), & \text{otherwise.} \end{cases} \tag{5.40}$$

The detailed solutions can be found in Equation A.15 and A.16. Together with the escape probability of the emission at different depth $P(z)$, the collected signal from the front surface is computed by

$$Dimg(x_m, y_n) = \int_z P(z)dz \iint_{x,y} PSL^{m,n}(x,y,z)dxdy, \tag{5.41}$$

which is equivalent to Equation 5.2.

Table 5.3: Scanning parameters.

Image definition	$M \times N$ pixels
Pixel size	l_{pxl}
Initial storage center distribution	$Limg(x,y,z)$
Scanning speed	v_{scan}
Dwell time on each pixel	$t_{scan} = l_{pxl}/v_{scan}$
Laser distribution function	$f(x,y,z)$
Laser power	P_{laser}

The final output image is computed using the following algorithm:

[14] For a commercial scanner, the dwell time is about 1 μs per pixel (Fasbender et al., 2003).

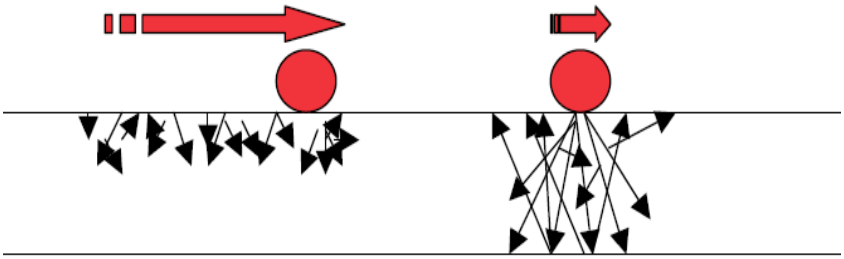

Figure 5.18: Effect of scanning velocity: a smaller pixel requires slower scanning velocity and longer dwell time, which might have a counterproductive effect on the image sharpness (Mango and Castro, 2009).

Initialize the digital image array $Dimg(x, y) = 0$.
for *each line:* $m \leftarrow 1$ ***to*** M **do**
  for *each pixel:* $n \leftarrow 1$ ***to*** N **do**
    Compute the residual storage center $n_{sc}^{m,n}$ using Eq. 5.39;
    Compute the output signal of the current pixel $Dimg(x_m, y_n)$ using Eq. 5.41;
  end
end

As the laser distribution function $f(x, y, z)$ is infinitely wide (in XY plane), it is impossible to operate an infinite array, therefore, one need to sample a reasonable finite region, beyond which the influence of the laser is neglected. Hence one need to define a cut-off intensity.

5.3.4 Cut-off intensity and laser distribution array dimension

We start by the reading rate of the storage center (Eq. 5.34). The PSL yielding rate depends on the product of the dwell time and the laser intensity (or laser power). Figure 5.18 shows the effect of a dwell time: smaller pixel requires a smaller scanning velocity, which leads a longer dwell time. This might have a counter-productive effect on the MTF. The longer the laser stays at one point, the larger the number of laser photons which can reach the depth of IP or affect the points in the neighborhood, and excite more storage centers. Similarly (see Figure 5.19), with greater laser power (photons/s), more photons can reach the depth of IP and the neighborhood.

We introduce a parameter: effective reading region. This parameter describes the region within which, the laser could partially stimulate the storage centers; beyond which, it is considered that the laser has no effect. In order to define this reading region, one needs to determine first the cut-off intensity. Starting with Eq. 5.34, if the PSL yield is less than or equal a threshold $PSL^{m,n}/n_{sc}^{m,n-1} \leq f_{th}$, one can consider that the laser has no effect, where f_{th} is a critical value, e.g. $f_{th} = 10^{-5}$. Then we have

$$1 - \exp(-\sigma f(x, y, z) P_{laser} t_{scan}) \leq f_{th} \tag{5.42}$$

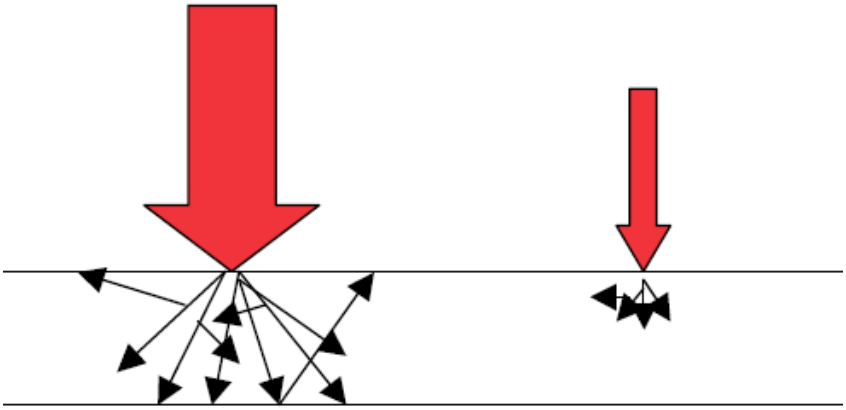

Figure 5.19: Higher laser power penetrates deeper into the phosphor layer,degrading MTF (Mango and Castro, 2009).

and finally we get

$$f(x,y,z) \leq -\frac{1}{\sigma P_{laser} t_{scan}} ln(1-f_{th}). \tag{5.43}$$

Thus the cut-off laser intensity is

$$f_{cutoff}(x,y,z) = -\frac{1}{\sigma P_{laser} t_{scan}} ln(1-f_{th}). \tag{5.44}$$

Equation 5.44 allows the definition of the reading region $[X_{min}\ X_{max}\ Y_{min}\ Y_{max}\ Z_{min}\ Z_{max}]$. Figure 5.20 shows the limits R_{min} and R_{max} which are defined using the above equation. We thus have the lower and upper limits in XY planes:

$$X_{min} = Y_{min} = R_{min}\ and\ X_{max} = Y_{max} = R_{max} \tag{5.45}$$

At high energies, a big part of the deposited energy is close to the back side (as we have seen in section 3.5.2.2), therefore in z direction we keep the entire PSP layer thickness, i.e. $Z_{min} = Z^P_{min}$ and $Z_{max} = Z^P_{max}$.

5.4 Summary of optical readout modeling

In brief, the CR optical readout modeling is based on the formula $Dimg(x_m, y_n) = \int_z P(z)dz \iint_{x,y} n^{m,n}_{sc}(x,y,z) \{1 - \exp[-\sigma \cdot f(x-x_m, y-y_n, z) \cdot P_{laser} t_{scan}]\} dxdy$. The final output image depends on the optical property ($f(x,y,z)$) of an imaging plate and the laser scanning history (other terms in the formula). The optical readout simulation follows two steps.

- Laser transport simulation. This step generates the laser light distribution function $f(x,y,z)$, which is the input required by the next step. The laser propagation is simulated using Monte Carlo models, where the imaging plate is described by

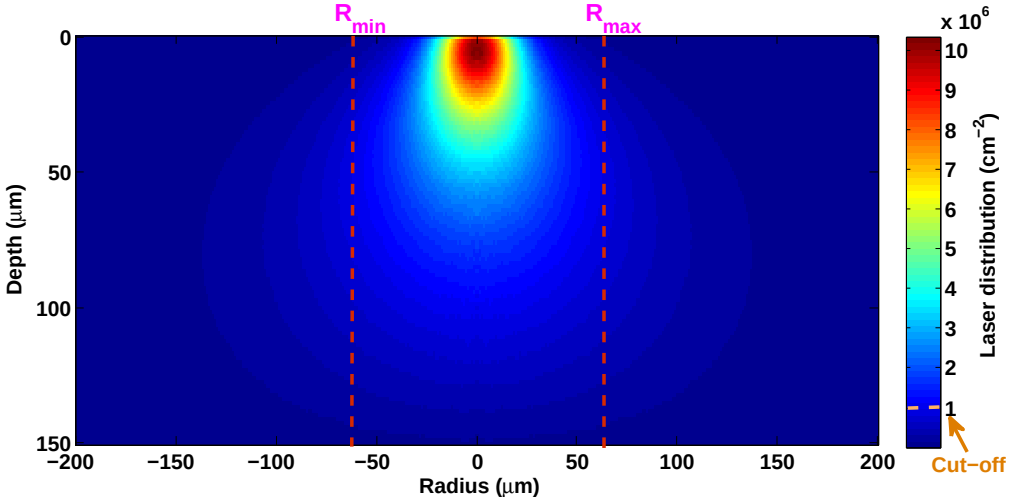

Figure 5.20: Determining reading region.(image not yet normalized.)

the parameters such as absorption coefficients, anisotropic factor, interface roughness etc. Based on the Monte Carlo model, a Matlab tool has been programmed which outputs a discrete laser distribution function. Data fitting has been applied to the discrete function to reduce the statistical noise and obtain an analytic function $f(x, y, z)$.

- Laser scanning. This step follows the laser scanning history pixel by pixel, and outputs the final digital image $Dimg(x, y)$. In this step, we model in detail the laser modification of the latent image when the laser spot moves from one pixel to another. Though in reality, the laser spot moves continuously on the imaging plate, as a numerical simulation, the laser movement is sampled according to the scanning pixel size.

Our model allows to simulate the effects of the following scanning parameters: pixel size, laser scanning time (laser dwell time), laser spot size and laser power. The effects of PSL afterglow, PSL collection, amplification and digitization are neglected.

5.5 Simulation results

The readout signal depends on the product of the laser power and dwell time, therefore, in the following, instead of using laser power or dwell time, we simply use a reading factor p_{read} to present different product values. Figure 5.21 shows the effect of the optical readout. The images in the upper half are the object image Obj_{2D} and the energy deposition image in IP alone obtained in the previous chapter. Only a fraction ($\sim 5\%$) of the object image is detected by IP. In the lower half, we show the readout images using two different reading factors $p_{read} = 10^{16}$ and $p_{read} = 10^{10}$. With great reading power, most of the storage centers can be released (not all the released storage center can contribute to the final image), however a visible shift is observed (comparing Figure 5.21(b) and 5.21(c)) in the IP translation direction.

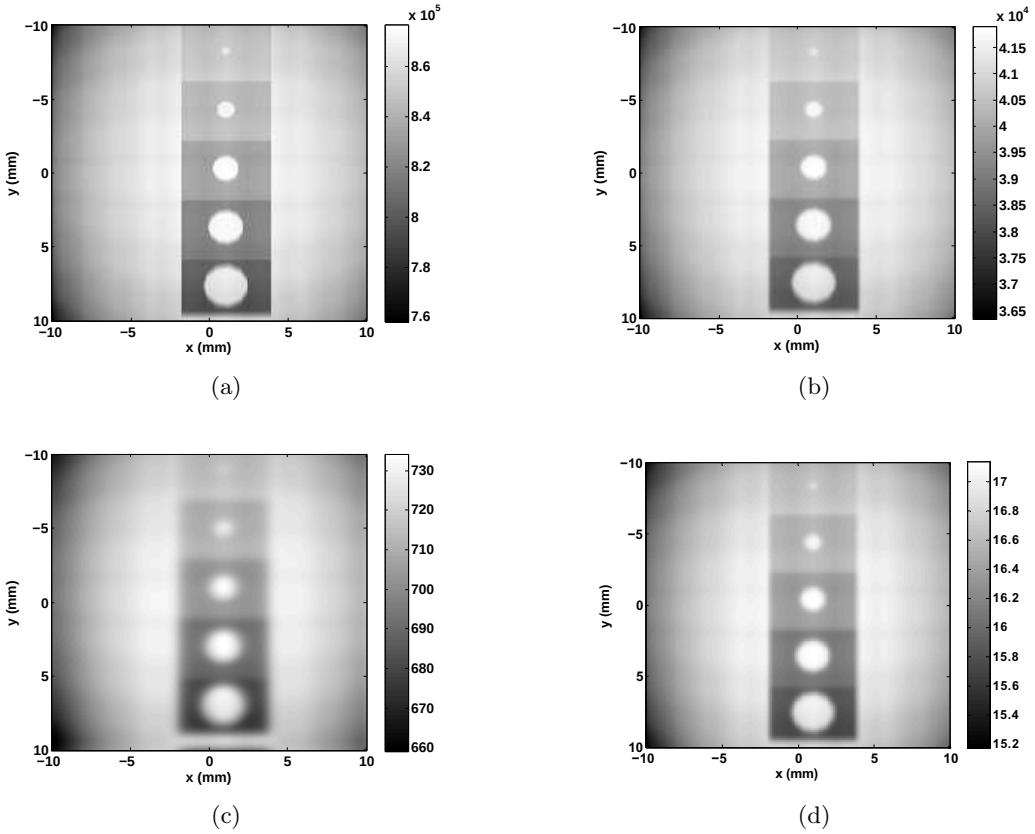

(a) (b)

(c) (d)

Figure 5.21: Simulation result: (a) Object image Obj_{2D}, (b) latent image $Limg(x, y, z)$, (c) readout image with $p_{read} = 10^{16}$ and (d) Readout image with $p_{read} = 10^{10}$.

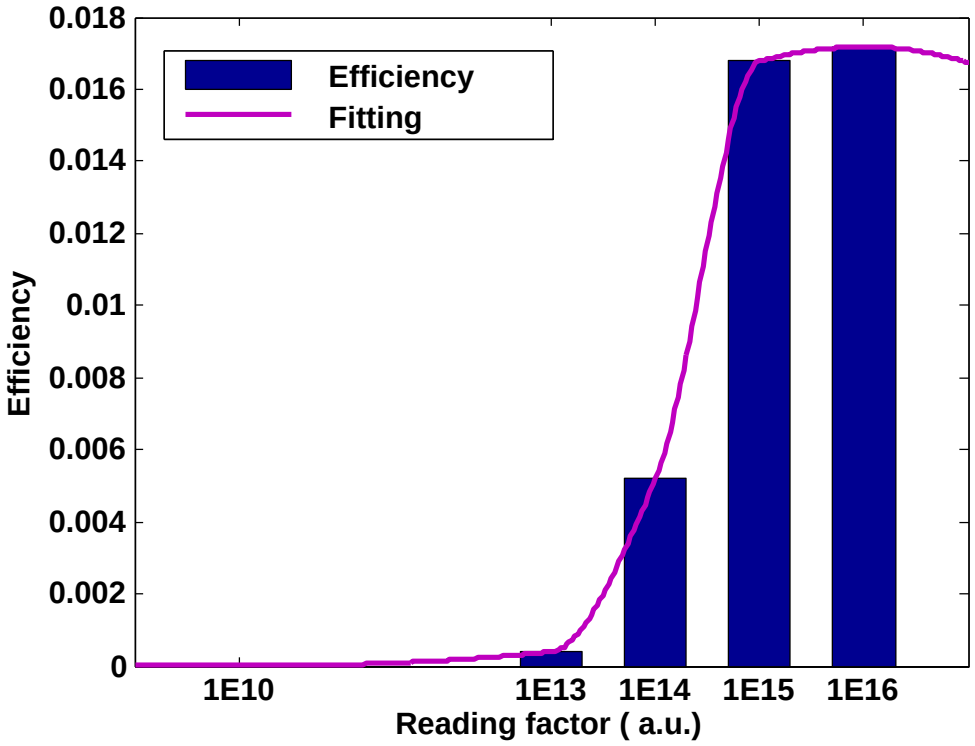

Figure 5.22: Readout efficiency versus reading factor.

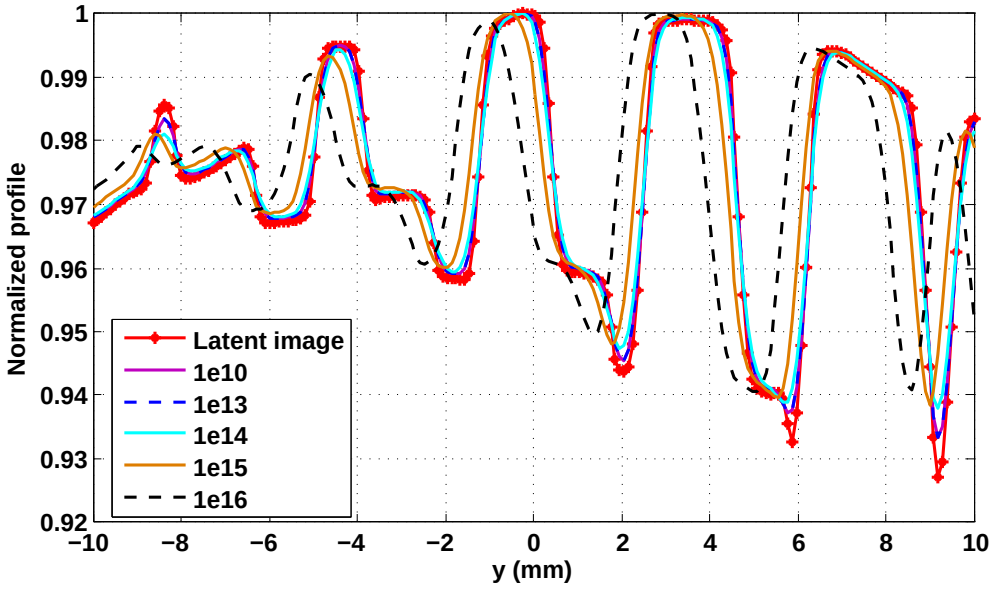

Figure 5.23: Result: normalized profiles.

We then plot the reading efficiency ($\sum_{m,n} Dimg(x_m, y_n) / \iiint_{x,y,z} Limg(x,y,z)dxdydz$) versus the reading factor (Figure 5.22). The efficiency increases slowly at low reading factors (high laser power and/or long dwell time), then we see a significant increase between 10^{13} and 10^{15}; and at 10^{16} the curve starts to reach its maximum. One may notice that the maximum efficiency does not equal to one. Indeed, a high reading factor increases the photoluminescence, but the photons are emitted isotropically and only a small fraction can escape from the front surface of IP and contribute to the final image.

In order to compare the image sharpness, the images have been normalized by their maximum values. In Figure 5.23, we present the profiles along the IQI (Image Quality Indicator). The red curve is the latent image profile. The curves of the first 2 powers overlap each other, then we lose contrast by increasing the power. Comparing the profiles, we also see an obvious shift between the black and the red curves in the IP translation direction during the scanning process.

Using higher laser power or longer dwell time, the reading efficiency is greater, but one loses the spatial resolution by affecting the neighboring pixels.

5.6 Conclusion

In this chapter, the modeling and simulation of the CR optical readout process have been discussed. Two successive steps are involved: the generation of the laser distribution function $f(x, y, z)$ within an imaging plate and the generation of the readout image ($Dimg(x, y, z)$). We have programmed two simulation tools in Matlab for laser light transport in IP and laser scanning process. For the former, the Monte Carlo method has been adopted, where the imaging plate is described by the following parameters: absorption coefficient, scattering coefficient, anisotropic factor of the PSP layer; refractive indexes of top layer, binder and bottom layer; the roughness of the top-PSP and PSP-bottom interfaces. For the laser scanning effect, we have modeled in detail the laser scanning process: the signal readout is tracked pixel by pixel, so that the influence of the laser power and scanning time can be accounted for. The laser modification of the latent image has also been taken into consideration; we have developed a detailed calculation of an 'up-to-date' image (see Appendix A.2).

With our Monte Carlo tool, several case studies have been performed to investigate the influence of PSP layer parameters. The results indicate that increasing the absorption or scattering coefficient can limit the scattering region, and the same conclusion has also been drawn in the works of (Thoms, 1996a; Fasbender et al., 2003). It is also found that the increase of the anisotropic factor (meaning forward-peaked photon scattering) can maintain a small laser size and makes more photon arrive in depth interacting with storage centers. A better resolution can also be achieved by decreasing the PSP layer thickness, which explains why most commercial high resolution imaging plates are thinner than standard imaging plates.

As regards the laser scanning simulation, we propose to sample the laser distribution function $f(x, y, z)$ within a reasonable small region in order to facilitate the numerical operation of the 3D laser distribution array. The array dimension is determined by a cut-off intensity which should be small enough so that the PSL stimulated by an intensity smaller than it can be neglected. A study of the reading factor (product of laser intensity and

dwell time) has been performed. We find that with the increase of the reading factor, the readout efficiency (output signal S over storage center n_{sc}) increases, while the sharpness first increases then decreases. The optimal condition is at $p_{read} = 10^{15}$, which provides a good reading efficiency without losing much the contrast. This tool takes into account the influence of the scanning parameters: pixel size, laser power and scanning velocity. It is useful for optimizing the output image.

5.7 Summary of the complete CR imaging chain simulation

The previous and this chapter present the complete CR image formation simulation method. The simulation is completed in three steps, which are summarized as follows.

- Object image generation. Deterministic and Monte Carlo codes can be applied in this step. The output of this step should be a spectral image $Obj(E, x, y)$.
- Latent image generation. This step is realized by the operator H1 and the detector response model PSF_{det}: $Limg(x, y, z) = \mathrm{H1}(Obj, PSF_{det})$.
- Digital image generation. The image is affected by the IP's optical response $f(x, y, z)$ and scanning parameters. The final digital image is generated through $Dimg(x, y, z) = \mathrm{H2}(Limg, f, scanning\ parameters)$.

With this method, one can simulate the complete CR image formation, and take into account the operating factors such as source (in the first step), detector configuration (in the second step) and scanning parameters (in the last step). The application of H1 and H2 requires the sampling match of Obj with PSF_{det} and $Limg$ with f. The computation efficiency strongly depends on the array size of $Obj(E, x, y)$, $Limg(x, y, z)$, $PSF_(x, y, z)$ and $f(x, y, z)$. Great accuracy requires a small sampling size, and thus a large array size, which makes the simulation slow.

As a future step, a comparison of simulation and experimental results will be performed.

Conclusion and perspectives

"I can't go back to yesterday because I was a different person then."

Alice in Wonderland

The PhD project was initiated in an industrial context of adapting the computed radiography system to fulfill the industrial inspection requirements. The thesis revolved around two aspects: physical phenomena investigation and a complete CR imaging chain simulation approach. The main results are described in the following two sections.

Physical phenomena investigation

The first part of this work focused on the physical phenomena comprehension. A dedicated Monte Carlo tool, based on PENELOPE, was developed for a fine investigation. The usefulness of the tool was demonstrated through the optimization study of a realistic industrial case (a 70 mm iron piece exposed to Cobalt-60), where the scattering issue was illustrated and the response of three detector configurations was characterized. The following understandings were achieved.

- Secondary radiation issue. The problem of image detection with IP alone was first visualized using the tool. The images due to direct radiation (of high energy) and secondary radiation (of relatively low energy) produced by an object were illustrated separately. It was found that the secondary radiation is responsible for the image unsharpness. As the detected image is mostly due to the secondary radiation (only 15.7% of the signal is from direct radiation), the global image has a poor spatial resolution. The problem is identified: in order to improve image quality, the direct to secondary radiation ratio (DSR) needs to be increased, namely intensification of high energy signal and elimination of low energy signal. Here we see the importance of detector response characterization.

- Detector characterization. We have characterized the responses of three detector configurations, IP alone, IP with 0.2 mm lead screen, and IP with 0.2mm lead and

0.8 mm tin screens. A detailed spectral and spatial analysis was applied to the characterization results. We had the following remarks.

- Role of metallic screens. By comparing the three detectors' response, it was found that the metallic screens can effectively intensify the high energy signal, filter low energy signal and shift the deposited energy towards the front surface of IP. However, they also degrade the spatial resolution, especially the fluorescence emitted from a lead screen. The DSR and the sharpness should both be considered while choosing screens for optimization. It turns out that the configuration IP with lead and tin screens is overall preferable, since it provides the best DSR of the three, and moreover, the tin screen can effectively attenuate the lead fluorescence. Note that this IP/screens combination is optimal for the case studied, and this cannot be generalized for all cases.
- Photon. High energy photons deposit their energy preferably towards the rear side of IP, which is not favorable for optical readout because of the laser light's penetration.
- Electron. We found that at high energies, more than half of the deposited energy is due to the electrons produced by the metallic screens. And these electrons are responsible for shifting the energy deposition towards the IP's front surface. Electrons play an important role on the signal intensification and signal distribution, and thus in practical experiment, one should make sure of a good contact between metallic screen and IP, to ensure the electrons can arrive at IP.
- Protective layer of IP. The IP's protective layer (of 6 μm) was evaluated. It was found that this layer has a negligible influence; it does not prevent the photons or electrons from entering the IP's phosphor layer.

With this case study, we see that to optimize image quality, the responses of both object and detector should be taken into consideration; a compromise of DSR and sharpness should be made; high energy fluorescence should be eliminated from entering IP (e.g. by adding an additional screen to filter the fluorescence).

Computed radiography modeling and simulation

This thesis developed a simulation approach which allows us to simulate the CR image formation from X-ray exposure until optical readout. The image simulation is undertaken through three steps: object image generation, latent image generation and final digital image generation. The precise simulation steps are summarized as follows.

- Object image generation. According to needs, it is flexible to choose a general purpose deterministic or a Monte Carlo code. The output of this step should be a spectral image $Obj(E, x, y)$.
- Latent image generation. This step is realized by the operator H1 and an off-line detector response model PSF_{det}: $Limg(x, y, z) = \mathrm{H1}(Obj, PSF_{det})$.
  The detector response model was obtained by means of Monte Carlo characterization

of the detector response at different energies. At high energies, a great part of the energy deposition in IP's sensitive layer is due to the scattering, fluorescence reabsorption and electron effects. With MC method, the accurate spectral and spatial response can be obtained. A detector model database has been created. So far, the database consists of 128 different detector configurations including all IP/screens combinations recommended in the current international standards (EN14784-2, 2005; ISO17636-2, 2013).
A case study demonstrates the use of this step. A complex shape object image was detected with three detector configurations. By comparing the latent images, we determined the optimal detector configuration. A comparison with full Monte Carlo simulation shows a good accordance. Another comparison of complex imaging set-up simulation is in progress.

- Digital image generation. The image is affected by the IP's optical response $f(x, y, z)$ and scanning parameters. The digital image is generated through $Dimg(x, y, z) =$ H2$(Limg, f, scanning\ parameters)$.
  In order to study the optical response of an imaging plate, a Monte Carlo tool for modeling laser transport in IP was developed, where the IP is described by the parameters such as absorption, scattering and interface conditions etc. A study on the influence of changing several parameters has been performed with the tool. The results show that the change of these parameters affects the scattering region and photon quantity within IP. The scattering region and photon quantity determines respectively the image sharpness and readout efficiency. It was found that when we gain the sharpness, we loose the efficiency and vice versa. The two are conflicting factors, and a trade-off should be made during fabrication. For a CR user, the IP's optical property is not accessible, however it is possible to adjust the scanning parameters.
  As the laser raster scanning is a destructive reading process, this effect is taken into account in the model H2, and the laser scanning is followed pixel by pixel. As a demonstration, the latent image obtained with IP alone in the second step was read with different reading powers (product of laser power and dwell time). The result shows that higher laser power (or longer dwell time) leads greater readout efficiency, but lower image contrast. Again, a compromise should be made to determine the suitable condition.

With this method, one can simulate the complete CR image formation, and take into account the operating factors such as source (in the first step), detector configuration (in the second step) and scanning parameters (in the last step). The application of H1 and H2 requires the sampling match of Obj with PSF_{det} and $Limg$ with f. The computation efficiency strongly depends on the array size of $Obj(E, x, y)$, $Limg(x, y, z)$, $PSF_(x, y, z)$ and $f(x, y, z)$. Great accuracy requires a small sampling size, and thus a large array size, which makes the simulation slow.

Along with the development of the simulation approach and physical understanding with the simulation tools developed, two experimental measurement campaigns have also been performed. The first one was performed at the European Synchrotron Radiation Facility aimed to characterize IP's response at high energies. Though some unexpected issues make the result exploitation difficult, we have extracted the data of metallic screens'

intensification. The simulation and experimental data overall show a good agreement. The other measurement has been performed recently at BAM, Germany (August 21-29, 2014). The objective of this experiment is to compare the simulation result of a complex imaging set-up with the experimental acquired image. The comparison is still in progress.

Based on the simulation approach developed, a complete CR imaging simulation tool is now available, with which a comprehensive study on the detector configurations and readout parameters can be applied to optimize a given imaging application.

Perspectives

The CR simulation approach developed in the thesis and its usefulness, as well as the physical understanding on the underlying phenomena were presented in the previous parts, while in this section, several avenues for the simulation improvement and for the physical phenomena investigation are discussed in the following.

- Comparison with experimental results. As mentioned at the end of the previous section, a comparison with experimental result will be performed next.
- Improvement on the simulation and modeling.
  - Detector response model database. The models are stored in the form of digital arrays so far. In the future, more detector models will be added to complete the database, thus more storage space is required. Moreover, the application of the image convolution requires that the object image and detector model have the same sampling rate, and thus one have to interpolate the detector model to match the object array. The kind of issue is overcome in the optical readout process where the laser distribution function is fitted by analytic functions. As avenue improvement, the fitting can also be applied to the detector model, so that it can be represented by several analytic function parameters. In such a way, the storage can be greatly reduced, and no more interpolation is needed.
  - While in the Monte Carlo modeling of laser propagation in IP, the IP's phosphor layer is described by the absorption, scattering and anisotropic factors, in future work, the Mie theory can be adopted so that the imaging plate can be modeled with more intrinsic parameters such as the refractive indexes of phosphor and binder, the phosphor grain size and the packing factor. A parameter study on these parameters can help to determine the optimal grain size, packing factor as well as the binder material, which is of interest from the IP fabrication perspective.
  - Afterglow effect. In the simulation approach proposed, the afterglow of the PSL emission has not been accounted for. After the bibliographic study, we find that it is difficult to model the afterglow effect with a complete phosphor physical band model, because of the lack of information. However an experimental measured afterglow decay curve can be applied to the model, and the calculation of course takes certain computational cost.
  - Effect of digitization and saturation due to IP or optical devices. The dynamic range of a CR system is limited by the dynamic range of both IP and the optical

device. Though an image plate has a large dynamic range (10^5 or more), due to the optical device, the CR output image gray level is limited to 2^{16}. For a realistic simulation, the modeling of digitization and saturation effect is also of interest.

- Future analysis. In the thesis, a systematic study on the CR detector response has been performed. Similar studies can also be performed on the laser readout parameters. In the work demonstrated in the thesis, we have demonstrated the influence of the reading factor (product of laser power and dwell time). A fine analysis on the influence of pixel size, laser power and dwell time might be of interest for scanner performance optimization.

As discussed in the thesis, the optimization always involves finding a compromise between sharpness and efficiency. Sometime it is confusing on making a choice. A more global factor will be of interest for an objective decision making.

A

Appendices

A.1 Modeling intrinsic property of medium with Mie theory

Most of the Monte Carlo models for simulating light transport in turbid medium are based on the use of absorption, scattering and anisotropic factors. These factors reflect the effects of intrinsic properties (e.g. volume density of granular particles, grain size, complex refractive indexes) of a medium. In the modeling work of Liaparinos (Liaparinos et al., 2007; Liaparinos et al., 2006; Liaparinos and Kandarakis, 2009), intrinsic parameters of a granular plate are used to describe the medium's absorption, scattering and anisotropic factors. Based on Mie theory, the general calculations are the followings.

The light absorption and scattering coefficients are given by:

$$\mu_\alpha = V_d A Q_{abs} \; and \; \mu_s = V_d A Q_{sct}, \tag{A.1}$$

where each coefficient depends on the density of phosphor screen's volume density V_d (number of grains per unit volume), the geometrical cross section A of the grain, as well as on the corresponding absorption (Q_{abs}) and scattering (Q_{sct}) efficiency factors, which are given below:

$$Q_{ext} = \frac{2}{x^2}\sum_{n=1}^{\infty}(2n+1)\mathrm{Re}(a_n + b_n), \; Q_{sct} = \frac{2}{x^2}\sum_{n=1}^{\infty}(2n+1) \times (|a_n|^2 + |b_n|^2), \tag{A.2}$$

where Q_{ext} is extinction efficiency factor, and the absorption efficiency factor is calculated from $Q_{abs} = Q_{ext} - Q_{sct}$, a_n and b_n are the Mie coefficients given afterwards (Equation A.3)

The geometrical cross section of grain (A) is proportional to the diameter of the grain (d) and is equal to $A = \pi d^2/4$. The extinction and scattering efficiency factors are obtained from Mie calculations using the size parameter $x = \pi d n_{mdedium}/\lambda$ of the Mie theory and the relative complex refractive index $m = n_{grain}/n_{medium}$, where λ is the wavelength of light, n_{grain} is the complex refractive index of the phosphor grain, and n_{medium} is the refractive index of the medium (binder). Finally, the Mie coefficients, a_n and b_n are given

by:

$$\begin{aligned} a_n &= \frac{\psi_n'(mx)\psi_n(x) - m\psi_n(mx)\psi_n'(x)}{\psi_n'(mx)\xi_n(x) - m\psi_n(mx)\xi_n'(x)}, \\ b_n &= \frac{m\psi_n'(mx)\psi_n(x) - \psi_n(mx)\psi_n'(x)}{m\psi_n'(mx)\xi_n(x) - \psi_n(mx)\xi_n'(x)}, \end{aligned} \tag{A.3}$$

where $\psi_n(x)$ and $\xi_n(x)$ are the Riccati-Bessel functions. The calculation of these functions can be carried out by the following recurrences, taking into account their corresponding properties:

$$\begin{aligned} &\psi_{n+1}(x) = (2n+1)\psi_n(x)/x - \psi_{n-1}(x), \\ &\xi_{n+1}(x) = (2n+1)\xi_n(x)/x - \xi_{n-1}(x), \\ &\psi_n'(x) = \psi_{n-1}(x) - n\psi_n(x)/x, \\ &\xi_n'(x) = \xi_{n-1}(x) - n\xi_n(x)/x, \\ &\psi_{-1}(x) = \cos(x), \psi_0(x) = \sin(x), \\ &\xi_{-1}(x) = \cos(x) - i\sin(x), \xi_0(x) = \sin(x) + i\cos(x). \end{aligned} \tag{A.4}$$

A.2 Scanning process

Here we detail the calculation of the up-to-date latent image $n_{sc}^{m,n}$. The initial value at $t = 0$ is the input latent image $n_{sc}^0 = Limg(x, y, z)$. The laser raster scanning modifies the latent image.

- Scanning the first line
  - after scanning the first pixel $t = t_{scan}$

$$n_{sc}^{1,1}(x, y, z, t_{scan}) = n_{sc}^0(x, y, z)\exp[-I(x, y, z) \cdot t_{scan} \cdot \sigma] \tag{A.5}$$

  - second pixel $t = 2t_{scan}$

$$\begin{aligned} n_{sc}^{1,2}(x, y, z, 2t_{scan}) =& n_{sc}^{1,1}(x, y, z)\exp\left[-I(x - v_{scan}t_{scan}, y, z) \cdot t_{scan} \cdot \sigma\right] \\ =& n_{sc}^0(x, y, z)\exp[-I(x, y, z) \cdot t_{scan} \cdot \sigma] \cdot \exp[-I(x - v_{scan}t_{scan}, y, z) \cdot t_{scan} \cdot \sigma] \\ =& n_{sc}^0(x, y, z)\exp\left\{-\left[I(x, y, z) + I(x - v_{scan}t_{scan}, y, z)\right] \cdot t_{scan} \cdot \sigma\right\} \end{aligned} \tag{A.6}$$

– third pixel $t = 3t_{scan}$

$$\begin{aligned} n_{sc}^{1,3}(x,y,z,3t_{scan}) =& n_{sc}^{1,2}(x,y,z)\exp\left[-I(x-2v_{scan}t_{scan},y,z)\cdot t_{scan}\cdot\sigma\right] \\ =& n_{sc}^{0}(x,y,z)\exp\left\{-\left[(x,y,z)+I(x-v_{scan}t_{scan},y,z)\right]\cdot t_{scan}\cdot\sigma\right\} \\ & \times\exp\left[-I(x-2v_{scan}t_{scan},y,z)\cdot t_{scan}\cdot\sigma\right] \\ =& n_{sc}^{0}(x,y,z)\exp\left\{-\left[I(x,y,z)+I(x-v_{scan}t_{scan},y,z)\right.\right. \\ & \left.\left.+I(x-2v_{scan}t_{scan},y,z)\right]\cdot t_{scan}\cdot\sigma\right\} \end{aligned} \tag{A.7}$$

...

– n-th pixel $t = nt_{scan}$

$$\begin{aligned} n_{sc}^{1,n}(x,y,z,nt_{scan}) =& n_{sc}^{0}(x,y,z)\exp\left\{-\left[I(x,y,z)+I(x-v_{scan}t_{scan},y,z)+I(x-2v_{scan}t_{scan},y,z)\right.\right. \\ & \left.\left.+\cdots+I(x-v_{scan}\cdot(n-1)t_{scan},y,z)\right[\cdot t_{scan}\cdot\sigma\right\} \\ =& n_{sc}^{0}(x,y,z)\exp\left\{-\left[\sum_{i=0}^{n-1}I(x-v_{scan}\cdot i\cdot t_{scan},y,z)\right]\cdot t_{scan}\cdot\sigma\right\} \end{aligned} \tag{A.8}$$

- Scanning the second line

– First pixel $t = (N+1)t_{scan}$

$$\begin{aligned} n_{sc}^{2,1}(x,y,z,(N+1)t_{scan}) =& n_{sc}^{0}(x,y,z)\exp\left\{-\left[\sum_{i=0}^{N-1}I(x-v_{scan}\cdot i\cdot t_{scan},y,z)\right]\cdot t_{scan}\cdot\sigma\right\} \\ & \times\exp\left[-I(x,y-l_{pxl},z)\cdot t_{scan}\cdot\sigma\right] \end{aligned} \tag{A.9}$$

– second pixel $t = (N+2)t_{scan}$

$$\begin{aligned} n_{sc}^{2,2}(x,y,z,(N+2)t_{scan}) =& n_{sc}^{2,1}(x,y,z,(N+1)t_{scan})\exp\left[-I(x-v_{scan}t_{scan},y-l_{pxl},z)\cdot t_{scan}\cdot\sigma\right] \\ =& n_{sc}^{0}(x,y,z)\exp\left\{-\left[\sum_{i=0}^{N-1}I(x-v_{scan}\cdot i\cdot t_{scan},y,z)\right]\cdot t_{scan}\cdot\sigma\right\} \\ & \times\exp\left[-I(x,y-l_{pxl},z)\cdot t_{scan}\cdot\sigma\right]\cdot\exp\left[-I(x-v_{scan}t_{scan},y-l_{pxl},z)\right. \\ =& n_{sc}^{0}(x,y,z)\exp\left\{-\left[\sum_{i=0}^{N-1}I(x-v_{scan}\cdot i\cdot t_{scan},y,z)\right]\cdot t_{scan}\cdot\sigma\right\} \\ & \times\exp\left\{-\left[I(x,y-l_{pxl},z)+I(x-v_{scan}t_{scan},y-l_{pxl},z)\right]\cdot t_{scan}\cdot\sigma\right\} \end{aligned} \tag{A.10}$$

...

– n-th pixel $t = (N+n)t_{scan}$

$$n_{sc}^{2,n}(x,y,z,(N+n)t_{scan}) = n_{sc}^{0}(x,y,z)\exp\left\{-\left[\sum_{i=0}^{N-1} I(x - v_{scan}\cdot i\cdot t_{scan}, y, z)\right]\cdot t_{scan}\cdot\sigma\right\} \times \exp\left\{-\left[\sum_{j=0}^{n-1} I(x - v_{scan}\cdot j\cdot t_{scan}, y - l_{pxl}, z)\right]\cdot t_{scan}\cdot\sigma\right\} \tag{A.11}$$

- Reading n-th pixel in m-th line $t = [(m-1)N+n]t_{scan}$

$$\begin{aligned} & n_{sc}^{m,n}(x,y,z,[(m-1)N+n]t_{scan}) \\ =& n_{sc}^{0}(x,y,z)\exp\left\{-\left[\sum_{j=0}^{m-2}\sum_{i=0}^{N-1} I(x - v_{scan}\cdot i\cdot t_{scan}, y - jl_{pxl}, z)\right.\right. \\ & \left.\left. + \sum_{k=0}^{n-1} I(x - v_{scan}\cdot k\cdot t_{scan}, y - (m-1)l_{pxl}, z)\right]\cdot t_{scan}\cdot\sigma\right\} \\ =& n_{sc}^{0}(x,y,z)\exp\left\{-\left[\sum_{j=0}^{m-2}\sum_{i=0}^{N-1} I(x - v_{scan}\cdot i\cdot t_{scan}, y - jl_{pxl}, z)\right.\right. \\ & \left.\left. + \sum_{k=0}^{n-1} I(x - v_{scan}\cdot k\cdot t_{scan}, y - (m-1)d, z)\right]\cdot\frac{l_{pxl}}{v_{scan}}\cdot\sigma\right\} \end{aligned} \tag{A.12}$$

With $I(x,y,) = f(x,y,z)\cdot P_{laser}$, Equation A.12 can be rewritten as

$$\begin{aligned} & n_{sc}^{m,n}(x,y,z,[(m-1)N+n]t_{scan}) \\ =& Limg(x,y,z)\exp\left\{-\left[\sum_{j=0}^{m-2}\sum_{i=0}^{N-1} f(x - il_{pxl}, y - j\cdot l_{pxl}, z)\right.\right. \\ & \left.\left. + \sum_{k=0}^{n-1} f(x - k\cdot l_{pxl}, y - (m-1)l_{pxl}, z)\right]\cdot P_{laser}t_{scan}\cdot\sigma\right\} \end{aligned} \tag{A.13}$$

- The emitted PSL at (m,n) is given by

$$PSL^{m,n}(x,y,z) = \begin{cases} n_{sc}^{m-1,N}(x,y,z) - n_{sc}^{m,n}(x,y,z), & \text{if } n = 1. \\ n_{sc}^{m,n-1}(x,y,z) - n_{sc}^{m,n}(x,y,z), & \text{otherwise.} \end{cases} \tag{A.14}$$

– If $n = 1$

$$\begin{aligned}
&PSL^{m,n}(x,y,z)\\
=&Limg(x,y,z)\exp\left\{-\left[\sum_{j=0}^{m-2}\sum_{i=0}^{N-1} f(x-il_{pxl},y-jl_{pxl},z)\right]P_{scan}t_{scan}\cdot\sigma\right\}\\
&-Limg(x,y,z)\exp\left\{-\left[\sum_{j=0}^{m-2}\sum_{i=0}^{N-1} f(x-il_{pxl},y-jl_{pxl},z)\right.\right.\\
&\left.\left.+f\left(x,y-(m-1)l_{pxl},z\right)\right]\cdot P_{laser}t_{scan}\cdot\sigma\right\}\\
=&Limg(x,y,z)\exp\left\{-\left[\sum_{j=0}^{m-2}\sum_{i=0}^{N-1} f(x-il_{pxl},y-jl_{pxl},z)\right]P_{scan}t_{scan}\cdot\sigma\right\}\\
&\times\left[1-\exp\left\{-f(x,y-(m-1)l_{pxl},z)\cdot t_{scan}\cdot\sigma\right\}\right].
\end{aligned}\tag{A.15}$$

– If $n \neq 1$

$$\begin{aligned}
&PSL^{m,n}(x,y,z)\\
=&Limg(x,y,z)\exp\left\{-\left[\sum_{j=0}^{m-2}\sum_{i=0}^{N-1} f(x-il_{pxl},y-jl_{pxl},z)\right.\right.\\
&\left.\left.+\sum_{k=0}^{n-2} f(x-kl_{pxl},y-(m-1)l_{pxl},z)\right]\cdot P_{laser}t_{scan}\cdot\sigma\right\}\\
&-Limg(x,y,z)\exp\left\{-\left[\sum_{j=0}^{m-2}\sum_{i=0}^{N-1} f(x-il_{pxl},y-jl_{pxl},z)\right.\right.\\
&\left.\left.+\sum_{k=0}^{n-1} f(x-kl_{pxl},y-(m-1)l_{pxl},z)\right]\cdot P_{laser}t_{scan}\cdot\sigma\right\}\\
=&Limg(x,y,z)\exp\left\{-\left[\sum_{j=0}^{m-2}\sum_{i=0}^{N-1} f(x-il_{pxl},y-jl_{pxl},z)\right.\right.\\
&\left.\left.+\sum_{k=0}^{n-2} f(x-kl_{pxl},y-(m-1)l_{pxl},z)\right]\cdot t_{scan}\cdot\sigma\right\}\\
&\times\left(1-\exp\left\{-\left[f(x-(n-1)\cdot l_{pxl},y-(m-1)l_{pxl},z)\right]\cdot P_{laser}t_{scan}\cdot\sigma\right\}\right).
\end{aligned}\tag{A.16}$$

Bibliography

AAPM Task Group 10 (2006). Acceptance testing and quality control of photostimulable storage phosphor imaging systems. Technical report.

Agostinelli, S., Allison, J., Amako, K., Apostolakis, J., Araujo, H., Arce, P., Asai, M., Axen, D., Banerjee, S., Barrand, G., Behner, F., Bellagamba, L., Boudreau, J., Broglia, L., Brunengo, A., Burkhardt, H., Chauvie, S., Chuma, J., Chytracek, R., Cooperman, G., Cosmo, G., Degtyarenko, P., Dell'Acqua, A., Depaola, G., Dietrich, D., Enami, R., Feliciello, A., Ferguson, C., Fesefeldt, H., Folger, G., Foppiano, F., Forti, A., Garelli, S., Giani, S., Giannitrapani, R., Gibin, D., Gómez Cadenas, J., González, I., Gracia Abril, G., Greeniaus, G., Greiner, W., Grichine, V., Grossheim, A., Guatelli, S., Gumplinger, P., Hamatsu, R., Hashimoto, K., Hasui, H., Heikkinen, A., Howard, A., Ivanchenko, V., Johnson, A., Jones, F., Kallenbach, J., Kanaya, N., Kawabata, M., Kawabata, Y., Kawaguti, M., Kelner, S., Kent, P., Kimura, A., Kodama, T., Kokoulin, R., Kossov, M., Kurashige, H., Lamanna, E., Lampén, T., Lara, V., Lefebure, V., Lei, F., Liendl, M., Lockman, W., Longo, F., Magni, S., Maire, M., Medernach, E., Minamimoto, K., Mora de Freitas, P., Morita, Y., Murakami, K., Nagamatu, M., Nartallo, R., Nieminen, P., Nishimura, T., Ohtsubo, K., Okamura, M., O'Neale, S., Oohata, Y., Paech, K., Perl, J., Pfeiffer, A., Pia, M., Ranjard, F., Rybin, A., Sadilov, S., Di Salvo, E., Santin, G., Sasaki, T., Savvas, N., Sawada, Y., Scherer, S., Sei, S., Sirotenko, V., Smith, D., Starkov, N., Stoecker, H., Sulkimo, J., Takahata, M., Tanaka, S., Tcherniaev, E., Safai Tehrani, E., Tropeano, M., Truscott, P., Uno, H., Urban, L., Urban, P., Verderi, M., Walkden, A., Wander, W., Weber, H., Wellisch, J., Wenaus, T., Williams, D., Wright, D., Yamada, T., Yoshida, H., and Zschiesche, D. (2003). Geant4—a simulation toolkit. *Nuclear Instruments and Methods in Physics Research Section A: Accelerators, Spectrometers, Detectors and Associated Equipment*, 506(3):250–303.

Als-Nielsen, J. and McMorrow, D. (2011). *Elements of Modern X-ray Physics*. John Wiley & Sons.

Ashikhmin, M., Premoze, S., Ramamoorthi, R., and Nayar, S. K. (2004). Blurring of light due to multiple scattering by the medium: a path integral approach.

Atif, M., Khan, A., and Ikram, M. (2011). Modeling of light propagation in turbid medium using Monte Carlo simulation techinique. *Optics and Spectroscopy*, pages 107–112.

Attix, F. H. (2008). *Introduction to Radiological Physics and Radiation Dosimetry*. John Wiley & Sons.

Badano, A. (2003). Optical blur and collection efficiency in columnar phosphors for X-ray imaging. *Nuclear Instruments and Methods in Physics Research Section A: Accelerators, Spectrometers, Detectors and Associated Equipment*, 508(3):467–479.

Badano, A. and Kanicki, J. (2001). Monte carlo analysis of the spectral photon emission and extraction efficiency of organic light-emitting devices. *Journal of Applied Physics*, 90(4):1827.

Badano, A. and Sempau, J. (2006). MANTIS: combined X-ray, electron and optical monte carlo simulations of indirect radiation imaging systems. *Physics in Medicine and Biology*, 51(6):1545–1561.

Baetzold, R. C. (1987). Atomistic simulation of defects in alkaline-earth fluorohalide crystals. *Physical Review B*, 36(17):9182–9190.

Baetzold, R. C. (1989). Atomistic computation of molecular species in alkaline-earth fluorohalide crystals. *Journal of Physics and Chemistry of Solids*, 50(9):915–920.

Bass, M., DeCusatis, C., Enoch, J., Lakshminarayanan, V., Li, G., MacDonald, C., Mahajan, V., and Stryland, E. V. (2009). *Handbook of Optics, Third Edition Volume I: Geometrical and Physical Optics, Polarized Light, Components and Instruments(set)*. McGraw Hill Professional.

Beutel, J., Kundel, H. L., and Van Metter, R. L., editors (2000). *Hand book of medical imaging: Volume 1. Physics and Psychophysics*, chapter 1. X-ray Production, Interaction, and Detection in Diagnostic Imaging. SPIE Press.

Bonin, A., Lavayssière, B., and Chalmond, B. (1998). 3D reconstruction of faults in industrial radiography. In *International Conference Computer Methods and Inverse Provlems in Nondestructive Testing and Diagnostics*.

Bonin, A., Lavayssière, B., and Chalmond, B. (1999). New developments in industrial radiography at EDF. In *International Symposium on Computerized Tomography for Industrial Applications and Image Processing in Radiology*.

Bonin, A., Lavayssière, B., and Chalmond, B. (2000). Moderato: A Monte-Carlo radiographic simulation. In *AIP Conference Proceedings*, volume 509, pages 651–656. AIP Publishing.

Boone, J. M., Seibert, J. A., Sabol, J. M., and Tecotzky, M. (1999). A Monte Carlo study of X-ray fluorescence in X-ray detectors. *Medical physics*, 26(6):905–916.

Born, M. and Wolf, E. (2002). *Principles of Optics: Electromagnetic Theory of Propagation, Interference and Diffraction of Light*, chapter 1. Basic properties of the electromagnetic field. Cambridge University Press.

Bos, A. J., Poolton, N. R., Wallinga, J., Bessière, A., and Dorenbos, P. (2010). Energy levels in $YPO_4 : Ce^{3+}, Sm^{3+}$ studied by thermally and optically stimulated luminescence. *Radiation Measurements*, 45(3):343–346.

Briesmeister, J. F. (2000). MCNP^{TM}-*A general Monte Carlo N-particle transport code*. Los Alamos National Laboratory.

Calmon, P., Mahaut, S., Chatillon, S., and Raillon, R. (2006). CIVA: an expertise platform for simulation and processing NDT data. 44 Suppl 1:e975–979.

Cashwell, E. D. and Everett, C. J. (1959). *A practical manual on the Monte Carlo method for random walk problems*. Pergamon Press.

Catlow, C. R. A. (1986). Computer simulation of defects in solids. In Chadwick, A. V. and Terenzi, M., editors, *Defects in Solids*, NATO ASI Series, pages 269–301. Springer US.

Chernov, S. A., Trinkler, L., and Popov, A. I. (1998). Photo- and thermo-stimulated luminescence of CsI—Tl crystal after UV light irradiation at 80 k. *Radiation Effects and Defects in Solids*, 143(4):345–355.

Cho, G., Kim, H., Chung, Y., Kim, D. K., Lee, H., Suh, T., and Joo, K. (2000). Monte Carlo analyses of X-ray absorption, noise and detective quantum efficiency considering therapeutic x-ray spectrum in portal imaging detector. In *2000 IEEE Nuclear Science Symposium Conference Record*, volume 3, pages 19/64–19/68 vol.3.

Correa, S., Souza, E., Silva, A., Cassiano, D., and Lopes, R. (2010). Computed radiography simulation using the Monte Carlo code MCNPX. *Applied Radiation and Isotopes*, 68(9):1662–1670.

Correa, S. C. A., Souza, E. M., Oliveira, D. F., Silva, A. X., Lopes, R. T., Marinho, C., and Camerini, C. S. (2009). Assessment of weld thickness loss in offshore pipelines using computed radiography and computational modeling. *Applied Radiation and Isotopes: Including Data, Instrumentation and Methods for Use in Agriculture, Industry and Medicine*, 67(10):1824–1828.

Cunningham, I. A., Westmore, M. S., and Fenster, A. (1994). A spatial-frequency dependent quantum accounting diagram and detective quantum efficiency model of signal and noise propagation in cascaded imaging systems. *Medical physics*, 21(3):417–427.

Cunningham, I. A., Yao, J., and Subotic, V. (2002). Cascaded models and the DQE of flat-panel imagers: noise aliasing, secondary quantum noise, and reabsorption. volume 4682, pages 61–72.

De Mul, F. F. M. (2003). Monte-carlo simulations of light scattering in turbid media. Technical report.

Duvauchelle, P., Freud, N., Kaftandjian, V., and Babot, D. (2000). A computer code to simulate x-ray imaging techniques. *Nuclear Instruments and Methods in Physics Research Section B: Beam Interactions with Materials and Atoms*, 170(1):245 – 258.

EN14784-2 (2005). Non-destructive testing - Industrial computed radiography with storage phosphor imaging plates - Part 2: General principles for testing of metallic materials using X-rays and gamma rays.

Fasbender, R., Li, H., and A., W. (2003). Monte carlo modeling of storage phosphor plate readouts. *Nuclear Instruments and Methods in Physics Research Section A: Accelerators, Spectrometers, Detectors and Associated Equipment*, 512(3):610–618.

Flock, S. T., Wilson, B. C., and Patterson, M. S. (1989). Monte carlo modeling of light propagation in highly scattering tissues–II: Comparison with measurements in phantoms. *IEEE transactions on bio-medical engineering*, 36(12):1169–1173.

Freud, N., Duvauchelle, P., Pistrui-Maximean, S., Létang, J.-M., and Babot, D. (2004). Deterministic simulation of first-order scattering in virtual X-ray imaging. *Nuclear Instruments and Methods in Physics Research Section B: Beam Interactions with Materials and Atoms*, 222(1-2):285–300.

Gavaldà, S., Fernández Varea, J. M., Sempau Roma, J., and Organització de Cooperació i Desenvolupament Econòmic (2009). PENELOPE 2008: A code system for Monte Carlo simulation of electron and photon transport : workshop proceedings, barcelona, spain 30 june-3 july 2008. OECD.

George, W. (1975). Apparatus and method for producing images corresponding to patterns of high energy radiation.

Hahn, D. W. (2006). Light scattering theory. *Department of Mechanical and Aerospace Engineering, Florida*.

Hashimoto, M., Tomita, T., Sawada, K., Fujibuchi, T., Nishio, T., and Nakagawa, K. (2009). Dose profile measurement using an imaging plate: Evaluation of filters using monte carlo simulation of 4 MV x-rays. *The Review of Scientific Instruments*, 80(4):045101.

Huang, H. K. (2010). *PACS and Imaging Informatics: Basic Principles and Applications*. John Wiley & Sons.

ISO17636-2 (2013). Non-destructive testing of welds – Radiographic testing – Part 2: X- and gamma-ray techniques with digital detectors.

Jaffray, D. A., Battista, J. J., Fenster, A., and Munro, P. (1995). Monte Carlo studies of X-ray energy absorption and quantum noise in megavoltage transmission radiography. *Medical Physics*, 22(7):1077–1088.

Kausch, C., Schreiber, B., Kreuder, F., Schmidt, R., and Dossel, O. (1999). Monte Carlo simulations of the imaging performance of metal plate/phosphor screens used in radiotherapy. *Medical Physics*, 26(10):2113–2124.

Klein, C. A. (1968). Bandgap dependence and related features of radiation ionization energies in semiconductors. *Journal of Applied Physics*, 39(4):2029–2038.

Koschnick, F. K., Spaeth, J.-M., and Eachus, R. S. (1992). Study of spatial correlations between radiation-induced defects and the activator Eu^{2+} in the x-ray storage phosphor $BaFBr : Eu^{2+}$ with optical detection of electron paramagnetic resonance. *Journal of Physics: Condensed Matter*, 4(45):8919.

Koschnick, n., Spaeth, n., Eachus, n., McDugle, n., and Nuttall, n. (1991). Experimental evidence for the aggregation of photostimulable centers in BaFBr : Eu^{2+} single crystals by cross relaxation spectroscopy. *Physical Review Letters*, 67(25):3571–3574.

Kotera, N., Eguchi, S., Miyahara, J., Matsumoto, S., and Kato, H. (1980). Method and apparatus for recording and reproducing a radiation image.

Lança, L. and Silva, A. (2009). Digital radiography detectors – a technical overview: Part 1. *Radiography*, 15(1):58–62.

Leblans, P., Struye, L., and Gebele, H. (1999). A new detector for digital radiography: the best of two worlds. volume XV.

Leblans, P., Struye, L., and Willems, P. (2000). A new needle-crystalline computed radiography detector. *Journal of Digital Imaging*, 13:117–120.

Leblans, P., Vandenbroucke, D., and Willems, P. (2011). Storage phosphors for medical imaging. *Materials*, 4(6):1034–1086.

Lewis, E. E. and Miller, W. F. (1984). *Computational methods of neutron transport*. Wiley.

Li, H. H., Gonzalez, A. L., Ji, H., and Duggan, D. M. (2007). Dose response of $BaFBrI$: Eu^{2+} storage phosphor plates exposed to megavoltage photon beams. *Medical physics*, 34(1):103–111.

Liaparinos, P. F. and Kandarakis, I. S. (2009). The Monte Carlo evaluation of noise and resolution properties of granular phosphor screens. *Physics in Medicine and Biology*, 54(4):859–874.

Liaparinos, P. F., Kandarakis, I. S., Cavouras, D. A., Delis, H. B., and Panayiotakis, G. S. (2006). Modeling granular phosphor screens by Monte Carlo methods. *Medical Physics*, 33(12):4502–4514.

Liaparinos, P. F., Kandarakis, I. S., Cavouras, D. A., Delis, H. B., and Panayiotakis, G. S. (2007). Monte Carlo study on the imaging performance of powder $Lu_2SiO_5 : Ce$ phosphor screens under X-ray excitation: Comparison with $Gd_2O_2S : Tb$ screens. *Medical Physics*, 34(5):1724.

Lubinsky, A. R., Owen, J. F., and Korn, D. M. (1986). Storage phosphor system for computed radiography: Screen optics. volume 0626, pages 120–132.

Maarek, J. M., Jarry, G., de Cosnac, B., Lansiart, A., and Bui-Mong-Hung, n. (1984). A simulation method for the study of laser transillumination of biological tissues. *Annals of Biomedical Engineering*, 12(3):281–304.

Mango, S. and Castro, L. (2009). MYTHS vesus reality in computed radiography image quality.

Margallo-Balbás, E. and French, P. J. (2007). Shape based monte carlo code for light transport in complex heterogeneous tissues. *Optics Express*, 15(21):14086–14098.

Martelli, F., Del Bianco, S., Ismaelli, A., and Zaccanti, G. (2010). *Light Propagation through Biological Tissue and Other Diffusive Media*. SPIE, 1000 20th Street, Bellingham, WA 98227-0010 USA.

Mathy, F., Schumm, A., Tabary, J., and Hugonnard, P. (2011). Modelling computed radiography detectors with a cascaded linear system model.

Meijerink, A. (1996). Photostimulated luminescence and thermally stimulated luminescence of $(Ba, Sr)F_{1+x}Rr_{1-x} - Eu^{2+}$. *Materials Chemistry and Physics*, 44(2):170 – 177.

Meijerink, A. and Blasse, G. (1991). Photostimulated luminescence and thermally stimulated luminescence of some new X-ray storage phosphors. *Journal of Physics D: Applied Physics*, 24(4):626.

Meijerink, A., Schipper, W. J., and Blasse, G. (1991). Photostimulated luminescence and thermally stimulated luminescence of $Y_2SiO_5 - Ce, Sm$. *Journal of Physics D: Applied Physics*, 24(6):997.

Mengkuo, W. (2006). CAD based monte carlo method: Algorithms for geometric evaluation in support of monte carlo radiation transport calculation.

Miyahara, J., Takahashi, K., Amemiya, Y., Kamiya, N., and Satow, Y. (1986). A new type of X-ray area detector utilizing laser stimulated luminescence. *Nuclear Instruments and Methods in Physics Research Section A: Accelerators, Spectrometers, Detectors and Associated Equipment*, 246(1–3):572–578.

Parker, S. C., Cooke, D. J., Kerisit, S., Marmier, A. S., Taylor, S. L., and Taylor, S. N. (2004). From hades to paradise—atomistic simulation of defects in minerals. *Journal of Physics: Condensed Matter*, 16(27):S2735.

Patwardhan, S. V., Dhawan, A. P., and Relue, P. A. (2005). Monte carlo simulation of light-tissue interaction: three-dimensional simulation for trans-illumination-based imaging of skin lesions. *IEEE transactions on bio-medical engineering*, 52(7):1227–1236.

Pelowitz, D. B. (2008). MCNPX^{TM} *USER'S MANUAL*. Los Alamos National Laboratory report LA-CP-07-1473.

Prahl, S. A., Keijzer, M., Jacques, S. L., and Welch, A. J. (1989). A monte carlo model of light propagation in tissue. *Dosimetry of laser radiation in medicine and biology*, 5:102–111.

Premože, S., Ashikhmin, M., Tessendorf, J., Ramamoorthi, R., and Nayar, S. (2004). Practical rendering of multiple scattering effects in participating media. In *Proceedings of the Fifteenth Eurographics conference on Rendering Techniques*, pages 363–374. Eurographics Association.

Rogers, D. W. O. (2006). Fifty years of Monte Carlo simulations for medical physics. *Physics in medicine and biology*, 51(13):R287–301.

Rowlands, J. A. (2002). The physics of computed radiography. *Physics in Medicine and Biology*, 47(23):R123–R166.

Salis, M. (2003). On the photo-stimulated luminescence of BaFBr : Eu^{2+} phosphors. *Journal of Luminescence*, 104(1):17–25.

Sattarivand, M. and Cunningham, I. A. (2005). Computational engine for development of complex cascaded models of signal and noise in x-ray imaging systems. *IEEE transactions on medical imaging*, 24(2):211–222.

Schipper, W. J., Hamelink, J. J., Langeveld, E. M., and Blasse, G. (1993). Trapping of electrons by H^+ in the x-ray storage phosphor $Ba_3(PO_4)_2 : Eu^{2+}, La^{3+}$. *Journal of Physics D: Applied Physics*, 26(9):1487.

Schweizer, S. (2001). Physics and current understanding of X-Ray storage phosphors. *physica status solidi (a)*, 187(2):335–393.

Seggern, H. v. (1999). Photostimulable X-ray storage phosphors: a review of present understanding. *Brazilian journal of physics*, 29(2):254–268.

Seggern, H. v., Voigt, T., Knüpfer, W., and Lange, G. (1988). Physical model of photostimulated luminescence of x-ray irradiated $BaFBr : eu^{2+}$. *Journal of Applied Physics*, 64(3):1405–1412.

Selling, J., Schweizer, S., Spaeth, J.-M., Corradi, G., Edgar, A., and Williams, G. (2005). Radiation defects in Ce-doped $BaCl_2$ and fluorochlorozirconate glass-ceramic x-ray storage phosphors. *physica status solidi (c)*, 2(1):592–595.

Slide, A. (2014). *The New Historical Dictionary of the American Film Industry*. Routledge.

Smithies, D. J. and Butler, P. H. (1995). Modelling the distribution of laser light in port-wine stains with the monte carlo method. *Physics in Medicine and Biology*, 40(5):701–731.

Sonoda, M., Takano, M., Miyahara, J., and Kato, H. (1983). Computed radiography utilizing scanning laser stimulated luminescence. *Radiology*, 148(3):833–838.

Souza, E. M., Correa, S. C. A., Silva, A. X., Lopes, R. T., and Oliveira, D. F. (2008). Methodology for digital radiography simulation using the Monte Carlo code MCNPX for industrial applications. *Applied radiation and isotopes: including data, instrumentation and methods for use in agriculture, industry and medicine*, 66(5):587–592.

Tabary, J., Hugonnard, P., and Mathy, F. (2007). SINDBAD: a realistic multi-purpose and scalable x-ray simulation tool for NDT applications. volume 1, pages 1–10.

Takahashi, K., Kohda, K., Miyahara, J., Kanemitsu, Y., Amitani, K., and Shionoya, S. (1984). Mechanism of photostimulated luminescence in BaFX : Eu^{2+} (X=Cl,Br) phosphors. *Journal of Luminescence*, 31–32, Part 1:266–268.

Tautges, T. J., Wilson, P. P., Kraftcheck, J., Smith, B. F., and Henderson, D. L. (2009). Acceleration techniques for direct use of CAD-based geometries in monte carlo radiation transport. In *International Conference on Mathematics, Computational Methods & Reactor Physics (M&C 2009)*.

Thoms, M. (1996a). Image properties of polycrystalline storage films. *Applied optics*, 35(19):3702–3714.

Thoms, M. (1996b). The quantum efficiency of radiographic imaging with image plates. *Nuclear Instruments and Methods in Physics Research Section A: Accelerators, Spectrometers, Detectors and Associated Equipment*, 378(3):598–611.

Thoms, M. (1997). The dynamic range of X-ray imaging with image plates. *Nuclear Instruments and Methods in Physics Research Section A: Accelerators, Spectrometers, Detectors and Associated Equipment*, 389(3):437–440.

Thoms, M. and Seggern, H. v. (1994). Method for the determination of photostimulable defect center concentrations, production rates, and effective formation energies. *Journal of Applied Physics*, 75(9):4658–4661.

Thoms, M., von Seggern, H., and Winnacker, A. (1991). Spatial correlation and photostimulability of defect centers in the x-ray-storage phosphor $BaFBr : Eu^{2+}$. *Physical Review B*, 44(17):9240–9247.

Tisseur, D., Costin, M., Mathy, F., and Schumm, A. (2014). Simulation of computed radiography with imaging plate detectors. In *AIP Conference Proceedings*, volume 1581, pages 1861–1867. AIP Publishing.

Vedantham, S. and Karellas, A. (2010). Modeling the performance characteristics of computed radiography (CR) systems. *IEEE transactions on medical imaging*, 29(3):790–806.

Wang, L., Jacques, S. L., and Zheng, Q. (1995). MCML—Monte Carlo modeling of light transport in multi-layered tissues. *Computer Methods and Programs in Biomedicine*, 47(2):131 – 146.

Willcox, M. and Downes, G. (2000). A brief description of NDT techniques.

Winch, N. M. (2008). Light scattering in glass ceramic X-ray imaging plates.

Wu, S., Jin, X., Xie, C., and Cao, G. (2005). Optimal steel thickness combined with computed radiography for portal imaging of nasopharyngeal cancer patients. *Medical Physics*, 32(10):3112–3116.

Zhu, C. and Liu, Q. (2013). Review of monte carlo modeling of light transport in tissues. *Journal of biomedical optics*, 18(5):050902–1–050902–12.

Zych, E., Trojan-Piegza, J., Hreniak, D., and Strek, W. (2003). Properties of Tb-doped vacuum-sintered Lu_2O_3 storage phosphor. *Journal of Applied Physics*, 94(3):1318.

Abbreviations

CAD Computer-aided Design. 26

CR Computed Radiography. 2

EAE Energy Absorption Efficiency. 41

IP Imaging Plate. 2, 140

MTF Modulation Transfer Function. 3, 41

NDT Non-Destructive Testing. 2

PSF Point Spread Function. 44

PSL Photo-stimulated Luminescence. xxxix, 5, 10, 87

PSP Photo-stimulated Phosphor. 9, 84

Main Symbols

$Limg(x, y, z)$ Latent image (unit: cm^{-3}). 67

$Obj(E, x, y)$ Spectral object image (Unit: $\mathrm{cm}^{-2} \cdot \mathrm{keV}^{-1}$). 66, 68, 69

μ_α Absorption coefficient (unit: cm^{-1}). 88

n_{binder} Refraction index of binder (unit: 1). 88

$DEP(x, y, z)$ 3D map of deposited energy in IP (unit: $\mathrm{keV} \cdot \mathrm{cm}^{-3}$). xxxvii, 43, 70

$f(x, y, z)$ Laser distribution function (unit: cm^{-2}). 118

D_{gs} Grain size (unit: cm). 88

g_{sc} Absorbed X-ray energy to storage center conversion efficiency (unit: keV^{-1}). 67

$I(x, y, z)$ Laser light intensity function (unit: $\mathrm{cm}^{-2}\mathrm{s}^{-1}$). 85

$n_{sc}^{m,n-1}(x, y, z)$ The storage center distribution map right before the laser beam arrives at pixel (m, n) (unit: cm^{-3}). 85

$f_{packing}$ Packing factor (unit: 1). 88

n_{PSP} Refraction index of phosphor (unit: 1). 88

$P(z)$ Probability that a photon emitted at z could escape from the front surface of IP (unit: 1). 85

$PSF_{det}(E, x, y, z)$ Detector response model (unit: cm^{-3}). 67, 69

μ_s Scattering coefficient (unit: cm^{-1}). 88

σ Optical cross section of photo-stimulation (unit: cm^2). 85

$Dimg(x_m, y_n)$ CR image signal at pixel (m, n) (unit: cm^{-2}). 85

d Thickness (unit: cm). 88

t_{scan} Laser spot dwell time on a pixel (unit: s). 85